

# ADTSC Science Highlights 2009

Associate Directorate for Theory, Simulation, and Computation

## *Preface*

The Theory, Simulation, and Computation (TSC) Directorate is central to the huge national need for new generations of ideas, concepts, and methodologies to improve the fidelity, reliability, certainty and usability of tools to guide and interpret experiments, and provide prediction and control for complex phenomena and systems: the “Information Science and Technology” capability between data and prediction. Working with teams across the Laboratory, TSC undertakes major interdisciplinary challenges of integrating theory, modeling, simulation, high-performance computing, and visualization with experimental and other data to expand LANL’s predictive and uncertainty quantification capability. The core nuclear weapons program depends critically on the viability of this approach. However, virtually every emerging mission initiative at LANL also relies centrally on a similar integrated capability: threat reduction, energy security, manufacturing science, and many discipline frontiers from biology to materials science to cosmology.

Each year, TSC staff select a collection of brief topical reports on their recent research results. This annual collection is not intended to be complete. Rather it aims to demonstrate, through timely examples, the interdisciplinary energy and progress across many scientific and program frontiers. The collection chosen this year represents work for the National Nuclear Security Administration and also presents examples from our “work with others” portfolio. This collection is representative of our outreach activities to universities, industry, and other research laboratories, and is a basis for providing the best science and scientists to both current and future national security missions at LANL.

**Alan R. Bishop**  
Associate Director, Theory, Simulation, and Computation Directorate

**Alan R. Bishop**  
*Associate Director*

**Paul J. Dotson**  
*Deputy Associate Director*

**Andrew B. White**  
*Deputy Associate Director  
for High-Performance  
Computing*

**Audrey L. Archuleta**  
*ADTSC Chief of Staff*

**Stephen R. Lee**  
*CCS Division Leader*

**John F. Morrison**  
*HPC Division Leader*

**Antonio Redondo**  
*T Division Leader*

## **Publications Team**

**Susanne King,**  
**Kathy Pallis**  
*Editors*

**Sharon Mikkelsen**  
*Design and Coordination*

**Guadalupe D. Archuleta**  
*Print Coordinator*

ADTSC web site: <http://www.lanl.gov/orgs/adtsc>





## Section 1. Advanced Computational Architectures

The New Mexico Supercomputing Challenge <i>David H. Kratzer, HPC-3</i> .....	2
Coordinating Government Investments in High-end Computing File Systems and I/O <i>Gary A. Grider, HPC-DO; James A. Nunez, John M. Bent, HPC-5</i> .....	4
Petascale Molecular Dynamics on Roadrunner <i>Timothy C. Germann, Kai Kadau, T-1; Sriram Swaminarayan, CCS-2</i> .....	6
Compressible Flow Simulation on Roadrunner <i>Jamaludin Mohd-Yusof, Daniel Livescu, Timothy Kelley, Mark R. Petersen, CCS-2</i> .....	8

## Section 2. Applied Mathematics, Fluid Dynamics, and Magnetohydrodynamics

Richtmyer-Meshkov Instability via Direct Simulation Monte-Carlo <i>John L. Barber, T-1</i> .....	12
Initial Growth of the Rayleigh-Taylor Instability via Molecular Dynamics <i>John L. Barber, Kai Kadau, Timothy C. Germann, T-1; Berni J. Alder, LLNL</i> .....	14
Memory Function Formalisms for System Reduction in Molecular Dynamics <i>John L. Barber, T-1</i> .....	16
Robust Rezoning in ALE Aided by Mesh Untangling <i>Markus Berndt, Milan Kucharik, Mikhail Shashkov, T-5</i> .....	18
Grid Generation and Adaptation Using an $L_p$ form of Monge-Kantorovich Optimization <i>Gian Luca Delzanno, John M. Finn, T-5</i> .....	20
Mimetic Finite Differences for Modeling Stokes Flow on Polygonal Meshes <i>Vitaliy Gyrya, Pennsylvania State University; Konstantin Lipnikov, T-5</i> .....	22
Mixing Asymmetry in Variable Density Turbulence <i>Daniel Livescu, CCS-2; J. R. Ristorcelli, X-3; Robert Gore, X-4; Sumner H. Dean, CCS-2</i> .....	24
Predicting Reservoir Performance: A New Multiscale Method for Well Modeling <i>Konstantin Lipnikov, David Moulton, Daniil Svyatskiy, T-5</i> .....	26





On the Role of Initial Deposition of Baroclinic Vorticity in Richtmeyer-Meshkov Instability <i>Balu Nadiga, CCS-2</i> .....	28
High Resolution Simulations of Compressible Isotropic Turbulence <i>Mark R. Petersen, Daniel Livescu, Sumner H. Dean, Jamaludin Mohd-Yusof, CCS-2</i> .....	30
Two Conjectures on the Crisis of Cell-Centered Diffusive Operators for the Iterative Acceleration of Neutron Transport Methods in the PHI Configuration <i>Massimiliano Rosa, CCS-2; Yousry Y. Azmy, North Carolina State University; Jim E. Morel, Texas A&amp;M University</i> .....	32
Multimaterial Incompressible Flow Simulation Using the Moment-of-fluid Method <i>Samuel P. Schofield, Rao V. Garimella, Blair K. Swartz, T-5; Mark A. Christon, SIMULIA; Vadim Dyadechko, Exxon Mobile; Robert B. Lowrie, CCS-2</i> .....	34
A Sharp-to-continuous Interface Tracking Transition Algorithm for Multicomponent Fluid Flow Simulation <i>Marianne M. Francois, Robert B. Lowrie, Edward D. Dendy, CCS-2</i> .....	36
Regularization of Particle Transport Models with Diffusive Relaxation <i>Cory D. Hauck, Robert B. Lowrie, CCS-2</i> .....	38

### Section 3. Astrophysics and Cosmology

Radiative Losses of the Solar Corona <i>James Colgan, Joseph Abdallah, Jr., Manolo E. Sherrill, T-1; Christopher J. Fontes, X-1-NAD; U. Feldman, Artep, Inc.</i> .....	42
Modeling Emissions from Supernovae: Preparation for the Joint Dark Energy Mission <i>Chris L. Fryer, CCS-2; Aimee Hungerford, X-4-PC; Gabriel Rockefeller, CCS-2; Christopher J. Fontes, X-1-NAD; Lucy Frey, X-3-MA; Steven Diehl, T-2; Paolo Mazzali, Instituto di Astrofisica-Osservatorio Astronomico; Stefan Immler, NASA Goddard Space Flight Center</i> .....	44
New Nucleosynthesis Process Discovered in the Crust of Neutron Stars <i>Sanjib S. Gupta, Peter Möller, Toshihiko Kawano, T-2</i> .....	46
The Coyote Universe <i>Salman Habib, T-2; Katrin Heitmann, ISR-1; David Higdon, Earl Lawrence, CCS-6; Christian Wagner, Astrophysikalisches Institut Potsdam; Martin White, University of California, Berkeley; Brian J. Williams, CCS-6</i> ....	48





The Structure of Dark Matter Halos <i>Salman Habib, T-2; Katrin Heitmann, ISR-1; Zarija Lukic, Darren Reed, T-2</i> .....	50
--	----

## Section 4. Atomic, Nuclear, and High Energy Physics

Electron-ion Temperature Relaxation in Dense Plasmas <i>Jérôme Daligault, T-5; Guy Dimonte, X-1</i> .....	54
The Neutron-neutron Scattering Length Using the Radiative $\pi^-$ Capture Reaction in Deuterium <i>William R. Gibbs, New Mexico State University; Benjamin F. Gibson, T-2</i> .....	56
Measurement and Analysis of the ${}^6\text{Li}(n,t){}^4\text{He}$ Cross Section <i>Gerald M Hale, T-2; Matthew J. Devlin, LANSCE-NS</i> .....	58
Uncertainty Quantification of Prompt Fission Neutrons Spectra <i>Patrick Talou, David G. Madland, Toshihiko Kawano, T-2</i> .....	60
Jayenne Implicit Monte Carlo Project: Y2008 Improvements <i>Todd Urbatsch, CCS-2; Scott Mosher, ORNL; Seth R. Johnson, University of Michigan; Michael Buksas, CCS-2; Aimee Hungerford, X-4-PC; Jeffery Densmore, Chris L. Fryer, Timothy Kelley, Paul Henning, Gabriel Rockefeller, CCS-2</i> .....	62
Jet Physics at the Large Hadron Collider <i>Ivan Vitev, Ben-Wei Zhang, T-2</i> .....	64

## Section 5. Chemistry and Bioscience

Interfacial Electron Transfer Dynamics of Ru(II)-polypyridine-sensitized $\text{TiO}_2$ <i>Elena Jakubikova, Richard L. Martin, Enrique R. Batista, T-1; Robert C. Snoeberger III, Victor S. Batista, Yale University</i> .....	68
Theoretical Studies on the Stability of Molecular Platinum Catalysts for Hydrogen Production <i>Lindsay E. Roy, Enrique R. Batista, T-1</i> .....	70
Accurate Calculation of Redox Potentials Using Density Functional Methods <i>Lindsay E. Roy, Elena Jakubikova, Enrique R. Batista, T-1</i> .....	72



The Role of the Hydration Shell of Proteins <i>Guo Chen, Paul W. Fenimore, T-6; Joel Berendzen, P-21; Hans Frauenfelder, Benjamin H. McMahon, T-6</i> .....	74
Structural Alterations of a Vaccine Target: Clade-specific Differences and Immune Escape of HIV-1 Surface Protein <i>S. Gnanakaran, T-6; Cynthia Derdeyn, Emory University; Bette Korber, T-6</i> .....	76
Hidden Structure in Protein Energy Landscapes <i>Dengming Ming, Marian Anghel, Michael E. Wall, CCS-3</i> .....	78
Computational Prediction of Bacterial Behavior <i>David W. Dreisigmeyer, Jelena Stajic, Ilya Nemenman, CCS-3; William S. Hlavacek, T-6; Michael E. Wall, CCS-3</i> .....	80

## Section 6. Climate Modeling

Age Characteristics in a Multidecadal Arctic Sea Ice Simulation <i>Elizabeth C. Hunke, T-3; Cecilia M. Bitz, Atmospheric Sciences, University of Washington</i> .....	84
Climate, Ocean, and Sea Ice Modeling <i>Philip Jones, Elizabeth Hunke, William Lipscomb, Mathew Maltrud, Stephen Price, Todd Ringler, Bin Zhao, T-3; Scott Elliott, Matthew Hecht, Balu Nadiga, Nicole Jefferey, Mark R. Petersen, Wilbert Weijer, Beth Wingate, CCS-2</i> .....	86
Tracking Chlorofluorocarbons in a Global Eddying Ocean Model <i>Mathew Maltrud, T-3; Synte Peacock, Frank Bryan, National Center for Atmospheric Research, Boulder, CO</i> .....	88
A New Dynamical Feature of Wind-driven Ocean Circulation <i>Balu Nadiga, CCS-2</i> .....	90
Ice Sheet Modeling for the Prediction of Sea Level Rise <i>Stephen Price, William Lipscomb, Todd Ringler, John Dukowicz, T-3; Antony Payne, Bristol Glaciology Centre, University of Bristol, Bristol, UK</i> .....	92
Modal Variability of the Southern Ocean <i>Wilbert Weijer, CCS-2</i> .....	94



## Section 7. Information Science and Technology

High Data-rate, Free-space Laser Communication Based on Frequency Encoding of a Partially Coherent Beam <i>Gennady Berman, Boris Chernobrod, T-4; Alan R. Bishop, ADTSC</i> .....	98
The Stability of Cellulose: A Perspective from the Statistical Mechanics of Hydrogen Bond Networks <i>Tongye Shen, CNLS and T-6; S. Gnanakaran, T-6</i> .....	100
Uncovering Computational Primitives that Endow Neural Networks with their Information Processing Abilities <i>Ilya Nemenman, CCS-3; Geoffrey Lewen, Hun High School, Princeton, NJ; Rob de Ruyter van Steveninck, Indiana University; William Bialek, Princeton University</i> .....	102
Derivation of Knowledge from Digital Content <i>A. Shelly Spearing, Jorge H. Román, HPC-1; M. Linn Collins, STBPO-RL</i> .....	104

## Section 8. Materials Science

Analysis of Dynamically Driven, Single-crystal Experiments <i>Irene J. Beyerlein, Francis L. Addessio, Zhiqiang Wang, T-3; George T. Gray, Ellen K. Cerreta, Fang Cao, MST-8</i> .....	108
Modeling the Microstructural Evolution of Metallic Polycrystalline Materials under Localization Conditions <i>Curt A. Bronkhorst, T-3; Benjamin L. Hansen T-3 and California Institute of Technology; Ellen K. Cerreta, John F. Bingert, MST-8</i> .....	110
Finding Relevant Atomic Processes Using Accelerated Molecular Dynamics <i>Abhijit Chatterjee, Arthur F. Voter, T-1</i> .....	112
The Effect of Inclusions on Phase Transformations in Dynamically Driven Plates <i>Bradford E. Clements, T-1; Francis L. Addessio, T-3; Jeeyeon N. Plohr, T-1</i> .....	114
Statistical Models for Understanding the Enduring Conventional and Nuclear Weapons Stockpile <i>Aparna V. Huzurbazar, Christine Anderson-Cook, Todd Graves, Michael Hamada, Geralyn Hemphill, David Higdon, Richard Klamann, Scott Vander Wiel, CCS-6</i> .....	116
Multifield Fragmentation <i>Bucky Kashiwa, Mark Schraad, T-3; Larry Hull, DE-6</i> .....	118

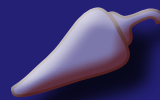




Molecular Dynamics Investigation of the Rapid Diffusion of Very Large Heteroepitaxial Islands <i>Obioma U. Uche, SNL; Danny Perez, Arthur F. Voter, T-1; John C. Hamilton, SNL</i> .....	120
Transformation Pathways and Energetics in Plutonium <i>Turab Lookman, Avadh B. Saxena, Robert C. Albers, Roman Groger, T-4</i> .....	122
Nanoscale Roughness and Cliffs in Low-temperature Growth of a Copper Surface <i>Yunsic Shim, Valery Borovikov, Jacques G. Amar, University of Toledo; Blas P. Uberuaga, MST-8; Arthur F. Voter, T-1</i> .....	124
Statistical Design for Uranium Corrosion Experiments <i>Joanne R. Wendelberger, Leslie M. Moore, CCS-6</i> .....	126
Blast Effects Analysis with the CartaBlanca Computer Code <i>Paul T. Giguere, Xia Ma, Duan Z. Zhang, T-3</i> .....	128

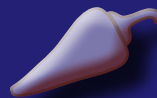
## Section 9. Modeling Complex Networks

How Far is Far from Equilibrium? A Deeper Understanding in the Presence of Noise <i>Antonio M. Cadilhe, T-1 and GCEP-Centro de Fisica da Universidade do Minho, Braga, Portugal; Arthur F. Voter, T-1</i> .....	132
BIOGRAM: Algorithms for Identifying Similar Proteins by Functional Annotation <i>Judith D. Cohn, Susan M. Mniszewski, CCS-3; Hong Cai, Jennifer F. Harris, B-7; Ruy M. Rubeiro, T-6; Cliff A. Joslyn, PNNL; Karin. M. Verspoor, University of Colorado Health Sciences Center</i> .....	134
ActivitySim: Large-scale Agent-based Activity Generation for Infrastructure Simulation <i>Emanuele Galli, Stephan Eidenbenz, Susan M. Mniszewski, CCS-3; Leticia Cuellar, D-6; Mary Ewers, D-4; Christof Teuscher, Portland State University</i> .....	136
Using the MIITS-Internet Tool to Perform Criticality Analysis of National Internet Infrastructure <i>Guanhua Yan, CCS-3; Pallab Datta, Neurosciences Institute; Stephan Eidenbenz, Sunil Thulasidasan, CCS-3; Venkatesh Ramaswamy, Airvana, Inc.</i> .....	138



## Funding Acknowledgment Cross Reference

Center for Nonlinear Studies (CNLS) .....	122
DoD and DOE Joint Munitions Technology Development Program .....	110, 114, 116, 118
DOE, National Nuclear Security Administration (NNSA), Advanced Simulation and Computing Program (ASC) .....	4, 6, 8, 18, 30, 36, 42, 54, 58, 60, 62, 108, 110, 114, 122
(ASC) Roadrunner Project .....	8
(ASC) Physics and Engineering Models Program .....	6
(ASC) Materials and Physics Program .....	42
(ASC) Hydrodynamics Program .....	36
(ASC) Reactivity and Compression Program .....	58
DOE, National Nuclear Security Administration (NNSA), Defense Programs and Core Surveillance .....	116
DOE, National Nuclear Security Administration (NNSA), Enhanced Surveillance Campaign .....	116, 126
DOE, Office of Biological and Environmental Research (OBER) Climate Change Prediction Program .....	84, 86, 88, 90, 92, 94
DOE, Office of Nuclear Energy, Science and Technology, Advanced Fuel Cycle Initiative (AFCI) .....	60
DOE, Office of Science (SC) .....	4, 16, 22, 26, 38, 48, 56, 64, 86, 92, 112, 120, 128, 132
(SC) High Energy Physics, Dark Energy Program .....	48
(SC) Office of Nuclear Physics .....	56
(SC) Office of Advanced Scientific Computing Research (ASCR) .....	16, 22, 26, 38, 128
(SC) Scientific Discovery through Advanced Computing Program (SciDAC) .....	4, 86, 92
(SC) Office of Basic Energy Sciences (BES) .....	112, 120, 132
Department of Homeland Security .....	136, 138
Glenn T. Seaborg Institute .....	122
LANL Directed Research and Development Program .....	8, 12, 14, 16, 20, 24, 30, 32, 34, 44, 46, 48, 50, 64, 68, 70, 72, 74, 76, 78, 80, 100, 102, 112, 122, 124, 134
LANL Postdoctoral Fellowship Program .....	92, 120



LANL Research Library, Emergency Situation Overview and Synthesis (ESOS).....	104
LANL Institute of Geophysics and Planetary Physics (IGPP).....	48, 50
LANL Institutional Computing Resources .....	28
LANL Institutional Supercomputing Awards.....	48, 50
National Science Foundation.....	84, 88, 124
Office of Naval Research .....	98
Sandia National Laboratories .....	2
State of New Mexico .....	2





## Author Cross Reference

### A

Abdallah, Joseph Jr. ....	42
Addessio, Francis L. ....	108, 114
Albers, Robert C. ....	122
Alder, Berni J. ....	14, 76
Amar, Jacques G. ....	124
Anderson-Cook, Christine ....	116
Anghel, Marian. ....	78
Azmy, Yousry Y. ....	32

### B

Barber, John L. ....	12, 14, 16
Batista, Enrique R. ....	68, 70, 72
Batista, Victor S. ....	68
Bent, John M. ....	4
Berendzen, Joel ....	74
Berman, Gennady ....	98
Berndt, Markus ....	18
Beyerlein, Irene J. ....	108
Bialek, William ....	102
Bingert, John F. ....	110
Bishop, Alan R. ....	98
Bitz, Cecilia M. ....	84
Borovikov, Valery ....	124
Bronkhorst, Curt A. ....	110
Bryan, Frank ....	88
Buksas, Michael ....	62

### C

Cadilhe, Antonio M. ....	132
Cai, Hong. ....	134
Cao, Fang. ....	108
Cerreta, Ellen K. ....	108, 110
Chatterjee, Abhijit ....	112

Chen, Guo ....	74
Chernobrod, Boris. ....	98
Christon, Mark A. ....	34
Clements, Bradford E. ....	114
Cohn, Judith D. ....	134
Colgan, James. ....	42
Collins, M. Linn ....	104
Cuellar, Leticia ....	136

### D

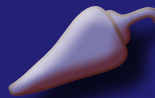
Daligault, Jérôme ....	54
Datta, Pallab ....	138
Dean, Sumner H. ....	24, 30
Delzanno, Gian Luca. ....	20
Dendy, Edward D. ....	36
Densmore, Jeffery ....	62
Derdeyn, Cynthia. ....	76
Devlin, Matthew J. ....	58
Diehl, Steven ....	44
Dimonte, Guy. ....	54
Dreisigmeyer, David W. ....	80
Dukowicz, John ....	92
Dyadechko, Vadim ....	34

### E

Eidenbenz, Stephan. ....	136, 138
Elliott, Scott ....	86
Ewers, Mary ....	136

### F

Feldman, U. ....	42
Fenimore, Paul W. ....	74
Finn, John M. ....	20
Fontes, Christopher J. ....	42, 44



Francois, Marianne M.....	36
Frauenfelder, Hans.....	74
Frey, Lucy.....	44
Fryer, Chris L.....	44, 62

## G

Galli, Emanuele .....	136
Garimella, Rao V.....	34
Germann, Timothy C. ....	6, 14
Gibbs, William R. ....	56
Gibson, Benjamin F. ....	56
Giguere, Paul T.....	128
Gnanakaran, S. ....	76, 100
Gore, Robert A. ....	24
Graves, Todd .....	116
Gray, George T. ....	108
Grider, Gary A. ....	4
Groger, Roman .....	122
Gupta, Sanjib S. ....	46
Gyrya, Vitaliy .....	22

## H

Habib, Salman .....	48, 50
Hale, Gerald M.....	58
Hamada, Michael.....	116
Hamilton, John C.....	120
Hansen, Benjamin L. ....	110
Harris, Jennifer F.....	134
Hauck, Cory D. ....	38
Hecht, Matthew .....	86
Heitmann, Katrin .....	48, 50
Hemphill, GERALYN .....	116
Henning, Paul .....	62
Higdon, David.....	48, 116
Hlavacek, William S. ....	80
Hull, Larry .....	118
Hungerford, Aimee.....	44, 62
Hunke, Elizabeth C.....	84, 86
Huzurbazar, Aparna V.....	116

## I

Immler, Stefan.....	44
---------------------	----

## J

Jakubikova, Elena .....	68, 72
Jefferey, Nicole .....	86
Jones, Philip .....	86
Johnson, Seth R. ....	62
Joslyn, Cliff A.....	134

## K

Kadau, Kai.....	6, 14
Kashiwa, Bucky .....	118
Kawano, Toshihiko.....	46, 60
Kelley, Timothy.....	8, 62
Klamann, Richard.....	116
Korber, Bette .....	76
Kratzer, David H.....	2
Kucharik, Milan.....	18

## L

Lawrence, Earl .....	48
Lewen, Geoffrey.....	102
Lipnikov, Konstantin.....	22, 26
Lipscomb, William .....	86, 92
Livescu, Daniel .....	8, 24, 30
Lookman, Turab .....	122
Lowrie, Robert B. ....	34, 36, 38
Lukic, Zarija .....	50

## M

Ma, Xia .....	128
Madland, David G.....	60
Maltrud, Mathew .....	86, 88
Martin, Richard L. ....	68
Mazzali, Paolo .....	44



McMahon, Benjamin H.....	74
Ming, Dengming .....	78
Mniszewski, Susan M.....	134, 136
Mohd-Yusof, Jamaludin.....	8, 30
Möller, Peter .....	46
Moore, Leslie M. ....	126
Morel, Jim E. ....	32
Mosher, Scott .....	62
Moulton, David.....	26

## N

Nadiga, Balu .....	28, 86, 90
Nemenman, Ilya .....	80, 102
Nunez, James A. ....	4

## P

Payne, Antony.....	92
Peacock, Synte .....	88
Perez, Danny .....	120
Petersen, Mark R. ....	8, 30, 86
Plohr, Jeeyeon N. ....	114
Price, Stephen .....	86, 92

## R

Ramaswamy, Venkatesh .....	138
Reed, Darren .....	50
Ribeiro, Ruy M. ....	134
Ringler, Todd .....	86, 92
Ristorcelli, J.R. ....	24
Rockefeller, Gabriel .....	44, 62
Román, Jorge H.....	104
Rosa, Massimiliano.....	32
Roy, Lindsay E. ....	70, 72
Ruyter van Steveninck, Rob de.....	102

## S

Saxena, Avadh B. ....	122
Schofield, Samuel P. ....	34
Schraad, Mark.....	118
Shashkov, Mikhail .....	18
Shen, Tongye.....	100
Sherrill, Manolo E. ....	42
Shim, Yunsic .....	124
Snoeberger, Robert C. III.....	68
Spearing, A. Shelly .....	104
Stajic, Jelena .....	80
Svyatskiy, Daniil .....	26
Swaminarayan, Sriram .....	6
Swartz, Blair K.....	34

## T

Talou, Patrick.....	60
Teuscher, Christof .....	136
Thulasidasan, Sunil .....	138

## U

Uberuaga, Blas P. ....	124
Uche, Obioma U.....	120
Urbatsch, Todd .....	62

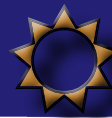
## V

Vander Weil, Scott.....	116
Verspoor, Karin M. ....	134
Vitev, Ivan .....	64
Voter, Arthur F.....	112, 120, 124, 132

## W

Wagner, Christian .....	48
Wall, Michael E.....	78, 80
Wang, Zhiqiang.....	108





Weijer, Wilbert.....	86, 94
Wendelberger, Joanne R. ....	126
White, Martin .....	48
Williams, Brian J.....	48
Wingate, Beth.....	86

## Y

Yan, Guanhua .....	138
--------------------	-----

## Z

Zhang, Ben-Wei.....	64
Zhang, Duan Z .....	128
Zhao, Bin.....	86



# Organizational Abbreviations (for this publication only)

## Applied Physics Division

X-1 Applied Science and Methods Development  
X-1-NAD Nuclear Atomic and EOS Data  
X-3-MA Methods and Algorithms  
X-4-PC Predictive Capability

## Bioscience Division

B-7 Biosecurity and Public Health Group

## Computer, Computational, and Statistical Sciences Division

CCS-2 Computational Physics and Methods Group  
CCS-3 Information Sciences Group  
CCS-6 Statistical Sciences Group

## Decision Applications Division

D-4 Energy and Infrastructure Analysis Group  
D-6 Risk Analysis and Decision Support Systems

## Dynamic and Energetic Materials Division

DE-6 Explosive Applications and Special Projects

## High Performance Computing Division

HPC-1 Scientific Software Engineering  
HPC-2 Computing Operations and Support  
HPC-3 High Performance Computing Systems  
HPC-5 System Integration  
HPC-DO High Performance Computing Division Office

## International, Space & Response Division

ISR-1 Space Science and Applications

## Los Alamos Institutes

INST-OFF Engineering Institute

## Los Alamos Neutron Science Center

LANSC-NS Los Alamos Neutron Science Center-Nuclear Science  
LANSC-WNR Los Alamos Neutron Science Center-Weapons Neutron Research

## Materials Science and Technology Division

MST-8 Structure/Property Relations Group

## Physics Division

P-21 Applied Modern Physics Group

## Science and Technology Base Program Office

STBPO-RL Science and Technology Base Program Office-Research Library

## Theoretical Division

T-1 Physics and Chemistry of Materials  
T-2 Nuclear and Particle Physics, Astrophysics & Cosmology  
T-3 Fluid Dynamics and Solid Mechanics  
T-4 Physics of Condensed Matter and Complex Systems  
T-5 Applied Mathematics and Plasma Physics  
T-6 Theoretical Biology and Biophysics  
CNLS Center for Nonlinear Studies

## Theory, Simulation and Computation Directorate

ADTSC

ANL	Argonne National Laboratory
DoD	Department of Defense
DOE	Department of Energy
LANL	Los Alamos National Laboratory
LLNL	Lawrence Livermore National Laboratory
NASA	National Aeronautics and Space Administration
NNSA	National Nuclear Security Administration
ORNL	Oak Ridge National Laboratory
PNNL	Pacific Northwest National Laboratory
SNL	Sandia National Laboratories
UK	(United Kingdom)





# Advanced Computational Architecture

Computational platforms are the tools of modern science. Computer science is centered on creating new methods and technologies and making computers accessible to scientists to enhance their creativity and pace of discovery. The ongoing development of advanced computational architectures is born out of a need for computational speed along with “Moore’s Law”—a statement made in 1965 by the cofounder of Intel, that the number of transistors on a microprocessor would double approximately every 18 months. Packing more technology into smaller packages translates into rapidly increasingly powerful computational architectures and, theoretically at least, application performance. Four decades later, we are seeing fundamental limits to taking advantage of Moore’s Law realizing actual dramatic performance improvements to applications that run on the new computational engines. Advanced computational architectures seek new, sometimes exotic, architectural designs that accelerate the performance of applications into new realms, and require increased application or software complexity to take advantage of the new designs. Such advances have already reached desktops in the form of dual- and quad-core processors, which will soon become homogeneous and heterogeneous many-core computational engines, outpacing available software and tools. The complexity caused by this many-core architectural direction is not limited to utilizing processors and memory—it permeates all the way through the computing infrastructure including networks and storage. This complexity even affects

computer support facilities like power, cooling, and floor space. The challenges to exploit the future of computing are formidable.

The revolutionary Roadrunner platform, built with PlayStation 3 chips at its core, is an instantiation of an advanced heterogeneous architecture using standard CPUs and “accelerator” chips simultaneously. Roadrunner is perhaps the most notable example of the High Performance Computing (HPC) community beginning to tackle the harnessing of the power of the future architectural reality. Two of the papers in this section are leading edge examples of how forward-thinking computational scientists are unleashing the power of such platforms for science. They describe the techniques used to make scientific applications harness the heterogeneous multicore forward-looking architecture at world-class scale.

Another article in this section gives an overview of how researchers have been tapped by the nation to provide multiagency coordination of all government-funded R&D in the data storage part of the overall computing infrastructure. The advancement of computational technology continues to outpace the capabilities of the mostly mechanical-based storage devices, especially in the performance area. This widening gap between computation and data storage capabilities is the focus of this nationally recognized set of researchers.

Another important part of dealing with and exploiting new architectural paradigms is education and outreach. One article describes a highly successful outreach by

scientists in the computational science area to New Mexico high school science teachers and students. This nationally recognized program has been a huge success for LANL, the State of New Mexico, and the HPC community in building talent for problem solving utilizing high performance computing.

## The New Mexico Supercomputing Challenge

David H. Kratzer, HPC-3



Since 1990, the New Mexico Supercomputing Challenge (the Challenge) has been inspiring students from around New Mexico to pursue their interests in science, technology, engineering, and mathematics. The Challenge is a school-year long, project-based competition/learning experience where teams of one to five students select a computational science project and work on it from September through April.

The vision of the Supercomputing Challenge is to be a nationally recognized program that promotes computational thinking in science and engineering so that the next generation of high school graduates is better prepared to compete in an information-based economy.



*Fig. 1. Logo winner for 2008-2009 done by one of the competing teams.*

The mission of the Supercomputing Challenge is to teach teams of middle and high schools students how to use powerful computers to analyze, model, and solve real-world problems.

A gratifying consequence of being held for 19 years is seeing former participants returning as mentors and judges for current participants. Many former participants have sought employment at LANL, SNL, and other high tech companies. Several students have thought that the Challenge is so worthy that they start “giving back” while they are in college.

Younger students are encouraged to learn about simulation and modeling by using languages like StarLogo The Next Generation and Netlogo, while more advanced students use high-level programming languages like C, C++, Fortran, and Java. A few teams use the Message Passing Interface to perform parallel processing.

Many LANL employees volunteer as instructors at the fall kickoff conference and as project mentors during the year. Approximately 100 LANL employees are involved in the year-end Project Exposition, which includes the judging of the projects, tours of the Laboratory, talks about current research, and an Awards Ceremony.

The Challenge has partnered with a new NSF program called GUTS (Growing Up Thinking Scientifically), which targets middle school students with after-school clubs to do place-based projects in modeling (see <http://projectguts.org>). GUTS is a feeder program into the Challenge. In July of 2008, the Challenge and GUTS cosponsored a Summer Teacher Institute (STI) that trained 34 teachers to be better coordinators and team sponsors. The 2-week STI was held at New Mexico Tech in Socorro, and the teachers received three units of graduate credit from NM Tech. The New Mexico Public Education Department provided much of the funding for the STI.

The Challenge is partnering with the New Mexico Computing Applications Center to be its educational outreach arm, taking advantage of the gateway sites that will be deployed around the state.



*Fig. 2. Tony Huang and Erika DeBenedictis, are all smiles after capturing the top prize during the 2008 New Mexico Supercomputing Challenge hosted by the Laboratory.*



*Fig. 3. Group picture of all the finalists and their team sponsors.*

The Challenge has partnered with New Mexico Innovative Digital Education and Learning (IDEAL) to offer an on-line Advanced Placement Computer Science course. More information about the Challenge can be found on the web page at: <http://www.challenge.nm.org>. Past final reports are available; see the Challenge archives on the web site.

**For more information contact David H. Kratzer at [dhk@lanl.gov](mailto:dhk@lanl.gov).**

### **Funding Acknowledgments**

- LANL
- SNL
- State of New Mexico
- Numerous educational and commercial partners

For a full list of sponsors see <http://www.challenge.nm.org/sponsors.shtml>.



## Coordinating Government Investments in High-end Computing File Systems and I/O

Gary A. Grider, HPC-DO; James A. Nunez, John M. Bent, HPC-5

**M**illion-way parallelism is around the corner and, with it, bandwidth needs to storage will go from tens of gigabytes/s to terabytes/s. Disk access times are not growing at a commensurate rate. These major challenges in file systems and I/O for high-end computing are being addressed through coordinated government agency planning designed to maximize the benefit of R&D investments.

Shortly after the deployment of Japan's Earth System Simulator Supercomputer and due to concerns with programming and optimizing applications to achieve substantial fractions of peak hardware computational power, the United States government realized that the U.S. no longer had clear leadership in the supercomputing arena. Due to this realization, federal budgets included language that required planning activities to guide future investment in high-end computing (HEC). In response, the President's Information Technology Advisory Council formed the High-End Computing Revitalization Task Force (RTF) and, in 2003, convened a workshop: The Roadmap for the Revitalization of High-End Computing. Gary Grider, from the LANL High Performance Computing Division Office, participated in this workshop and helped to craft a set of recommendations [1] to provide guidance in future government spending, and in all aspects of HEC including specification, procurement, and deployment of future HEC systems. One outcome of these recommendations was the formation of the HEC Inter-Agency Working Group (HECIWG) to develop a 5-year plan to find ways to coordinate government R&D in order to make a much more coordinated investment strategy for HEC. The HECIWG is composed of federal agencies including the Department

of Commerce, the Department of Defense, the Department of Energy, the Department of Health and Human Services, the Department of Homeland Security, and the National Science Foundation. The HECIWG decided to pilot Technical Advisory Groups (TAG) in a few important R&D areas to see if coordinating government funding of HEC R&D could help the nation regain leadership in HEC. Due to a persuasive multigovernmental agency white paper [2], file systems and I/O was designated as the first technical advisory group for national focus.

Under the direction of Gary Grider, the HECIWG Technical Advisory Group for File Systems and I/O (HECIWG FSIO) was formed from a variety of government agencies, including SNL, ORNL, ANL, PNNL, NASA, and DARPA. The purpose of the HECIWG FSIO is to coordinate government spending on file systems and I/O R&D by all of the government agencies involved in the HECIWG. The mandate of the HECIWG FSIO is to list, categorize, and prioritize HEC I/O and File Systems R&D needs in particular, and to understand the gap areas that currently exist between the R&D that is being done in industry and the research that is being done in academia.

To collect a broader set of research needs in this area, the first HEC File Systems and I/O workshop was organized by Gary Grider, James Nunez of High Performance Computing Systems Integration (HPC-5) group, and others and held in August 2005 in Grapevine, TX. Government agencies, top universities in the I/O area, and commercial entities that fund file systems and I/O research were invited to help the HECIWG FSIO determine and rank the topics within the FSIO area that in most need of research. The recommended research topics were organized around these themes: metadata, measurement and understanding, quality of service, security, next-generation I/O architectures, communication and protocols, archive, and management and RAS. Additionally, university I/O center support in the forms of computing and simulation equipment availability, and availability of operational data to enable research, and HECIWG institutions involvement in the educational process were called out as areas needing assistance.



As a result of the information gathered at the 2005 workshop, the National Science Foundation (NSF) issued a call to fund research in I/O, and in file and storage systems for the high-end computing environment under the High End Computing University Research Activity (HECURA) program. In the first year, the NSF HECURA solicitation resulted in 62 proposals from over 80 universities with 19 HECURA awards made in areas ranging from autonomies and self-managing, self-healing storage systems to design theoretic approach to data placement.

Grider, Nunez, and John Bent of HPC-5 continue to help organize and set the agenda for the HECIWG FSIO workshop, held every year in August in Washington, D.C. The HECIWG FSIO workshop is very well attended by leaders in the FSIO area and a variety of government agencies. The recommendations and work done through the HECIWG FSIO have been so successful that a second NSF HECURA call focused on FSIO was released in 2009 and will continue to fund R&D in this vital HEC technical area—because without a pipeline of R&D, breakthrough concepts will not emerge. The solicitation will concentrate on areas that are still considered to be gaps and will seek to round out the overall portfolio of R&D to cover the gaps as well as seek proposals that are both evolutionary and revolutionary. A paper in the January 2009 issue of the *Operating Systems Review* [3] reviews the 2008 HECIWG FSIO identified research gaps and previews the forthcoming HECURA solicitation.

For further information contact James A. Nunez at [jnunez@lanl.gov](mailto:jnunez@lanl.gov).

- [1] NITRD High End Computing Revitalization Task Force (HECRTF). *Report of the Workshop on the Roadmap for the Revitalization of High-End Computing*. Daniel A. Reed, Ed. Washington, D.C., June 16-20, 2003.
- [2] R. Ross et al., 2005 *HPC File Systems and Scalable I/O: Suggested Research and Development Topics for the Fiscal 2005-2009 Time Frame*, (2005)  
<http://institutes.lanl.gov/hec-fsio/docs/FileSystems-DTS-SIO-FY05-FY09-R&D-topics-final.pdf>
- [3] G.A. Grider et al., *SIGOPS Oper. Syst. Rev.* **43**:1, 2-7 (2009).

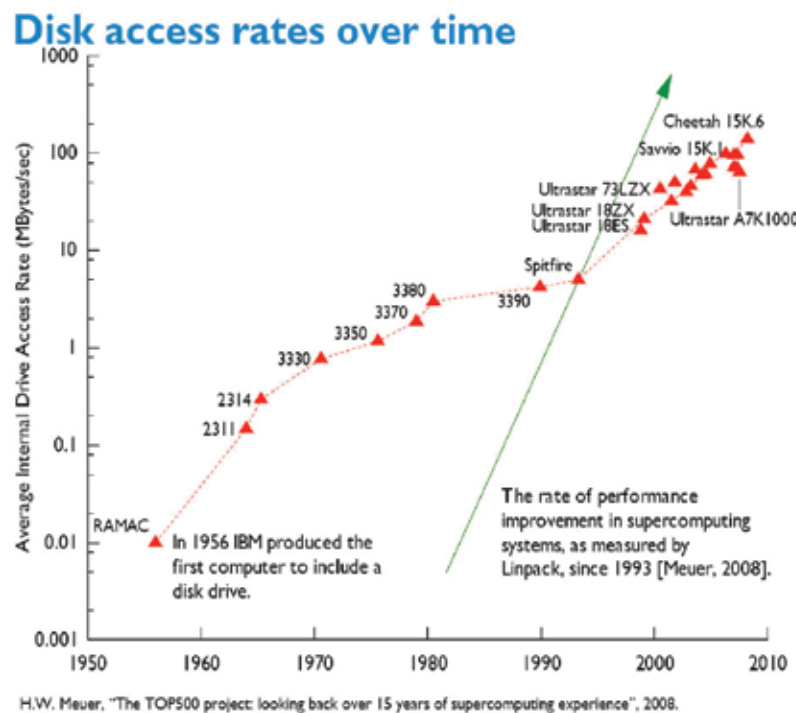


Fig. 1. Disk access rates lag behind increase in supercomputer performance. Chart provided by Rob Ross, ANL.

### Funding Acknowledgments

- DOE, NNSA, Advanced Simulation and Computing
- DOE, Office of Science, Scientific Discovery through Advanced Computing Program
- Petascale Data Storage Institute

# Petascale Molecular Dynamics on Roadrunner

Timothy C. Germann, Kai Kadau, T-1; Sriram Swaminarayan, CCS-2

The scalable parallel short-range molecular dynamics (SPaSM) code was developed in the early 1990s by David Beazley, Peter Lomdahl, and collaborators at LANL to simulate the dynamical behavior of materials under extreme conditions. Over the past decade SPaSM has been successfully used to provide insight into dislocation dynamics in metals [1], shock compression-induced plasticity [2] and phase transformations [3], and hydrodynamic instabilities [4,5]. These phenomena are important in aspects of many applications that range from inertial confinement fusion and nuclear weapons performance to supernovae explosions. A major breakthrough occurred recently when the SPaSM code was successfully used to perform the fastest molecular dynamics simulation to date, reaching  $\sim 369$  TFlop/s on the full Roadrunner machine.

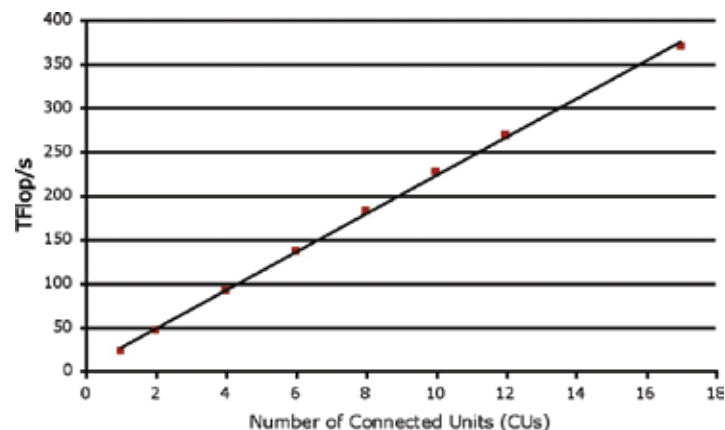
Molecular dynamics (MD) is a computational approach that embodies the concept of scientific reductionism—that is, the idea that the nature of a complicated process can be understood by understanding the interaction of the parts. In this case, the parts are the individual atoms and MD works by first determining the fundamental interactions between the atoms (from experimental data and theoretical insights into the interatomic force description) and then building a picture of how a macroscopic material should behave by simulating the interactions of millions to billions of atoms. (Similarly, national-level mitigation strategies for pandemic influenza spread can be assessed by simulating the interactions between the  $\sim 300$  million people within the United States [6].)

The original SPaSM code design was targeted at massively parallel computer architectures, and written in an era when memory and arithmetic operations were the typical performance bottlenecks, while interprocessor communication was relatively cheap. The efficiency of this

original SPaSM implementation is demonstrated by its use in earning an IEEE Gordon Bell Performance Prize in 1993 (50 GFlop/s on the CM-5), an IEEE Gordon Bell Prize/Performance Prize in 1998 (\$15/Mflop/s on the Avalon Beowulf cluster), and an IEEE Gordon Bell finalist in 2005 (50 TFlop/s on BlueGene/L). With the arrival of Roadrunner the original design considerations were wholly obsolete: memory is plentiful and computation on the IBM Cell Broadband Engine (Cell BE) synergistic processing unit (SPU) cores is virtually free, but memory accesses to and from the SPUs are the bottleneck. We have rewritten almost the entire SPaSM code base, particularly its communication infrastructure and data structures, to accommodate the Cell BE processor and allow for better asynchrony between the Opteron and Cell BE processors. The resulting code demonstrates excellent parallel scaling, reaching 369 TFlop/s on the full 17 connected units (CUs) of Roadrunner (see Fig. 1), and was an IEEE Gordon Bell Prize finalist again in 2008.

The key benefit of Roadrunner for atomistic simulations is this remarkable gain in speed, not just size. This gain in speed is because large-scale parallel MD codes, such as SPaSM, have typically been compute-bound rather than memory-bound—while one trillion atoms (in single precision) can fit into memory on either Roadrunner or the 212,992-CPU BlueGene/L platform at LLNL, few phenomena

*Fig. 1. Weak scaling of SPaSM on Roadrunner for the benchmark Lennard-Jones (LJ) problem, measured over 20 time steps. The symbols are measured data while the solid line is the best linear fit through all the data.*



occur within the picosecond timescale accessible by such MD simulations. The order-N linear scaling down to as few as several thousand atoms per processor allows us to sacrifice system size for longer simulation times, until the communication overhead begins to dominate for smaller system sizes. For this reason, recent extended (day- to week-long) full-system runs on BlueGene/L by us and another group at LLNL have independently chosen the “sweet spot” around 1 billion atoms for 1 ns, the longest time scale accessible before performance degradation sets in on BlueGene/L. (The basic time step in MD simulations must be short enough to resolve atomic vibrations, typically 1–5 femtoseconds, so up to a million time steps may be required to reach ns timescales.) However, longer times are clearly essential for many phenomena—1 ns is barely enough time for the round-trip traversal of a sound or shock wave through a micron-long sample. Similarly, a model of the entire world population of 6.6 billion people can readily fit within many existing supercomputers, but the SPaSM-based EpiCast code has thus far been limited to the US population (300 million people) due to the computational time required (several minutes to simulate a single day of disease progression). The acceleration that is provided by the Cell BE processors in Roadrunner directly addresses this important time scale issue, enabling unprecedented insight into materials, fluid, and infectious disease dynamics.

The materials science community is extremely excited about the discovery opportunities now presenting themselves with the Roadrunner-class petascale computers. Our initial focus will be in understanding how shock waves can create material damage and ejecta (see Fig. 2) and how hydrodynamic instabilities initiate and evolve. Subsequent studies will investigate a major yet-unsolved question, namely how to simulate polycrystal grain effects at the relevant length and time scales. This is important because grain effects are known to play an essential role in the deformation and failure of metallic materials under extreme loading conditions, such as in nuclear weapons, nuclear reactors, bridges, and buildings. A petascale computer like Roadrunner is essential to simulate the grains at the proper scale and duration.

**For further information contact Timothy C. Germann at [tcg@lanl.gov](mailto:tcg@lanl.gov).**

- [1] S.J. Zhou et al., *Science* **279**, 1525-1527 (1998).
- [2] B.L. Holian, P.S. Lomdahl, *Science* **280**, 2085-2088 (1998).
- [3] K. Kadau et al., *Science* **296**, 1681-1684 (2002).
- [4] K. Kadau et al., *Proc. Natl. Acad. Sci. (USA)* **101**, 5851-5855 (2004).
- [5] K. Kadau et al., *Proc. Natl. Acad. Sci. (USA)* **104**, 7741-7745 (2007).
- [6] T. C. Germann et al., *Proc. Natl. Acad. Sci. (USA)* **103**, 5935-5940 (2006).

*Fig. 2. Demonstration run showing the ejection of material from a shocked copper surface, run on 1 CU. The sample is 3-D, but with a thin cross section into the plane—only a small section of the total sample height is shown, at two different times during the simulation. (Top) Free surface prior to shock arrival. (Bottom) Initial jet formation after a shock wave has reflected from the free surface. Three different surface defects are initially present, with the same volume but different shapes, leading to different jetting patterns that will subsequently break up into ejecta particles with different size and velocity distributions.*



**Funding  
Acknowledgments**  
DOE, NNSA, Advanced  
Simulation and  
Computing Physics and  
Engineering Models  
Program

## Compressible Flow Simulation on Roadrunner

Jamaludin Mohd-Yusof , Daniel Livescu, Timothy Kelley, Mark R. Petersen, CCS-2

**T**urbulence is an inherently multiscale phenomenon, encompassing a large range of length and time scales, all of which must be resolved in a direct numerical simulation (DNS). The DNS technique also requires that the numerical errors remain small and not affect the solution. DNS allows a degree of control of specific physical phenomena not accessible in experiments, leading to improved understanding and, ultimately, to models for large multiphysics codes. However, the numerical requirements significantly restrict the range of accessible flows and parameters, as they require very large grids. Recent progress in computer hardware, based on heterogeneous architectures, could significantly advance our state-of-the-art turbulence simulations and, thus, turbulence theory and modeling.

The IBM Cell Broadband Engine (Cell BE) used in the Roadrunner supercomputer is an example of the newest generation of accelerators. Common to many of these architectures is the existence of multiple processing cores (synergistic processing units, or SPUs, in this case) with independent, high bandwidth access to local memory.

CFDNS is a Fortran-structured grid code that simulates the compressible Navier-Stokes equations in 3D. Multiple species are allowed, each with realistic material properties equation of state (EOS), as well as Cartesian, cylindrical, and spherical grid geometries. The bulk of the time in the code is spent in either computing the update equations or computing the derivatives of the various fields. The update equation is computed in a pointwise manner throughout the domain and is straightforward to vectorize once all the terms have been evaluated. The derivative step uses a compact finite difference (Pade) scheme that requires a tridiagonal inversion along the direction in which the derivative is being

performed. Since the data is laid out in 3D, this requires a strided load of the data.

A subset of the base code was ported to the Cell BE architecture and implemented in C with SPU extensions. The derivative calculation vectorizes naturally in the x and y directions, since the data is contiguous in z. For the z derivative, the data must be reordered in local store for good performance, but is not reordered in main memory. Each SPU works on a different portion of the data and executes its own direct memory access (DMA) calls independently in order to maximize performance. Similar data partitioning is used for the update step.

The Cell BE implementation of the code was benchmarked against a functionally identical C code running on the Opteron. Significant speedups of 40X (64<sup>3</sup>) to 50X (128<sup>3</sup>) were observed. The primary benefit for the Cell BE implementation is the ability to independently access main memory, allowing an effective memory access rate of ~ 12 GB/s (50 percent of theoretical peak) [1].

A full parallel implementation of the code on the hybrid Roadrunner architecture [2] is currently in final testing, in anticipation of the full Roadrunner deployment, which will allow simulations at resolutions of 4096<sup>3</sup>. These will be by far the largest compressible turbulence simulations ever performed, and we expect them to allow significant advancement on the theory and modeling of compressible turbulence. Targeted applications include Type 1a supernova and inertial-confinement fusion (ICF) modeling.

The parallel code exhibits speedup on the order of 20X (128<sup>3</sup> per node). Extensive reorganization of the code was required to achieve this speedup, to reduce internode data movement. The speed of the new code, combined with advances in graphics performance, makes 'live' visualization of evolving turbulent flows feasible in the near future (Fig. 1).

For further information contact Jamaludin Mohd-Yusof at [jamal@lanl.gov](mailto:jamal@lanl.gov).

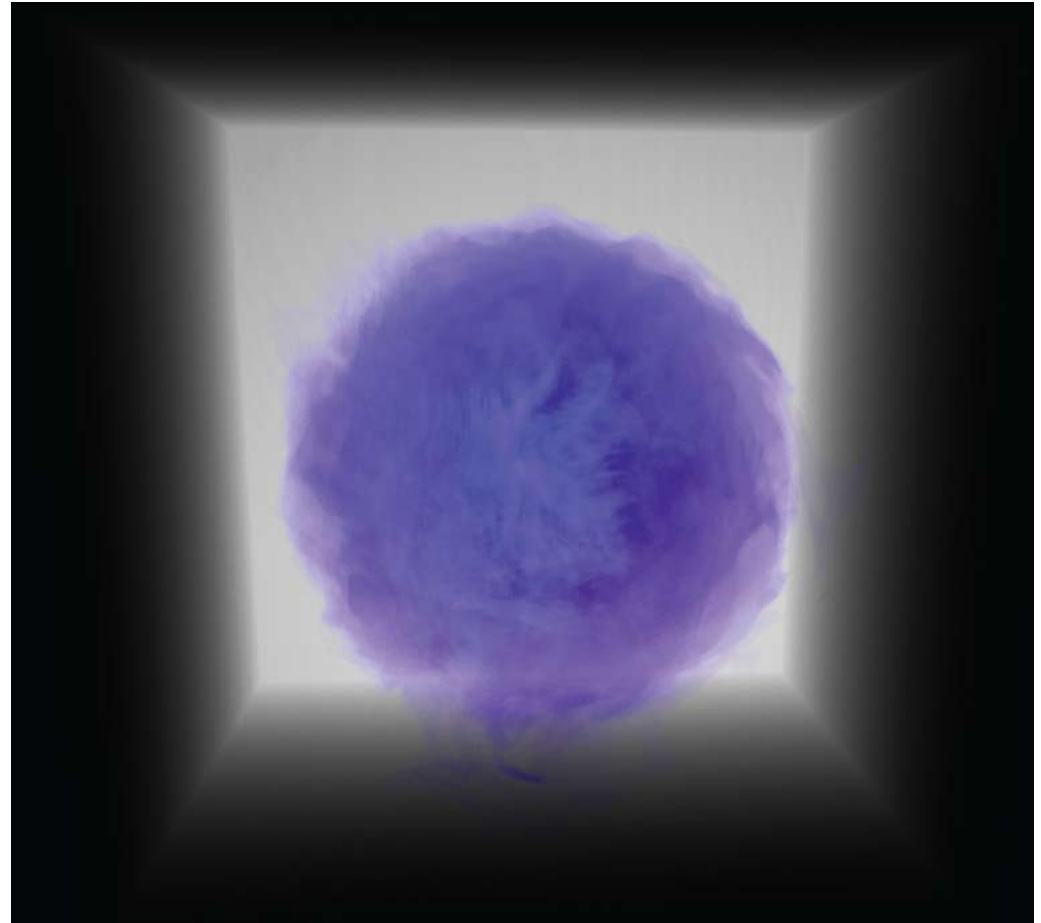
[1] J. Mohd-Yusof, D. Livescu, M.R. Petersen, "Roadrunner: Compressible Turbulence Simulation" at SC07 (International Conference for High Performance Computing, Network, Storage and Analysis) (2007).

[2] J. Mohd-Yusof et al., "Simulation of Compressible Fluid Flow on Roadrunner" at SC08 (International Conference for High Performance Computing, Network, Storage and Analysis) (2008).

---

*Fig. 1. Volume-rendering of scalar concentration from a test simulation using the Roadrunner code. The rendering is done using graphics processing unit (GPU)-accelerated custom code, which will eventually allow realtime visualization of turbulence simulation results. (Courtesy of Pat McCormick, CCS-1)*

---



### **Funding Acknowledgments**

- DOE, NNSA, Advanced Simulation and Computing Program Roadrunner Project
- LANL Directed Research and Development Program







# Applied Mathematics, Fluid Dynamics, and Magnetohydrodynamics

The fields presented in the Applied Mathematics, Fluid Dynamics, and Magnetohydrodynamics section have a long history at LANL, including many of the current and precursor groups and divisions in the Theory, Simulation and Computing Directorate. The ten short articles in this section describe the recent work of members of our Directorate in Applied Mathematics, Fluid Dynamics and Magnetohydrodynamics.

The first two articles report studies of hydrodynamic instabilities using the direct simulation Monte Carlo and molecular dynamics methods. The third article describes an approach to get around one of the weaknesses of molecular dynamics, namely the

inability to carry out the simulations beyond time scales of microseconds and length scales of micrometers.

The next three articles deal with meshing and discretization of problems that are described by partial differential equations or that can be formulated in terms of optimization problems. Although two of the articles are presented in the context of hydrodynamics, the work described in them can be extended to other systems.

Turbulence is the topic of the next article. This is followed by a discussion of fluid reservoir performance and another article on hydrodynamic instabilities. The next article returns to the topic of turbulence. The last two

discussions in this section deal with two conjectures on the numerical solution of neutron transport problems and the application of the moment-of-fluid method to incompressible flows.

# Richtmyer-Meshkov Instability via Direct Simulation Monte-Carlo

John L. Barber, T-1

In recent years, there has been increasing interest in the simulation of fluid flows via atomistic methods rather than the more traditional continuum techniques based on the Navier-Stokes equations. Atomistic methods include molecular dynamics (MD), in which Newton's equations of motion for a large number of interacting particles are solved numerically, and direct simulation Monte-Carlo (DSMC), a related technique in which explicit interparticle forces are replaced by stochastically simulated collisions [1]. Examples of such atomistic fluid dynamics simulations include the simulation of Rayleigh-Benard convection by MD [2,3] and the simulation of the Rayleigh-Taylor instability by MD [4] and by DSMC [5].

In this highlight, results are presented from some preliminary simulations of the Richtmyer-Meshkov instability (RMI) using DSMC [6]. The RMI occurs when a shock front passes through the interface between two fluids of differing densities. Any roughness or disturbances initially present on the interface before the passage of the shock grow in magnitude, and the two fluids subsequently mix in a characteristic fashion. The RMI is not a true classical instability, since modes on the interface do not experience an initially exponential growth. However, RMI has many traits in common with certain classical instabilities, particularly the Rayleigh-Taylor instability.

The simulations for which results are presented here were done using a one-processor 2D DSMC code, and each simulation required several days on a single workstation. A shock was induced in the fluid by a piston at one end of the domain. The resulting shock front passed through the denser fluid and crossed the interface into the lighter fluid. In order for turbulent mixing to occur in the RMI, the initial shape

of the interface must possess perturbations, and in these simulations the shape of the interface was initially set to be a sine curve of wavelength  $\lambda$  and amplitude  $a(0)$ .

Figure 1 shows a sequence of snapshots from the evolution of the RMI from a DSMC simulation spanning approximately  $7\mu\text{m}$  in length by  $1\mu\text{m}$  in height. The number of particles present varied over the course of the simulation from approximately 15 to 39 million. The density of the light fluid was

$\rho_l = 0.41 \text{ g/cm}^3$ , and that of the heavy fluid was  $\rho_h = 10 \rho_l = 4.1 \text{ g/cm}^3$ , for an Atwood number of:

$$A = \frac{\rho_h - \rho_l}{\rho_h + \rho_l} = 0.818$$

The piston velocity was 280 m/s, which created a shock front that moved through the heavy fluid at a velocity of 420 m/s. The initial perturbation amplitude-to-wavelength ratio was relatively large,  $a(0)/\lambda = 0.16$ . In order for the interface to avoid diffusion and remain sharp, all particles in front of the shock were frozen in position relative to one another. This is equivalent to a temperature of 0 in front of the shock. After passage of the shock, particles were allowed to move freely.

Note the development of the characteristic “mushroom caps” in the mixing zone in Fig. 1, as well as the shear-induced curl-up at the fringes of each structure. This behavior is typical of several fluid instabilities, including the RMI,

*Fig. 1. A series of snapshots in the development of the Richtmyer-Meshkov instability as simulated by DSMC. White indicates the heavy fluid, black indicates the light fluid, and the red line indicates the position and profile of the shock front.*



Rayleigh-Taylor instability, and Kelvin-Helmholtz instability. Also notice that the two structures present do not remain identical, as they would for a periodically perturbed interface in a typical continuum simulation. Atomistic methods, via the thermal fluctuations they contain and that are physically present at the microscopic scale, provide their own mechanisms for symmetry breaking.

In addition to considering the overall development of the RMI, it is interesting to examine the initial growth of the interface width for times shortly after the passage of the shock front. Using only hydrodynamic considerations, Richtmyer [7] has shown that for small  $a(0)$ , the velocity at which the amplitude of interfacial perturbations grows is given for small times by:

$$\dot{a}(t) = a(0)k A \Delta v$$

Here  $a(t)$  is the amplitude as a function of time,  $k = 2\pi / \lambda$  is the wavenumber of the perturbation, and  $\Delta v$  is the change in velocity experienced by the interface as a result of the passage of the shock front. Figure 2 shows a comparison between Richtmyer's prediction and results from a DSMC simulation. This simulation was identical to the one described above, except that the amplitude-to-wavelength ratio was smaller,  $a(0)/\lambda = 0.02$ .

Note that for small times  $t$ , the slope of the  $a(t)$  curve from the simulation agrees well with Richtmyer's prediction. This serves as a partial validation of linearized hydrodynamics on the small scales described by these simulations, and fits in well with a previous study performed for the initial growth of the Rayleigh-Taylor instability [8].

For animations and other details of the two simulations described above, see <http://www.lanl.gov/orgs/t/t17/staff/jlb/BarberResearch.html>.

**For further information contact John L. Barber at [jlbarber@lanl.gov](mailto:jlbarber@lanl.gov).**

- [1] G.A. Bird, *Molecular Gas Dynamics and the Direct Simulation of Gas Flows*. Oxford University Press (1994).
- [2] M. Mareschal, E. Kestemont, *Nature* **329**, 427-429 (1987).
- [3] D.C. Rapaport, *Phys. Rev. E* **73**, 025301(R) (2006).
- [4] K. Kadau et al., *Proc. Nat. Acad. Sci.* **101**, 5851-5855 (2004).
- [5] K. Kadau et al., *Proc. Nat. Acad. Sci.* **104**, 7741-7745 (2007).
- [6] J.L. Barber et al., *AIP Proceedings* **955**, 301-304 (2007).
- [7] R.D. Richtmyer, *Comm. Pure Appl. Math.* **13**, 291-319 (1960).
- [8] J.L. Barber et al., *Eur. Phys. J. B* **64**, 271-276 (2008).

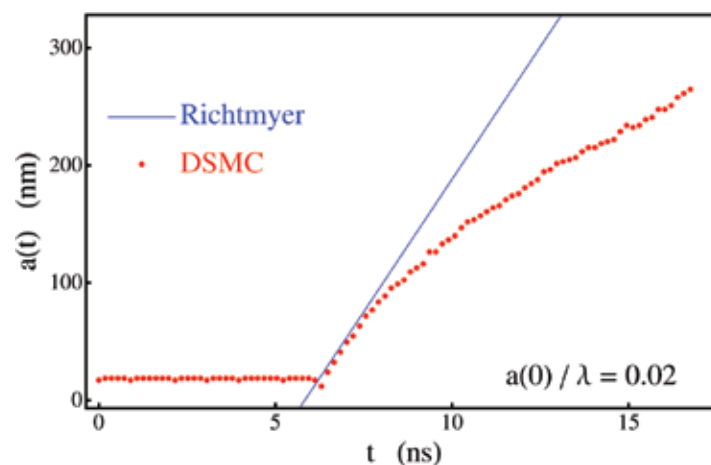


Fig. 2. The amplitude  $a(t)$  of an initially sinusoidal perturbation on the interface of the Richtmyer-Meshkov instability as a function of time, as predicted for small  $t$  by Richtmyer, and as simulated by DSMC.

**Funding  
Acknowledgments**  
LANL Directed  
Research and  
Development Program

# Initial Growth of the Rayleigh-Taylor Instability via Molecular Dynamics

John L. Barber, Kai Kadau, Timothy C. Germann, T-1; Berni J. Alder, LLNL

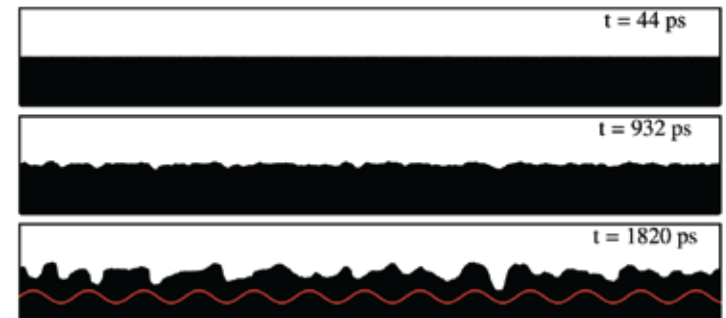
**M**olecular dynamics (MD) is a material simulation technique in which Newton's equations of motion for a large number of interacting particles are solved numerically [1]. In recent years, there has been increasing interest in the simulation of various problems in fluid dynamics using MD (and other atomistic methods) rather than the more traditional continuum techniques based on the Navier-Stokes equations [2-6]. The advantages of MD stem from the fundamental nature of the processes upon which it is based, as well as the fact that it includes the thermal fluctuations present in real fluids and that are lacking in most continuum solvers. The main disadvantage is the computational cost associated with the large number of particles present in most MD simulations. The microscale thermal fluctuations captured by MD allow us to directly probe the emergence of macroscopic hydrodynamic quantities as averages over the molecular randomness that underpins real-world fluids. In this highlight, we describe such an investigation in the context of the initial growth behavior of the Rayleigh-Taylor instability (RTI) [6].

The RTI occurs when a heavy fluid lies on top of a light fluid in the presence of a gravitational field  $g$ . This arrangement is unstable, and the two fluids subsequently combine in an archetypical example of turbulent fluid mixing. Figure 1 shows several stages in the early development of the RTI in an MD simulation with quasi-2D (or "thin slab") geometry. Given an initial interface between the two fluids possessing only small deviations from perfect flatness, it can be shown that the amplitude of a perturbation of wave number  $k$  will grow exponentially in time for small  $t$  as  $A_k(t) = A_k(0)\exp[n(k)t]$ . In his 1961 book *Hydrodynamic and Hydromagnetic Stability* [7], Chandrasekhar derived, via linearization of the incompressible Navier-Stokes equations, a function  $f$  such that the growth rate spectrum  $n(k)$  satisfies

$f(n(k), k) = 0$ . This equation can be solved numerically to yield continuum-based predictions for the shape of  $n(k)$ . In particular, note that  $n(k)$  has a maximum at  $k_{max}$ , known as the mode of maximum instability. In addition, for the systems with surface tension we consider here,  $n(k)$  has a cutoff at  $k_{cut}$ , at which  $n(k)$  passes from positive to negative.

The growth-rate spectrum of the RTI can be measured directly in MD simulations by taking Fourier transforms of the early development of the interface. We have performed such an analysis for a sequence of MD simulations, each describing a quasi-2D domain approximately 1  $\mu\text{m}$  in width by 0.2  $\mu\text{m}$  in height and containing approximately 2,000,000 Lennard-Jones particles. Due to the small length scales considered, it was necessary for the gravity  $g$  to be very large in order for the instability to develop in a reasonable number of time steps. The three values for  $g$  considered were  $g = 2.7 \times 10^{10} g_{Earth}$ ,  $g = 1.3 \times 10^{10} g_{Earth}$ , and  $g = 0.3 \times 10^{10} g_{Earth}$ . The presence of entirely physical fluctuation-induced variations in the growth rate spectrum from one simulation to the next necessitated that we perform many runs at each gravity to obtain an adequate average  $n(k)$  for comparison with Chandrasekhar's prediction. The results are shown in Fig. 2. Note that despite the vastly different levels of description between the MD simulations and the continuum theory, the agreement between the two is quite good. To within fluctuations, MD captures both the existence and value of the mode of maximum instability  $k_{max}$ , as well as the presence of the cutoff wave number  $k_{cut}$ . At large values of  $k$ , there is some discrepancy between the growth rate values manifested by MD and the theoretical predictions. This can

*Fig. 1. Three snapshots from the initial stages of the Rayleigh-Taylor instability as simulated by MD. The red curve in the last frame is a reference sine curve of wavelength  $\lambda_{max} = 2\pi/k_{max}$  illustrating that modes near the mode of maximum instability quickly dominate the shape of the interface.*





be attributed to a number of factors, including the existence of nonexponential oscillations of the interface and the presence of nonlinear transport effects for low-wavelength disturbances.

In addition to the mean growth rate  $n(k)$ , it is instructive to consider the physical variation  $\Delta n(k)$  in the growth rate as a function of  $k$ . This quantity is graphed in Fig. 3 for each of the three gravities we considered, along with a curve representing a polynomial fit to the low- $k$  segment of all three sets of data to aid in recognizing the general trend. The important point to note is that the physical spread in the growth rate with respect to its mean is a monotonically increasing function of the wave number  $k$  (i.e., a decreasing function of the wavelength  $\lambda$ ). Since the predicted mean is derived from purely hydrodynamic considerations, this is a clear demonstration that the validity of the Navier-Stokes equations emerges statistically as an average over the microscopic fluctuations in a fluid, and that individual instances of real fluid systems deviate from this average to an increasing degree as smaller scales are considered.

**For further information contact John L. Barber at [jlbarber@lanl.gov](mailto:jlbarber@lanl.gov).**

- [1] M. Allen, D. Tildesley, *Computer Simulation of Liquids*, Oxford Science Publications (1987).
- [2] M. Mareschal, E. Kestemont, *Nature* **329**, 427-429 (1987).
- [3] D.C. Rapaport, *Phys. Rev. E* **73**, 025301(R) (2006).
- [4] K. Kadau et al., *Proc. Nat. Acad. Sci.* **101**, 5851-5855 (2004).
- [5] K. Kadau et al., *Proc. Nat. Acad. Sci.* **104**, 7741-7745 (2007).
- [6] J.L. Barber et al., *Eur. Phys. J. B* **64**, 271-276 (2008).
- [7] S. Chandrasekhar, *Hydrodynamic and Hydromagnetic Stability*, Dover (1961).

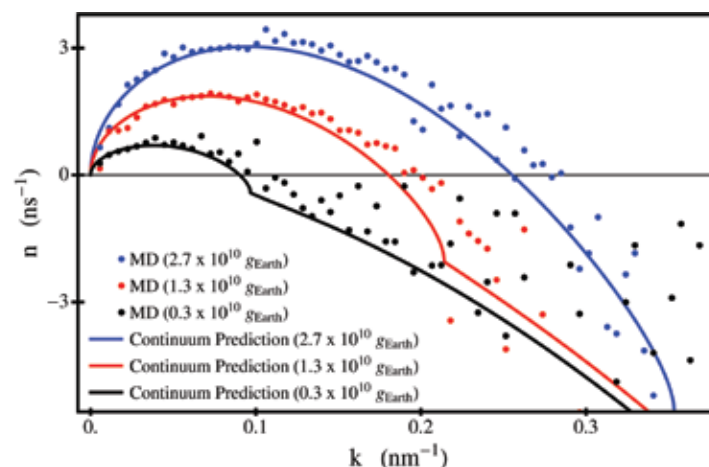


*Fig. 2. Growth-rate spectra from MD simulations for each of the three gravities considered, along with the corresponding predictions from continuum theory.*

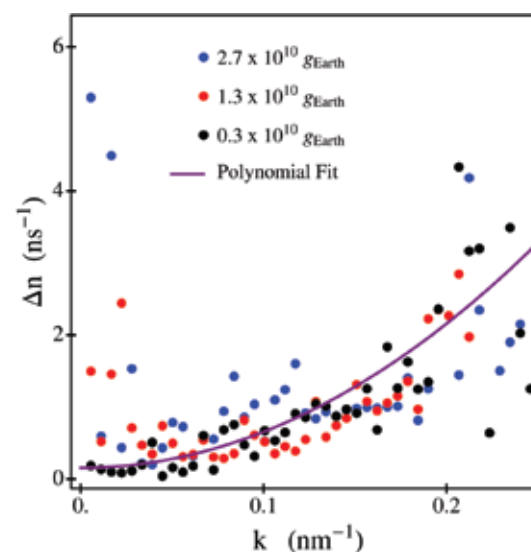


*Fig. 3. Physical variation in the growth rate as a function of  $k$  from MD simulations, along with a curve representing a rough polynomial fit to the moderate- $k$  segment of the data. Note that the apparent increase in  $\Delta n(k)$  at very small  $k$  is an artifact of the periodic boundary conditions we employed and may be ignored.*

## Funding

## Acknowledgments

LANL Directed Research and Development Program

# Memory Function Formalisms for System Reduction in Molecular Dynamics

John L. Barber, T-1

**M**olecular dynamics (MD) [1] is a popular material simulation technique based on Newton's equations of motion for a large number of interacting particles. The power and accuracy of MD stems from the relatively fundamental nature of the processes it describes. MD consists of the numerical integration of the following system of ordinary differential equations (ODE):

$$(1) \quad \frac{d}{dt} q_i = \frac{1}{m_i} p_i, \quad \frac{d}{dt} p_i = -\nabla_{q_i} \Phi(q), \quad 1 \leq i \leq N$$

Here  $q_i$ ,  $p_i$ , and  $m_i$  are the position, momentum, and mass of the  $i^{\text{th}}$  particle, respectively, and  $\Phi(q)$  is the interaction potential. The number of particles  $N$  is often very large in a realistic system, which can be computationally intensive to simulate. For this reason, MD is currently confined to the description of length and time scales on the order of microns and nanoseconds, respectively [2]. It is often the case, however, that only the trajectories of some subset of the particles in (1) are needed to extract useful information from an MD simulation. In this article, we outline a technique for constructing a set of differential equations for the evolution of such a subset and present some results from a simple toy problem.

Suppose we wish to keep—without loss of generality—the first  $M$  of the particles in equation (1). We can split the variables  $(q_i, p_i)$  into two groups: (a) the resolved particles with positions and momenta  $\hat{q}_i$  and  $\hat{p}_i$ , where  $1 \leq i \leq M$ , and (b) the discarded unresolved particles with variables denoted by  $\tilde{q}_i$  and  $\tilde{p}_i$ , where  $1 \leq i \leq N - M$ . Via a sequence of mathematical steps too involved to reproduce here, it can be proven [3] that the  $\hat{q}_i$  and  $\hat{p}_i$  are governed by the following reduced system of differential equations:

$$(2) \quad \begin{aligned} \frac{d}{dt} \hat{q}_i &= \frac{1}{m_i} \hat{p}_i, \\ \frac{d}{dt} \hat{p}_i &= -\nabla_{\hat{q}_i} \varphi(\hat{q}) - \int_0^t ds K_i(s) \hat{p}(t-s) + F_i(t), \quad 1 \leq i \leq M \end{aligned}$$

The derivation of this set of stochastic integro-differential equations is a generalization of the Mori-Zwanzig memory function formalism [4,5]. Here  $\varphi(\hat{q})$  is known as the renormalized potential,  $K_i(t)$  is a memory kernel, and  $F_i(t)$  is a random force. These quantities take somewhat different forms depending on the details of the system in question and the nature of the variable splitting that is chosen, though general expressions exist for their calculation.

As a simple (yet fundamental) example to illustrate some details of the system in (2), we consider the toy problem of a fluid of identical particles at thermal equilibrium governed by the potential:

$$(3) \quad \Phi(q) = \sum_{i < j}^N u_{ij}(|q_i - q_j|)$$

where  $u_{ij}$  is the Lennard-Jones pair potential. For such a system, it can be shown that it is optimal to choose the renormalized potential as the potential of mean force of the resolved particles, namely:

$$(4) \quad \varphi(\hat{q}) \propto -k_B T \log \left\{ \int d\tilde{q} \exp(-\Phi(q)/k_B T) \right\}$$

The form of  $\varphi(\hat{q})$  will then be that of a modified pair potential plus a three-body interaction, a four-body interaction, and so on. The statistical isotropy inherent in (3) implies that the memory kernel  $K_i(t)$  is a scalar, and the fact that these are identical particles implies that  $K_i(t) = K(t)$  is the same for all  $i$ . Furthermore, it can be proven that  $K(t)$  decays relatively slowly for large  $t$  as  $t^{-d/2}$ , where  $d$  is the spatial dimensionality of the system. Several examples of the memory kernel for this system are shown in Fig. 1 for various  $M/N$  ratios. These were calculated from the Volterra integral equation (not shown here) that defines  $K(t)$ . Finally, note that in this simple equilibrium system the random force



$F_i(t)$  is a Gaussian stochastic process, and that its correlation is given by the familiar fluctuation-dissipation theorem:

$$(5) \quad \langle F_i(t+t') \cdot F_j(t') \rangle = d m k_B T K(t) \delta_{ij},$$

though this is not necessarily the case in general.

Equations (1) and (2) are relatively straightforward to integrate numerically for reasonable values of  $N$  and  $M$ . Results for the trajectory of a single particle chosen from a full system of  $N = 500$  particles are shown in Fig. 2, along with the trajectory of the single particle remaining in a reduced system of  $M = 1$ . Despite the fact that the environments of these two particles are profoundly different – the former interacts with 499 other particles, the latter explicitly with none – the qualitative character of their trajectories is the same. This notion can be made more quantitative by noting that both the diffusion coefficient and the velocity autocorrelation function of the two particles can be shown to be identical both in theory and simulation. Results regarding the invariance of other properties between the full and reduced systems can be both derived and verified.

The formalism outlined above has relevance to many MD applications where variable splitting may be desirable. These include systems with a significant difference in size between resolved and unresolved particles (i.e., colloidal systems), as well as systems with a large difference in time scale between different parts of the system (e.g., proteins, where high-energy bonds vibrate at a much higher frequency). Further refinement and application of such techniques in these and other contexts may have a significant impact on the type and scale of problems accessible to MD.

For further information contact John L. Barber at [jlbarber@lanl.gov](mailto:jlbarber@lanl.gov).

- [1] M. Allen, D. Tildesley, *Computer Simulation of Liquids*, Oxford Science Publications (1987).
- [2] K. Kadau, T.C. Germann, *Int. J. Mod. Phys. C* **19**, 1315-1319 (2008).
- [3] J.L. Barber, *Memory function formalisms for system reduction in molecular dynamics*, *J. Chem. Phys.* (submitted)
- [4] H. Mori, *Prog. Theor. Phys.* **33**, 423-455 (1965).
- [5] R. Zwanzig, *Phys. Rev.* **124**, 983-992 (1961).

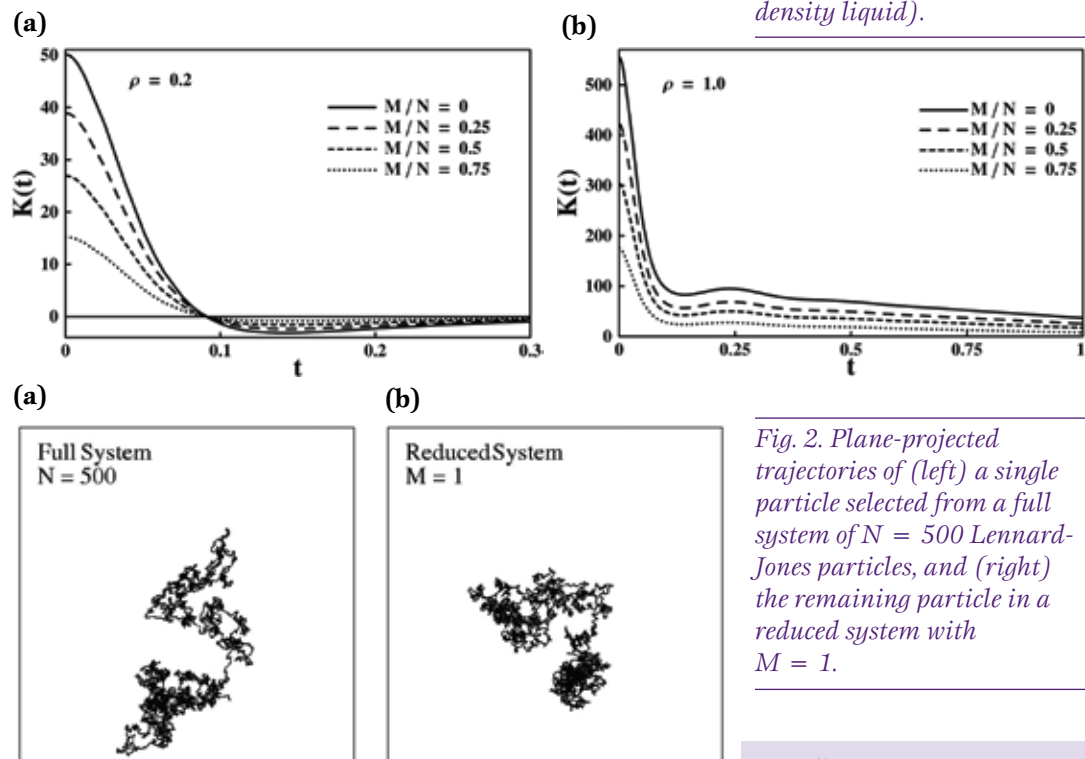


Fig. 1. Memory kernels  $K(t)$  calculated in the example system for various  $M/N$  ratios. Sets of curves for two full system dimensionless number densities  $\rho = N/V$  are shown: (a)  $\rho = 0.2$  (low-density gas), and (b)  $\rho = 1.0$  (high-density liquid).

Fig. 2. Plane-projected trajectories of (left) a single particle selected from a full system of  $N = 500$  Lennard-Jones particles, and (right) the remaining particle in a reduced system with  $M = 1$ .

## Funding

### Acknowledgments

- DOE, Office of Science, Office of Advanced Scientific Computing Research
- LANL Directed Research and Development Program

## Robust Rezoning in ALE Aided by Mesh Untangling

Markus Berndt, Milan Kucharik, Mikhail Shashkov, T-5

**L**agrangian methods are popular in the field of hydrodynamics. Such discretizations, in which the mesh moves with the fluid, have desirable features such as conservation of mass. However, in 2D and 3D when the simulated flow exhibits some rotation, the mesh can easily become tangled. In this case, the simulation fails. A common remedy to this entanglement problem is to introduce occasional mesh improvement (rezoning) followed by the remapping of physical quantities to the new and improved mesh. Such methods are referred to as arbitrary Lagrangian Eulerian (ALE) methods.

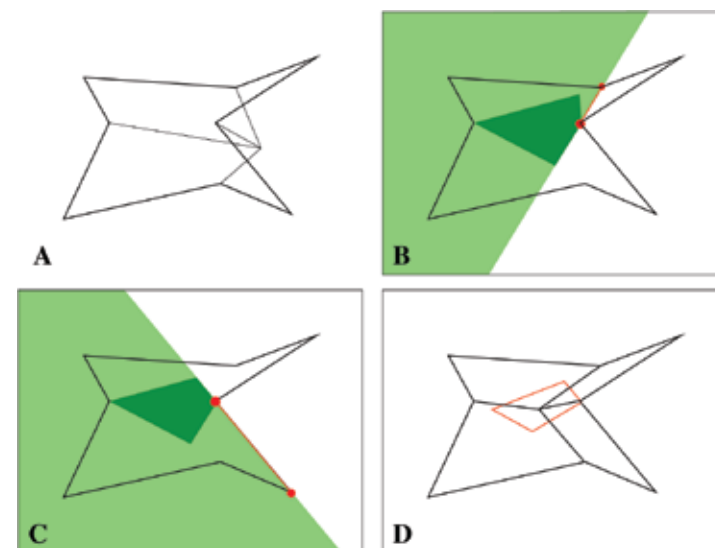
The rezone step in an ALE method typically relies on mesh smoothing which is perhaps triggered by some mesh quality indicators to keep the computational mesh in a valid state throughout a simulation. (An invalid mesh that has negative cell volumes results in simulation failure.) One drawback to this approach is that it is inherently heuristic and cannot guarantee a valid mesh throughout a simulation. In the case where, despite the rezoning step, a mesh becomes tangled, user intervention becomes necessary since conventional mesh smoothing algorithms typically cannot repair such a failed mesh.

We have developed a mesh untangling method that is based on the method presented in [1] and has improved robustness. The method is a purely geometric algorithm in 2D that is computationally efficient with a predictable cost per mesh vertex. Most importantly, it can be used not only as a mesh untangling method, but also as a mesh improvement method. In contrast to our method, most other existing robust mesh untangling algorithms are minimization-based and, thus, costly (for example, see [2]).

*Fig. 1. The construction of the feasible set of a tangled vertex.*

Our algorithm builds on two approaches to mesh untangling. The first approach is the feasible set method, in that a convex polygon, the feasible set, is constructed for each vertex in the mesh. This feasible set is the set of all coordinate positions that a vertex can occupy while maintaining mesh validity relative to its immediate neighbor cells. After the feasible set is constructed for a particular vertex in the mesh, this vertex then is placed at the centroid of the feasible set, resulting in an untangled mesh. The second approach is our weak untangling method. This method can be viewed as a discrete and, hence, efficient version of a more standard minimization-based untangling method. We use it to move severely tangled vertices, which cannot be untangled using the feasible set approach, closer to a configuration that is amenable to untangling by the feasible set method.

Figure 1 illustrates the construction of the feasible set for a patch of four cells whose center vertex is tangled. The feasible set method is the intersection of a number of half planes that are determined by the geometry of the patch surrounding the tangled vertex. For a patch of four quadrilaterals there are 12 half-plane intersections. The first image (A) in the sequence depicts the initial tangled mesh fragment. The second image (B) depicts the intersection of



one of the half planes and the bounding box (light green) with the current feasible set (dark green). In the third image (C) we see another such half-plane intersection, and finally, image (D) depicts the feasible set in red with the previously tangled vertex placed at its centroid.

The feasible set untangling method alone can be used as a mesh smoothing method and, if used that way, is robust. Alternatively, it can be used in conjunction with a more traditional mesh smoothing method, such as Winslow's method, to repair the mesh when it tangles. Figure 2 depicts a snapshot of a simulation where a high pressure gas spills through a gap in a wall from the left to the right. In this example, our feasible set untangling method was used in tandem with standard Winslow mesh smoothing. Without mesh untangling the mesh becomes tangled at the corners of the wall gap soon after the start of the simulation, and the simulation fails. In contrast, with mesh untangling the simulation continues to run robustly.

**For further information contact Markus Berndt at [berndt@lanl.gov](mailto:berndt@lanl.gov).**

- [1] P. Vachal, R.V. Garimella, M.J. Shashkov, *J. Comput. Phys.* **196**, 627-644 (2004).
- [2] P. Knupp, L. Margolin, M. Shashkov, *J. Comput. Phys.* **176**, 93-128 (2002).

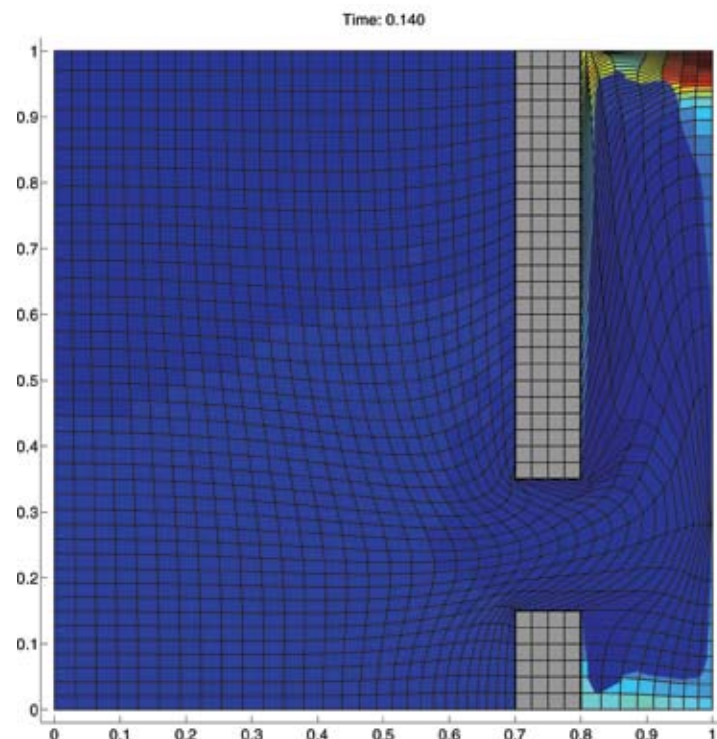


*Fig. 2. Snapshot of an ALE simulation of high pressure gas on the left that spills through a hole in a wall. Feasible set untangling is employed in tandem with standard Winslow mesh smoothing during the rezone step. Without untangling, the simulation would fail at a much earlier time.*

**Funding  
Acknowledgments**  
DOE, NNSA,  
Advanced Simulation  
and Computing Program

# Grid Generation and Adaptation Using an $L_p$ form of Monge-Kantorovich Optimization

Gian Luca Delzanno, John M. Finn, T-5

Grid generation and adaptation by Monge-Kantorovich optimization [1] produces optimal grids that equidistribute the local grid error, thereby minimizing the total error [2]. Optimality [1] was defined as minimizing the  $L_2$  norm

$$\|\mathbf{x}' - \mathbf{x}\|_2 = \left[ \frac{1}{2} \int |\mathbf{x}' - \mathbf{x}|^2 \rho(\mathbf{x}) d\mathbf{x} \right]^{1/2}$$

with the local constraint that the map  $\mathbf{x}' = \mathbf{x}'(\mathbf{x})$  has Jacobian  $\det[\partial(\mathbf{x}')/\partial(\mathbf{x})]$  equal to  $\rho(\mathbf{x})/\rho'(\mathbf{x}')$ , where  $\rho(\mathbf{x})$  and  $\rho'(\mathbf{x}')$  are the local errors at successive time steps (initial and target densities). In [1] it was shown that this method approximately minimizes the distortion of the map (the trace of the covariant metric tensor), and that the resulting equation, the Monge-Ampère equation, can be effectively solved by multigrid preconditioned Newton-Krylov methods.

In [3] we extended this approach to more general domains in 2D and to 3D, showing that the advantages detailed in [1] apply to these more general cases.

We have recently investigated the  $L_p$  form of this error equidistribution problem. That is, we minimize

$$\|\mathbf{x}' - \mathbf{x}\|_p = \left[ \frac{1}{p} \int |\mathbf{x}' - \mathbf{x}|^p \rho(\mathbf{x}) d\mathbf{x} \right]^{1/p}$$

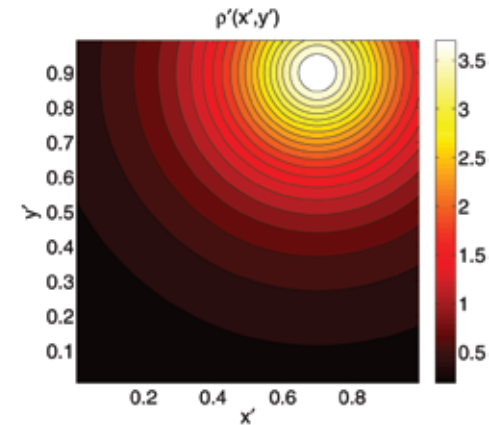
with the same Jacobian (equidistribution) constraint  $\det[\partial(\mathbf{x}')/\partial(\mathbf{x})] = \rho(\mathbf{x})/\rho'(\mathbf{x}')$ , for  $p > 1$ . The motivation for considering  $p \neq 2$  is that, relative to  $\|\mathbf{x}' - \mathbf{x}\|_p$  for  $1 < p < 2$ ,  $\|\mathbf{x}' - \mathbf{x}\|_2$  penalizes very little for small excursions but greatly for large excursions. Also, there has been a considerable amount of work in the mathematics

literature for  $p = 1$ , involving the use of the deformation method, discussed in [1]. Minimizing  $\|\mathbf{x}' - \mathbf{x}\|_p$  with the Jacobian constraint, we conclude that

$$\mathbf{x}' = \mathbf{x} + |\nabla \mu|^{\frac{2-p}{p-1}} \nabla \mu(\mathbf{x}) \quad (1)$$

where  $\mu(\mathbf{x})$  is the Legendre transform of a Lagrange multiplier enforcing the Jacobian constraint. The form corresponding to (1) for  $p = 2$  is  $\mathbf{x}' = \mathbf{x} + \nabla \mu(\mathbf{x})$ . In the difficult limit  $p \rightarrow 1$ , we find that  $\mu(\mathbf{x})$  satisfies the Eikonal equation  $|\nabla \mu| = 1$ . Substituting equation (1) into the Jacobian condition, we obtain a generalized Monge-Ampère equation for  $\mu(\mathbf{x})$ . We have found that this equation can also be solved by Newton-Krylov methods.

In Fig. 1 we show a target density  $\rho'(\mathbf{x}')$ , which is peaked at  $x = 0.7, y = 0.9$ , and the ratio of the maximum to the minimum density is  $\sim 22$ . The initial density is  $\rho(\mathbf{x}) = 1$ . In Fig. 2 we show the grid  $\mathbf{x}'$  obtained with these densities for a uniform initial grid  $\mathbf{x}$ , using various values for  $p$ . For  $p \gtrsim 1.5$ , the grids seem reasonable, concentrated near the peak of  $\rho'$  and with little distortion, i.e., the cells are close to square.



For  $p = 2$ , the grid lines are orthogonal to the boundary. For  $p < 1.5$ , and especially for  $p \rightarrow 1$ , some of the cells are seriously distorted and stretch from the origin to the peak of  $\rho'$  at  $x = 0.7, y = 0.9$ . (The darker grid lines have  $x = 0.25$ ,

Fig. 1. Target density.



$\downarrow p_c \backslash p_m \rightarrow$	1	1.01	1.02	1.05	1.1	1.25	1.5	1.75	2	2.25	2.5	Distortion
1.01	0.0000	0	0.0000	0.0004	0.0018	0.0103	0.0320	0.0572	0.0833	0.1093	0.1348	0.2501
1.02	0.0001	0.0000	0	0.0002	0.0013	0.0091	0.0295	0.0534	0.0782	0.1029	0.1270	0.2367
1.05	0.0006	0.0004	0.0002	0	0.0005	0.0063	0.0236	0.0444	0.0661	0.0878	0.1089	0.2130
1.1	0.0021	0.0017	0.0013	0.0005	0	0.0031	0.0162	0.0330	0.0510	0.0690	0.0867	0.1687
1.25	0.0092	0.0084	0.0076	0.0054	0.0028	0	0.0043	0.0132	0.0238	0.0351	0.0464	0.0716
1.5	0.0223	0.0210	0.0198	0.0164	0.0118	0.0036	0	0.0020	0.0063	0.0118	0.0178	0.0158
1.75	0.0334	0.0319	0.0304	0.0264	0.0208	0.0096	0.0017	0	0.0011	0.0035	0.0068	0.0018
2	0.0425	0.0408	0.0392	0.0348	0.0285	0.0155	0.0050	0.0010	0	0.0006	0.0022	0.0014
2.25	0.0499	0.0482	0.0464	0.0417	0.0349	0.0207	0.0085	0.0029	0.0006	0	0.0004	0.0069
2.5	0.0561	0.0542	0.0525	0.0475	0.0404	0.0254	0.0118	0.0052	0.0019	0.0004	0	0.0154

Table 1. Values of the  $p_m$  norm and the mean distortion for calculations with  $p = p_c$

$x = 0.75$ ,  $y = 0.25$ ,  $y = 0.75$  and are shown to emphasize the distortion for small  $p$ .) Further, the grid lines are far from orthogonal to the boundary. This adverse behavior near the boundary and especially near the corner  $(0, 0)$  for  $p \rightarrow 1$  is traced to the fact that for  $p = 1$ ,  $\mu$  satisfies the Eikonal equation, which leads to a boundary layer for  $p$  close to unity.

More quantitative measures of the grid quality are contained in Table 1. The rows are labeled by  $p_c$ , which specifies the value of  $p$  used in the computations. The columns are labeled by  $p_m$ , the value of  $p$  for which the norm is measured. For example, for the highlighted in red entry with  $p_c = 1.01$  and  $p_m = 2$ , we computed the map solving the generalized Monge-Ampère equation with  $p = p_c$ , but measured  $\|x' - x\|_p$  for  $p = p_m$ . (The norms are scaled to the diagonal value with  $p_m = p_c$  with unity subtracted.) Note that in all cases, the terms below the diagonal are smaller than the transposed values  $p_m \leftrightarrow p_c$ . That is, computing the grid with large  $p_c$  works well even when quality is measured by small  $p_m$ , whereas computing with small  $p_c$  leads to large norms  $\|x' - x\|_p$  for large  $p_m$ . It appears that  $p_c = 2$  works well, but from this measure larger  $p_c$  seems slightly better. Note, however, that the measured distortion (mean of the trace of the metric tensor) is minimal at  $p_c = 2$ , orders of magnitude larger for small  $p_c$  and a factor of 10 larger for  $p = 2.5$ . Overall, these results indicate that  $p_c = 2$  leads to the highest quality grids.

Based on these results, we conclude that grid generation and adaptation works best with  $p = 2$ . We have also observed that the domain of attraction of Newton's method is largest for  $p = 2$  and becomes much smaller for  $p$  close to unity. Further, there is a well-developed preconditioning strategy for  $p = 2$  [1].

**For further information contact J. M. Finn at [finn@lanl.gov](mailto:finn@lanl.gov).**

- [1] G.L. Delzanno et al., *J. Comput. Phys.* **227**, 9841 (2008).
- [2] G. Lapenta, *J. Comput. Phys.* **193**, 159 (2004).
- [3] J.M. Finn, G.L. Delzanno, L. Chacón, *Proc. 17th International Meshing Roundtable* **551** (2008).

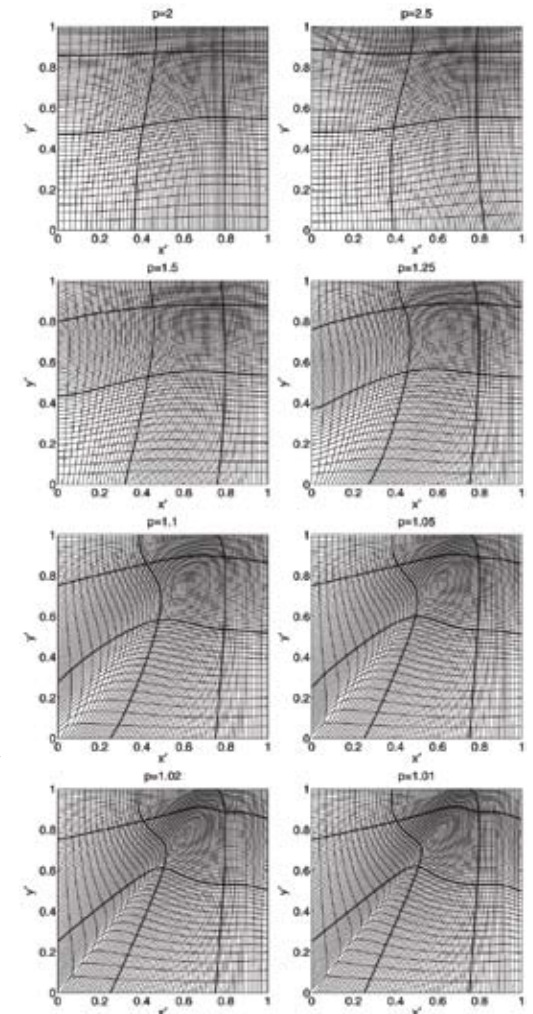


Fig. 2. Grids for various  $p$ .

#### Funding

#### Acknowledgments

LANL Directed  
Research and  
Development Program



# Mimetic Finite Differences for Modeling Stokes Flow on Polygonal Meshes

Vitaliy Gyrya, Pennsylvania State University; Konstantin Lipnikov, T-5

Stokes flow is fluid flow where advective inertial forces are negligibly small compared with viscous forces. This is a typical situation on a microscale or when the fluid velocity is very small. Stokes flow is a good and important approximation for a number of physical problems such as sedimentation, modeling of biosuspensions, construction of efficient fibrous filters, and developing energy efficient microfluidic devices (e.g., mixers). Efficient numerical solution of Stokes flow requires unstructured meshes adapted to geometry and solution as well as accurate discretization methods capable of treating such meshes. We developed a new mimetic finite difference (MFD) method that remains accurate on general polygonal meshes, and that may include nonconvex and degenerate elements [1].

Triangular meshes allow one to model complex geometric objects. However, compared with quadrilateral and more general polygonal meshes, the triangular meshes with the same resolution do not provide optimal cover of the space, which result in larger algebraic problems. The MFD method was designed to provide accurate approximation of differential operators on general meshes. These meshes may include degenerate elements, as in adaptive mesh refinement methods, nonconvex elements, as in moving mesh methods, and even elements with curved edges near curvilinear boundaries.

The incompressible Stokes equations are

$$\begin{aligned} -\operatorname{div}(\mu(\nabla \mathbf{u} + (\nabla \mathbf{u})^T)) &= \mathbf{F} - \nabla p \\ \operatorname{div} \mathbf{u} &= 0 \end{aligned}$$

where  $\mathbf{u}$  is the fluid velocity,  $p$  is the pressure,  $\mathbf{F}$  is the given external force, and  $\mu$  is the fourth-order symmetric positive definite tensor viscosity. Since  $\mu$  is a tensor, the developed

MFD method can be applied to problems of linear elasticity that can be written in a similar form.

The MFD method has many similarities with a low-order finite element (FE) method. Both methods try to preserve fundamental properties of physical and mathematical models. Various approaches to extend the FE method to nonsimplicial elements have been developed over the last decade. Construction of basis functions for such elements is a challenging task and may require extensive analysis of geometry. Contrary to the FE method, *the MFD method uses only boundary representation of discrete unknowns* to build stiffness and mass matrices. Since no extension inside the mesh element is required, practical implementation of the MFD method is simple for general polygonal meshes.

The MFD method is flexible in selecting discrete unknowns. In [1], the velocity is approximated at mesh vertices, and the velocity flux is approximated at mesh edges. The pressure is approximated by one constant (e.g., average) on each mesh element. This set of discrete velocity unknowns is abundant and will be reduced in the future. On triangular meshes, the MFD method coincides with the FE method that uses the same set of discrete unknowns. The numerical experiments in [1] have shown the *second-order* convergence for the velocity variable and the *first-order* for the pressure on unstructured polygonal meshes. The convergence rates have remained the same in experiments with anisotropic tensor  $\mu$ .

Like the MFD method for the diffusion problem [2,3], the novel MFD method [1] is a parametric family of methods with equivalent properties. In numerical experiments, we have used a particular member of this family. Analysis of this family is an open question. The answer to this question may result in new adaptive methods. In addition to traditional mesh refinement (h-adaptation) and enrichment of discretization space (p-adaptation), the MFD method provides a basis for selecting an optimal discretization method.

The novel MFD method has been developed for elements with straight edges. Applying ideas from [2], it will be possible to extend it to meshes with curved edges. The ideas

described in the last two paragraphs will be the topics of future research.

A similar MFD method has been developed independently by Lourenco Beirão da Veiga and Marco Manzini [1].

**For further information contact Konstantin Lipnikov at [lipnikov@lanl.gov](mailto:lipnikov@lanl.gov).**

- [1] L. Beirão da Veiga, V. Gyrya, K. Lipnikov and G. Manzini, Report LA-UR-09-00753 (2009).
- [2] F. Brezzi, K. Lipnikov, M. Shashkov and V. Simoncini, *Comput. Methods Appl. Mech. Engrg.* **196**, 3682-3692 (2007).
- [3] F. Brezzi, A. Buffa, K. Lipnikov, *Math. Model. Numer. Anal.*, accepted (2008).

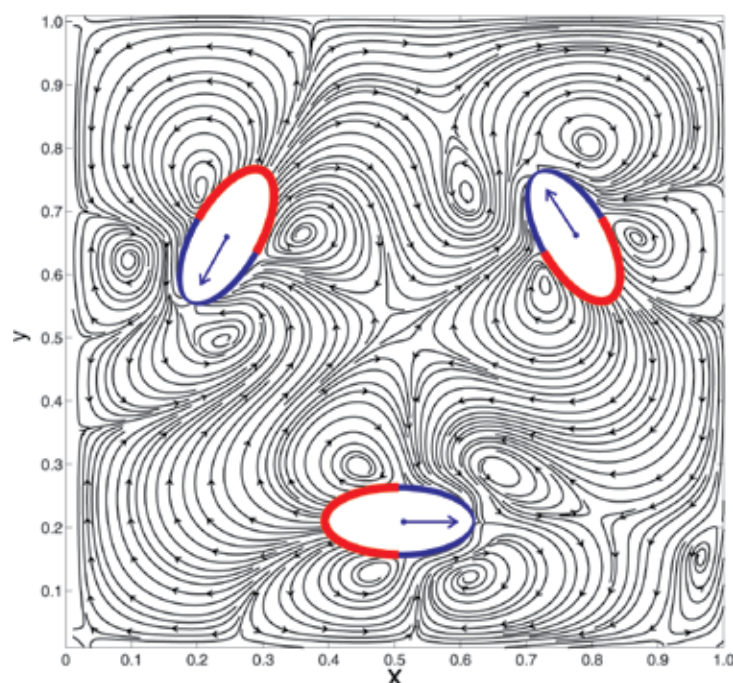


*Fig. 1. Streamlines for the flow generated by three self-propelled bacteria (colored ellipses) moving counterclockwise in a closed box with no-slip conditions on the walls. Fluid sticks to bacteria on blue parts of the ellipses, whereas on red parts fluid is pushed back to generate propulsion. Calculations were performed with the MFD method on a polygonal mesh obtained by intersection of a square 50 x 50 mesh with ellipses.*

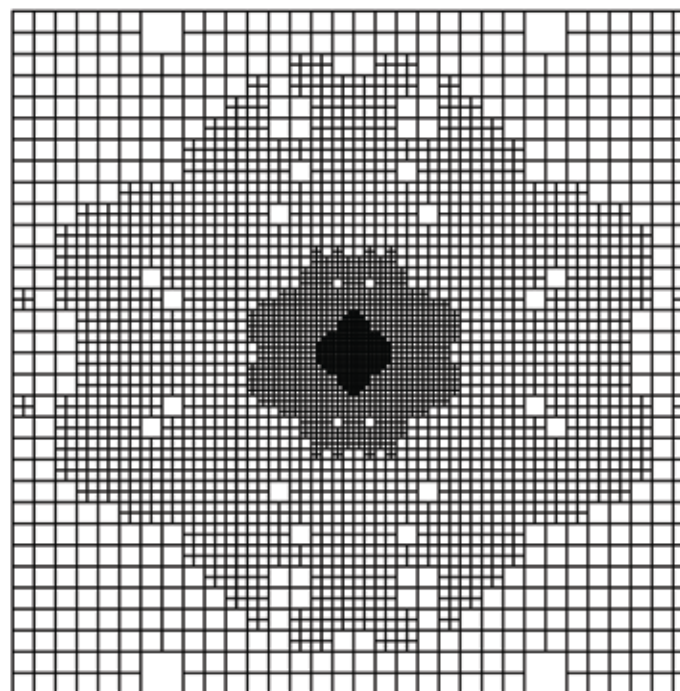


*Fig. 2. Example of an adapted mesh in Stokes flow with a singular point force in the middle of the domain. The mesh consists of regular quadrilateral elements and degenerate elements with five, six, and eight edges. The MFD method uses the same construction for all these elements.*

## Funding Acknowledgments

DOE, Office of Science,  
Office of Advanced  
Scientific Computing  
Research Applied  
Mathematics Science  
Program

# Mixing Asymmetry in Variable Density Turbulence

Daniel Livescu, CCS-2; J. R. Ristorcelli, X-3; Robert A. Gore, X-4-PC; Sumner H. Dean, CCS-2

**M**olecular mixing as a consequence of stirring by turbulence is an important process in many practical applications. If the microscopic densities of the fluids participating in the mixing are very different, we refer to such flows as variable density (VD) flows in contrast to the Boussinesq approximation, in which the densities are close. In VD flows, the velocity field is no longer solenoidal, and the specific volume, a function of the amount of each material present, is a new dependent variable. VD mixing is encountered in atmospheric and ocean flows, astrophysical flows, combustion, and many flows of chemical engineering interest [1,2]. Many of these flows are driven by acceleration (e.g., gravity in geophysical and astrophysical flows), which, because the density is not uniform, leads to large differential fluid accelerations. If the acceleration is constant and the fluid configuration is unstable (i.e., density gradient points opposite to the body force), a fluid instability is generated in which small perturbations of the initial interface between the two fluids grow, interact nonlinearly, and lead to turbulence. This instability is known as the Rayleigh-Taylor (RT) instability and is of fundamental importance in a multitude of applications, from fluidized beds, oceans, and atmosphere, to inertial confinement fusion (ICF) and supernova explosions.

The homogenization of a heterogeneous mixture of two pure fluids with different densities by molecular diffusion and stirring induced by buoyancy-generated motions was studied using direct numerical simulations (DNS) in two configurations: a) classical Rayleigh-Taylor instability using a  $3072^3$  data set [3,4], and b) an idealized triply periodic Rayleigh-Taylor flow named hereafter homogeneous Rayleigh-Taylor (HRT), using up to  $1024^3$  meshes [2,5].

The datasets used represent the largest simulations to date for each configuration. For the classical RT problem, the simulation achieves a bulk Reynolds number,  $Re = \frac{H\bar{H}}{\nu} = 32,000$ , at an Atwood number,  $A \equiv \frac{\rho_2 - \rho_1}{\rho_2 + \rho_1} = 0.5$ , where  $\rho_1, \rho_2$  are the pure fluid densities (PDF), and a Schmidt number,  $Sc = 1$ . The HRT flows start from rest, with the two fluids in a nonpremixed state corresponding to a double-delta density PDF. The turbulence is generated as the two fluids move in opposite directions due to the body force and eventually dies as the fluids become molecularly mixed. The DNS results are used to follow the turbulence birth-life-death process and examine the influence of various parameters, Atwood, Reynolds, and Schmidt numbers on the mixing rate and the morphology of the active scalar fields. The cases considered cover the Atwood number range  $A = 0.05 - 0.5$ , in order to examine small departures from the Boussinesq approximation as well as large Atwood number effects.

As a consequence of the differential accelerations experienced by the fluids, important differences between the mixing in a VD flow, as compared with the Boussinesq approximation, are observed. In short, the pure heavy fluid mixes more slowly than the pure light fluid—in HRT, an initially symmetric double delta density PDF is rapidly skewed, as the pure light fluid vanishes, and only at long times and small density differences does it relax to asymmetric, Gaussian-like PDF. The density PDF skewness generation mechanism,  $\langle p(p_{,j})^2 \rangle$ , is shown to be determined, through changes in the magnitude of the density gradient, by the eigenvalues of the strain rate tensor and the relative alignment between the density gradient and the eigenvectors of the strain rate tensor, which are different in the pure heavy and light fluid regions. Thus, the local structure of the flow changes in response to the inertia of the fluid particles. Consequently, the inertia of the heavy fluid reduces the rate at which it is broken up by stirring, decreasing the local surface area of the pure heavy fluid blobs, which is related to  $\sqrt{(\rho_{,j})^2}$ . As a result, the magnitude of the density gradient is lower in the pure, heavy fluid regions, along with the rate of molecular mixing, and the density PDF becomes skewed.

For the RT configuration at large density differences, this suggests that molecular mixing proceeds differently on the two sides of the RT layer. Experiments to date have not investigated this possibility. The results show that one consequence of the mixing asymmetry identified in HRT is that the penetration distance of the pure heavy fluid is larger than that of the pure light fluid. The mixing asymmetry is likely also the cause of the bubble-spike anomaly (higher growth rate on the spike side compared with the bubble side), which was observed experimentally [6].

**For further information contact Daniel Livescu at [livescu@lanl.gov](mailto:livescu@lanl.gov).**

- [1] A.W. Cook, P.E. Dimotakis, *J. Fluid Mech.* **343**, 69 (2001).
- [2] D. Livescu, J.R. Ristorcelli, *J. Fluid Mech.* **591**, 43 (2007).
- [3] W.H. Cabot, A.W. Cook, *Nature Phys.* **2**, 562 (2009).
- [4] D. Livescu, J.R. Ristorcelli, R. A. Gore, S. H. Dean, W. H. Cabot and A. W. Cook, to appear in *J. Turb.* (2008).
- [5] D. Livescu, J.R. Ristorcelli, *J. Fluid Mech.* **605**, 145 (2008).
- [6] G. Dimonte, M. Schneider, *Phys. Fluids* **12**, 304 (2000).

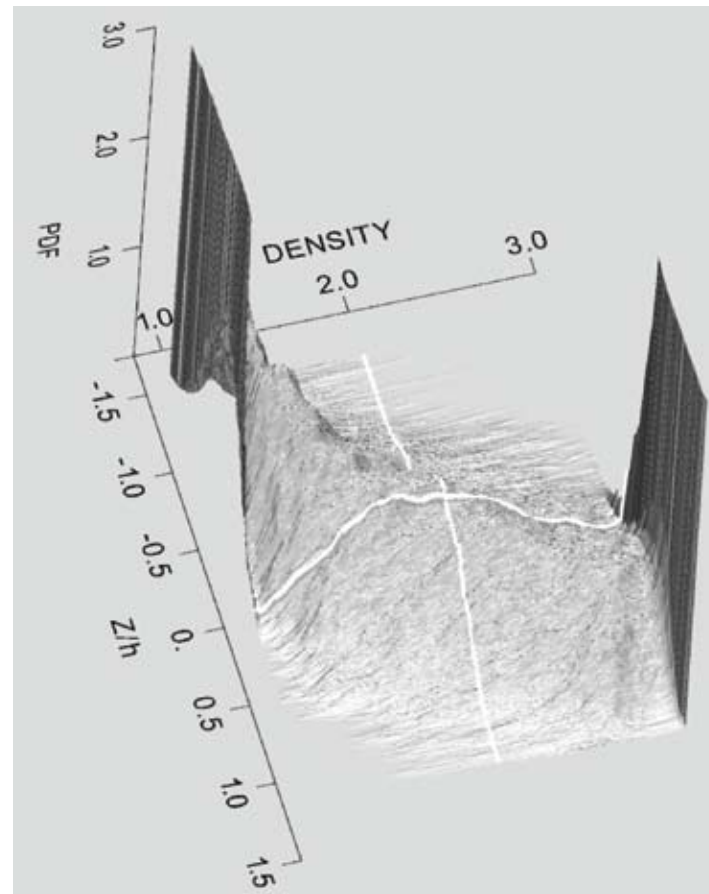


*Fig. 1. Surface plot of the density.*

### Funding

### Acknowledgments

LANL Directed  
Research and  
Development Program



# Predicting Reservoir Performance: A New Multiscale Method for Well Modeling

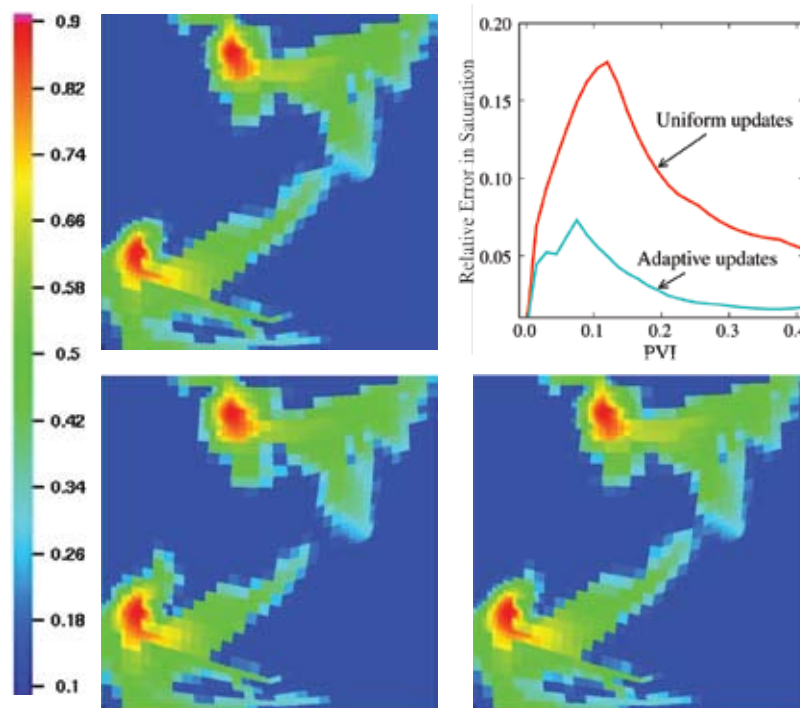
Konstantin Lipnikov, David Moulton, Daniil Svyatskiy, T-5

**M**ultiple strongly coupled space and time scales pose a significant challenge for high-fidelity simulations of real-world applications, including power generation in fission reactors and carbon dioxide sequestration in geologic formations. Here system response is measured at engineering-length scales (meters to kilometers) and yet depends crucially on information at microscopic-length scales. A simulation that fully resolves the microscopic details in a large-scale application is well beyond the computational power of modern supercomputers. A naive simulation that does not address the influence of

the fine scales is terribly inaccurate. In [1] we developed a novel multilevel multiscale mimetic ( $M^3$ ) method that strives to balance these extremes, and recently we enhanced its temporal adaptivity [2].

The  $M^3$  method recursively builds a problem-dependent *multilevel hierarchy of models*. Each model preserves important physical properties of the system, such as local mass conservation. In contrast with classical two-level methods that achieve a total coarsening factor of approximately 10 in each coordinate direction, the multilevel hierarchical approach facilitates large total coarsening factors of 100 or more. Maintenance of the hierarchy of models incurs only a modest computational overhead due to the efficiency of recursive coarsening and adaptive update strategies. The  $M^3$  method supports unstructured polyhedral meshes and accommodates general coarsening strategies to capture the geometric complexity of the heterogeneous subsurface environment.

Fig. 1. Using the composite grid (Fig. 2), the reference water saturation in a two-phase immiscible flow model after 240 days with injection of 200 ft<sup>3</sup> of water per day was generated (top left). The multiscale solution obtained using temporally uniform updates of the coarsening factors is shown at the bottom left. Although some features are captured well, later breakthrough of water moving along the low permeability barrier situated in the middle of the domain is apparent. The new adaptive strategy (bottom right) captures this feature precisely, achieving a 3 to 4 times reduction in the saturation error without increasing the computational cost (top right).



Wells in reservoir simulations, which are several centimeters in diameter, are effectively singular features on the reservoir scale and require special treatment to capture the nearby flow accurately. The popular Peaceman well model [3] assumes a homogeneous permeability field and a simple analytic form of the near-well flow in order to approximate its influence on the reservoir. However, these simple approximations are inadequate in practice because heterogeneities often exist near wells, and their influence is accentuated by the rapidly changing flow. To address this problem, various flow-based upscaling methods have been developed that use the solution of a local well-driven flow problem to define the well model. Unfortunately, this localization of the well-driven flow is achieved with approximate internal boundary conditions that often generate large uncontrolled errors.

To overcome these deficiencies we propose combining local mesh refinement around the wells, which naturally provides a multilevel structure, with the



M<sup>3</sup> method. It is important to note that unlike typical mesh refinement applications, a coarse-scale model is not known a priori. Instead, the M<sup>3</sup> method must build the hierarchy of scale-dependent models, including the coarsest-scale model, from the fine-scale data.

To efficiently maintain fine-scale accuracy in the multiscale solution, the M<sup>3</sup> method incorporates two *adaptive strategies*. First, the hierarchy of models is updated locally when the relative permeability, which depends on the water saturation, changes significantly. Second, an efficient error indicator, which was recently developed in [2], controls the temporal updates of the flux coarsening parameters. In contrast with the uniform updates used in [1], this new strategy concentrates updates around critical times when the invading fluid (water) first enters key features of the reservoir.

In this study we considered cell-based mesh refinement around four wells in a highly heterogeneous permeability field (see Fig. 2). Using the IMplicit Pressure and Explicit Saturation (IMPES) time-stepping scheme, we simulated 3000 days of water injection at 200 ft<sup>3</sup> per day. The numerical results (Fig. 1) demonstrated that with the new adaptive updating strategy [2] and a large coarsening factor, close to 250 in each coordinate direction around the wells and 8 far from the wells, the M<sup>3</sup> solution remained within 7% of the fine-scale solution. Moreover, the computational cost was reduced by a factor of 5.

**For further information contact David Moulton at [moulton@lanl.gov](mailto:moulton@lanl.gov).**

- [1] K. Lipnikov, J.D. Moulton, D. Svyatskiy, *J. Comput. Phys.* **227**, 6727-6753 (2008).
- [2] K. Lipnikov, J.D. Moulton, D. Svyatskiy, in preparation (2009).
- [3] D. W. Peaceman, *SPE* **18**, 183-194 (1978).

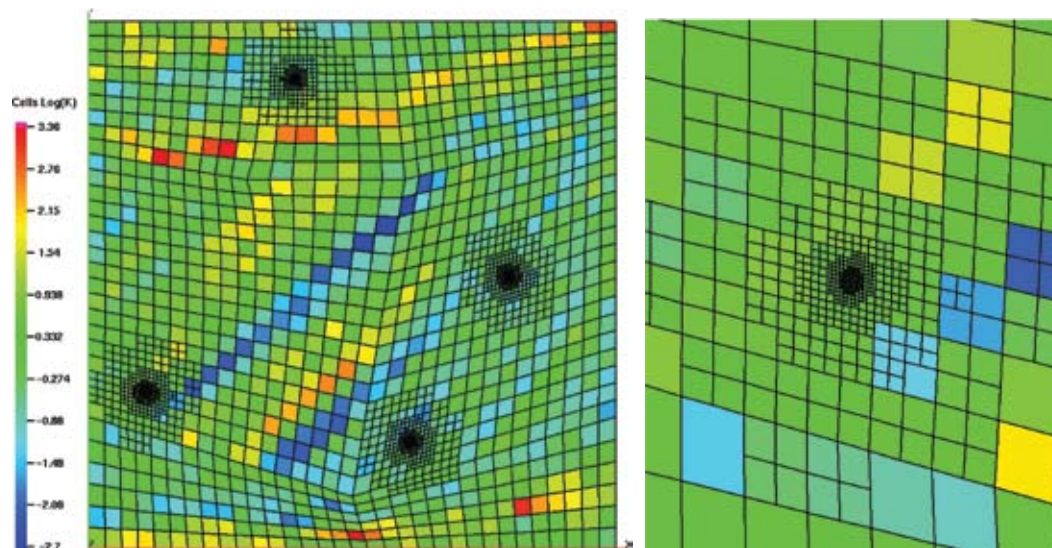


*Fig. 2. We considered a highly heterogeneous field that is aligned with the distorted, logically structured, 32 x 32 base grid (left). Five levels of local refinement are used around each of the four wells. For the left-most well, the local refinement is shown more clearly in the zoomed image on the right. Two injection wells are on the left, and two producing wells are on the right of the domain.*

## Funding

### Acknowledgments

DOE, Office of Science,  
Office of Advanced  
Scientific Computing  
Research Program  
Applied Mathematics  
Sciences

# On the Role of Initial Deposition of Baroclinic Vorticity in Richtmeyer-Meshkov Instability

Balu Nadiga, CCS-2

**I**mpulsive acceleration of an interface separating two fluids of different densities, as due to the passage of a shock wave, can lead to amplification of interfacial perturbations in a process termed Richtmeyer-Meshkov instability (RMI) (e.g., [1]). Since this instability mechanism has been recognized as playing a fundamental role in a wide array of natural and manmade phenomena, ranging from stellar evolution to supersonic combustion to inertial-confinement fusion, LANL has a keen interest in the study and description of RMI.

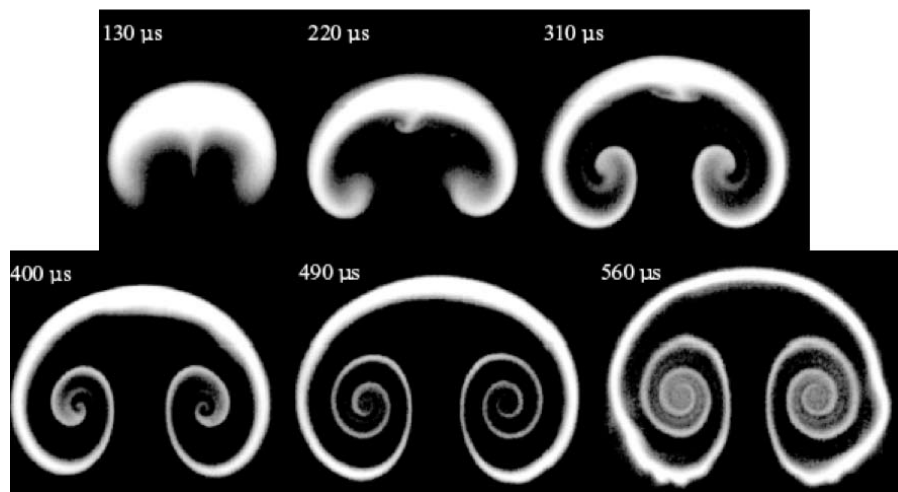
While it has long been recognized that the basic mechanism for the amplification of perturbations is the initial baroclinic deposition of vorticity (resulting from a misalignment of the density and pressure gradients), it is only recently that measurement and analysis of RMI at LANL have highlighted the importance of this mechanism in determining mixing and its characteristics (Fig. 1, [2]).

In this work, we consider a minimal description based on the initial baroclinic deposition of vorticity to describe some of the salient aspects of RMI (necessarily incompletely). For example, Fig. 2 shows the typical evolution of a cylinder of heavy gas. In this case, the initial deposition of baroclinic vorticity is such that there is no secondary instability. In Fig. 3, however, the initial deposition is such that secondary instabilities arise in the course of the evolution. In both these cases, however, the velocity field stretches and folds the density field and increases the power at higher wave numbers, a salient mechanism associated with mixing. Being an inherently unsteady

phenomenon, the scalar variance initially grows due to the stretching and folding of the interface, after which diffusive effects lead to its decay. (The time to reach the peak depends on the details of the setup and could be shorter or longer than the reshock time.) Figure 4 shows the evolution of the power spectral density (as a function of wave number) of the density field increasing from left to right with time. In other studies, we are considering the influence of the subsequent subdominant production of baroclinic vorticity.

From a different point of view, the deformation of the interface in any of the above realizations of RMI constitutes a free-boundary evolution problem. Other instances of free-boundary evolution in problems of importance include solidification (dendritic growth, casting) and viscous fingering. There is a project underway at the Laboratory to develop minimal descriptions of the complex shapes that arise in these cases of unstable and nonequilibrium free-boundary evolution processes [3]. The present computational framework is an ideal testbed for this project and will be used to test, verify, and further develop such minimal descriptions of complex shapes.

*Fig. 1. Experimental measurements of heavy gas concentration in Richtmeyer-Meshkov instability. Figure (adapted) from [2]. Such measurements have highlighted the importance of the initial deposition of baroclinic vorticity on the ensuing mixing.*



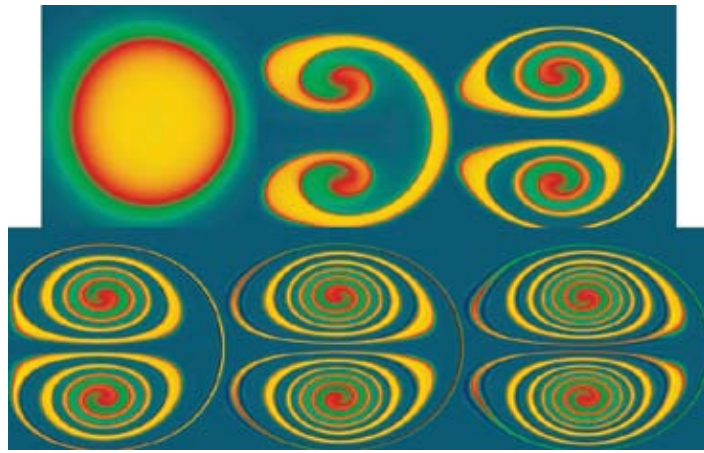


*Fig. 2. The rollup of a cylinder of heavy fluid in a numerical setup of Richtmyer-Meshkov instability that retains only the initial deposition of baroclinic vorticity. In this case the initial deposition is such that no secondary instabilities develop.*

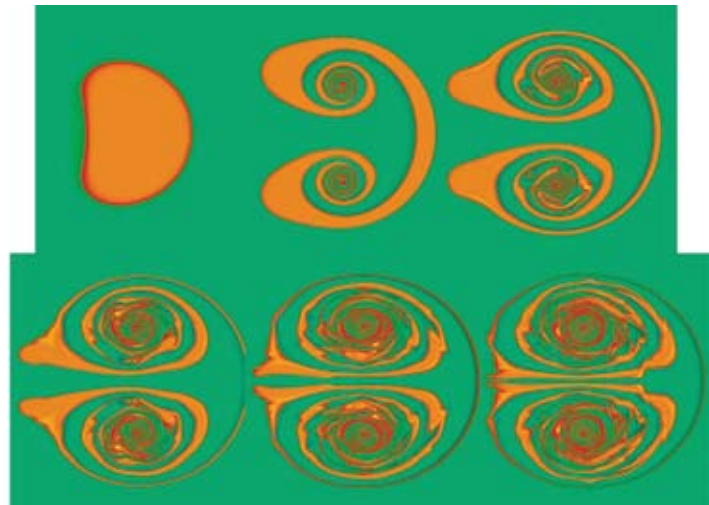


*Fig. 3. In a setup similar to that in Figure 2, secondary instabilities are seen to develop (seen in the breakup of the initial spiral rollup) if the magnitude of the initial deposition is higher.*

For further information contact Balu Nadiga at [balu@lanl.gov](mailto:balu@lanl.gov).

- [1] M. Brouillette, *Ann. Rev. Fluid Mech.* **34**, 445-468 (2002).
- [2] C. Tomkins et al., *J. Fluid Mech.* **611**, 131-150 (2008).
- [3] M. Mineev, LA-UR-06-5904 (2006).

**Funding**  
**Acknowledgments**  
LANL Institutional  
Computing Resources

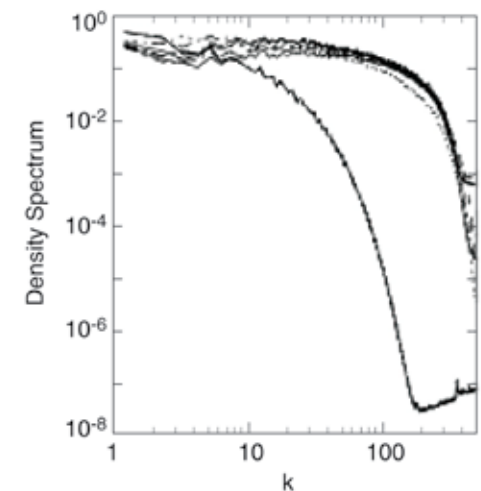
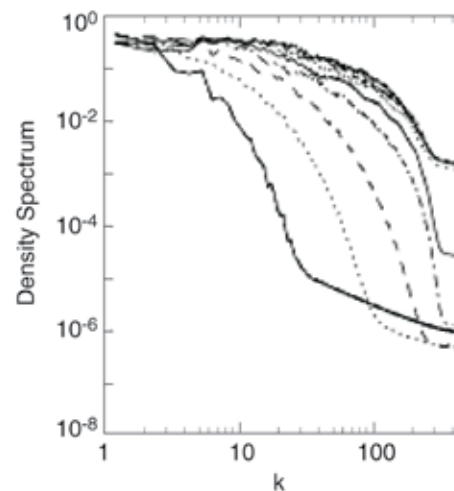


*Fig. 4. Power spectral density against wave number for cases in Fig. 2 and Fig. 3 shows that in this unsteady problem, the stretching and folding of the interface by the velocity field increases the variance in the density field, setting the stage for further diffusive mixing.*



# High Resolution Simulations of Compressible Isotropic Turbulence

Mark R. Petersen, Daniel Livescu, Sumner H. Dean, Jamaludin Mohd-Yusof, CCS-2

*Fig. 1. Energy spectrum from a  $1024^3$  isotropic simulation. The total spectrum (black) and solenoidal spectrum (red) closely follow a slope of  $k^{-5/3}$  (dashed line), while the dilatational spectrum (blue) has a slope of  $k^{-5/3}$  for small  $k$ , but has a steeper slope for larger  $k$ .*

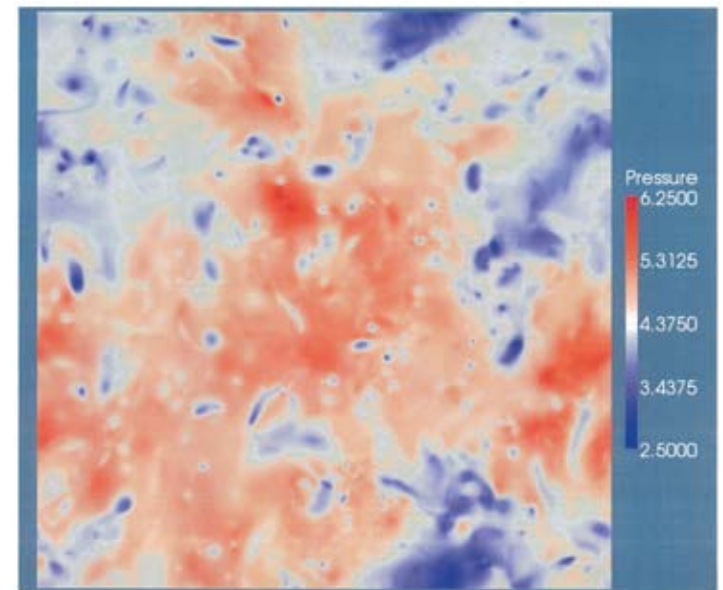
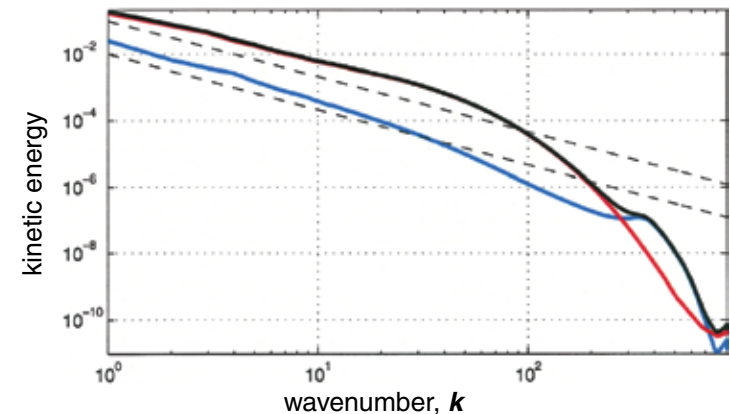
*Fig. 2. Large variations in pressure and density are typical in compressible turbulence.*

Understanding the nature of compressible turbulence is of fundamental importance in many applications ranging from astrophysics to combustion and aerospace engineering. Highly compressible turbulence is now thought to control star formation in dense molecular clouds [1]. The ability to parameterize the effects of turbulence is necessary for the modeling of exothermic reacting flows and high-speed flows and is a required ingredient for designing the next generation of ramjet engines and hypersonic vehicles.

There are many differences between compressible turbulence and the more commonly studied incompressible turbulence. In many applications, such as ocean dynamics and large-scale atmospheric motion, the velocity fluctuations are small compared with the speed of sound, the density is nearly constant, and the irrotational effects are small. However, as the velocity fluctuations become comparable to the sound speed and/or exothermic reactions take place, new phenomena occur: shock waves, localized expansion and contraction providing a distinct dissipation mechanism, new nonlinearities leading to additional scale coupling, and strong fluctuations of the thermodynamic quantities.

We research the nature of compressible turbulence using direct numerical simulation (DNS), where all scales down to the viscous dissipation range are fully resolved (see [2]). Our simulations use a 3D triply periodic domain with up to  $1024^3$  grid points, and are by far the highest resolution compressible Navier-Stokes DNS to date. The Taylor Reynolds number is 300 or greater, which is much higher than previous studies. Each large simulation requires a week of run time using 1024 processors on Purple, a supercomputer at LLNL. Preliminary results show that the total energy spectrum follows the Kolmogorov 1941  $k^{-5/3}$

law, while the dilatational (compressive) spectrum is steeper than  $k^{-5/3}$  (Fig. 1). The characteristics of compressibility can be observed in visualizations of pressure and density, where large variability and gradients can be seen (Fig. 2). Shocklets are small, isolated shock waves that occur in these areas, and are thought to be responsible for many of the effects of compressible turbulence [3].





In order to control the dilatational energy in these simulations, we have developed a new method of forcing for compressible fluid simulations. Forced simulations inject energy so that the dynamics reach a stationary state where the injection rate (usually at large scales) is equal to the rate of energy dissipated at small scales. We chose deterministic forcing, because it has more realistic properties than traditional stochastic forcing. However, deterministic forcing methods developed for incompressible fluids do not apply directly, because the dilatational energy component may grow without bound, resulting in an unstable simulation. Our new method allows the user to specify the dilatational and solenoidal (incompressible) energy dissipation, as well as the Kolmogorov scale, ensuring that the simulation is stable and well resolved.

The control of the new forcing method allowed us to conduct a large study of  $M_t$  -  $\chi$  parameter space, where  $M_t$  is the turbulent Mach number, and  $\chi$  is the ratio of dilatational to solenoidal kinetic energy. These parameters exhibit the effects of compressibility—low  $M_t$ , low  $\chi$  simulations are nearly incompressible, while high  $M_t$ , high  $\chi$  simulations have strong density gradients and shock waves. Plots of long-time averages of statistics in  $M_t$  -  $\chi$  parameter space show how these quantities vary (Fig. 3). This type of data is useful for developing parameterizations of the effects of compressible turbulence in engineering-scale simulations where the smallest scales are not resolved. For this study, 18 simulations with a Taylor Reynolds's number of  $\sim 100$  were conducted on the San Diego Supercomputer Center's Blue Gene system.

The next topic in our study of compressible fluids is turbulence-shock interaction. To this end, we record data from the isotropic simulations and introduce it as an inlet condition in a shock tube domain, where the isotropic turbulence is passed through a shock. Statistics such as streamwise stress anisotropy, streamwise mass flux, and density-volume correlation, which are useful to modelers focusing on moment closures, are recorded over the shock. Our study will use shock Mach numbers of 1.2 to 3,

turbulent Mach numbers of 0.02 to 0.5, and Taylor Reynolds numbers of 70 to 300. This range of parameters is much larger than previous studies [4,5], and approaches realistic values of physical experiments [6].

**For further information contact Mark Petersen at [mpetersen@lanl.gov](mailto:mpetersen@lanl.gov).**

- [1] M.M. Mac Low, R.S. Klessen, *Rev. Mod. Phys.* **76**(1), 125-194 (2004).
- [2] D. Livescu, F.A. Jaberi, C.K. Madnia, *J. Fluid Mech.* **450**, 35-66 (2002).
- [3] R. Samtaney, D.I. Pullin, B. Kosovic, *Phys. Fluids* **13**, 1415-1430 (2001).
- [4] S. Lee, S.K. Lele, P. Moin, *J. Fluid Mech.* **340**, 225-247 (1997).
- [5] S. Jamme, et al., *Flow, Turbulence and Combustion* **68**, 227-268 (2002).
- [6] Y. Andreopoulos, J.H. Agui, G. Briassulis, *Ann. Rev. Fluid Mech.* **32**(1), 309-345 (2000).

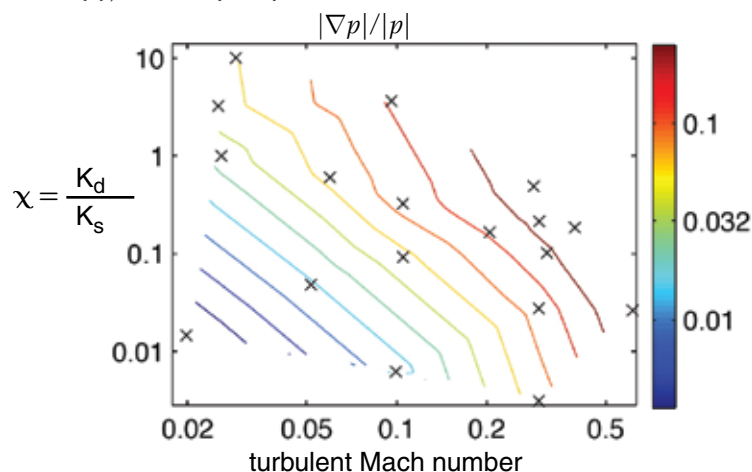


*Fig. 3. Numerous simulations, each denoted by x, were performed to explore the behavior of turbulence as a function of dilatational energy ratio,  $\chi$ , and the turbulent Mach number,  $M_t$ . This contour plot shows that normalized pressure gradients increase with both  $\chi$  and  $M_t$ .*

## Funding

### Acknowledgments

- DOE, NNSA, Advanced Simulation and Computing Program
- LANL Directed Research and Development Program

# Two Conjectures on the Crisis of Cell-Centered Diffusive Operators for the Iterative Acceleration of Neutron Transport Methods in the PHI Configuration

Massimiliano Rosa, CCS-2; Yousry Y. Azmy, North Carolina State University;  
Jim E. Morel, Texas A&M University

A recent study examined the asymptotic behavior of the elements of the integral transport matrix **B** in the thick-cell limit for homogeneous configurations in 2D [1]. It was shown that **B** acquires a sparse structure, implying a strong local coupling of a cell-averaged scalar flux with only its nearest Cartesian neighbors. Here we extend this work to the Periodic Horizontal Interface (PHI) configuration, where layers of two different materials are stacked in the  $y$  direction in an alternating fashion. The asymptotic properties of **B** lead to the formulation of two conjectures on the structural deficiency of the Adjacent-cell Preconditioner (AP) [2,3], and potentially of other diffusive operators, notably Diffusion Synthetic Acceleration (DSA) [4,5], in PHI. The two conjectures are verified by devising two novel acceleration schemes, named APB and OAP. A loss of unconditional robustness has been observed, both for AP and DSA, in strongly heterogeneous multidimensional configurations. In this respect, the verification of the above conjectures represents a first step in understanding and possibly resolving the crisis of diffusive operators in such configurations.

**Integral Transport Matrix in PHI.** For PHI we seek estimates for the strength of coupling of a cell-averaged scalar flux for a cell in the thick (K) or thin (N) layer with the fluxes in its neighbors. We consider an even number of layers,  $J$ , comprising  $I$  computational cells along the  $x$ -axis. The cells' properties are:

$$K \text{ cell, } j \text{ even: } \delta_x, \delta_y, \Sigma_K = \sigma_K \Delta, c_K$$

$$N \text{ cell, } j \text{ odd: } \delta_x, \delta_y, \Sigma_N = \sigma_N / \Delta, c_N$$

The scattering ratios  $c_l$ , with  $l = N, K$ , are fixed parameters, and a uniform mesh with fixed cell size  $\delta_x, \delta_y$  is assumed. The total cross sections  $\Sigma_l$  are scaled according to the dimensionless parameter  $\Delta$ , vanishing like  $\Delta^{-1}$  in the N layer and diverging like  $\Delta$  in the K layer as  $\Delta \rightarrow \infty$ . The results pertaining to an N cell are of particular relevance. Hence, the results summarized in Fig. 1 refer to cell (1,1) in an N layer. Denoting the cell aspect ratio  $R \equiv \delta_x / \delta_y$  the behavior of the **B** elements for square cells,  $R = 1$ , is distinct from their behavior for rectangular cells,  $R \neq 1$ . The results in Fig. 1 indicate that the coupling of an N cell's scalar flux with

Fig. 1. Strength of coupling of N cell's flux with its neighbors for PHI.

$j=4$	<b>K</b>				
$r=3$					
$j=3$	N	$O(\Delta^{-3})$	$O(\Delta^{-3})$	$O(\Delta^{-3})$	$O(\Delta^{-3})$
$r=2$					
$j=2$	K	$O(\Delta^0)$	$O(\Delta^0)$	$O(\Delta^0) \text{ } R \neq 1$	$O(\Delta^0) \text{ } R \neq 1$
$r=1$			$O(\Delta^{-1}) \text{ } R=1$	$O(\Delta^0)$	$O(\Delta^{-1}) \text{ } R=1$
$j=1$	N	$O(\Delta^0)$	$O(\Delta^{-1})$	$O(\Delta^{-1})$	$O(\Delta^{-1})$
		$c_N \leq 1$			
		$i=1$	$i=2$	$i=3$	$i=4$
			$r=1$	$r=2$	$r=3$
				$r=3$	$r=4$

the fluxes in the next K layer (interlayer coupling) can be of the same order as self-coupling and coupling with the first Cartesian neighbors. Also, the coupling of an N cell's scalar flux with the fluxes in the same N layer (intralayer coupling) is of the same order, independent of the distance between the cells in the layer. The long-range nature of the latter coupling plays an important role in the loss of robustness of AP.

**APB.** The AP ignores the strong cross-derivative coupling between a cell and its diagonal neighbors, displayed by the full **B**. Therefore, we conjecture, and establish via numerical experiments, that extended low-order operators that account

for cross-derivative coupling can recover acceleration robustness in PHI. Specifically, the APB extends AP by including cross-derivative coupling in a nine-point stencil operator that was implemented in the AP2 code [2]. The  $L_2$  estimates of the spectral radius  $\rho$  obtained from the code with increasing mesh size for vacuum boundary conditions are contrasted with the values predicted from the Fourier analysis for a model PHI in Table 1. In the model  $c_{K,N} = 1 - 10^{-8}$ ,  $\delta_{x,y} = \sigma_{K,N} = 1$ , and  $S_6$  level symmetric angular quadrature are used. The number of iterations consumed to achieve  $10^{-5}$  convergence of the scalar fluxes for the same problem driven by a uniform unit fixed source is also reported in Table 1. The APB's spectral radius is bounded below 0.55 for all  $\Delta$ , whereas AP's approaches 1 as  $\Delta \rightarrow \infty$ . Indeed, in contrast to APB, which converges for all values of  $\Delta$ , AP did not converge in 50 iterations for  $\Delta > 10^2$ . Results of further testing beyond the model problem indicate that robustness of APB decreases with increasing  $R$ , with  $\rho$  exceeding 0.8 for  $R$  larger than 4:1. This behavior appears consistent with the dependence on  $R$  of the asymptotic results in Fig. 1.

Table 1. Spectral radius and APB iterations in PHI.

	$\Delta$					
$I \times J$	$10^0$	$10^1$	$10^2$	$10^3$	$10^4$	$10^5$
<b>10 × 10</b>	0.103 5	0.392 12	0.460 13	0.468 14	0.468 14	0.468 14
<b>20 × 20</b>	0.117 5	0.444 12	0.515 14	0.523 15	0.524 15	0.523 14
<b>40 × 40</b>	0.123 5	0.463 13	0.534 15	0.542 15	0.543 15	0.542 15
<b>80 × 80</b>	0.124 5	0.468 13	0.539 15	0.547 15	0.548 15	0.547 15
<b>160 × 160</b>	0.124 5	0.470 13	0.540 15	0.548 15	0.549 15	0.548 15
<b>Fourier</b>	<b>0.125</b>	<b>0.471</b>	<b>0.541</b>	<b>0.549</b>	<b>0.550</b>	<b>0.549</b>

**OAP.** A second conjecture we propose attributes the crisis of AP to its overestimating the strength of intralayer coupling

in an N layer. The OAP maintains the five-point stencil of AP while optimizing the value of the elements exerting intralayer coupling in the N and K layers. The optimization procedure is time consuming and was performed only for  $\Delta$  equal to  $10^4$  and  $10^5$ , to test the validity of the conjecture in the asymptotic regime. The  $L_2$  estimates of  $\rho$  and the iterations consumed to achieve  $10^{-5}$  convergence of the scalar fluxes are contrasted with the values predicted from Fourier analysis for the model problem in Table 2. The OAP is more resilient to adverse effects of material discontinuities than APB. Though numerical results beyond the model problem show that its robustness is also conditional with respect to  $R$ —namely, it is guaranteed that  $\rho$  does not exceed 0.8 up to an aspect ratio of 5:1. Further research is envisioned for a nine-point OAP that holds promise to improve the spectral properties of OAP by incorporating cross-derivative coupling. We also wish to find a prescription for computing the optimization coefficients from the geometric and material properties of the transport problem.

Table 2. Spectral radius and OAP iterations in PHI.

	$\Delta$			
	$10^4$		$10^5$	
$I \times J$	$\rho$	$It$	$\rho$	$It$
<b>10 × 10</b>	0.282	9	0.281	9
<b>20 × 20</b>	0.341	9	0.340	9
<b>40 × 40</b>	0.369	10	0.363	10
<b>80 × 80</b>	0.378	10	0.381	10
<b>160 × 160</b>	0.388	10	0.388	10
<b>Fourier</b>	<b>0.390</b>		<b>0.390</b>	

For further information contact Massimiliano Rosa at [maxrosa@lanl.gov](mailto:maxrosa@lanl.gov).

- [1] M. Rosa et al., *Trans. Am. Nucl. Soc.* **95**, 585-587 (2006).
- [2] Y.Y. Azmy, *Nucl. Sci. Eng.* **136**, 202-226 (2000).
- [3] Y.Y. Azmy, *J. Comp. Phys.* **182**, 213-233 (2002).
- [4] E.W. Larsen, *Nucl. Sci. Eng.* **82**, 47-63 (1982).
- [5] J.S. Warsa et al., *Nucl. Sci. Eng.* **147**, 218-248 (2004).

**Funding  
Acknowledgments**  
LANL Directed  
Research and  
Development Program

# Multimaterial Incompressible Flow Simulation Using the Moment-of-fluid Method

Samuel P. Schofield, Rao V. Garimella, Blair K. Swartz, T-5; Mark A. Christon, SIMULIA; Vadim Dyadechko, Exxon Mobile; Robert B. Lowrie, CCS-2

We have incorporated the moment-of-fluid (MOF) interface reconstruction method into a finite element-based, variable-density, incompressible Navier-Stokes solver for the simulation of fluid flows involving large numbers of different materials. This method provides a significant improvement in accuracy while eliminating the nonphysical material order dependence.

For multimaterial flow simulations, accurate and robust management of material interfaces is essential. A proven computational technique, the volume-of-fluid (VOF) method [1], tracks the fractional volumes of materials in each computational cell and is widely used. When the material interfaces are required they are recreated from the volume fraction data in a process known as interface reconstruction.

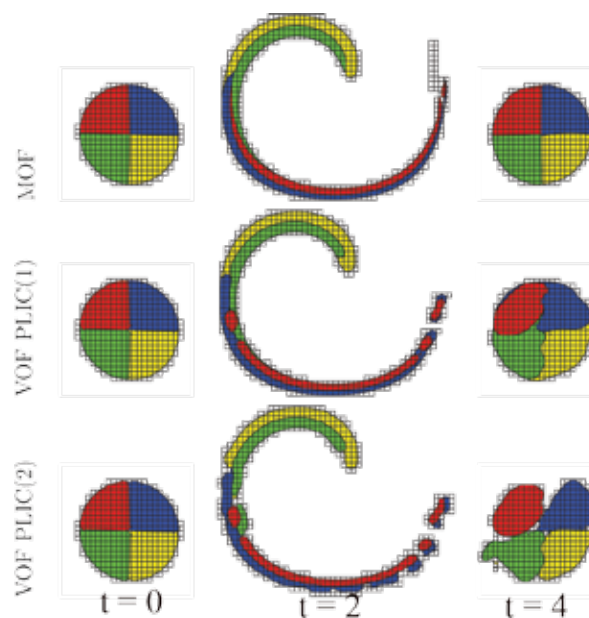
In the interface reconstruction process, the material interfaces are reconstructed on a cell basis using arbitrarily oriented lines. These are referred to as piecewise linear interface reconstruction (PLIC) methods. The original PLIC method developed by Youngs [2] defined the outward interface normal as the negative gradient of the volume fraction function. It is first-order accurate, but gives reliable results. These methods and their second-order accurate extensions such as LVIRA [3], create different interfaces depending on the order in which materials are processed and can only resolve features larger than two to three mesh cells.

In contrast, the second-order-accurate MOF method [4], developed at LANL by V. Dyadechko and M. Shashkov, has

subcell accuracy and is material-order independent. MOF tracks the material volumes and cell-wise first moments and then recreates the interfaces by minimizing the discrepancy in the first moment between the actual and the reconstructed interface while exactly matching the volume. The superior accuracy and robustness of the MOF method is shown in advection and incompressible fluid flow simulations.

The advection of scalar quantities and materials is frequently encountered in complex multiphysics applications. To demonstrate the performance of MOF for advection problems, a simulation with significant deformation of the materials was performed. In this test case described in [5], a four-material circle is placed in a time-dependent vortex given by a solenoidal velocity field. At time  $t = 2$ , the circle will be at maximum deformation. From there, the flow reverses and at time  $t = 4$ , it should exactly match the initial condition. The superior accuracy of MOF is clearly shown in Fig. 1. In addition, the PLIC method results show strong dependence on material ordering.

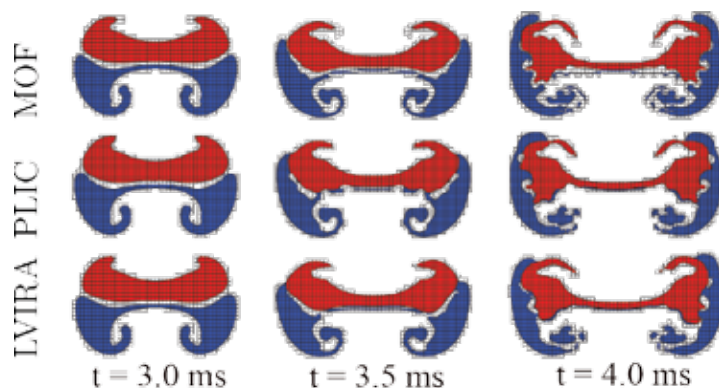
*Fig. 1. Time-reversed vortex advection test. For VOF PLIC(1), the material order was (White, Red, Blue, Yellow, Green); for VOF PLIC(2) the order was (Red, Blue, Yellow, Green, White). At time  $t = 4$ , the material configuration should exactly match the initial condition at time  $t = 0$ .*





For most problems of interest, the advection of material quantities impacts the evolution of the flow field. To explore these problems, we have incorporated MOF in a second-order accurate projection-based finite element method for numerical simulation of the variable density incompressible Navier-Stokes equations that describe the flow of immiscible, viscous fluids. In the simulation, the volume of each fluid in a cell is updated by geometrically solving an advection equation using interface reconstruction and a backward-Lagrangian technique.

As a demonstration, we consider the simple test case of two colliding bubbles where density differences drive the flow and the material interfaces and positions are strongly coupled to the flow field. The top and bottom bubbles have a density of  $1.5 \text{ g/cm}^3$  and  $0.5 \text{ g/cm}^3$  respectively and are placed in a fluid with a density of  $1.0 \text{ g/cm}^3$ . As shown in Fig. 2, MOF better preserves the thin material interfaces than the first-order PLIC method and the second-order LVIRA method.



**For further information contact Sam Schofield at [sams@lanl.gov](mailto:sams@lanl.gov).**

- [1] W.J. Rider, D.B. Kothe, *J. Comput. Phys.* **141**, 112–152 (1998).
- [2] D. L. Youngs, in *Numerical Methods for Fluid Dynamics*, Ed. K. W. Morton and M. J. Baines, Academic Press, **273–285** (1982).
- [3] J.E. Pilliod, E.G.J. Puckett, *Comput. Phys.* **199**, 465–502 (2004).
- [4] V.D. Dyadechko, M.J. Shashkov, *Comput. Phys.* **227**, 5361–5384 (2008).
- [5] Schofield, et al., *J. Comput. Phys.* **228**, 731–745 (2009).

*Fig. 2. Colliding bubbles simulations. The LVIRA and PLIC methods show stronger numerical surface tension and the breakup of the thin filaments. MOF preserves the thin white fluid layer separating the red and blue fluids.*

By integrating MOF into a variable density incompressible flow solver, we have demonstrated the capability of MOF to provide more accurate and reliable material interface treatment in dynamic simulations. In such simulations, the MOF method clearly outperforms existing first- and second-order methods and represents a significant advance in material treatment.

**Funding  
Acknowledgments**  
LANL Directed  
Research and  
Development Program

# A Sharp-to-continuous Interface Tracking Transition Algorithm for Multicomponent Fluid Flow Simulation

Marianne M. Francois, Robert B. Lowrie, Edward D. Dendy, CCS-2

The volume tracking method [1], also known as volume-of-fluid (VOF) method with interface reconstruction, is a broadly used numerical method that simulates immiscible multicomponent fluid flow where the interface is represented as a sharp boundary and is evolved as part of the solution of the flow equations. In volume tracking, the underlying mesh is fixed (Eulerian framework) and the interface is not explicitly tracked as in the front-tracking approach—it is captured by the material volume fraction and is geometrically reconstructed by piecewise linear interface planes (PLIC) [1]. Geometric reconstruction allows accurate estimation of mass and momentum fluxes and avoids numerical diffusion of the interface. The method's main drawback is when the interface reconstruction becomes under-resolved, i.e., when the interface length scale becomes smaller than three to four grid points. Interface reconstruction is known to introduce numerical surface tension, which breaks a filament into a series of droplets whenever the filament is under-resolved [1]. Adaptive mesh refinement can help avoid under-resolution, but a fully developed flow will still generate filaments that cannot be resolved without enormous computational cost. The goal here is to propose a complementary new approach that consists of transitioning locally from volume tracking to a continuous interface representation (i.e., without interface reconstruction) in regions where volume tracking has become erroneous.

In order to locally identify the regions where the interface reconstruction has become erroneous, we base the switch criterion of the transition algorithm on the interface curvature information. A good indication that the mesh size

is too coarse to resolve the interface length scale is when the interface curvature is becoming too large with respect to the underlying mesh size. To compute interface curvatures, we employ the height function method, a very efficient and accurate technique [2]. For the sharp representation of the interface we employ the volume tracking method of Rider and Kothe [1]. For the continuous interface representation we employ the interface preserver approach of Dendy and Rider [3], also known as the artificial steepening or compressive limiter method, in which the volume fraction gradients are steepened in order to keep the numerical diffusion to a minimum. Our algorithm is the following: at every time step, we compute the interface curvatures. Based on the interface curvature value, we then assign the interface treatment flag either to volume tracking or interface preserver. The advection fluxes at the cell faces are then estimated based on the flow velocity direction and the interface treatment flag (volume tracking or interface preserver). Finally, the volume fractions are updated in time.

To illustrate the transition algorithm potential, we present the test case of a single vortex deformation flow field, a common test case used for testing material advection algorithms. Initially a circular interface of radius 0.15 is located at (0.5, 0.75) in a unit square domain, and a vortex velocity field is specified on the entire domain as a function of time. We run our simulation until  $T/2$ —the time at which the maximum stretching occurs on a  $32 \times 32$  mesh (a coarse mesh to highlight the benefit of a transition algorithm). The volume fraction contours are shown in Fig. 1 at time  $t = 2$ . Note that for the volume tracking method the interface planes are not plotted, but the volume fraction contours are plotted to facilitate the comparison with the interface preserver and transition algorithm methods. We observe that on the  $32 \times 32$  mesh the (1) volume tracking algorithm leads to the breaking of the interface into droplets, (2) interface preserver method slightly diffuses the interface but keeps the correct interface topology, and (3) transition algorithm avoids the interface break-up. In order to quantify our results, we define a global error metric  $\delta$  as a function of time to measure the advection error on the coarse mesh with respect to a

reference solution on a fine mesh ( $512 \times 512$ ). The error  $\delta$  is plotted in Fig. 2. This plot shows that the overall accuracy is greatly improved by using our material interface transition algorithm based on a curvature switch criterion. Additional numerical test cases of complex deformation flow field and Rayleigh-Taylor instability are given in [4].

A new algorithm has been designed to transition locally from volume tracking to interface capturing within a single fluid field Eulerian formulation. The transition criterion of the algorithm is based on interface curvature, a geometric measure. This algorithm has the potential to lead to a more accurate prediction of surface areas, which is very valuable when modeling coupled multiphysics phenomena.

**For further information contact Marianne Francois at [mmfran@lanl.gov](mailto:mmfran@lanl.gov).**

- [1] W.J. Rider, D.B. Kothe, *J. Comp. Phys.* **141**, 112-152 (1998).
- [2] M.M. Francois et al., *J. Comp. Phys.* **213**, 141-173 (2006).
- [3] E.D. Dendy, W.J. Rider, LA-UR-04-1971 (2004).
- [4] M.M. Francois et al., *Proceedings of the FEDS ASME*, LA-UR-08-1264 (2008).

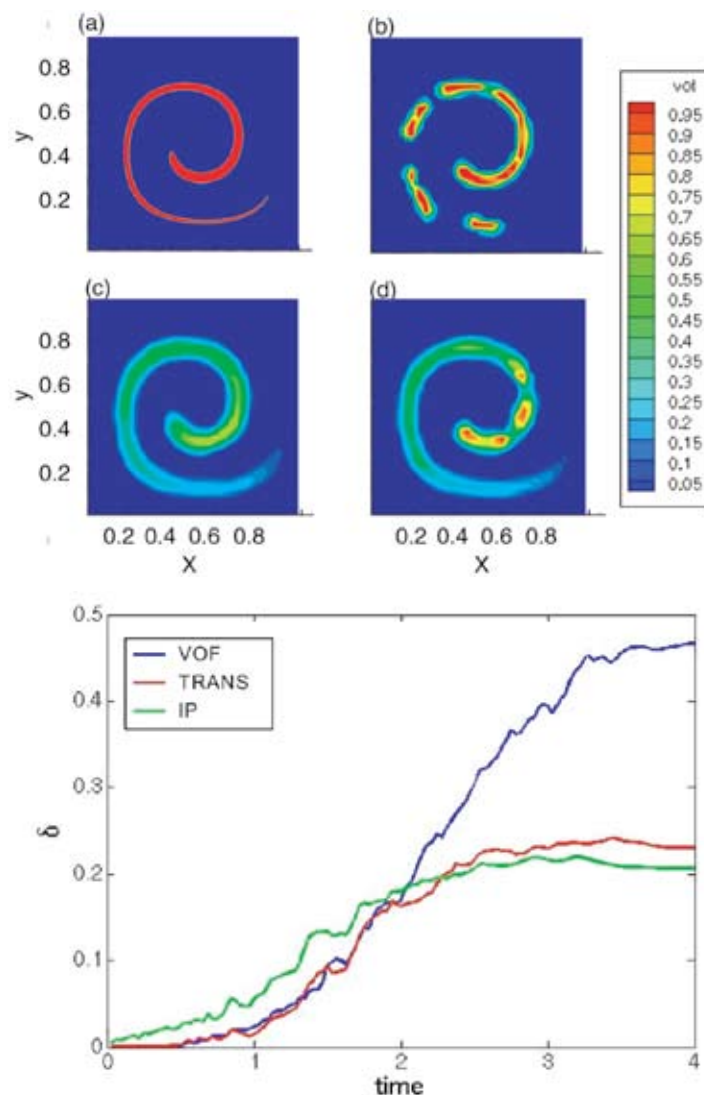


Fig. 1. Volume fraction contours at time  $t=2$  for the single vortex deformation flow field of period  $T=8$  on a  $32 \times 32$  mesh. (a) Reference volume tracking solution on a  $512 \times 512$  mesh, (b) volume tracking, (c) interface preserver, and (d) transition algorithm.

Fig. 2. Volume fraction error versus time for the single vortex deformation flow field on a  $32 \times 32$  mesh.

## Funding

## Acknowledgments

DOE, NNSA, Advanced Simulation and Computing Hydrodynamics Program

# Regularization of Particle Transport Models with Diffusive Relaxation

Cory D. Hauck, Robert B. Lowrie, CCS-2

We present recent progress on numerical methods for a family of linear hyperbolic balance laws with stiff diffusive relaxation that model particle transport in a material medium. In diffusive regimes, conventional hyperbolic solvers for these systems suffer from excessive numerical dissipation, numerical stiffness, or both. We have developed a regularization technique to address such issues at the continuum level.

In kinetic models of particle transport, diffusive relaxation is a common phenomenon that occurs when the mean free path between particle collisions with a material medium is small when compared with the macroscopic scales of interest. In such cases, particles undergo frequent collisions with the material so that, over long time scales, the predominant macroscopic behavior of the system is diffusive.

We are specifically interested in simulating the time-dependent  $P_N$  equations, a linear hyperbolic system of  $N + 1$  moment equations that is used to approximate kinetic transport in neutron and photon applications. Using operator-splitting techniques, we have formally derived a regularized version of the  $P_N$  system for which the diffusive limit is explicitly built-in. Our method is a nontrivial extension of an approach used in [1]. It applies to a large family of balance laws, allows for large time steps, and handles spatial variations in the material medium, which affect the local collision rate. Moreover, the regularization does not suffer from oscillations that sometimes appear in other splitting methods [4].

The derivation of the regularized  $P_N$  system proceeds in three steps: 1) separation of the equations into two subsystems, each containing either fast or slow dynamics;

2) discretization of each subsystem in time, keeping spatial derivatives in continuum form; and 3) recombining the semidiscretized subsystems and taking specific limits to get back the continuum time derivative. The result is a hyperbolic-parabolic system with the following properties [2,3]:

- In diffusive regimes, standard numerical methods for the regularized equations capture the diffusion limit with a mesh spacing based on the macroscopic solution profile and not the mean free path. This is the so-called asymptotic preserving (or AP) property [1].
- In cases where the mean free path is not resolved by the spatial mesh, there is no hyperbolic Courant-Friedrichs-Lewy (CFL) condition. Thus an implicit discretization of the diffusion operator allows for large time steps. Moreover, the diffusion operator is diagonal, so that implicit solvers are relatively easy to implement.
- In streaming regimes, where the mean free path is relatively large and collision rates are low, the regularized system behaves like the standard  $P_N$  equations.

Computational results for 1D test problems confirm that the regularization gives accurate results in different regimes and that, in the diffusion regime, it does so at a fraction of the cost of upwind or discontinuous Galerkin solvers for the original  $P_N$  system.



Results from a sample simulation are given in Figs. 1 and 2, where the particle concentration based on a P3 calculation is plotted. An important parameter here is the cell optical depth, which gives the number of mean free paths in a computational cell. When this value is large, upwind schemes tend to be overly dissipative and numerically stiff. These results confirm the properties of the regularization outlined above.

**For further information contact Cory Hauck at [cdhauck@lanl.gov](mailto:cdhauck@lanl.gov).**

- [1] S. Jin, *SIAM J. Sci. Comp.* **21**, 441-454 (1999).
- [2] C.D. Hauck, R.B. Lowrie, LA-UR-07-995 (2007) to appear in *SIAM J. Multiscale Model. Anal.*
- [3] C.D. Hauck et al., LA-UR-08-04966 (2008) to appear in *Numerical Methods for Relaxation Systems and Balance Equations, Quaderni di Matematica*.
- [4] J.R. Haack, C.D. Hauck, LA-UR-08-0571 (2008) *Kinet. Related Model* **1**, 573-590.

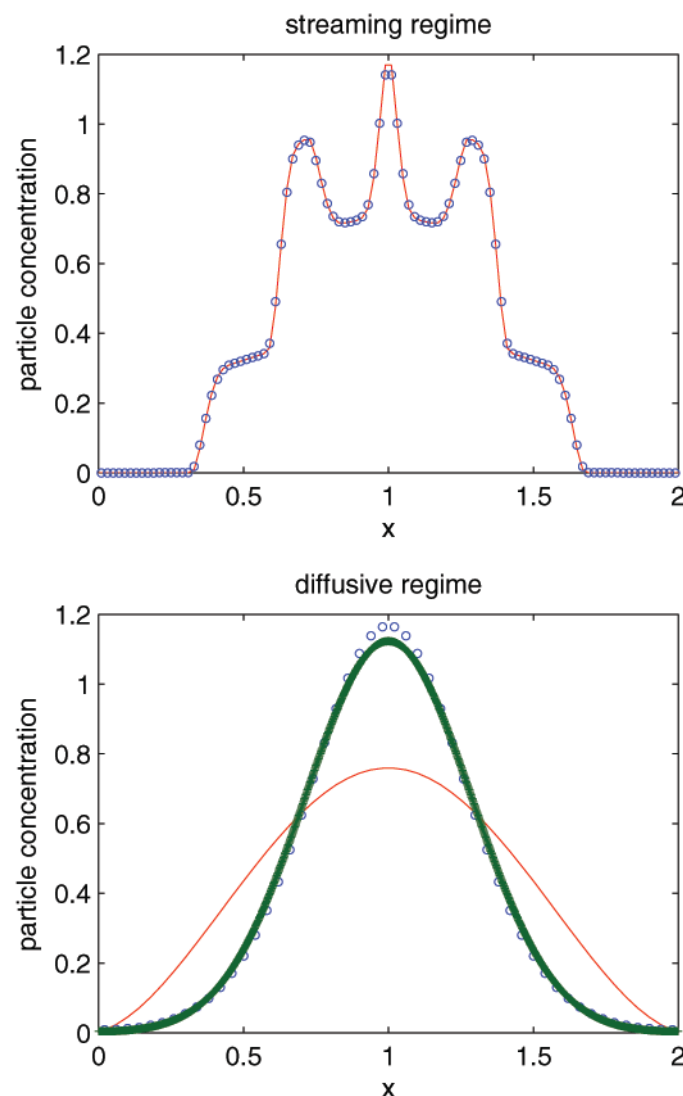


*Fig. 1. Snapshot in time of the particle concentration for P3 (red line) and regularized P3 (blue circles). The initial condition is a characteristic function with height two and support  $[0.8, 1.2]$ . Both computations use upwind methods that are first order in time and second order in space, with 100 spatial cells and a CFL number of 0.1. The cell optical depth is 0.01.*

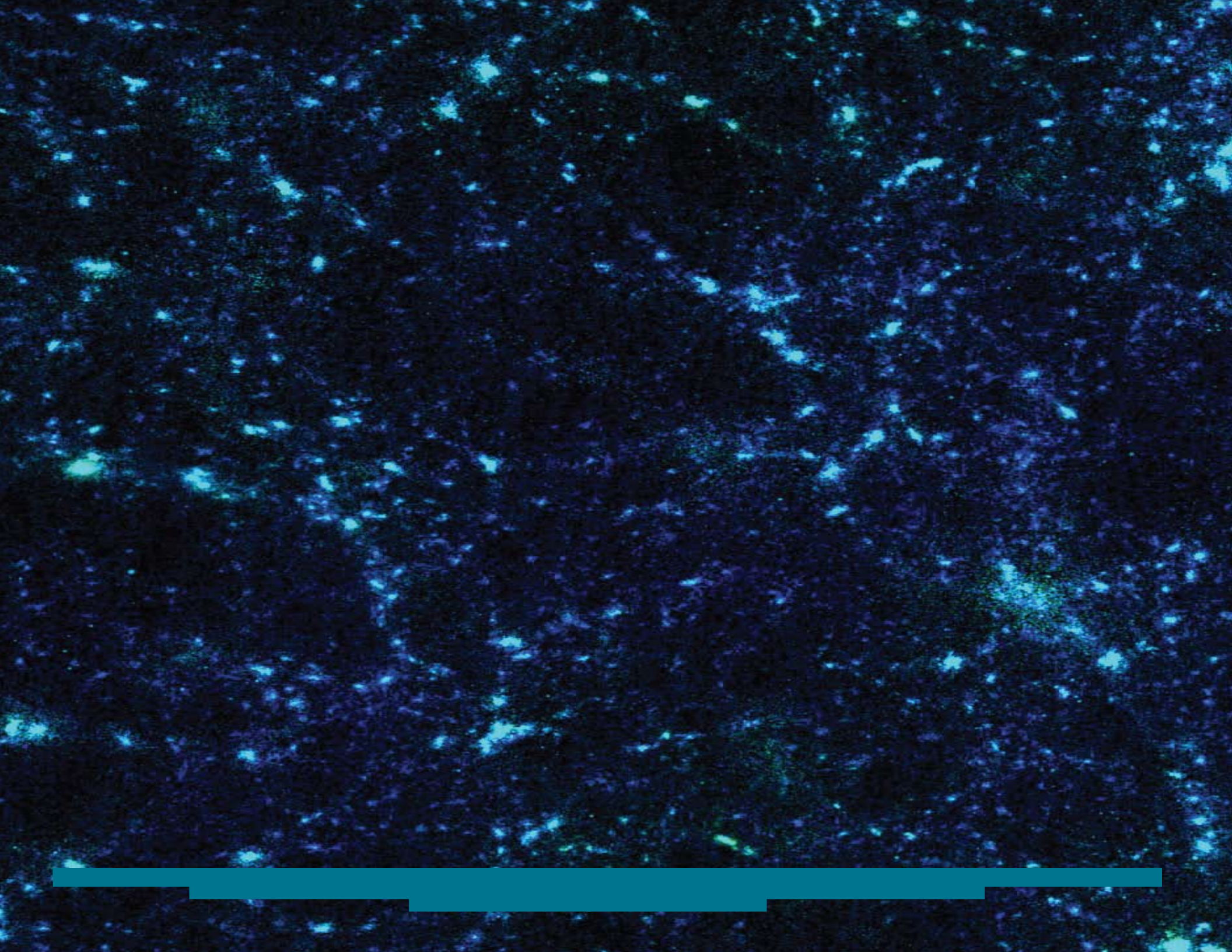
*Fig. 2. Repeat of Fig. 1, but with 50 spatial cells and a cell optical depth of 250. Based on the CFL restriction, the P3 computation (red line) takes roughly 30,000 time steps, while the regularized version (blue circles) uses less than 10. The thick green line is a highly resolved numerical solution for the limiting diffusion equation.*

## Funding

### Acknowledgments

DOE, Office of Science,  
Office of Advanced  
Scientific Computing  
Research Applied  
Mathematics Sciences  
Program







# Astrophysics and Cosmology

The work described in the Astrophysics and Cosmology section involves collaborations among scientists and researchers in the Computer, Computational and Statistical Sciences (CCS), Theoretical (T), Applied Physics (X), and International, Space and Response (ISR) Divisions, as well as an industrial partners. The five articles in this section describe topics on the physics of the solar corona, supernovae, nucleosynthesis, modeling and simulations of structure formation in the Universe, dark energy, and dark matter. The reader will find in these articles a great breadth of the work in the astrophysics and cosmology arena both in our directorate and across the Laboratory.



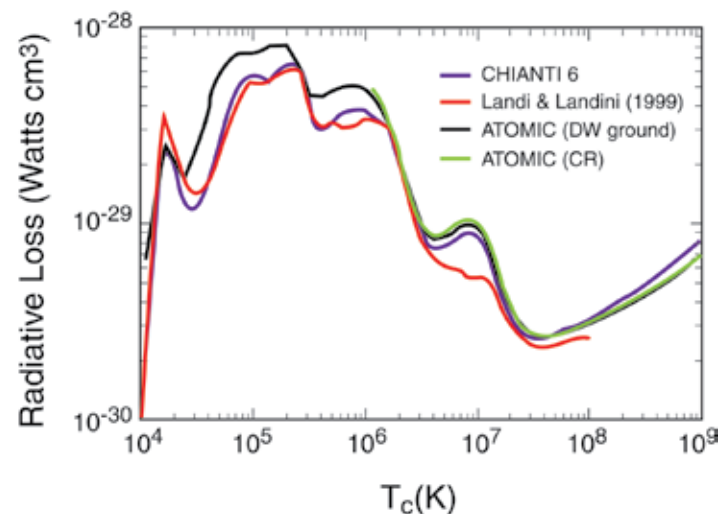
## Radiative Losses of the Solar Corona

James Colgan, Joseph Abdallah, Jr., Manolo E. Sherrill, T-1; Christopher J. Fontes, X-1-NAD; U. Feldman, Artep, Inc.

*Fig. 1. Radiative losses from a coronal plasma containing 15 elements. ATOMIC calculations (solid black line) are compared with those of [4] (dashed red line) and a calculation made using the most recent version of CHIANTI [5] (dot-dashed magenta line). Also shown is an ATOMIC calculation obtained by solving the full set of collisional-radiative equations, labeled ATOMIC (CR) (green line).*

A comprehensive set of calculations of the radiative losses of solar coronal plasmas has recently been made [1]. The radiative losses of the solar corona are an important quantity in evaluating the plasma energy balance of the Sun, which provides an understanding of the corresponding energy source. The LANL suite of atomic structure and collision codes [2] was used to generate a comprehensive set of collisional data for 15 coronal elements. These data were then used in the plasma kinetics code, ATOMIC [3], to generate the radiative losses as a function of the electron temperature. The calculations were made using a new capability of ATOMIC to consider all elements under the influence of one global electron density. The coronal equilibrium model was used in all calculations and the validity of this approach was checked by also solving the full set of collisional-radiative equations for selected temperatures.

The radiative losses computed by ATOMIC are shown in Fig. 1. We compare this calculation, labeled ATOMIC (DW ground), with previous work [4]. The agreement between the sets of calculations is fair in that the broad structure of the radiative losses as a function of temperature is qualitatively the same in both calculations. However, in some regions there are large differences in the magnitude of the radiative losses. In particular, the peak in the ATOMIC calculations of the radiative loss around a temperature of  $10^7$  K is not seen in the calculations of [4]. Also, below  $10^6$  K, our ATOMIC calculations are larger by around a factor of two than the calculations of [4]. The continuum contribution also appears to be different between the two sets of calculations, since we see a difference in the magnitude of the radiative loss at the highest temperatures considered. We also show a comparison with a calculation made using the most recent version of the CHIANTI software [5] (labeled CHIANTI6). This version



contains significantly higher quality atomic data than the much older 1999 version, especially for heavier elements, and so appears to produce a more accurate radiative loss than the older calculations of [4]. For example, the CHIANTI6 calculations find a peak in the radiative loss at a temperature of around  $10^7$  K, also found in our ATOMIC calculations. However, the CHIANTI6 calculations are still significantly lower than the ATOMIC calculations between  $3 \times 10^4$  K and  $10^6$  K.

Figure 2 shows the contributions to the radiative losses from the 15 individual elements in the study. For a given temperature, several elements contribute to the total radiative loss, with the most prominent contributions coming from C, O, Si, and Fe. A study was also made of the variation in the radiative losses as a function of changes in the elemental abundances of the corona. This study considered the various compositions that are thought to exist in the solar upper atmosphere (SUA) that can have different abundances of elements, which have a low first ionization potential (FIP) compared with the photosphere. The radiative losses show a marked dependency on the relative abundance of these low-FIP elements, even at high temperatures, due in part to the strong contribution from Fe to the total radiative loss.



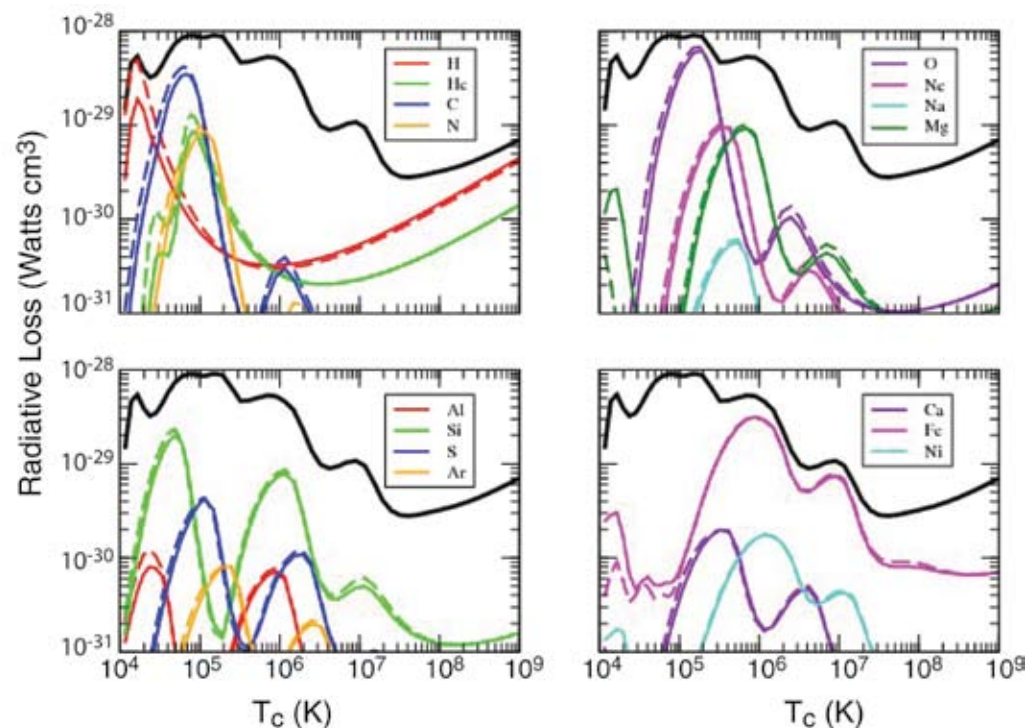


Fig. 2. Radiative losses from individual elements as labeled. The solid lines from each element indicate calculations made using distorted-wave collisional data from the ground configuration, and the dashed lines for each element indicate calculations made using plane-wave Born and scaled-hydrogenic data from the ground configuration. The thick solid line in each panel represents the total radiative losses summed over all 15 elements.

This study suggests that an independent determination of the solar coronal radiative loss could provide an alternative method of determining solar abundances, a topic of some controversy in recent years [6].

**For further information contact James Colgan at [jcolgan@lanl.gov](mailto:jcolgan@lanl.gov).**

- [1] J. Colgan et al., *Astrophys. J.* **689**, 585 (2008).
- [2] J. Abdallah, Jr., R.E.H. Clark, R.D. Cowan, LANL 11436-M-I. <http://aphysics2.lanl.gov/tempweb>
- [3] N.H. Magee et al., in *Atomic Processes in Plasmas*, Eds. J.S. Cohen, S. Mazevet, D.P. Kilcrease (Melville: AIP), *AIP Conf Proc.* **730**, 168 (2004).
- [4] E. Landi, M. Landini, *Astron. Astrophys. Supplement Series* **133**, 411 (1998).
- [5] E. Landi, private communication (2008).
- [6] M. Asplund et al., *Astron. Astrophys.* **417**, 751 (2004).

#### Funding

#### Acknowledgments

DOE, NNSA, Advanced Simulation and Computing Materials and Physics Program

## Modeling Emissions from Supernovae: Preparation for the Joint Dark Energy Mission

Chris L. Fryer, CCS-2; Aimee Hungerford, X-4-PC; Gabriel Rockefeller, CCS-2;  
Christopher J. Fontes, X-1-NAD; Lucy Frey, X-3-MA; Steven Diehl, T-2;  
Paolo Mazzali, Instituto di Astrofisica-Osservatorio Astronomico;  
Stefan Immler, NASA Goddard Space Flight Center

Supernovae play an important role across a wide range of fields in physics and astronomy—they mark the endpoint in the life of stars but are an important source of energy to galaxies and play a role in the formation of new stars. They are produced in the formation of stellar-massed compact objects and, possibly, the seeds of the most massive black holes in the universe. They produce the bulk of the heavy elements in the universe and are the foundations of nuclear astrophysics. Finally, they require many of the same broad numerical and physics expertise in which LANL scientists have excelled, placing LANL in an ideal position to model these objects.

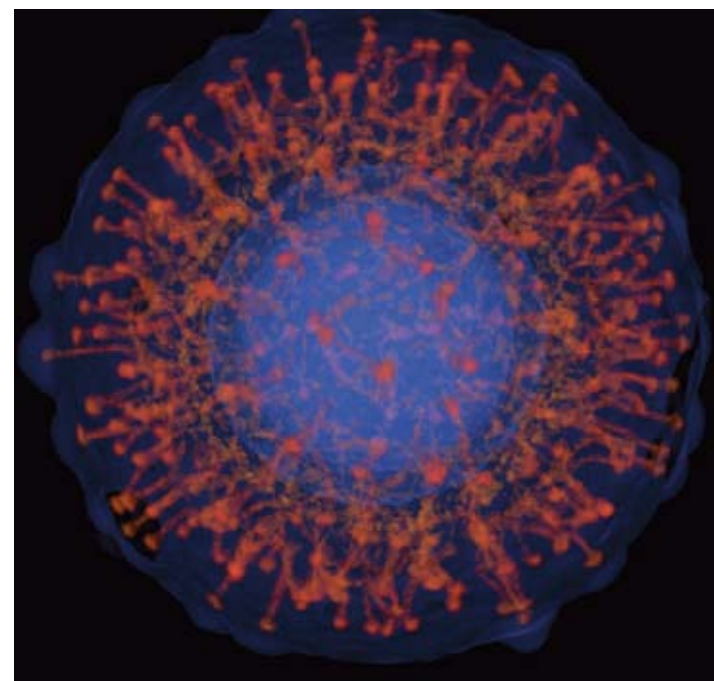
*Fig. 1. Explosion of a massive star, color coded by temperature using the SNSPH code [3]. Rayleigh-Taylor and Richtmyer-Meshkov instabilities drive mixing in the star. Understanding this mixing is important both for nucleosynthetic yields and calculating the emission from supernovae.*

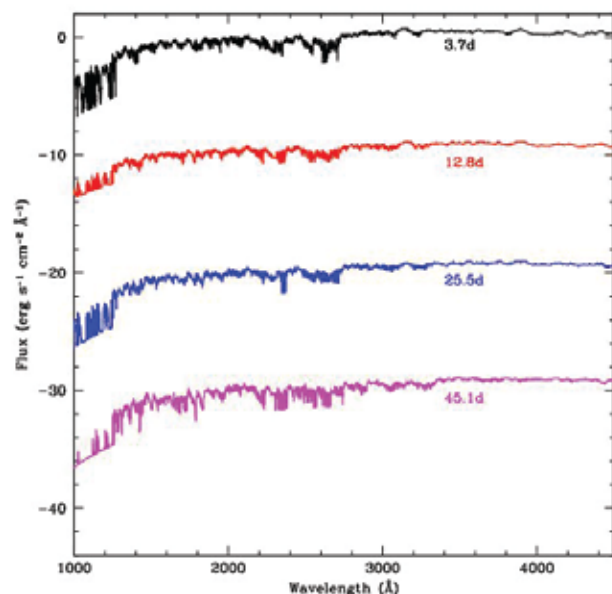
The importance of supernovae has become even more critical with the realization that type Ia supernovae can be used as distance estimators based on the fact that their peak luminosity can be calibrated and determined from the time-dependent behavior of these supernovae, allowing the discovery of dark energy. This discovery has marked one of the major scientific discoveries of the past decade and has galvanized the scientific community to use supernovae to do more than discover—to characterize dark energy using supernovae. Many new supernova search projects have grown out of this exciting result, immensely increasing the data we have on supernovae. Both NSF (Large Synoptic Survey Telescope - LSST) and NASA/DOE (Joint Dark Energy Mission - JDEM) are sponsoring major missions to study supernovae, representing a multibillion-dollar U.S. scientific effort.

The expertise at LANL in numerical hydrodynamics, radiation transport, atomic opacities, and nuclear physics, both theoretical and experimental, provides an ideal

opportunity for LANL to make major contributions to the study of supernovae. In this report, we present LANL's successes over the past year in this effort, including the first-ever spectra from radiation-hydrodynamics calculations of supernovae.

The bulk of what we know about supernovae is derived from photon observations from the infrared through the ultraviolet wavebands. Hundreds of supernovae are observed in these wavebands and, with the planned LSST and JDEM missions, this number will rise to 100,000! For the next few decades, the spectra and time-dependent light curves will dominate the data we have from supernovae. Unfortunately, it is very difficult to tie the actual explosion and exact yields to the emission in these wavebands. The explosion produces both radioactive elements (principally  $^{56}\text{Ni}$ ) and strong shocks, both of which contribute to the radiation observed in these bands. But, especially in the case of radioactive elements, this contribution arises along a very indirect path:  $^{56}\text{Ni}$  decays, emitting  $\gamma$ -rays that are then reprocessed into the





optical bands. Currently, the state-of-the-art in calculating light curves has focused only on this source of radiation, calculating the radiation transport on homologous outflows without calculating the hydrodynamic effects. These calculations do not include any heating by shocks and can only include the mixing in supernovae through a simplified estimate.

Such simplified calculations are not valid for many supernovae. Fryer et al. [1], using the LANL RAGE code, found that for gamma ray burst (GRB)-associated supernovae, shock heating, not  $^{56}\text{Ni}$  decay, dominates the light curve. Their discovery showed that shock heating can dominate the luminosity from supernovae blasting through large stellar envelopes (type II supernovae), strong stellar winds (type Ib/c supernovae including those associated with long-duration GRBs), or any other extended stellar environment (some supernovae Ia progenitors – e.g., [2]). To truly understand the light curves of these supernovae, the explosion must be followed using a radiation-hydrodynamics code to include shock heating. With supernova 1987A, it was

also realized that mixing in the supernova, possibly enhanced by asymmetries in the explosion, is also critical to modeling accurate light curves.

The exploding star is subject to both Richtmyer-Meshkov and Rayleigh-Taylor instabilities. The detailed mixing (Fig. 1) caused by these instabilities is crucial to understanding the emission of supernovae. Figure 1 represents the first step LANL scientists have made in better understanding this mixing. Working with scientists at the Museum of Natural History in New York, a movie of this simulation is being produced for the Hayden Planetarium. But we still have a long way to go to understand this mixing completely, and we are already planning simulations using Roadrunner.

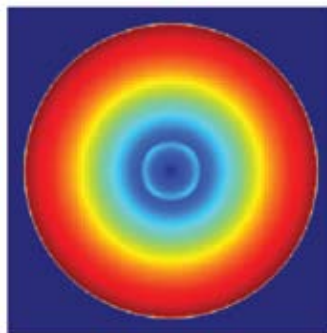


Figure 2 shows detailed spectra derived using the RAGE radiation-hydrodynamics code developed at LANL coupled with the detailed opacities produced by the atomic physics group at LANL. These spectra are the first produced by a radiation hydrodynamics code. But

the simulation in Fig. 2 was 1D. We are now moving to 3D simulations (Fig. 3). With Roadrunner, we expect to complete full calculations in 3D next year, including studies of asymmetric supernovae.

**For further information contact Chris L. Fryer at [fryer@lanl.gov](mailto:fryer@lanl.gov).**

- [1] C.L. Fryer, A.L. Hungerford, P.A. Young, *Astrophys. J.* **662**, L55 (2007).
- [2] I. Hachisu, M. Kato, K. Nomoto, *Astrophys. J.* **679**, 1390 (2008).
- [3] C.L. Fryer, G. Rockefeller, M.S. Warren, *Astrophys. J.* **643**, 292 (2006).

*Fig. 2. Spectra (emission as a function of photon wavelength) of the explosion of a type Ib supernova at four different times. All of the structure in this plot is real, mostly due to blends of atomic lines. Here we use opacities derived by the atomic physics group at LANL.*

*Fig. 3. Velocity plot of the first 3D radiation-hydrodynamics simulation. This simulation marks a first step in being able to model asymmetric simulations.*

**Funding  
Acknowledgments**  
LANL Directed  
Research and  
Development Program

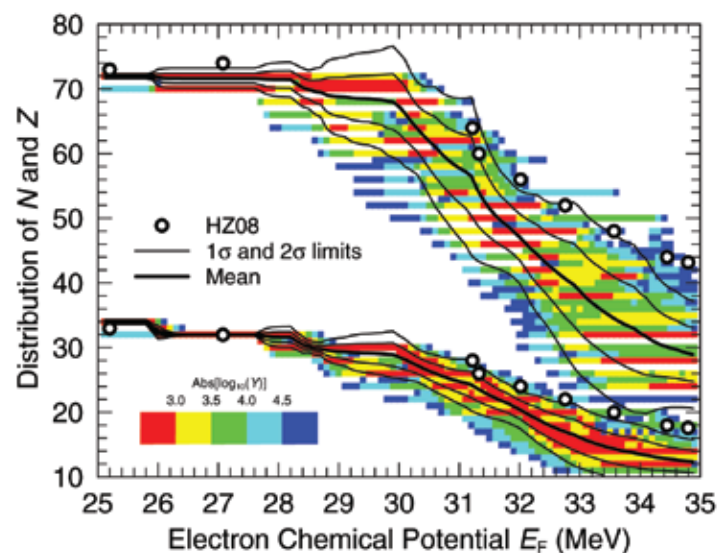


# New Nucleosynthesis Process Discovered in the Crust of Neutron Stars

Sanjib S. Gupta, Peter Möller, Toshihiko Kawano, T-2

Neutron stars (NS) are unique stellar laboratories for the study of matter at the most extreme density and exotic neutron-rich nuclei. However, finding a unique observable feature of neutron stars that can directly probe these properties has been challenging. In the past decade, observations of neutron stars in X-ray binary systems, where the NS accretes matter (hydrogen/helium) from a companion star, have provided promising new insights about various nuclear burning phases on the NS surface and deeper inside the crust. Thermonuclear burning on the NS surface occurs through a sequence of rapid proton (rp) captures, the rp-process, and powers the light curves of the commonly observed Type I X-ray bursts. As ashes of the rp-process sink deeper into the NS under the weight of freshly accreted matter, they undergo electron capture (EC) reactions that convert the proton-rich nuclei to increasingly neutron-rich

*Fig. 1. Heterogeneity (a spread in proton number along the y-axis) will be retained in the NS Crust due to nuclear shell structure effects affecting the newly discovered SEC process of nucleosynthesis. This spread is shown as a function of depth in the NS (denoted by increasing electron Fermi energy in MeV along the x-axis).*



nuclei—the energetically favored state in the neutron star crust. Eventually, with increasing depth, the EC proceeds to the point where neutron-rich nuclei begin to lose neutrons into the continuum beyond a certain density called the “neutron-drip” point.

Nuclear reactions that convert proton-rich ashes into neutron-rich nuclei in the crust directly impact thermal properties of the outer regions of the neutron star. This in turn is critical to interpreting observations of explosive events such as X-ray bursts and superbursts, and also the quiescent thermal luminosity of transiently accreting NS. The nuclear reactions not only determine where and how efficiently energy is released to heat the crust, but also how efficiently the heat can be conducted in the crust or radiated away in neutrinos. This is because thermal conduction and neutrino cooling rates have a sensitive dependence on the composition of nuclei produced by these nuclear reactions. Until recently, both the heat release and the composition in the crust were poorly known, and depended sensitively on the composition of the initial rp ashes.

The authors have calculated for the first time the composition of matter in an accreting NS post-neutron drip using modern nuclear structure and reaction information for exotic neutron-rich nuclei. This published work [1] uses a large reaction network to follow the heterogeneous X-ray burst ashes as they sink deeper in the NS crust. The multicomponent plasma simulation unearths a new nucleosynthesis process, named the Superthreshold Electron capture Cascade (SEC) process in [1], which shows that heterogeneity (a spread in proton number) will be retained in the NS Crust due to nuclear shell structure effects. This spread is shown in Fig. 1 as a function of depth in the NS (denoted by increasing electron Fermi energy in MeV). The efficiency of the SEC process in heating the NS crust as a function of depth is shown in Fig. 2 where the cumulative SEC heatings in units of MeV/accreted baryon from different initial crust compositions (xM and XM) are compared with the heating from the one-component plasma simulations (HZ08) that exist in the literature. Interestingly, this new finding also suggests that the composition and heating in



accreting neutron star crusts are fairly insensitive to the initial crust composition resulting from the rp-process on the NS surface. This is a major breakthrough because it strongly constrains theoretical models needed to interpret the observations, thereby allowing us to probe fundamental questions about the state of matter inside neutron stars.

**For further information contact Sanjib S. Gupta at [guptasanjib@lanl.gov](mailto:guptasanjib@lanl.gov).**

[1] S.S. Gupta, P. Möller, T. Kawano, *Phys. Rev. Lett.* **101**, 231101 (2008).

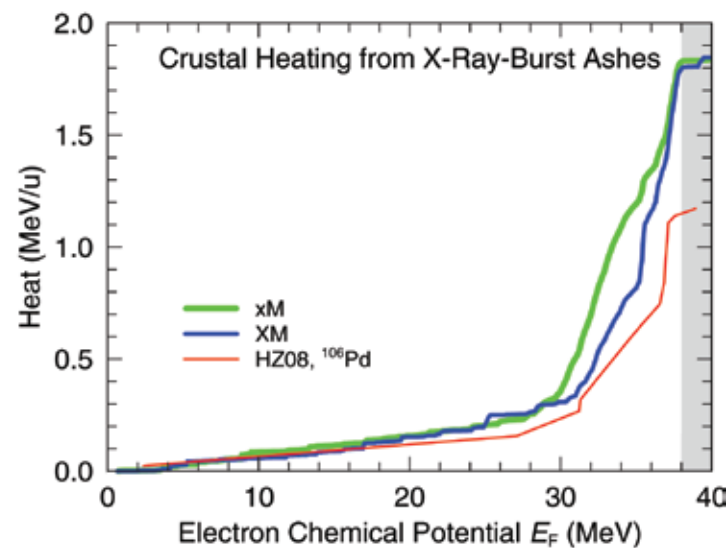


*Fig. 2. The efficiency of the SEC process in heating the NS crust as a function of depth. The cumulative SEC heatings in units of MeV/accreted baryon (along the y-axis) from different initial crust compositions (xM and XM) are compared with the heating from the one-component plasma simulations (HZ08). The x-axis has the same meaning and units as in Fig. 1.*

**Funding  
Acknowledgments**  
LANL Directed  
Research and  
Development Program

## The Coyote Universe

Salman Habib, T-2; Katrin Heitmann, ISR-1; David Higdon, Earl Lawrence, CCS-6; Christian Wagner, Astrophysikalisches Institut Potsdam; Martin White, University of California, Berkeley; Brian J. Williams, CCS-6

Over the last decade, a powerful and diverse suite of cosmological observations has led to remarkable discoveries in fundamental physics. Dark energy and dark matter form the nexus of an intense global endeavor to fathom the deep mysteries posed by their existence. Remarkably, the statistical quality of cosmological measurements is such that our ability to interpret them will become theory-limited in the very near future, if the state-of-the-art in modeling and simulation of structure formation in the Universe cannot keep pace with the observations.

In order to overcome this challenge, structure-formation probes of dark energy and dark matter are the current focus area of a computational cosmology program at LANL. This program covers studies of the galaxy and galaxy cluster distribution, cosmological mass mapping via weak gravitational lensing observations, and baryon acoustic oscillations—the signature of acoustic waves in the primordial fireball as imprinted on the distribution of galaxies today—as a probe of the geometry of the Universe.

A major new effort in this area is represented by the Coyote Universe simulation suite, named after the high-performance computing cluster at LANL on which the simulations were carried out. The simulation suite ranges over 38 sets of cosmological parameters and consists of 800 simulations with an associated database of 60 TB—one of the very largest cosmological simulation databases today.

The requisite error constraints on theoretical predictions are very tight—for the temperature anisotropy in the cosmic microwave background, at better than 0.1%, and only slightly worse for statistical measures of the large-scale distribution of matter, such as the two-point correlation function or, equivalently, the fluctuation power spectrum.

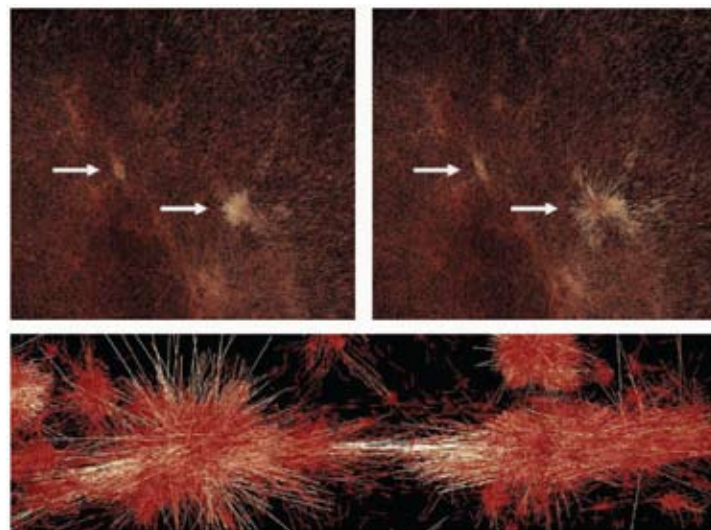
These levels of accuracy have rarely been attained for theoretical predictions of complex nonlinear structure formation in any field, not just in cosmology.

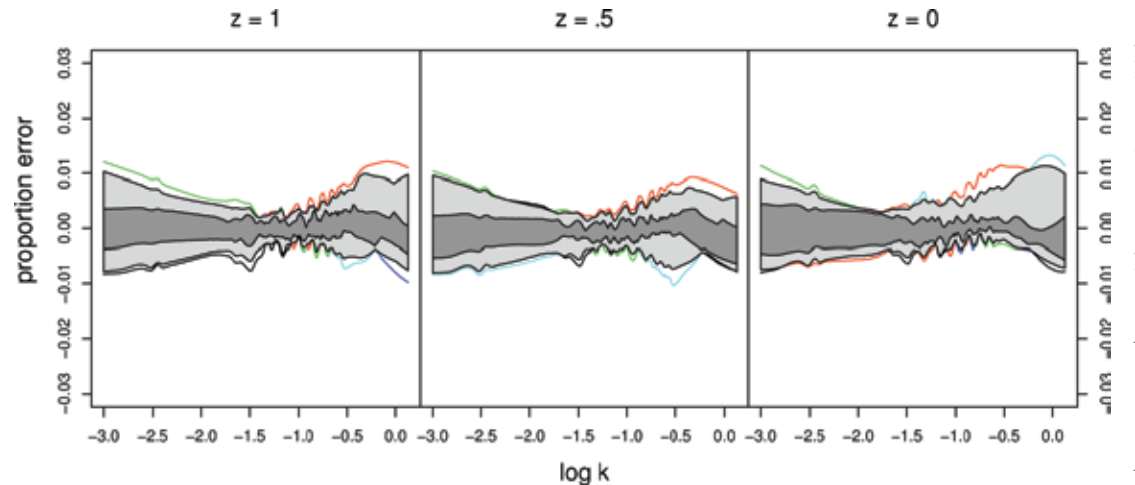
The second important problem is that inverse analysis of cosmological observational datasets requires running many simulations with different cosmological parameters, typically tens to hundreds of thousands of simulations. Given the temporal cost of large-scale supercomputer runs, this is far from being achievable in practice. A more realistic target is in the range of tens to perhaps hundreds of simulations.

Consequently, our approach is first to show that it is possible to attain the required subpercent error control in numerical simulations of the formation of structure in the Universe, and following that, to show how only a limited set of high-quality simulations can take the place of tens to hundreds of thousands of simulations. This can be achieved using a statistical methodology developed by us—the Cosmic Calibration Framework [1-3].

The nonlinear epoch of structure formation in the Universe, responsible for the dark matter clumps within which individual galaxies, groups, and clusters of galaxies reside, is studied via N-body simulations. The matter density is represented by a large number of point particles interacting

*Fig. 1. Top two panels: Early (left) and late (right) start simulations compared. Particle color coding is with respect to velocity. Note the less-tight structures due to the late start (arrows). The bottom panel shows this behavior along a density filament, displayed as differences between the two simulation particle positions (the needle-like lines).*





via gravity in an expanding Universe. To control errors in these simulations, we have identified several key factors, some of which had heretofore not been properly understood. One of these factors is the importance of beginning the simulations sufficiently early on in the history of the Universe—start too late and structures tend to be too diffuse (Fig. 1). Special visualization techniques were developed in order to be able to see and understand such subtle effects. Other components of precision simulations, as identified by us, include very large simulation volumes, accurate time-stepping, and sufficient mass resolution.

The reduction in the required number of simulations is made possible by a sophisticated interpolation scheme (“emulation”) applicable to high-dimensional datasets. This interpolation scheme uses several of the most powerful ideas in modern Bayesian statistical methods: advanced sampling schemes, Gaussian process modeling, and principal component basis representation of the data. With a sampling scheme based on only 37 simulations, it is possible to accurately predict several observational quantities to subpercent accuracy for any cosmological model with parameters that fall within a preset prior, determined (conservatively) from the current uncertainties in measured cosmological parameters. Figure 2 shows an example of

the tight error control possible with our emulation methodology.

Results from the Coyote Universe simulations are being reported in an initial series of three papers: the first showing that sufficiently accurate simulations can in fact be carried out [4], and the second showing that a limited number of simulations can be bootstrapped to represent the results of many more

simulations with little or no loss of accuracy [5]. The third and final paper will encapsulate the results from all the simulations in terms of “emulators,” very fast interpolators, which are based on the results from the simulations and can give predictions for observable quantities for any cosmology within some prescribed cosmological parameter range [6]. The final dataset will be made publicly available.

**For further information contact Salman Habib at [habib@lanl.gov](mailto:habib@lanl.gov).**

- [1] M. Schneider, et al., *Phys. Rev. D* **78**, 063529 (2008).
- [2] S. Habib, et al., *Phys. Rev. D* **76**, 083503 (2007).
- [3] K. Heitmann, et al., *Astrophys. J. Lett.* **646**, L1 (2006).
- [4] K. Heitmann, et al., *Astrophys. J.* (submitted) arXiv:0812.1052v1.
- [5] K. Heitmann, et al., *Astrophys. J.* (to be submitted).
- [6] E. Lawrence, et al. (in preparation).

*Fig. 2. Emulator performance at three cosmological epochs, with red shifts,  $z = 1, 0.5$ , and  $0$  (left to right). The emulator is tested on 10 additional runs — runs not used to build it — within the parameter priors. The emulator error with respect to these results is shown. The central gray region contains the middle 50 % of the residuals, the wider light gray region, the middle 90 %. Errors are at the subpercent level.*

#### **Funding Acknowledgments**

- DOE, Office of Science, High Energy Physics, Dark Energy Program
- LANL Directed Research and Development Program
- LANL Institutional Supercomputing Awards
- LANL IGPP Collaboration Awards Program

# The Structure of Dark Matter Halos

Salman Habib, T-2; Katrin Heitmann, ISR-1; Zarija Lukic, Darren Reed, T-2

A large number of astronomical and cosmological observations now provide compelling evidence for the existence of dark matter. Although the ultimate nature of the dark matter remains unknown, its large-scale dynamics is completely consistent with that of a self-gravitating collisionless fluid. In an expanding universe, the gravitational instability is the driver of the growth of structure in the dark matter, the final distribution arising from the nonlinear amplification of primordial density fluctuations. The existence of localized, highly overdense clumps of dark matter, termed halos, is an essential feature of nonlinear gravitational collapse in cold dark matter models.

Dark matter halos occupy a central place in the paradigm of structure formation—gas condensation, resultant star formation, and eventual galaxy formation occur within halos. The distribution of halo masses, and the halo mass function and its time evolution are sensitive probes of cosmology, particularly so at low redshifts,  $z < 2$ , and high masses. This last feature allows cluster observations to constrain the dark energy content and its equation of state. In addition, phenomenological modeling of the dark matter in terms of halos requires knowledge of the halo mass distribution and density profiles, as does the halo occupancy distribution (HOD) approach to modeling galaxy bias.

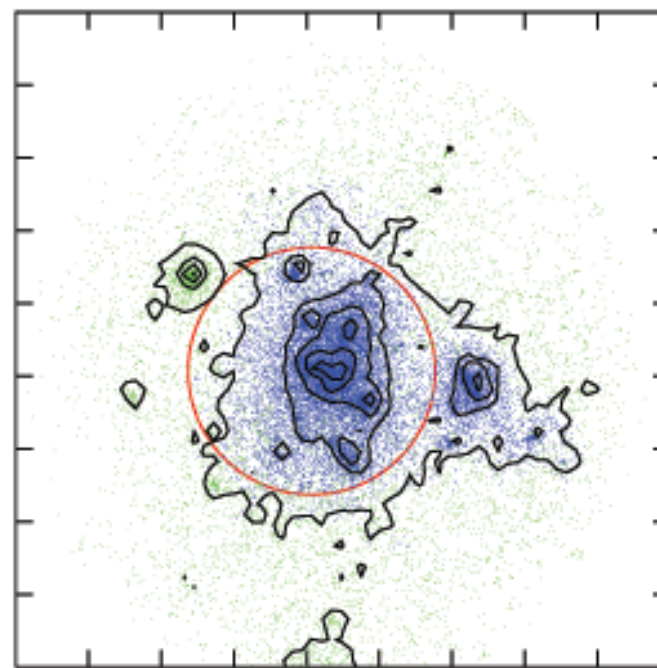
Because accurate theoretical results for the mass function (and other halo properties) do not exist, many numerical studies of halos and their properties have been carried out. Despite the intuitive simplicity and practical importance of the halo paradigm, halo definitions and characterizations have been somewhat ad hoc, mostly because of the lack of an adequate theoretical framework. Currently there are two main ways to define halos: the isodensity based “friends-of-friends” (FOF) algorithm, and the spherical overdensity

(SO) approach (Fig. 1), which includes all particles within a spherical domain the boundary of which is determined by an overdensity criterion.

Depending on the application, one definition may be favored over the other. For X-ray observations of relaxed clusters, the SO approach appears to be more natural since one fits directly to a spherically averaged profile as is observational practice. However, the mass function of FOF halos has a well-characterized “universal” form often used in theoretical studies. It is therefore highly desirable to find a mapping between these two halo definitions.

In recent work we have succeeded in solving this problem [1], first by establishing a connection between the FOF and SO definitions for a class of idealized dark matter halos described by the Navarro-Frenk-White (NFW) profile [2,3] (Fig. 2). The NFW profile fits results from simulations very well, and is determined by two parameters. We showed how the FOF and SO descriptions of an NFW halo can be mapped

*Fig. 1. Different halo definitions for the same particle distribution in a simulation (green points). The black contours are for the projected density field. The blue particles show FOF halo members as determined by a numerical algorithm. The red circle shows the corresponding SO halo centered around the same point as the FOF halo.*





into each other as a function of these two parameters with a small scatter dependent on the number of sampling particles. (Previous studies hoping for a simple one-to-one map had failed to properly connect the two mass definitions.)

We next determined that 80-85 percent of the halos found in simulations are relatively isolated and the simple mapping mentioned above is also successful in describing realistic halos. The remaining halos cannot be easily described in simple terms (Fig. 2). A key issue is the occurrence of major substructure (smaller halos associated with a larger parent), leading to what we termed “bridged halos.” These halos consist of apparently localized structures linked via density ridges into a common FOF halo.

We have found that the bridged halo fraction rises as a function of mass, and like the FOF mass function itself, also appears to be universal. We also find that in the cluster mass regime the fraction of halos with major satellites as a function of the satellites mass fraction is cosmology dependent. Thus, bridged halos may turn out to be another way to test the dark matter paradigm for structure formation.

The predicted degree of bridging from our simulations is roughly consistent with X-ray observations of clusters, where there is a significant second component within the expected distance in approximately 10-20 % of all cases [4]. As cluster catalogs improve, stronger tests of these predictions may be anticipated, especially by combining multispectral information (microwave, optical, radio, X-ray) from upcoming surveys.

**For further information contact Salman Habib at [habib@lanl.gov](mailto:habib@lanl.gov).**

- [1] Z. Lukic et al., *Astrophys.J.* **692**, 217 (2009).
- [2] J.F. Navarro, C.S. Frenk, S.D.M. White, *Astrophys.J.* **462**, 563 (1996).
- [3] J.F. Navarro, C.S. Frenk, S.D.M. White, *Astrophys.J.* **490**, 493 (1997).
- [4] A. Vikhlinin, (private communication).

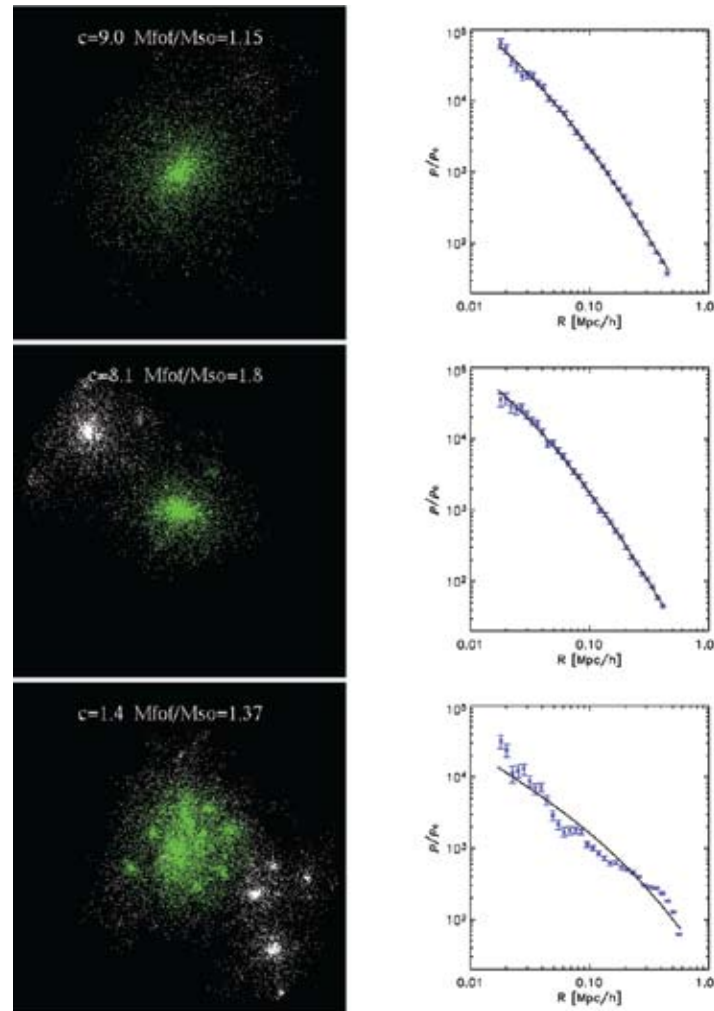
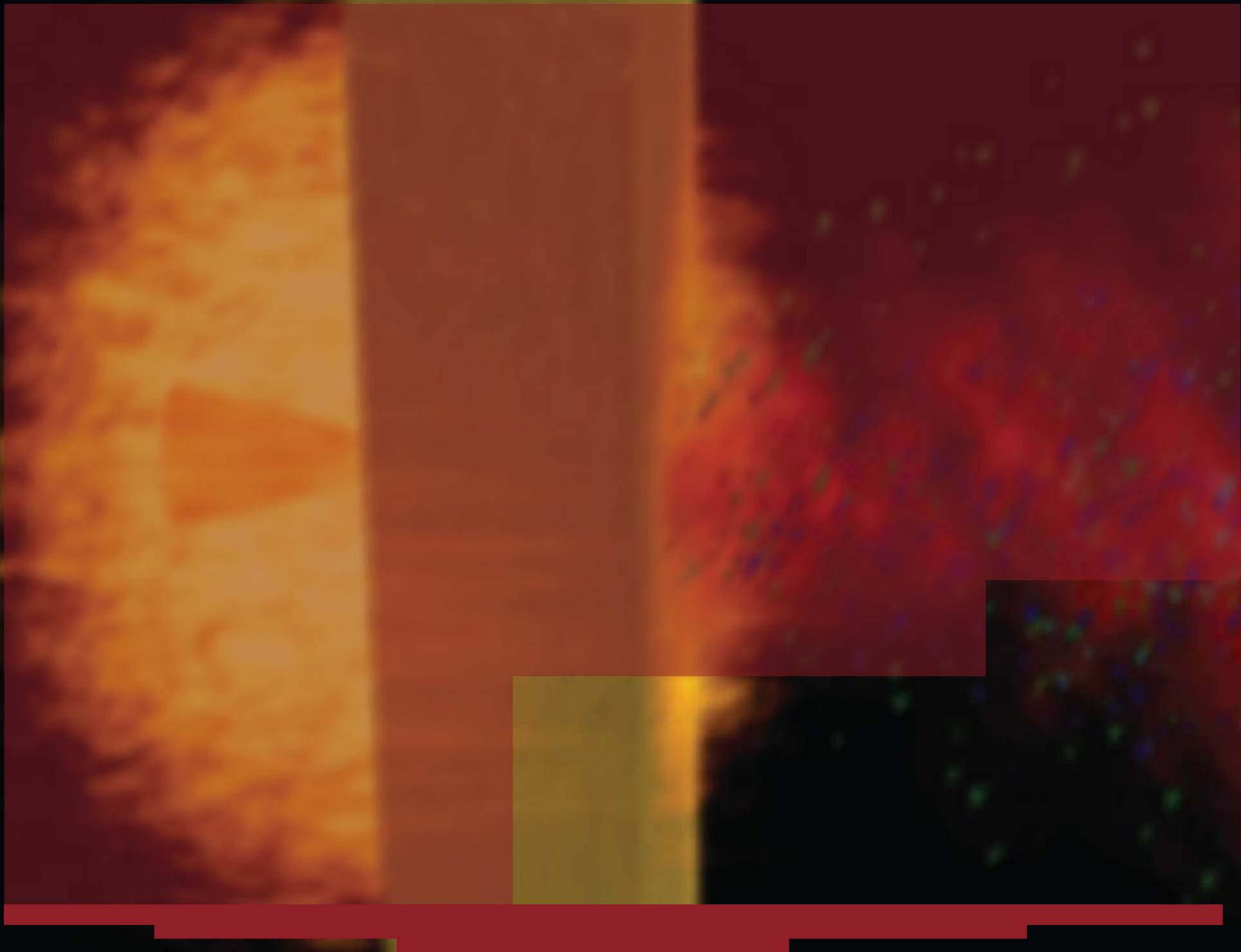


*Fig. 2. Top panel: A typical isolated FOF halo (FOF-linked particles shown as white dots) with NFW profile fit to the right. Green dots are particles belonging to the corresponding SO halo. Middle panel: An example of a bridged halo. Bottom panel: A halo with major substructure, for which the NFW profile is not a good fit.*

### Funding Acknowledgments

- LANL Directed Research and Development Program
- LANL Institutional Supercomputing Awards
- LANL IGPP Collaboration Awards Program



# Atomic, Nuclear, and High Energy Physics

In this section we highlight some examples of recent research accomplishments in Atomic, Nuclear, and High Energy Physics. The highlights illustrate the research that supports the Laboratory and DOE's mission in the Office of Science, Advanced Simulation and Computing and Science Campaigns, and in Threat Reduction. Examples include work on plasma physics, which has solved a longstanding problem on electron-ion energy exchange rates, nuclear reaction physics for actinides (as well as for light-nucleus thermonuclear reactions), and radiation transport methods that are taking advantage of LANL's Roadrunner computer, currently the fastest computer in the world.

The Directorate has developed a major capability in Material Science, from fundamental approaches to constitutive modeling. This is exemplified by the highlights that include molecular dynamics (including algorithms for acceleration), nanoscience, a new understanding of phase transitions in plutonium, and material strength, damage, and fragmentation phenomena. All these examples show how LANL's breadth of capabilities in experiment, theory, modeling, and simulation are brought together to enhance our predictive capabilities, and our understanding of basic phenomena in nature.



## Electron-ion Temperature Relaxation in Dense Plasmas

Jérôme Daligault, T-5; Guy Dimonte, X-1

In a high-temperature hydrogen plasma, such as in inertial confinement fusion (ICF) or in the center of stars, the ions undergo fusion reactions to produce energetic helium nuclei (alpha particles). The alpha particles then share their energy with the plasma ions and electrons via Coulomb collisions, but at different rates because the electrons are lighter than the ions. This causes an imbalance in the electron and ion temperatures that triggers energy exchange between them in order to reach temperature equilibrium. This electron-ion temperature relaxation is one of the key processes that must be modeled in order to accurately describe the temperature runaway (ignition) of a thermonuclear plasma.

The electron-ion temperature relaxation rates, i.e., the rate at which electrons and ions exchange their energy to equilibrate, were first calculated by Lev Landau and Lyman Spitzer over 70 years ago for classical plasmas with weak collisions. Since then, there have been several improvements proposed to account for the collective effects (e.g., screening, wave oscillations) inherent to plasmas, or the quantum nature of the electrons or the correlation effects in the particle motions. None of the models had been validated to sufficient accuracy for ICF conditions until now with the advent of plasma molecular dynamics (MD) simulations on sufficiently large-scale computers. We performed hundreds of MD simulations under a variety of physical and numerical conditions to test the most modern theories of temperature relaxation with sufficient numerical accuracy and convergence [1]. We found very good agreement with the most rigorous theory in the weakly coupled (gaseous) regime [2]. We extended the calculations to the correlated (liquid-like) regime where the theories are much more complicated. Both regimes must be understood because ICF capsules

traverse these regimes as they become heated from solid-state plasma to the thermonuclear state. We successfully devised a compact model that includes self-consistently the effects of screening, electron degeneracy and correlation between electron and ions [3]. The model reproduces well our accurate MD data and joins the weakly and strongly coupled regime (see Fig. 1). We applied our model to dense hydrogen and could unravel the relative importance of quantum and correlation effects on the energy exchanges between electrons and ions. A complete formula is now being devised for the ICF design codes.

**For further information contact Jérôme Daligault at [daligaul@lanl.gov](mailto:daligaul@lanl.gov).**

- [1] G. Dimonte, J. Daligault, *Phys. Rev. Lett.* **101**, 135001 (2008).
- [2] L.S. Brown, D.L. Preston, R.L. Singleton, *Phys. Rep.* **410**, 237 (2005).
- [3] J. Daligault, G. Dimonte, submitted for publication (2008).



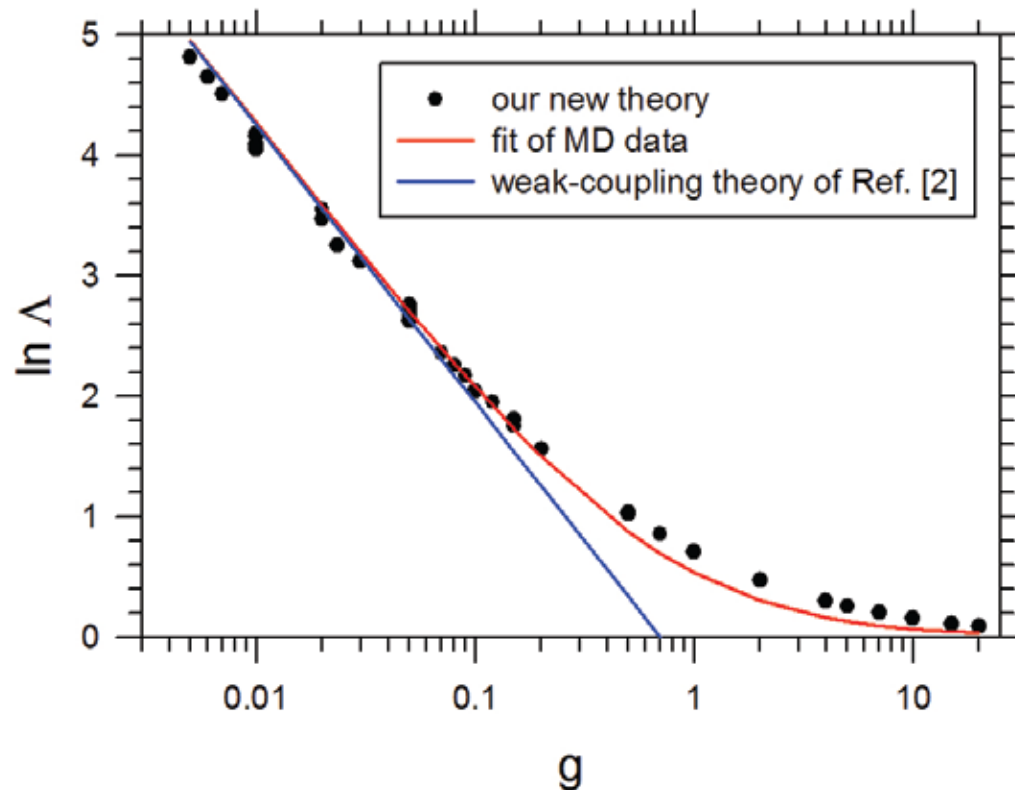


*Fig. 1. We have calculated with MD simulations the temperature relaxation rate  $\nu_{ei}$  between electrons ( $e$ ) and ions ( $i$ ) in a like-charge, classical hydrogen plasma over a wide range of plasma coupling parameter  $g$  ( $g$  = mean potential per particle/mean kinetic energy per particle). The rate  $\nu_{ei}$  can generally be written as the product of a simple, universal energy transfer rate  $\nu_0$ , times a dimensionless quantity  $\ln \Lambda$ , the so-called Coulomb logarithm, which corrects for all the correlation and many-body effects arising in a plasma. The figure shows the Coulomb logarithm from various calculations as a function of the plasma coupling  $g$ . The red line is a simple fit to our MD simulations [1], the blue is the weak-coupling result of Ref.[2] and the dots are the results of our compact model Ref.[3].*

**Funding  
Acknowledgments**  
DOE, NNSA, Advanced  
Simulation and  
Computing Program

# The Neutron-neutron Scattering Length Using the Radiative $\pi^-$ Capture Reaction in Deuterium

William R. Gibbs, New Mexico State University; Benjamin F. Gibson, T-2

Charge symmetry breaking (CSB) in the nuclear force results from the difference in masses of the d and u quarks, which is reflected in the different hadron (e.g., neutron and proton) masses and the mixing of mesons exchanged in the interaction of two nucleons (e.g.,  $\rho - \omega$  and  $\pi - \eta$ ) [1]. The difference between the neutron-neutron ( $nn$ ) and proton-proton ( $pp$ ) scattering lengths ( $a_{nn} - a_{pp}$ ) is one of the few experimental quantities that provides a measure of the magnitude of CSB. The value of  $a_{pp}$  is measured directly in proton-proton scattering—the primary error comes from the uncertainty in modeling electromagnetic effects due to the Coulomb scattering of the two charged protons. The resulting value for  $a_{pp}$  is  $-17.3 \pm 0.005$  (expt)  $\pm 0.4$  (thy) fm. Until direct measurement of  $a_{nn}$  is made, we must rely upon the analysis of three-body final states in few-nucleon reactions.

An impressive number of determinations of  $a_{nn}$  have been made using neutron-induced deuteron breakup. However, there are significant discrepancies among  $a_{nn}$  values obtained from different neutron-deuteron (nd) breakup experiments. Therefore we analyzed the theoretical uncertainty in radiative  $\pi^-$  capture by deuterium (see Fig. 1), because there are only two strongly interacting particles (two neutrons) in the final state, along with a photon that interacts with the two hadrons only electromagnetically [2,3]. This analysis was employed in two experiments at the Paul Scherrer Institut (PSI) in Switzerland by a Laussane-Zuerich-Muenchen collaboration. The first determination was a kinematically incomplete measurement in which only the  $\gamma$ -ray spectrum was obtained, resulting in a value for  $a_{nn}$  of  $-18.6 \pm 0.5$  fm that includes a theoretical uncertainty of  $\pm 0.3$  fm. [4-6]. The second determination was a kinematically complete

measurement in which the neutron time-of-flight spectrum was measured along with the  $\gamma$ -ray spectrum. The value of  $a_{nn}$  was determined to be  $-18.7 \pm 0.6$  fm, which again includes a theoretical uncertainty of  $\pm 0.3$  fm [4-6].

Because of the large variance in values of  $a_{nn}$  obtained from kinematically complete and incomplete nd breakup experiments, the recommended value for  $a_{nn}$  was a combined value from the two radiative  $\pi^- d$  capture experiments by the same experimental group. Therefore, a new measurement was proposed at Los Alamos Meson Physics Facility (LAMPF now known as LANSCE). Our theoretical analysis again explored the sensitivity of the extracted value of the scattering length to the numerous aspects of the model. The two largest uncertainties were confirmed to arise from the short-range characterization of the  $nn$  final-state wave function and from the treatment of the pion wave function in the initial state. We reconfirmed that the value of  $a_{nn}$  could indeed be extracted from a kinematically complete experiment with a theoretical uncertainty of less than 0.3 fm.

A conclusive analysis of the LAMPF kinematically complete capture-at-rest  ${}^2H(\pi^-, n\gamma)n$  reaction measurement has now been completed and was recently published [7]. High precision neutron time-of-flight measurements and high spatial resolution  $\gamma$ -ray detection enabled the experimentalists to make a detailed assessment of the systematic uncertainties in the experiment. The resulting value of  $a_{nn}$  was determined to be  $-18.63 \pm 0.10$  (stat)  $\pm 0.44$  (sys)  $\pm 0.30$  (thy) fm. Combining this LAMPF result with the previous PSI measurements gives a world average value of  $a_{nn} = -18.63 \pm 0.27$  (expt)  $\pm 0.30$  (thy) fm. The value of  $a_{nn}$  when corrected for the magnetic moment interaction of the two neutrons [1] is then  $-18.9 \pm 0.4$  fm. This differs from the recommended value for  $a_{pp}$  by  $1.6 \pm 0.5$  fm, thereby confirming charge symmetry breaking at the 1 % confidence level.

For further information contact Ben Gibson at  
[bfgibson@lanl.gov](mailto:bfgibson@lanl.gov).

- [1] G.A. Miller et al., *Phys. Rep.* **194**, 1 (1990).
- [2] W.R. Gibbs et al., *Phys. Rev. C* **11**, 90 (1975).
- [3] W.R. Gibbs et al., *Phys. Rev. C* **12**, 2130 (1975).
- [4] B. Gabioud et al., *Phys. Rev. Lett* **44**, 1508 (1979).
- [5] B. Gabioud et al., *Phys. Lett. B* **103**, 9 (1981).
- [6] B. Gabioud et al., *Nucl. Phys. A* **420**, 496 (1984).
- [7] Q. Chen et al., *Phys. Rev.* **77**, 054002 (2008).

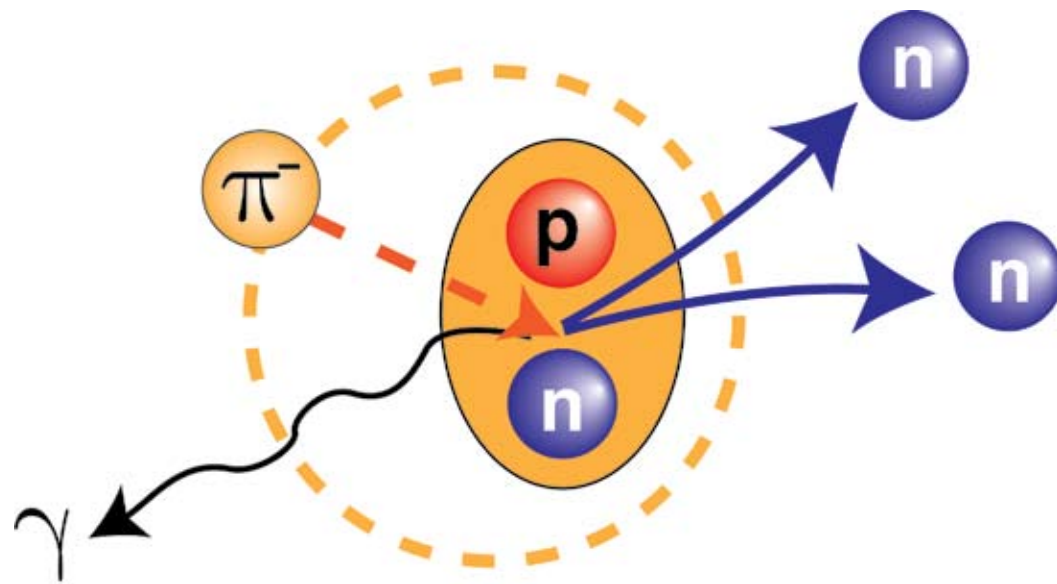


*Fig. 1. Schematic picture of radiative pion capture by deuterium.*

**Funding**

**Acknowledgments**

DOE, Office of Science,  
Office of Nuclear  
Physics

## Measurement and Analysis of the ${}^6\text{Li}(n,t){}^4\text{He}$ Cross Section

Gerald M. Hale, T-2; Mathew J. Devlin, LANSCE-NS

The reaction  ${}^6\text{Li}(n,t){}^4\text{He}$  has important applications as a neutron flux monitor and as a breeder of tritium. Surprisingly, although its cross section has been well measured in the region below a few hundred keV where it is used as a standard, it is not so well known at energies above 1 MeV. A high-priority measurement at the Weapons Neutron Research (LANSCE-WNR) Facility has been to determine this cross section and its angular distributions in the MeV energy range.

Final values of the measured angular distributions for the  ${}^6\text{Li}(n,t){}^4\text{He}$  reaction were obtained by Nuclear Science (LANSCE-NS) in May 2008. The overall normalization of the data set (measured relative to the  ${}^{235}\text{U}$  fission cross section) was determined to within about 5%. This information has been included in a large, multichannel R-matrix analysis of reactions in the  ${}^7\text{Li}$  system at neutron energies up to 4 MeV in order to obtain better information about the  ${}^6\text{Li}(n,t)$  integrated cross section. Some of the results are summarized in Fig. 1. The shape of the angular distribution around 2 MeV confirms the presence of the  $J^\pi = 3/2^-$  resonance, which had been obtained earlier, and indicates that a pronounced shoulder in the integrated cross section due to that resonance is nearly 9% higher than that obtained in a previous LLNL evaluation [1], and more than 4% higher than the recent ENDF/B-VII/IAEA evaluation [2].

Another result of the measurement and analysis is a reduction in the uncertainty of the reaction cross section in the region above 100 keV. This result is shown in Fig. 2, where the red curve gives the uncertainty estimate in 2006 that was based on the ENDF/B-VII evaluation and

differences with the LLNL evaluation and other data, and the blue curve gives the present cross section uncertainties based on the covariances from the R-matrix analysis, including the new LANSCE-WNR differential cross sections. The reduction in uncertainty is almost a factor of three at 2 MeV, where the increased cross section due to the resonance may have applied significance.

**For further information contact Gerald M. Hale at [ghale@lanl.gov](mailto:ghale@lanl.gov).**

- [1] Lawrence Livermore National Laboratory Evaluated Nuclear Data Library (1999).
- [2] ENDF/B-VII/IAEA Standards Evaluation for the  ${}^6\text{Li}(n,t){}^4\text{He}$  Reaction (2006).
- [3] M. Drosog, D.M. Drake, J. Masarik, *Nucl. Institute Meth. B* **94**, 319 (1994).
- [4] R.L. Macklin, R.W. Ingle, J. Halperin, *Nucl. Sci. Eng.* **71**, 205 (1979). [ratio converted using revised  ${}^{235}\text{U}(n,f)$  cross sections (2004)]



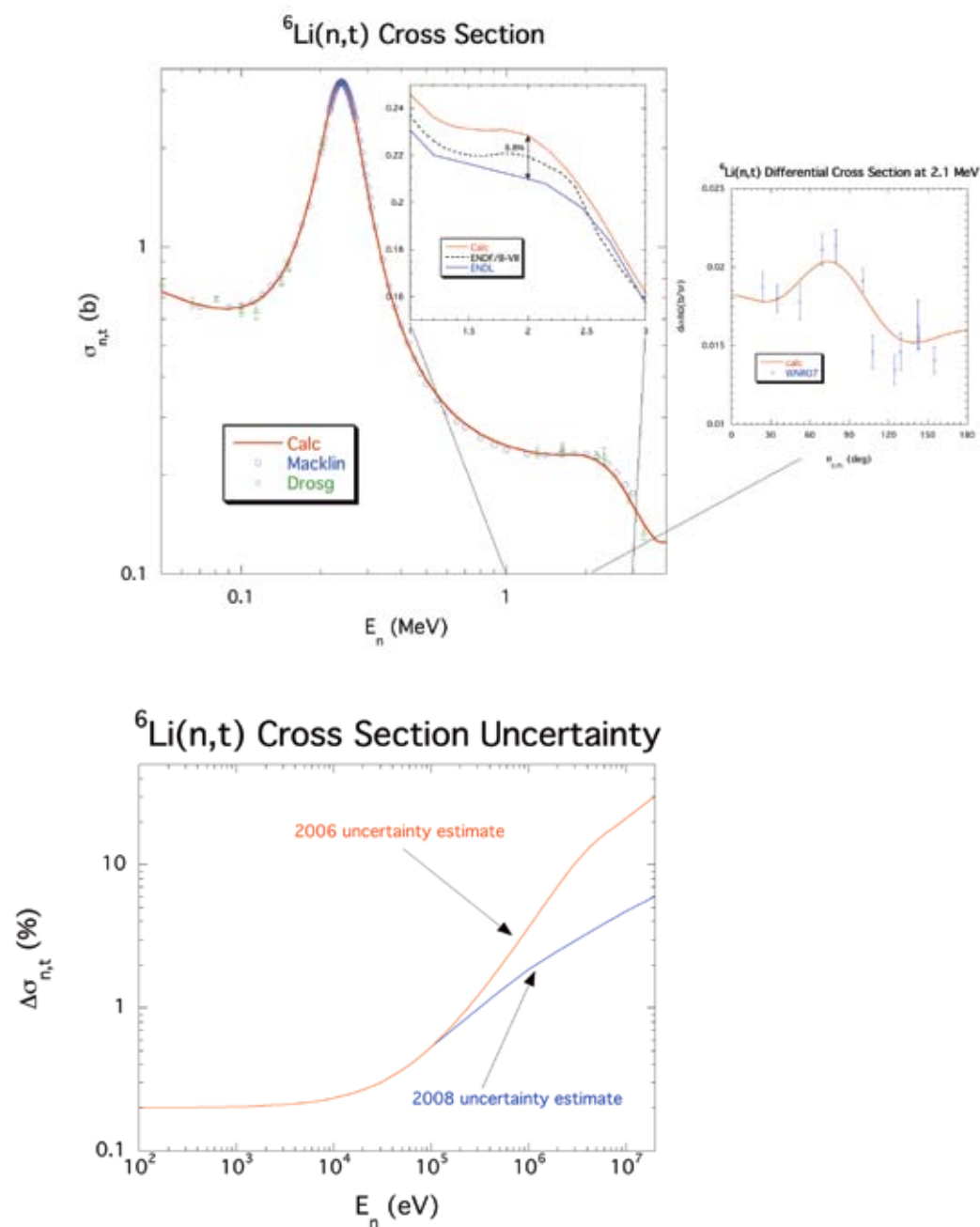


Fig. 1. Integrated cross sections for the  ${}^6\text{Li}(n,t)$  reaction. The solid red line gives the calculation from the R-matrix fit. The blue curve in the insert is ENDL99 [1], and the dashed black line is the recent ENDF/B-VII (and IAEA standards) evaluation [2]. The measurements shown are from [3] (green crosses) and from [4] (blue circles). The fit to the new WNR measurement at 2.1 MeV is shown in the insert to the right.

Fig. 2. Uncertainties of the evaluated  ${}^6\text{Li}(n,t)$  cross sections obtained in 2006 (red curve) and in 2008 (blue curve).

#### Funding

#### Acknowledgments

DOE, NNSA, Advanced Simulation and Computing Reactivity and Compression Program

# Uncertainty Quantification of Prompt Fission Neutrons Spectra

Patrick Talou, David G. Madland, Toshihiko Kawano, T-2

The nuclear fission process is usually accompanied by the emission of neutrons and  $\gamma$ -rays. Indeed, right after scission, the two (or more) primary fission fragments are in excited states due to collective as well as intrinsic excitations. In turn, they release this excitation energy to get back to their ground or an isomeric state by emitting neutrons and  $\gamma$ -rays. Those are called prompt (strong interaction) to distinguish them from the delayed neutrons and  $\gamma$ -rays, which get emitted later by the nuclei that have been formed following the  $\beta$ -decay (weak interaction) of the fission products (after prompt neutron emission).

Both prompt and  $\beta$ -delayed neutrons play crucial roles in nuclear reactors. As the world is designing new and advanced fast nuclear reactors, a precise knowledge of the spectrum and the average multiplicity of neutrons is absolutely necessary. In addition, an accurate evaluation of the uncertainties associated with those quantities is needed to estimate the impact of current knowledge on the simulated quantities of interest for reactor design.

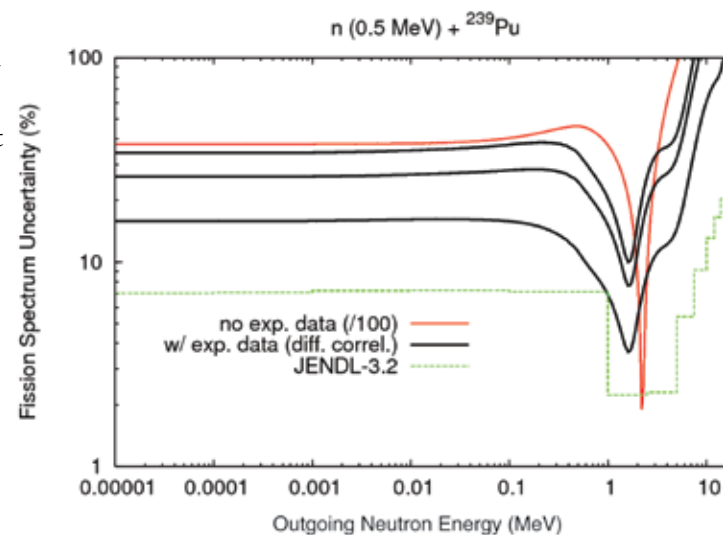
A very common and successful tool for evaluating the prompt fission neutrons spectrum (PFNS) is to use the so-called Los Alamos model developed by D. G. Madland and J. R. Nix at LANL [1]. In this model, the PFNS is calculated from a sampling of the most important fission fragments produced in a given fission process (for a specific isotope and incident neutron energy), and represents an average of all possible neutron emissions over an initial temperature distribution in the primary fragments. With only a few adjustable parameters, the PFNS for incident neutrons below 20 MeV on any fissioning isotope can be calculated with reasonable accuracy.

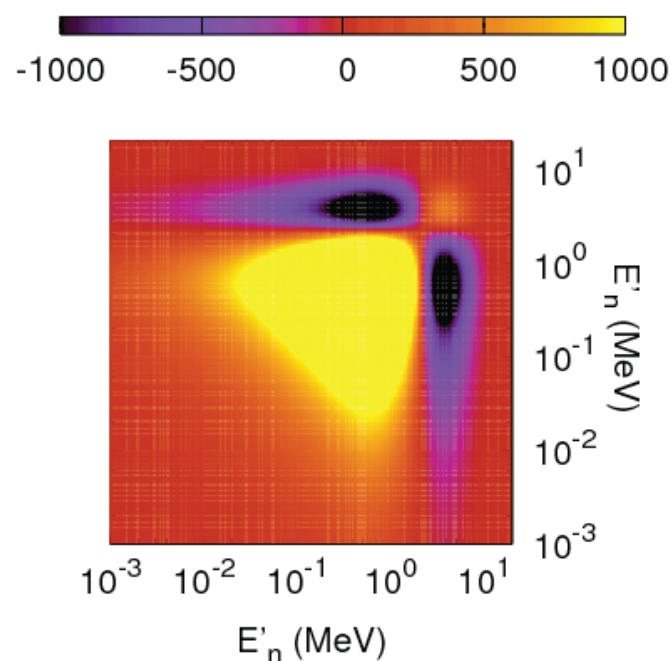
*Fig. 1. PFNS standard deviations (in %) for the neutron-induced fission reaction on  $^{239}\text{Pu}$  for incident neutron energy  $E_n = 0.5 \text{ MeV}$ . See text for explanations.*

Our present efforts aim at quantifying the uncertainties associated with the calculated spectra for isotopes important to the Advanced Fuel Cycle Initiative (AFCI). These uncertainties can then be propagated using transport codes such as Monte Carlo N-Particle code (MCNP) and their impact on the overall design, safety, and efficiency of a reactor can be assessed.

In the present approach, uncertainties in the PFNS are evaluated using both experimental data and model calculations. First, Los Alamos model calculations are performed to best represent available experimental data (if any). Then, sensitivity coefficients are obtained by varying the model parameters around their central values. On the other hand, experimental data sets are analyzed and an experimental covariance matrix, containing both standard deviations and correlations, is produced from known or estimated statistical and systematic uncertainties. The final result is obtained by combining experimental and theoretical results using a Bayesian Kalman filtering technique.

Figure 1 shows the evaluated standard deviations obtained for the PFNS of 0.5 MeV neutron-induced fission of  $^{239}\text{Pu}$ . The red curve (times 100!) depicts the result when no experimental data is used, and only *prior* uncertainties





are assumed for the model parameters. The very large uncertainties are due to the great sensitivity of the result to the total excitation energy available in the system, a quantity which stems from the difference between two large numbers: average energy release minus average total kinetic energy. With further constraints from experimentally measured spectra, the standard deviations drop significantly, as shown with the three black curves, which correspond to three different assumptions for the experimental covariance matrix.

The dip appearing on all these curves occurs just below the average energy of the spectrum, which is the most well-known quantity experimentally. However, uncertainties in the tails of the spectrum are evaluated at more than 15 %, which is quite significant for the simulation of reactors. A similar Japanese work is also shown in green (JENDL-3.2) and does not exhibit such large uncertainties, albeit they are still nonnegligible.

The covariance matrix obtained is shown in Fig. 2. Regions in black correspond to negative terms characteristics of anticorrelation factors. They are primarily due to the physical requirement that the PFNS be normalized to unity.

Further work will include more experimental data sets, other important isotopes ( $^{235,238}\text{U}$ ), and a study of the model errors. In particular, the Los Alamos model is based on several physical assumptions, which may have to become more detailed in view of new experimental data, especially in the low-energy part of the spectrum where experimental data are scarce. Also, new model calculations based on the statistical decay theory of the excited fission fragments are being pursued, and may constitute a very promising tool to go beyond our current model [2].

Preliminary results of the uncertainty quantification work can be found in [3].

**For further information contact Patrick Talou at [talou@lanl.gov](mailto:talou@lanl.gov).**

- [1] D.G. Madland, J.R. Nix, *Nucl. Sci. Eng.* **81**, 213-271 (1982).
- [2] P. Talou, in *Proceedings of the International Conference on Nuclear Data for Science & Technology*, ND2007, April 2007, Nice, France, EDP Sciences, 317 (2008).
- [3] P. Talou, D.G. Madland, T. Kawano, *Nuclear Data Sheets* **109**, 2858 (2008).

*Fig. 2. Final correlation matrix evaluated for the reaction  $n(0.5\text{MeV}) + {}^{239}\text{Pu}$ . Correlation matrix coefficients span the  $[-1000, 1000]$  interval. A stringent physical requirement is that the PFNS is normalized to unity. This is the primary reason for the negative terms (purple and black regions) in this matrix.*

#### **Funding Acknowledgments**

- DOE, Office of Nuclear Energy, Science and Technology, Advanced Fuel Cycle Initiative
- DOE, NNSA Advanced Simulation and Computing Program

## Jayenne Implicit Monte Carlo Project: Y2008 Improvements

Todd Urbatsch, CCS-2; Scott Mosher, ORNL; Seth R. Johnson, University of Michigan; Michael Buksas, CCS-2; Aimee Hungerford, X-4-PC; Jeffery Densmore, Chris L. Fryer, Timothy Kelley, Paul Henning, Gabriel Rockefeller, CCS-2

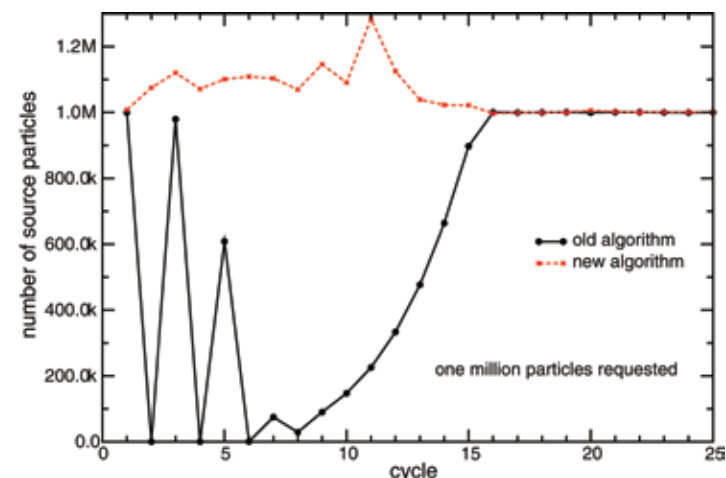
*Fig. 1. The new particle sourcing algorithm avoids the undersampling problems with the old algorithm and typically gives at least the number of particles requested.*

The Jayenne Implicit Monte Carlo (IMC) Project [1] in CCS-2 is a computational physics software project for simulating thermal X-ray transport using the Fleck and Cummings IMC algorithm [2]. These thermal X-ray simulations often are part of larger radiation-hydrodynamic simulations of such high-energy-density phenomena as supernovae and inertial confinement fusion. We highlight three of the improvements made during the year 2008.

**Calculating the Number of Source Particles.** In the IMC method, the X-ray energy is represented by Monte Carlo particles. For each timestep, the particles can come from different types of sources (emission, spatial boundary sources, and initial-time step source), and they can be distributed throughout the spatial domain of the simulation problem. Constraints are to keep the total number of particles at the user requested value and to give each particle approximately the same energy-weight. Determining the particle distribution is, roughly, an integer optimization problem. Algorithmically, we are trying to find the root of:

$$F = N(N_{\text{guess}}) - N_{\text{requested}} = 0$$

where  $N()$  is the function that determines the full distribution of particles for a given guess of total numbers of particles. The old algorithm was based on a linear residual between iterations and could catastrophically and surreptitiously fail by giving the user nearly zero particles in any given time step, thus propagating large errors thereafter. Our new algorithm is a composite method (similar to that of Brent's [3]) that uses the old linear residual to start, false position, Ridder's method [4], and bisection, and that



uses a new stopping criterion. As shown in Fig. 1, the new algorithm solves the issues with the old algorithm, and, when coupled to a temperature cutoff to avoid sampling particles in unimportant regions, it becomes a very robust algorithm for sourcing IMC particles.

**Asynchronous Transport Schemes.** When the Jayenne Project started in 1997, one of its goals was to be massively parallel. Large, highly resolved problems cannot fit an entire mesh on a single processor, so hopes of “embarrassingly parallel” IMC via mesh replication were limited. Thus, domain decomposition (DD) parallelism was built into the Jayenne Project at the outset. With DD, a particle transports until it reaches the edge of the spatial domain on that processor, then it is buffered, and the buffers are sent to the processor containing the next spatial domain. The management of communicating these buffers poses a problem for efficiency and robustness. Our original asynchronous algorithm had each processor performing a continuous loop over the following prioritized options: a) transport  $N$  source particles, b) look for incoming particles and transport them, c) flush outgoing buffers, d) check for incoming buffers, or e) send number of particles completed to Node0 and check for all-finished flag. Running on LANL’s SGI O2 Bluemountain supercomputer of that era, we could not run with  $N > 1$ .



In 2004, Tom Brunner, SNL, started comparing and improving both our method and a method from LLNL. He started with  $N > 1$ , added a binary tree on the work-completed and all-finished messages, and replaced loops over MPI Test with one MPI\_Testsome call [5]. Subsequently, he added true asynchronous Sends and a way to handle a dynamically changing number of particles as happens with Monte Carlo splitting. We analyzed his results and found that, although we would like to make our individual Sends truly asynchronous, the biggest bang for the buck was using  $N > 1$ . We came up with an empirical formula for automatically setting  $N$ . Speedups were on the order of 2 to 4.

**Opacity Distribution Functions.** The usual way to represent particle-frequency dependence in the material opacity data is to divide the frequency span into groups and, with an assumed weighting function, average the data to get one opacity value per group. Unfortunately, this multigroup (MG) approach cannot practically resolve the detailed structure in the data. The Opacity Distribution Function (ODF) method was first presented in 1935 [6] to represent a fuller range of opacities inside each frequency group. Thus, each group has multiple opacity values. Used mainly in stellar atmosphere simulations, ODFs were not typically used in high-energy-density simulations. We have implemented ODFs using opacity data from the X-1 code TOPS. Our results for a Marshak wave in iron, Fig. 2, show that the 32-group/8-band ODF reproduces 1024 groups in standard MG for a factor of four in memory savings.

Nevertheless, the ODF method loses all frequency dependence within a group, which adversely affects transporting to new materials/cells, and could reduce the accuracy of material motion and Compton algorithms. We initiated research on a modification to the ODF method that attempts to better correlate the band opacity values to the frequency. Our approach was to retain, from the underlying data, the minimum and maximum frequency within each band. Then, allowing for shadowing between bands, we could sample a frequency given a band (and the inverse)

accurately within a group for monotonic or single-peaked opacity-versus-frequency data. Our approach does not have the desired accuracy-to-memory value, but it can pave the way for more sophisticated ways to represent high-order opacity-frequency data in low-order forms.

**For further information contact Todd Urbatsch at [tmonster@lanl.gov](mailto:tmonster@lanl.gov).**

- [1] T.J. Urbatsch, T.M. Evans, LANL Report LA-14195-MS (2005).
- [2] J.A. Fleck, Jr., J.D. Cummings, *J. Comp. Phys.* **8**, 313 (1971).
- [3] W.H. Press et al., *Numerical Recipes in FORTRAN: The Art of Scientific Computing*, 2nd Ed., Cambridge University Press (1992).
- [4] C.J.F. Ridders, *IEEE Transactions on Circuits and Systems*, CAS-26, **11**, 979-980 (1979).
- [5] T.A. Brunner et al., *J. Comp. Phys.* **212**, 527-539 (2006).
- [6] J. Van Paradijs, M.S. Vardya, *Astrophys. Space Sci.* **33**, L9-L12 (1975).

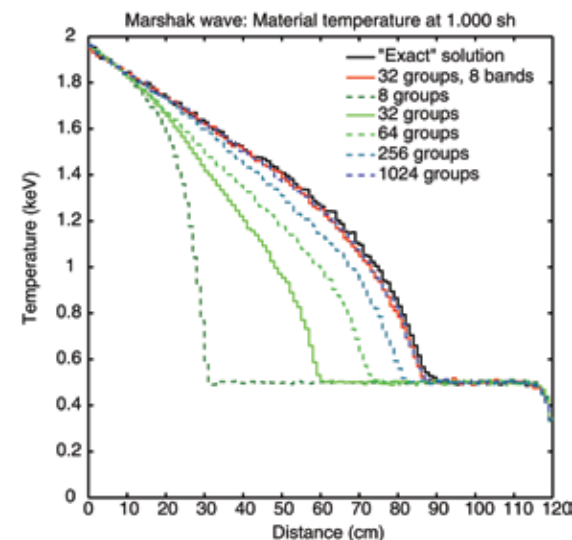


*Fig. 2. Opacity distribution functions here require four times less memory and, thus, appear to converge much quicker than the regular multigroup approach.*

### Funding

### Acknowledgments

DOE, NNSA, Advanced Simulation and Computing Program

# Jet Physics at the Large Hadron Collider

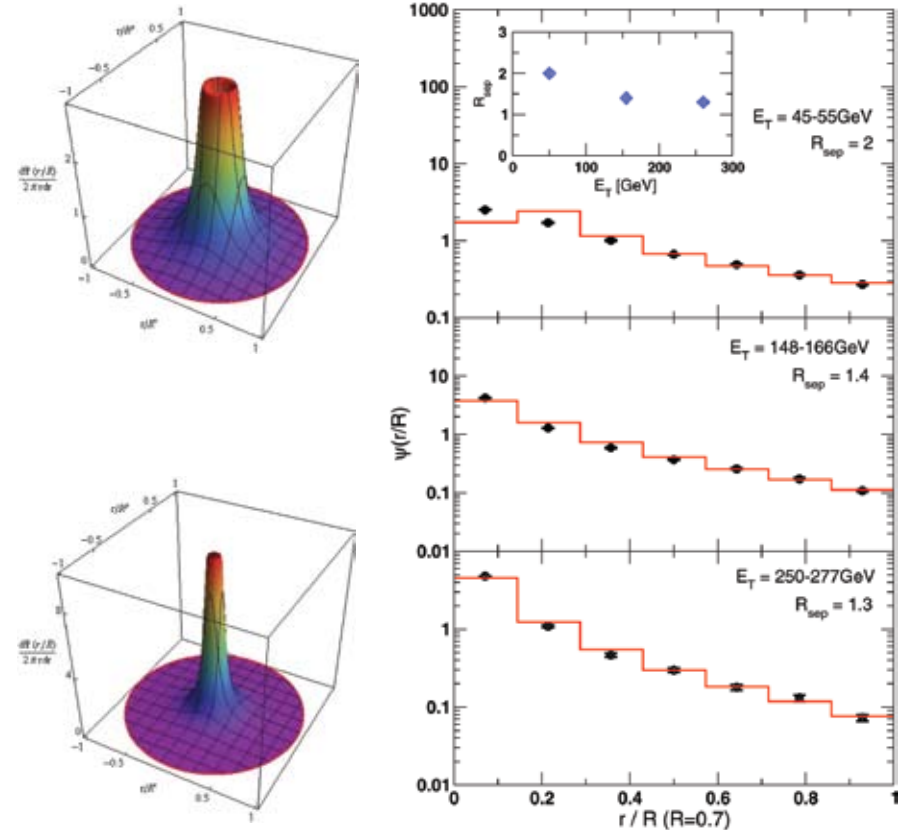
Ivan Vitev, Ben-Wei Zhang, T-2

*Fig. 1. Left panel: 3D plot of the differential jet shapes at two different jet energies  $E_T = 20, 100 \text{ GeV}$  with a radius  $R = 0.7$  in  $p + p$  collisions at  $\sqrt{s} = 5.5 \text{ TeV}$  at the LHC. Right panel: Comparison of numerical results from our theoretical calculation to experimental data on the differential jet shapes at  $\sqrt{s} = 1960 \text{ GeV}$  by CDF II. Insert shows the  $E_T$  dependence of  $R_{\text{sep}}$*

For jets, collimated showers of energetic particles, with great power comes great opportunity. The unprecedented center of mass energies available at the Large Hadron Collider (LHC), the most complex scientific machine ever built, opens new windows on the studies of the quark-gluon plasma (QGP), a new state of matter created in the ultra-relativistic collisions of heavy nuclei [1]. We demonstrate that jet shape and jet cross-section measurements become feasible as a new, differential, and accurate test of the underlying theory of Quantum Chromo-Dynamics (QCD). We present a first step in understanding these shapes and cross sections in heavy ion reactions [2]. Our approach allows for detailed simulations of the experimental acceptance/cuts that help isolate jets in such high-multiplicity environments. It is demonstrated for the first time that the pattern of stimulated gluon emission can be correlated with a variable quenching of the jet rates, providing an approximately model-independent approach to determining the characteristics of the medium-induced bremsstrahlung spectrum. Surprisingly, in realistic simulations of parton propagation through the QGP we find a minimal increase in the mean jet radius even for large jet attenuation. Jet broadening is manifest in the tails of the energy distribution away from the jet axis, and its quantification requires high statistics measurements that will be possible at the LHC. In summary, we expect that the theoretical developments reported here will allow us to pinpoint the correct mechanisms of quark and gluon interaction with the hot nuclear medium and thereby

eliminate the order-of-magnitude of uncertainty in the determination of the QGP properties, such as temperature, density, and equation-of-state (EOS) [3].

We first refine an analytic calculation of jet shapes, a measure of the intrajet energy flow in a cone of radius  $R$  around the center of the jet [4], to include experimental acceptance cuts  $\omega^{\text{min}}$ . Our numerical results include all contributions from leading order processes, resummation, and power corrections with infrared scale  $Q_0 = 2 \text{ GeV}$ . Variation in the jet-finding algorithm is simulated with a transverse energy-dependent parameter  $R_{\text{sep}}$ . We employ this theoretical model to obtain predictions for the LHC at  $\sqrt{s} = 5.5 \text{ TeV}$ . The emphasis is to produce a baseline in proton-proton ( $p + p$ ) reactions for comparison with the full in-medium jet shapes



and cross sections in nucleus-nucleus (A + A) collisions. A 3D representation of the jet shapes in p + p at the LHC for transverse energy  $E_T = 20, 100$  GeV and jet radius  $R = 0.7$  is shown in the left panel of Fig. 1. Our predictions for the still unexplored center of mass energies build upon the successful comparison of this theory with the experimental measurements in proton-antiproton collisions at  $\sqrt{s} = 1960$  GeV at Fermilab from Run II (CDF II) (shown in the right panel of Fig. 1). At high jet ET our theoretical model gives very good descriptions of the large  $r/R$  experimental data with  $R_{\text{sep}} = 1.3\text{--}1.4$ . For  $E_T = 45\text{--}55$  GeV, the largest meaningful value  $R_{\text{sep}} = 2$  can describe the data fairly well, except at very small  $r/R$  regions.

The main idea behind the proposed improvement in the determination of the QGP properties with jets is that their shapes in p + p and A + A collisions are expected to be different. The energy of a fast quark or gluon is redistributed as it loses energy in the plasma via gluon bremsstrahlung and the energy flow pattern in hot nuclear matter is much broader than in the vacuum [5]. Consequently, selecting different jet cone radii  $R^{\text{max}}$  will affect the amount of energy recovered inside the cone and the experimentally measured cross section. Radiative energy loss in QCD generally proceeds through soft gluon radiation. Another handle for studying the radiation intensity spectrum is the minimum energy cut for the particles accepted in the jet,  $\omega^{\text{min}}$ , which also controls the amount of energy recovered in the cone,  $r < R^{\text{max}}, \omega > \omega^{\text{min}}$ .

Figure 2 demonstrates the sensitivity of the relative suppression of the jet cross section  $R_{\text{AA}}^{\text{jet}}(R^{\text{max}}, \omega^{\text{min}})$  to the properties of the medium-induced gluon radiation through the independent variation of  $R^{\text{max}}$  and  $\omega^{\text{min}}$ , advocated in our paper [2]. Note that for perfect acceptance  $R^{\text{max}} \rightarrow \infty$ ,  $\omega^{\text{min}} = 0$ , there should not be any difference between the jet cross section per elementary nucleon-nucleon collision in the vacuum and in the QGP,  $R_{\text{AA}}^{\text{jet}} = 1$ . The top panel shows a smooth evolution of the nuclear suppression factor with the jet cone radius  $R^{\text{max}}$ , a signature of the large-angle bremsstrahlung [5]. The bottom panel presents the

corresponding change in  $R_{\text{AA}}^{\text{jet}}$  with the acceptance cut  $\omega^{\text{min}}$ . Our results on the *variable* quenching rate of jets are quite striking when compared with the known single-suppression value for leading particles at any given  $E_T/p_T$  and centrality from the currently operating Relativistic Heavy Ion Collider [6]. In summary, the continuous variation of quenching values may help differentiate between competing models of parton energy loss, thereby eliminating the order of magnitude of uncertainty in the extraction of the QGP properties.

**For further information contact  
Ivan Vitev at [ivitev@lanl.gov](mailto:ivitev@lanl.gov).**

- [1] M. Gyulassy et al., *Quark-Gluon Plasma III*, **123**, Eds. R.C. Hwa and X.-N. Wang, World Scientific (2004).
- [2] I. Vitev et al., *J. High Energy. Phys.* **0811**, 093 (2008).
- [3] G.J. Kunde et al., LA-UR-08-06010 (2008).
- [4] M.H. Seymour, *Nucl. Phys. B* **513**, 269 (1998).
- [5] I. Vitev, *Phys. Lett. B* **630**, 78 (2005).
- [6] I. Vitev, M. Gyulassy, *Phys. Rev. Lett.* **89**, 252301 (2002).

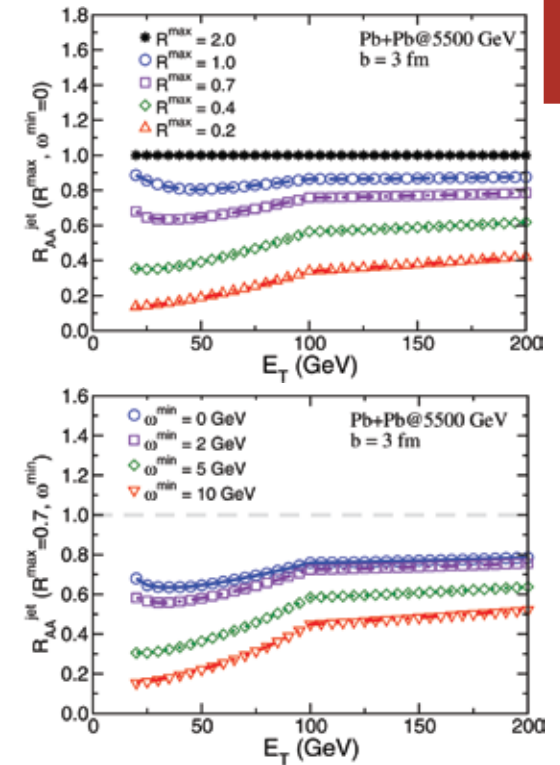


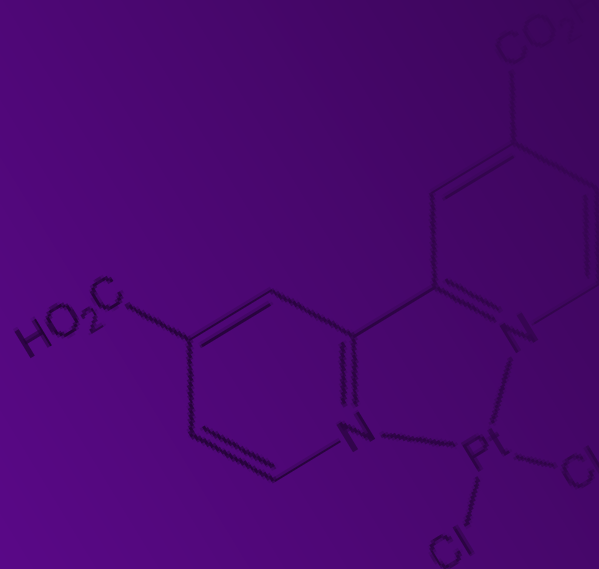
Fig. 2. Transverse jet energy-dependent nuclear modification factor  $R_{\text{AA}}^{\text{jet}}(R^{\text{max}}, \omega^{\text{min}})$  for different jet cone radii  $R^{\text{max}}$  (top panel) and at different acceptance cuts  $\omega^{\text{min}}$  (bottom panel) in central Pb + Pb collisions at  $\sqrt{s} = 5.5$  TeV.

## Funding

## Acknowledgments

- DOE, Office of Science
- LANL Directed Research and Development Program







# Chemistry and Bioscience

The seven articles in the Chemistry and Bioscience section describe the work of scientists in the Theory, Simulation and Computing Directorate. These scientists, together with collaborators elsewhere in the Laboratory as well as academia, have employed quantum chemistry, concepts from the physics of glasses and protein energy landscapes, molecular dynamics, applied numerical analysis, and experimental data.

In the chemistry articles, these techniques are applied to a variety of systems, ranging from inorganic compounds with the potential to convert luminous energy into chemical or electrical energy to the generation of

hydrogen from water to the understanding of the origin of redox potentials in some transition metal compounds to the application of regularization methods to solve problems in a diffusive relaxation.

The bioscience articles explore the role of hydration in proteins, vaccine-protein interactions, and the structure of protein energy landscapes.

# Interfacial Electron Transfer Dynamics of Ru(II)-polypyridine-sensitized TiO<sub>2</sub>

Elena Jakubikova, Richard L. Martin, Enrique R. Batista, T-1; Robert C. Snoeberger III, Victor S. Batista, Yale University

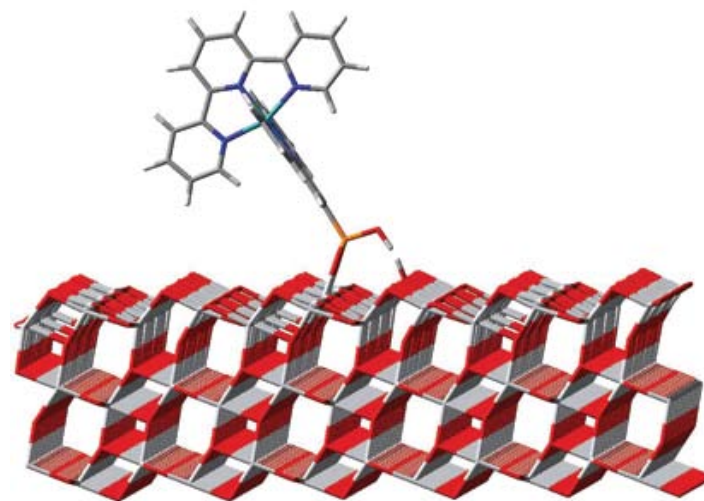
*Fig. 1. Ru(tpy)<sub>2</sub> attached to the (101) surface of anatase TiO<sub>2</sub>.*

Ruthenium polypyridyl complexes are a class of compounds displaying rich photophysics and photochemistry. Due to their favorable excited state properties, they have been widely used in the design of artificial systems capable of converting the energy of light into chemical or electrical energy. In particular, [Ru(tpy)<sub>2</sub>]<sup>2+</sup> is often used in molecular assemblies [1] and dye-sensitized solar cells [2,3] due to its advantageous linear directionality.

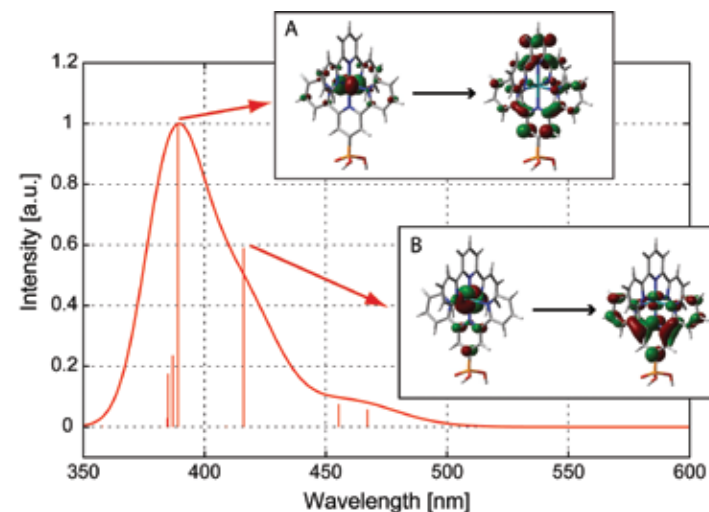
Electron injection from [Ru(tpy)(tpy(PO<sub>3</sub>H<sub>2</sub>))] <sup>2+</sup> adsorbate into TiO<sub>2</sub> will occur upon the excitation of the adsorbate molecule by visible light. Once the adsorbate molecule is in an excited state, several competing processes can occur: 1) radiative or nonradiative transition back into the ground state, 2) intersystem crossing into the lowest triplet excited state, or 3) interfacial electron transfer (IET) from an excited state of the dye into the conduction band of the semiconductor. Intersystem crossing will play an important role in case of the [Ru(tpy)<sub>2</sub>]<sup>2+</sup> molecule, whose lowest triplet excited state has a metal to ligand charge transfer (MLCT) character with a lifetime of 250 ps at room temperature [4].

Density functional theory (DFT) was used to obtain the geometry of the dye-sensitized TiO<sub>2</sub> nanoparticle (see Fig. 1), as well as the absorption spectra and the lowest triplet excited states of the [Ru(tpy)(tpy(PO<sub>3</sub>H<sub>2</sub>))] <sup>2+</sup> dye. Quantum dynamics simulations based on extended Hückel Hamiltonian [5] were then used to study the IET dynamics from the excited states localized on Ru(II) bisterpyridine dye into the nanoparticle. The IET rate was defined as the survival probability  $P(t)$ , which is the probability that the photoexcited electron remains in the adsorbate molecule at a time  $t$  after the excitation.

*Fig. 2. Absorption spectra of [Ru(tpy)(tpy(PO<sub>3</sub>H<sub>2</sub>))] <sup>2+</sup> obtained with TD-DFT and natural transition orbitals corresponding to the most intense excitations.*



The absorption spectra obtained by the use of time-dependent DFT formalism in the visible region for the free [Ru(tpy)(tpy(PO<sub>3</sub>H<sub>2</sub>))] <sup>2+</sup> molecule are shown in Fig. 2. The two most intense peaks correspond to the excitation of the electron into the orbitals with substantial electron density on the tpy(PO<sub>3</sub>H<sub>2</sub>) ligand. Natural transition orbitals, which describe these excitations, are also shown in Fig. 2. The excited [Ru(tpy)(tpy(PO<sub>3</sub>H<sub>2</sub>))] <sup>2+</sup> molecule can then undergo





intersystem crossing into the  $^3\text{MLCT}$  state, in which the excited electron localizes on the  $\text{tpy}(\text{PO}_3\text{H}_2)$  ligand. This state is virtually identical with the  $^1\text{MLCT}$  state shown on insert B in Fig. 2.

Density of states (DOS) obtained by the extended Hückel method for  $[\text{Ru}(\text{tpy})(\text{tpy}(\text{PO}_3\text{H}_2))]^{2+}$  adsorbed on  $\text{TiO}_2$  is shown in Fig. 3. The plot shows the introduction of  $[\text{Ru}(\text{tpy})(\text{tpy}(\text{PO}_3\text{H}_2))]^{2+}$  energy levels into the  $\text{TiO}_2$  bandgap. Additionally, there are a number of virtual orbitals, LUMO through LUMO + 13 (LUMO = lowest unoccupied molecular orbital), positioned within the conduction band. These are the adsorbate orbitals that are responsible for promoting the IET. The results of the electron dynamics simulations from the four lowest LUMOs are shown in Fig. 4. In general, the IET rate from the adsorbate orbitals with significant electron populations on the terpyridine ligand not attached to  $\text{TiO}_2$  and those with the electron population on Ru  $d$  orbital do not show significant adsorbate electron population loss in the time scale of our simulations and, therefore, no electron injection into  $\text{TiO}_2$ .

In conclusion, we showed that photoexcited  $[\text{Ru}(\text{tpy})(\text{tpy}(\text{PO}_3\text{H}_2))]^{2+}$  will inject electrons into the surface of  $\text{TiO}_2$  at a competitive rate. The computed injection rate (1 to 10 ps) is faster than the experimental recombination rate (250 ps). Excited states involving electron excitation into the  $d$  orbital of Ru or the terpyridine ligand not attached to the  $\text{TiO}_2$  surface will not undergo IET into the semiconductor.

**For further information contact Enrique R. Batista at [erb@lanl.gov](mailto:erb@lanl.gov).**

- [1] F.S. Han et al., *J. Am. Chem. Soc.* **130**(6), 2073-2081 (2008).
- [2] C. Houarner-Rassin et al., *J. Photochem. Photobiol. A* **192**(1), 56 (2007).
- [3] M. Beley et al., *Inorg. Chim. Acta* **318**(1,2), 197 (2001).
- [4] J.P. Sauvage et al., *Chem. Rev.* **94**(4), 993-1019 (1994).
- [5] L.G.C. Rego, V.S. Batista, *J. Am. Chem. Soc.* **125**(26), 7989-7997 (2003).

*Fig. 3. DOS obtained from the extended Hückel method for the  $[\text{Ru}(\text{tpy})(\text{tpy}(\text{PO}_3\text{H}_2))]^{2+}$ -anatase model nanostructure. Shows (a) the valence and conduction bands, and (b) the expanded conduction band. In both plots, the blue line shows the total DOS and the black line represents the projected DOS onto the adsorbate orbitals. The levelset lines give the molecular orbital energies of the free adsorbate in vacuum. DOS is convoluted with a Gaussian function (FWHM = 0.1 eV).*

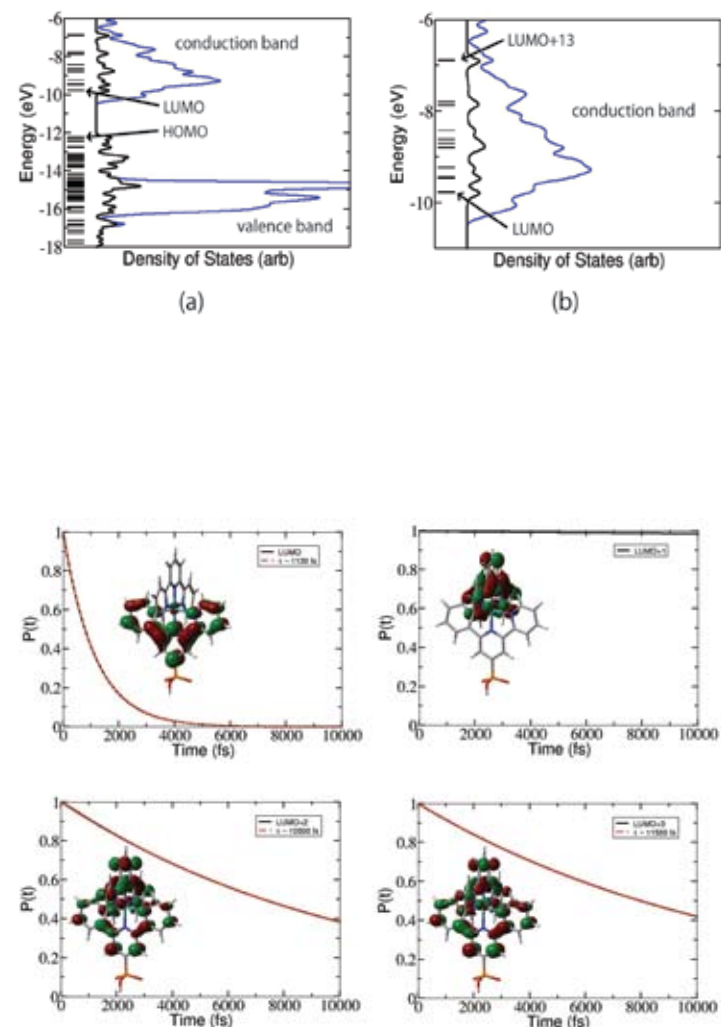


*Fig. 4. Survival probability for electron relaxation starting from the LUMO, LUMO + 1, LUMO + 2, and LUMO + 3 virtual orbitals of  $[\text{Ru}(\text{tpy})(\text{tpy}(\text{PO}_3\text{H}_2))]^{2+}$  adsorbate. An estimated rate is plotted with the red dashed line.*

**Funding  
Acknowledgments**  
LANL Directed  
Research and  
Development Program

# Theoretical Studies on the Stability of Molecular Platinum Catalysts for Hydrogen Production

Lindsay E. Roy, Enrique R. Batista, T-1

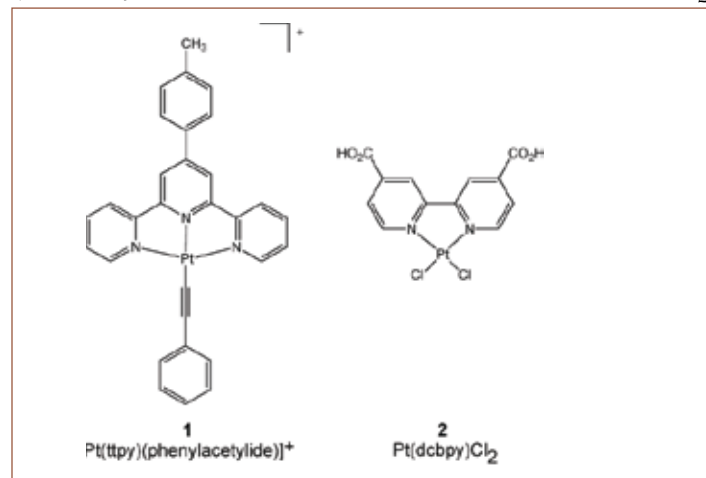
Photochemical generation of hydrogen from water has received intense interest over the past several years. Numerous studies have focused on systems that use a metal complex sensitizer such as Ru<sup>II</sup> polypyridyl complex or TiO<sub>2</sub>, an electron transfer relay molecule such as methyl viologen, a sacrificial electron donor, and colloidal Pt as a hydrogen-generating catalyst. Recently, several researchers have suggested that Pd<sup>II</sup> or Pt<sup>II</sup> diimine complexes can act as efficient molecular catalysts in these systems.

When either [Pt(tpy)phenylacetylide] + (tpy = 4-tolyl-2,2':6',2''-terpyridine) (**1**), Pt(dcbpy)Cl<sub>2</sub> (dcbpy = 4,4'-dicarboxyl-2,2'-bipyridine) (**2**) (see Scheme 1), or a derivative thereof is employed in place of colloidal Pt, large quantities of H<sub>2</sub> are observed. However, Hammarstrom and Eisenberg published separate reports outlining the photodecomposition of these molecular catalysts to colloidal Pd or Pt, the true H<sub>2</sub>-generating catalysts occurring in these molecular systems [1,2]. Eisenberg reported that after some induction period, irradiation of the **1**-, and **2**-TiO<sub>2</sub> systems at 410 nm > λ > 455 nm leads to the presence of Pt nanoparticles on the surface of TiO<sub>2</sub>. To provide some insight into this work, we have performed density functional (DFT) calculations on these purported Pt<sup>II</sup> molecular catalysts to determine if and how these compounds decompose.

All DFT calculations have been performed with the Gaussian suite of programs, using both the commercial and development versions. Geometry optimizations were carried out using the B3LYP functional and verified by vibrational analysis. The vertical transition energies to the valence excited states were computed with time dependent density

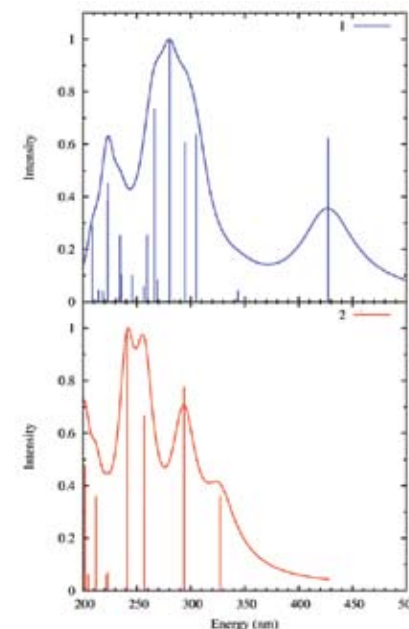
Fig. 1. Calculated absorption spectra for **1** and **2** in CH<sub>3</sub>CN.

(Scheme 1) Molecular Pt(II) Complexes Used to Generate H<sub>2</sub>



functional theory (TD-DFT) using the Coulomb-attenuating method applied to the B3LYP functional (CAM-B3LYP), and the bulk solvent effects of acetonitrile (CH<sub>3</sub>CN) were evaluated using the polarizable continuum model (PCM). For both molecules, we neglect spin-orbit coupling.

The optimized structures of **1** and **2** are in excellent agreement with reported crystallographic data. The calculated TD-DFT absorption spectra for **1** and **2** with CH<sub>3</sub>CN are shown in Fig. 1 and several of the experimental features are reproduced. The high-energy bands (~300 nm) in both **1** and **2** are attributable to intraligand and Cl-Pt





ligand to metal (LMCT) transitions. The less intense band in **1** is a  $\text{dp(Pt)}\text{-p}^*$ -terpy metal to ligand charge transfer (MLCT) transition. The experimental UV/Vis spectrum of compound **2** shows a shoulder at  $\sim 340$  nm with weak transitions at  $\sim 355$  nm; our results are consistent with experiment.

To initiate the degradation sequence, one would expect the formation of an unstable  $\text{Pt}^{\text{I}}$  or  $\text{Pt}^0$  species, either photochemically or chemically, by occupying a strongly antibonding Pt orbital with the surrounding ligands. However, examination of the natural transition orbitals (NTOs) for both the allowed and forbidden transitions of **1** and **2** reveals that it is hard to justify photodegradation of the parent compound in the irradiation range. Firstly, compound **1** has not been reported to degrade upon UV/Vis excitation and all NTOs show that the transitions are MLCT or LLCT in character to  $\sim 300$  nm. The NTOs of **2** suggest that photodegradation might occur, but only at excitations  $\sim 350$  nm.

These results then suggest that in the Hammarstrom and Eisenberg experiments the catalysts decompose once an electron is transferred from the metal complex sensitizer (e.g.,  $\text{Ru}^{\text{II}}$  polypyridyl or  $\text{TiO}_2$ ) to **1** or **2**. Previous electrochemical studies have shown that the diimine ligand influences the reduction potential and the  $\text{Pt}^{\text{II}}$  ion is not reduced. Geometry optimization calculations of **1** and **2** verify that the electron resides on the diimine ligand upon reduction. Since these reduced species are also subjected to UV/Vis irradiation, we probed the photostability of **1** and **2** using TD-DFT methods. To our surprise, both **1** and **2** have a low energy transition from the pyridyl ligand to a strongly antibonding Pt-ligand orbital within the range of the experimental excitation energy for  $\text{H}_2$  generation ( $\sim 435$  nm). Figures 2 and 3 depict the MOs of major contributions from the one-electron excitations to the transitions for **1** and **2**, respectively. Also, it is equally important to point out that both of these transitions are either very weak or spin-forbidden. A very weakly allowed transition ( $f = 0.0001$ ) might explain the long induction period for **1** prior to  $\text{H}_2$  generation ( $> 8$  h with  $\text{TiO}_2$  and at

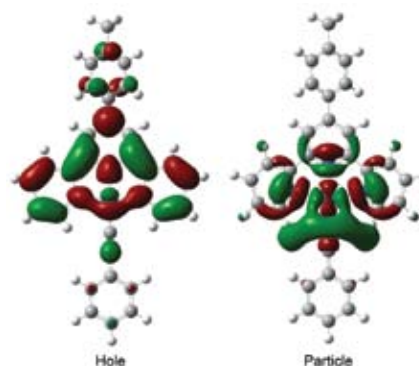


*Fig. 2. MOs of the relevant excited state at 435 nm for 1.*

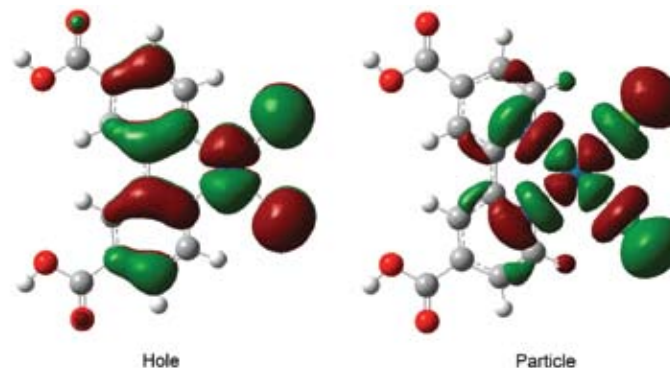


*Fig. 3. MOs of the relevant excited state at 433 nm for 2.*

least 18 h with  $\text{MV}^{2+}$ ). For **2**, although we cannot predict an oscillator strength for a spin-forbidden transition, spin-orbit coupling is likely to be substantial for these Pt-based systems due to the heavy participation of Pt and will likely confer allowed character to the transition.

In conclusion, from our calculations we can postulate that the molecular catalyst dissociates upon photoexcitation of the reduced species and that the  $\text{H}_2$  production observed in the experiments is the result of the colloidal Pt in the vicinity of the semiconducting surface.

**For further information contact Enrique R. Batista at [erb@lanl.gov](mailto:erb@lanl.gov).**

- [1] P. Lei et al., *J. Am. Chem. Soc.* **130**, 26 (2008).
- [2] P. Du et al., *J. Am. Chem. Soc.* **130**, 5056 (2008).

**Funding  
Acknowledgments**  
LANL Directed  
Research and  
Development Program

## Accurate Calculation of Redox Potentials Using Density Functional Methods

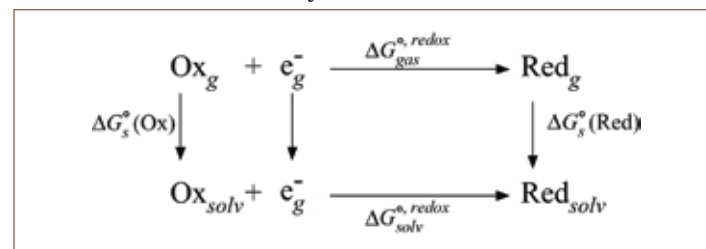
Lindsay E. Roy, Elena Jakubikova, Enrique R. Batista, T-1

Density functional theory (DFT) has provided insight into the mechanisms of several important catalytic cycles in environmental, bioinorganic, and industrial chemistry. Many chemical reactions utilizing transition metal complexes describe the loss and gain of electrons through the formation or breaking of chemical bonds. Combined with electrochemical and spectroscopic evidence of the pertinent intermediates, theoretical chemists have been able to deduce favorable thermodynamic and kinetic pathways to these cycles. The abilities of DFT have also been pushed in hopes of facilitating in the rational design of catalysts with specific properties. One such property that has garnered much attention over the past several years has been the ability of DFT to accurately predict redox potentials of transition metal complexes. The ability to predict redox potentials a priori is highly desirable, and one can imagine a combinatorial-computational approach to finding a redox potential within a specific range.

There are currently several protocols that exist for the theoretical prediction of the standard redox potentials in solution [1,2]. One of the more popular methods uses the Born-Haber cycle shown in Scheme 1 where the standard Gibbs free energy of redox half reaction,  $\Delta G_{solv}^{e, redox}$ , consists of the free energy change in the gas phase and the solvation free energies of the oxidized and reduced species. These values are then used to calculate the overall reaction of the standard Gibbs free energy energy,  $\Delta G_{solv}^{e, redox}$  /kcal · mol<sup>-1</sup> (Eq. 1);

$$\Delta G_{solv}^{e, redox} = \Delta G_g^{e, redox} + \Delta G_s^o(\text{Red}) - \Delta G_s^o(\text{Ox}) \quad (1)$$

**Scheme 1.** Born-Haber Cycle.



and the Nernst equation then determines the standard one-electron redox potentials,  $E^\circ/V$

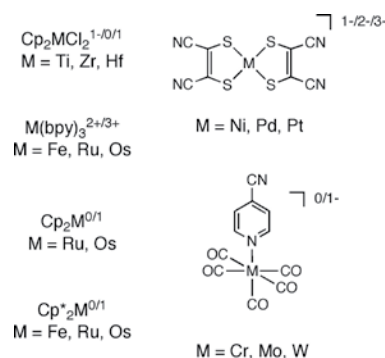
$$\Delta G_{solv}^{e, redox} = -FE_{calc}^\circ \quad (2)$$

where  $F$  is the Faraday constant, 23.06 kcal mol<sup>-1</sup> V<sup>-1</sup>.

Although this method has been successful for several organic systems using an implicit solvent model, modeling transition metal complexes has proven to be less reliable [3]. Previously, we showed that values of the calculated redox potential for a series of small models based on the diiron hydrogenase enzymes reproduced the trends experimentally with an average error of 0.12V using the gradient-corrected DFT, and results using the hybrid DFT functional required a systematic shift [4]. There, we realized the importance of referencing our results to the calculated absolute half-cell potential for the Ferrocene couple (i.e.,  $Fc + A \rightarrow Fc^+ + A^{\bullet-}$ ) in order to eliminate additional assumptions such as the solvent surface potential and the electron transfer process at the electrode surface necessary when referencing results to the experimental absolute potential of the standard hydrogen electrode (SHE). These results suggest that a fairly high degree of accuracy can be achieved for first-row transition elements. To resolve these issues, we set out to provide a rigorous quantum-chemical treatment of systems comprised of first-, second-, and third-row transition elements. These compounds contain varying oxidation states and charges and provide a good benchmark, considering the potentials are not necessarily reversible on the electrochemical time scale. Scheme 2 depicts the inorganic and organometallic compounds chosen for our study. A plot of our results

is illustrated in Fig. 1 for a typical generalized gradient approximation (GGA), functional (PBE, [5]), and the hybrid generalized gradient (H-GGA) Density Functional, (B3LYP, [6,7]), respectively. Firstly, the data are all consistent with one another for a given functional, regardless whether the redox occurs at the metal center or on the ligand.

**Scheme 2.** Transition metal complexes considered in this study.



The errors also appear to be systematic and are not dependent on whether the compound is a first-, second-, or third-row element. The PBE functional provides excellent agreement with experiment, and analysis of the data show that the quality of fit is 0.97. The B3LYP functional fared the worst in terms of fit and deviation with a systematic error of 0.83. In fact, B3LYP results require a consistent shift of -0.48 V for all the data

(shown as a dashed line in Fig. 1). When including a baseline shift for B3LYP, correlation is improved to 0.96. Examination of the data reveals that the only variation occurring with each calculation is the gas-phase free energy term,  $\Delta G_g^{\text{redox}}$ —the free energy of solvation,  $\Delta\Delta G_s^\circ$ , only differs by  $\sim 1$  kcal mol<sup>-1</sup> for all the functionals that were studied. The better performance of the GGA functional with respect to the H-GGA could be the result of an improved gas phase ionization potential.

The average error one can expect using PBE to calculate a redox couple is  $<0.23$  V. The deviation is  $\sim 0.16$  V for the redox couple of neutral species, but larger for highly anionic or cationic complexes. This protocol is a powerful tool that will allow theoretical chemists to aid in the design of redox-active catalysts.

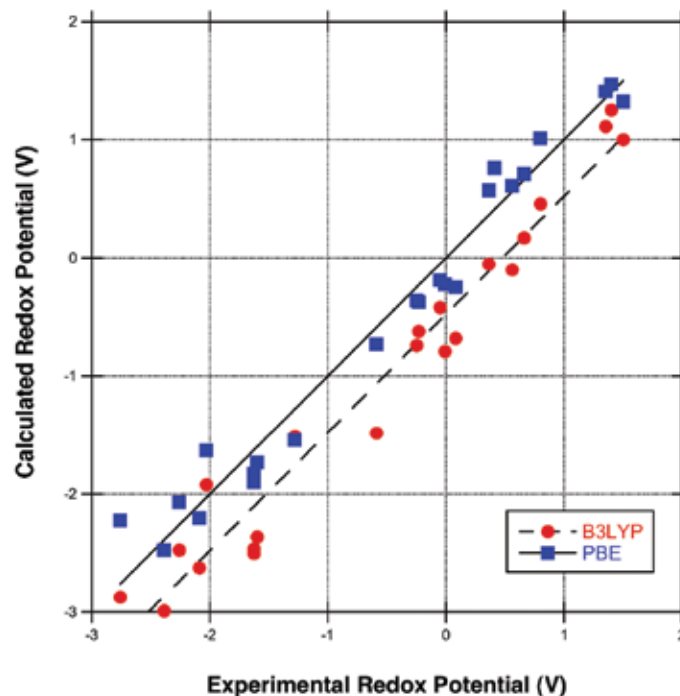


Fig. 1. Correlation diagram of experimental vs. calculated redox potential, V/Cp<sub>2</sub>Fe, for Scheme 2 complexes using PBE and B3LYP functionals. The solid line illustrates 1:1 correlation.

For further information contact Enrique R. Batista at [erb@lanl.gov](mailto:erb@lanl.gov).

- [1] J. Li et al., *Inorg. Chem.* **35**, 4694 (1996).
- [2] I. Tavernelli, R. Vuilleumier, M. Sprik, *Phys. Rev. Lett.* **88**, 213002 (2002).
- [3] M.-H. Baik, R.A. Friesner, *J. Phys. Chem. A* **106**, 7407 (2002).
- [4] L.E. Roy, E.R., Batista, P.J. Hay, *Inorg. Chem.* **47**, 9228 (2008).
- [5] J.P. Perdew, K. Burke, M. Ernzerhot, *Phys. Rev. Lett.* **77**, 3865 (1996).
- [6] A.D. Becke, *J. Chem. Phys.* **98**, 5648 (1993).
- [7] C. Lee et al., *Phys. Rev. B* **37**, 785 (1988).

**Funding  
Acknowledgments**  
LANL Directed  
Research and  
Development Program



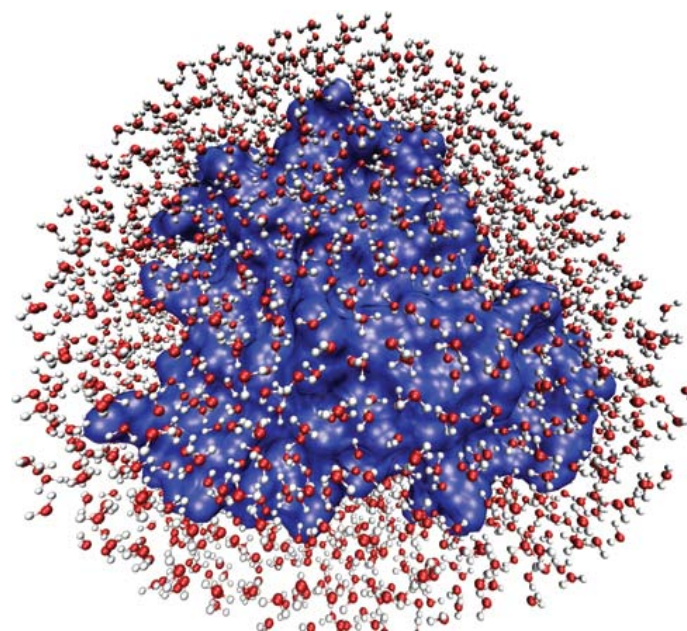
## The Role of the Hydration Shell of Proteins

Guo Chen, Paul W. Fenimore, T-6; Joel Berendzen, P-21; Hans Frauenfelder, Benjamin H. McMahon, T-6

*Fig. 1. The hydrated protein myoglobin (blue surface) with 1911 water molecules (red and white sticks-and-balls), the approximate number needed for optimal function ( $h = 2$ ). The water forms a shell about 5 Å thick around the protein.*

Proteins perform most of the functions necessary for life. A quantitative understanding of how proteins work and how their functions can be controlled is essential for many of the missions of LANL such as biodefense. Water is also essential for life and for the workings of proteins, but a real understanding of why water is crucial has been lacking. Our research now provides at least some of the answers to this fundamental query. Proteins are surrounded by a hydration shell of one to two layers of water (Fig. 1). This water is crucial for the functioning of proteins—dehydrated proteins do not work. Despite a very large number of publications, the workings of the hydration shell have not been clarified [1]. We believe that we understand the role of the hydration shell and how it controls internal protein motions that are involved in function [2]. Our model is based on insights from the physics of glass-forming liquids, new experiments, and the concept of a hierarchically organized energy landscape. Glass-forming liquids exhibit two major types of fluctuations,  $\alpha$  and  $\beta$  [3]. The  $\alpha$ -fluctuations represent structural changes that affect large-scale motions of the protein, but do not depend on hydration. Here we are concerned with the  $\beta$ -fluctuations in the hydration shell.  $\beta$ -fluctuations depend on hydration and occur even if the environment is rigid. We assert that their role is the driving of internal protein motions. To prove this claim, we have measured the  $\beta$ -fluctuations in the hydration shell and compared them with internal fluctuations determined with the Mössbauer effect and incoherent neutron scattering. The result is unambiguous: internal motions are slaved to the  $\beta$ -fluctuations in the hydration shell.

The experiments that led to the understanding are in principle simple. Myoglobin (Mb), an oxygen storage protein,



is used as a model system. Experiments performed a long time ago showed that carbon monoxide moves through the interior of hydrated Mb even if Mb is embedded in a solid [4]. However, it was not clear what permitted the motion. Much later we guessed that it could be  $\beta$ -fluctuations in the hydration shell [5]. To test this claim, we use dielectric relaxation to measure the  $\beta$ -fluctuations. To ensure that the fluctuations originate in the hydration shell, Mb at various hydration levels is embedded in solid poly(vinyl) alcohol. The temperature dependence of the relaxation rate coefficient,  $k_\beta(T)$ , for various hydration levels is shown in Fig. 2a. A typical spectrum is shown in Fig. 2b. The internal protein fluctuations are determined using published data on the Mössbauer effect of  $^{57}\text{Fe}$  in the heme group of Mb [6]. A fraction  $f(T)$  of  $\gamma$ -rays emitted by  $^{57}\text{Fe}$  in Mb suffers no energy loss.  $f(T)$  is controlled by the fluctuations experienced by the  $^{57}\text{Fe}$  nuclei. In the simplest approximation,  $f(T) = 1$  if the fluctuations are slower than the lifetime  $\tau_{\text{Mö}} = 140\text{ns}$  of the nuclear level that emits the  $\gamma$ -rays, and  $f(T) = 0$  if the fluctuations are faster. The crucial feature now is the inhomogeneity of protein samples. The broad spectrum



shown in Fig. 2b implies that each protein has a unique fluctuation frequency  $\nu$  and that the spectrum represents the probability of finding proteins with a given frequency  $\nu$ . Proteins with circular frequencies  $\omega = 2\pi\nu < 1/\tau_{\text{Mö}}$  emit  $\gamma$ -rays without energy loss. The line at  $k_{\text{Mö}} = 1/\tau_{\text{Mö}}$  in Fig. 2b demarcates the two areas—the red area to the left labeled  $a_\beta$  gives the fraction of recoilless emitters. The test of our hypothesis is now clear. The  $\beta$  fluctuations in the hydration shell drive the internal motions if  $f(T) = a_\beta(T)$ . We have determined  $a_\beta(T)$  and Parak and collaborators have measured  $f(T)$ . The two functions are plotted in Fig. 3. The close agreement proves that the  $\beta$ -fluctuations in the hydration shell indeed drive the internal protein motions. The result suggests a large number of new experiments.

This work has been done in collaboration with Izabela R. Stroe, Jan Swenson, Helén Jansson, Robert D. Young and Albert Migliori.

**For further information contact Paul W. Fenimore at paulf@lanl.gov.**

- [1] I. Brovchenko, A. Oleinikova, *Chem. Phys. Chem.* **9**, 2695-2702 (2008).
- [2] H. Frauenfelder et al., *Proc. Nat'l Acad. Sci. USA* (in press 2009).
- [3] E. Donth, *The Glass Transition*, Springer Series in Materials Science **48** (2001).
- [4] R.H. Austin et al., *Biochemistry* **14**, 5355-5373 (1975).
- [5] P.W. Fenimore et al., *PNAS USA* **99**, 16047-16051 (2004).
- [6] F.G. Parak, K. Achterhold, *J. Phys. Chem. Solids* **66**, 2257-2262 (2005).

**Funding**  
**Acknowledgments**  
 LANL Directed  
 Research and  
 Development Program

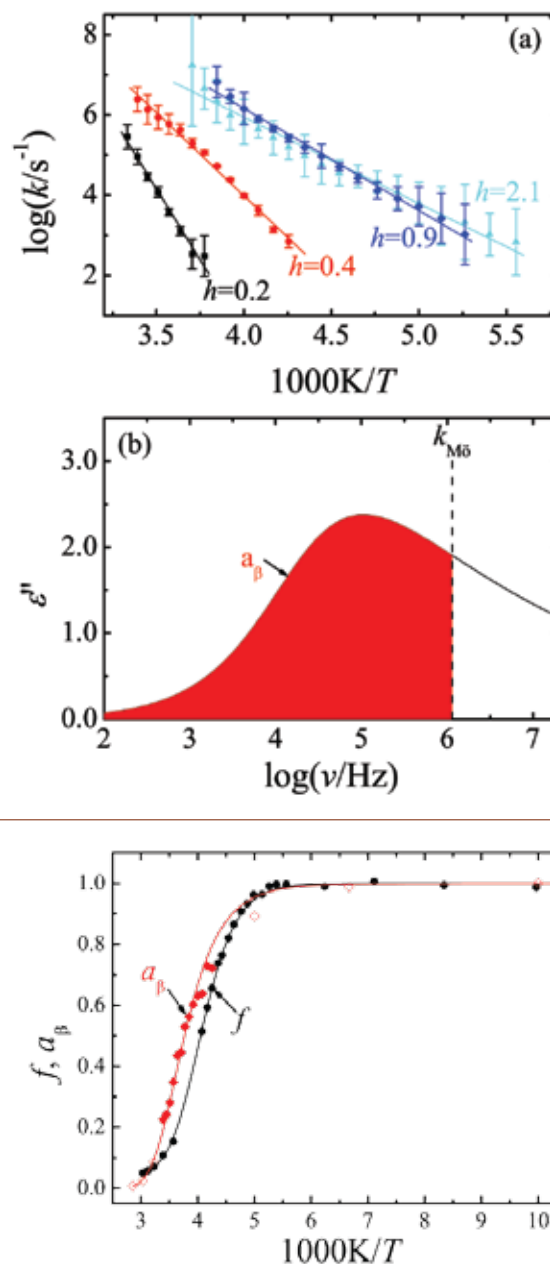


*Fig. 2. Hydration-relaxation processes in myoglobin. (a) An Arrhenius plot of the  $\beta$ -processes for Mb embedded in PVA for various values of the hydration  $h$ . (b) The smoothed dielectric relaxation spectrum of the  $\beta$ -relaxation in Mb at 265K. The vertical line denoted by  $k_{\text{Mö}}$  gives the dephasing rate corresponding to  $\tau_{\text{Mö}} = 140$  ns, the mean Mössbauer lifetime of  $^{57}\text{Fe}$ . The fractional area to the left of  $k_{\text{Mö}}$  is denoted by  $a_\beta$ .*

*Fig. 3. The temperature dependence of the dielectric relaxation area  $a_\beta(T)$  and the recoilless fraction  $f(T)$  of the Mössbauer effect. The similar temperature dependence between the two independently measured functions demonstrates that the internal protein motions, characterized by  $f(T)$ , are determined by the hydration shell, characterized by  $a_\beta(T)$ . Note that  $f(T)$  is difficult to measure at low temperature because small uncertainties in protein vibrational motions change  $f(T)$  strongly. It is also difficult to measure at high temperature because the elastic component becomes very small.*

## Structural Alterations of a Vaccine Target: Clade-specific Differences and Immune Escape of HIV-1 Surface Protein

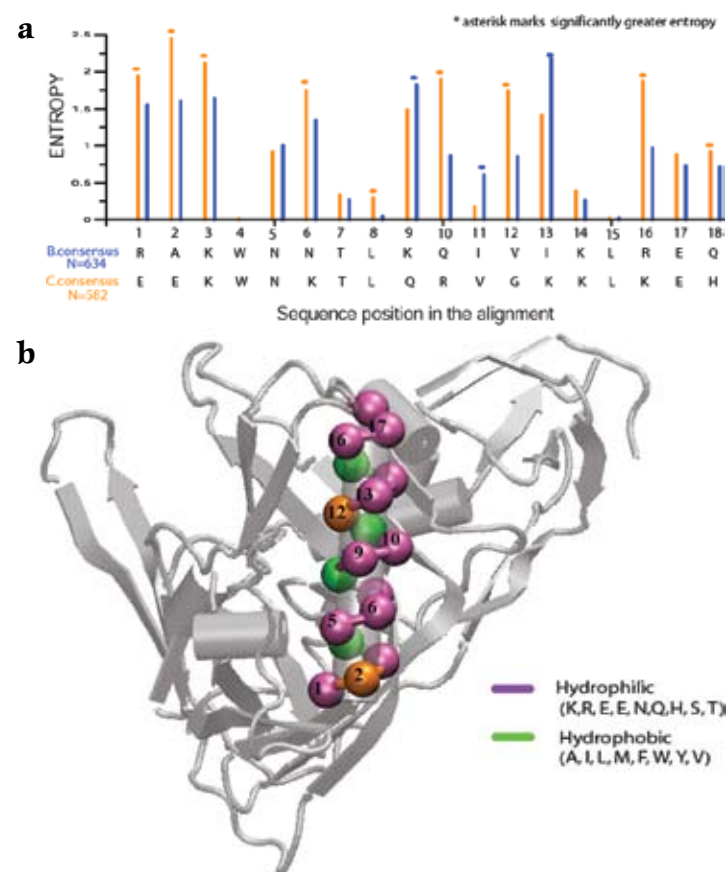
S. Gnanakaran, T-6; Cynthia Derdeyn, Emory University; Bette Korber, T-6

*Fig. 1. (A) Sequence entropy profiles of  $\alpha 2$  helix for B (blue) and C (orange) clades. (B) Mapping of residue positions from (A) onto the X-ray structure of gp120.*

The genetic diversity of HIV-1 is characterized by a relatively small number of genetically defined clades, or subtypes, A to K, and their recombinants. The envelope (Env) glycoproteins, gp120 and gp41, are the main targets of antibody (Ab) neutralization and are among the most variable of HIV proteins, with typical inter- and intra-clade differences of 20-35% and 10-15% respectively. An antibody-based HIV vaccine would ideally be capable of neutralizing viruses from diverse variants. Whether this will be feasible, and how one might design a polyvalent cocktail that could improve the crossreactive breadth of vaccine-induced responses, can be informed by detailed examination of clade-specific differences in structure and mutational patterns.

Codon-specific ratios of nonsynonymous to synonymous substitution rates (dN/dS) are dramatically different in the B and C subtypes in C3 and V3 regions of gp120. Subtype C is more variable in the C3 region, which is relatively conserved in the B subtype. Conversely, the V3 domain of subtype C exhibits less sequence variation compared with subtype B. Such differences could result from the evolution of lineage-specific structural or functional constraints in the proteins. They could also be due to transmission pressures, or spatially localized differences in neutralizing antibody binding sites, or different HLA frequencies in the circulating populations and the consequent immune escape pressures. By utilizing a synergetic approach that combines sequence and structure, we explore mutational patterns and their structural implications to better understand how positive selection might be driven by immune escape.

We have utilized a variety of simulation techniques to characterize the structure, motion, and thermodynamics of gp120 of B and C clades. The characterization includes longtime all-atom molecular dynamics simulations to capture the dynamics of the gp120 protein, replica exchange enhanced sampling method to capture the conformational variability of loops, and coarse-grained models to capture interactions of V3 with the gp120 core. Coupling these simulation studies with phylogenetic analysis provided several pieces of evidence of sequence and structure differences in viral glycoprotein gp120 between clades B and C. In the C clade, the C3 region  $\alpha 2$ -helix exhibits high sequence entropy at the polar face but maintains its



amphipathicity, whereas in the B clade it accommodates hydrophobic residues (Fig. 1). The V4 hypervariable domain in the C clade is shorter than that in the B clade. Generally, shorter V4 loops are incompatible with a glycine occurring in the middle of the  $\alpha 2$ -helix in the C clade, an intriguing association that could be exploited to inform the design of Env immunogens.

Recently, we have been investigating why the C clade V3 domain lacks sites of strong positive selection analogous to those found in the B clade V3. In the all-atom simulation, we observe the formation of a cluster of hydrophobic residues flanking the V3 tip of C clade (Fig. 2). Importantly, results from the clinical studies at Emory Vaccine Center are consistent with the existence of such a hydrophobic cluster. Stabilizing forces may drive this hydrophobic cluster to avoid solvent exposure by packing within V3 or, possibly, into the core. Our coarse-grained models provide potential sites in gp120 core that interact with this hydrophobic cluster. It is likely that V3 may not be exposed in the C clade since it does not serve as an antibody-mediated neutralization target. Our studies indicate that sequence conservation preserved in structurally specific places within V3 of the C clade may be enabling the V3 itself to play a role in concealing its epitopes.

**For further information contact S. Gnanakaran at [gnana@lanl.gov](mailto:gnana@lanl.gov).**

### References

- S. Gnanakaran, et al., *J. Virol.* **81**, 4886-4891 (2007).
- S. Rong, et al. *J. Virol.* **81**, 5658-5668 (2007).
- R.M Lynch et al., LA-UR-08-05424 (2008).
- R.M Lynch et al., *Aids Res Hum Retroviruses*, in press (2009).

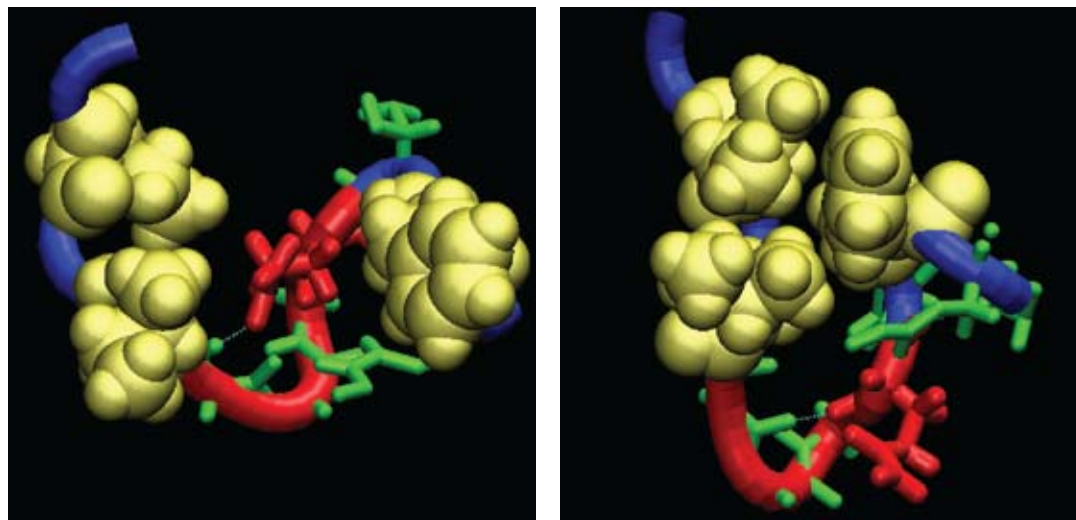


*Fig. 2. Formation of a hydrophobic cluster (anchored by residues I307, I309, and F317) near the V3 loop tip.*

### Funding

#### Acknowledgments

LANL Directed  
Research and  
Development Program

# Hidden Structure in Protein Energy Landscapes

Dengming Ming, Marian Anghel, Michael E. Wall, CCS-3

**P**rotein activity is controlled by dynamical transitions among conformational substates [1]—the transitions may be understood in terms of motions on an energy landscape [2]. Substates correspond to local minima in the energy landscape, and transitions correspond to the hurdling of barriers between minima. The shape of basins strongly influences the kinetics of transitions, which in turn determine the time scales for important processes such as protein folding and communication of allosteric effects.

*Fig. 1. (left) Schematic illustration of the immunoglobulin-binding domain of Streptococcal protein G (GB1).*

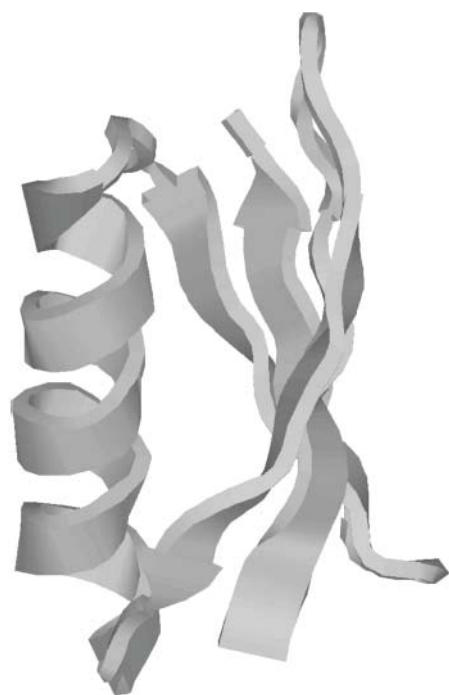
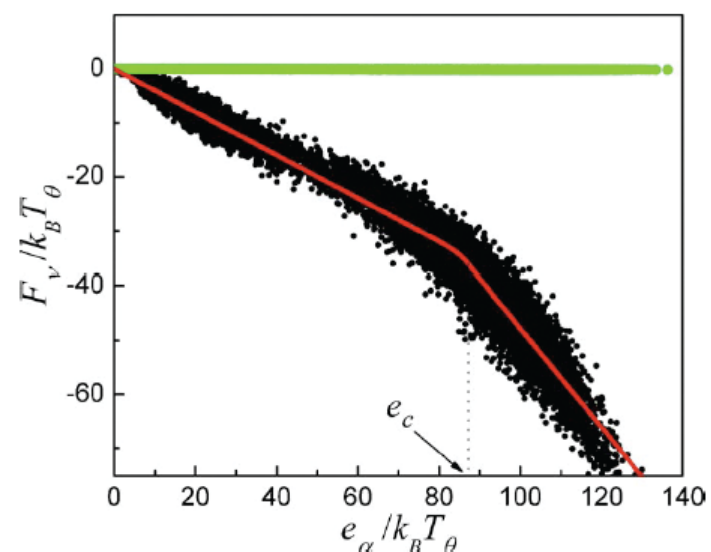


*Fig. 2. (right) Vibrational free energies,  $F_v$ , of minima versus their potential energies  $e_a$  (black points). The contribution from vibrations between bonded atoms is constant (green points following  $y = 0$ )—the diversity is due to differences in the energetics of perturbing other degrees of freedom.*

To gain insight into protein energy landscapes, we performed a computational study to investigate diversity among basins in the energy landscape of a coarse-grained model of the immunoglobulin-binding domain of Streptococcal protein G (GB1) (Fig. 1) [3]. We found that different basins had different curvatures in the neighborhood of the minimum. The differences were characterized using the free energy of small vibrations

about the minimum (Fig. 2). The spectrum of vibrational free energies produced a density of minima versus energy, resembling that of a structural glass (Fig. 3). Interestingly, both the vibrational free energy and the potential energy of a minimum could be simply modeled in terms of the native contacts that are lost in moving the protein from the native structure to the minimum (Fig. 4).

Studies of energy landscapes frequently assume that different basins have a similar shape. Our finding of diversity in the vibrational free energy of different basins in a model of GB1 challenges this assumption. For the present model, the diversity still exhibits a relatively simple structure, and is consistent with the previously noted similarity between the energy landscapes of proteins and glasses [4]. The vibrational free energy is similar for basins about minima with similar energy, enabling simpler and faster computations of thermodynamic properties using inherent structure theory [5,6]. In addition, the vibrational free energy can be modeled using elementary measures of the network of native contacts, which can be used in theoretical studies of protein energy landscapes. Our methods are extensible to more detailed models of proteins, and we expect them to yield analogous





results in more general applications, revealing relatively simple structures that are hidden in complex protein energy landscapes.

**For further information contact Michael E. Wall at [mewall@lanl.gov](mailto:mewall@lanl.gov).**

- [1] H. Frauenfelder, P.G. Wolynes, *Science* **229**, 337 (1985).
- [2] H. Frauenfelder et al., *Science* **254**, 1598 (1991).
- [3] D. Ming et al., *Phys. Rev. E* **77**, 021902 (2008).
- [4] A. Ansari et al., *Proc. Natl. Acad. Sci. U.S.A.* **82**, 5000 (1985).
- [5] F.H. Stillinger, T.A. Weber, *Phys. Rev. A* **25**, 978 (1982).
- [6] F.H. Stillinger, T.A. Weber, *Science* **225**, 983 (1984).

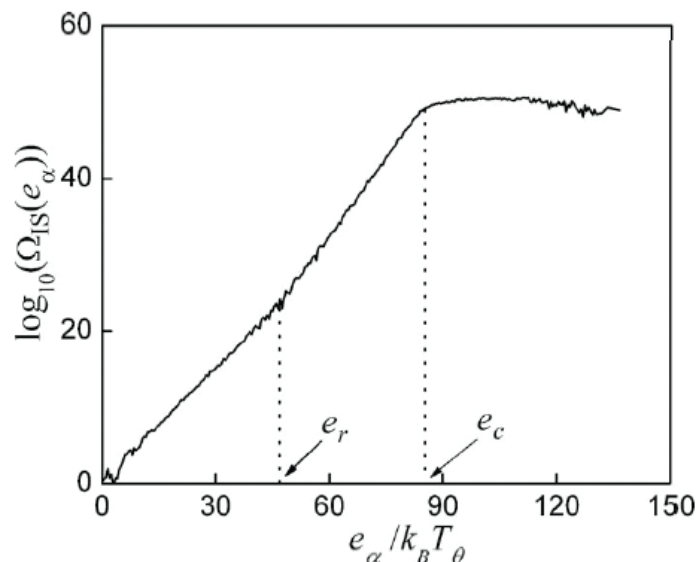


*Fig. 3. Density of minima  $W_{IS}(e_\alpha)$ . The knee at  $e_r = 47.4k_B T$  is due to a change in stress, and the plateau beginning at roughly  $e_c = 88.4k_B T$  is due to a change in rigidity—both are understood in terms of the network of native contacts.*

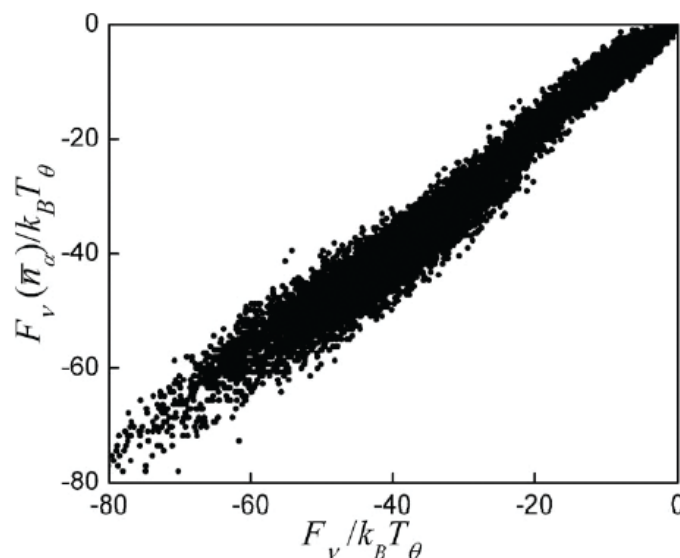


*Fig. 4. Comparison of vibrational free energies calculated from the model (y axis) or estimated from numerical simulations (x axis).*

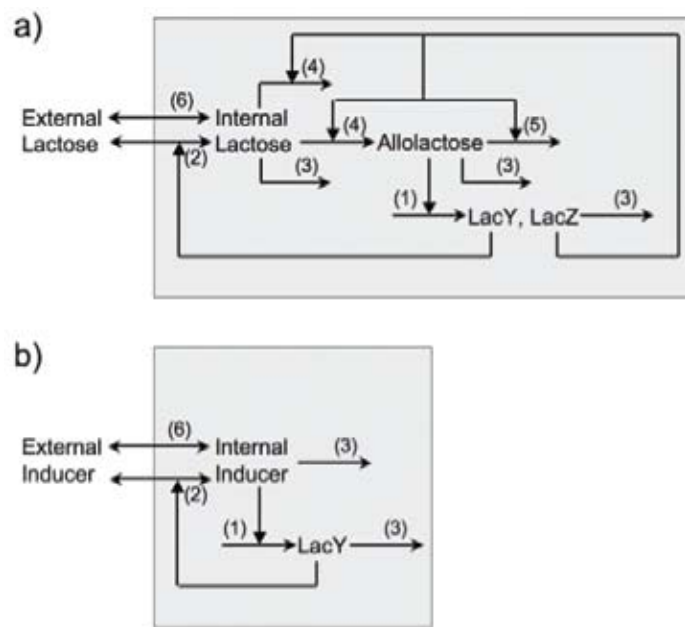
**Funding  
Acknowledgments**  
LANL Directed  
Research and  
Development Program

# Computational Prediction of Bacterial Behavior

David W. Dreisigmeyer, Jelena Stajic, Ilya Nemenman, CCS-3; William S. Hlavacek, T-6; Michael E. Wall, CCS-3

**Fig. 1. Models of *lac* induction.** (a) Model for *lac* induction by lactose, including the following processes: (1) proportional production of permease (*LacY*) and  $\beta$ -gal (*LacZ*), (2) permease-mediated transport of lactose, (3) dilution of intracellular species by cell growth, (4)  $\beta$ -gal catalyzed degradation of lactose, producing both the metabolic intermediate allolactose, and the ultimate products of degradation, glucose and galactose, (5)  $\beta$ -gal catalyzed degradation of allolactose, producing glucose and galactose, and (6) passive transport of inducer. (b) Induction by artificial inducers, including: (1) proportional production of permease (*LacY*) and  $\beta$ -gal (*LacZ*), (2) permease-mediated transport of inducer, (3) dilution of intracellular species by cell growth, and (6) passive transport of inducer.

Can we use a computational model to predict the response of a microbe to new environmental signals? The answer to this question is important—in part because the ability to make accurate predictions would vastly reduce the experimental effort required to harness microbes for biofuels and carbon management. To better understand the technical challenges involved, we investigated this question for a well-characterized system: induction of lactose utilization genes from the *lac* operon in *Escherichia coli* [1].



In 1957, Novick and Weiner [2] studied expression of the *lac* operon in response to an artificial inducer, thio-methylgalactoside (TMG), which is not degraded by the induced enzyme  $\beta$ -galactosidase ( $\beta$ -gal). They discovered that this system can exhibit discontinuous switching, with some cells expressing a large amount of enzyme, other cells expressing a small amount, and an insignificant number of cells expressing an intermediate amount. Recently, this effect was further characterized using single-cell assays of fluorescence levels in a population of *E. coli* cells carrying a *lac::gfp* reporter [3]. Cells were grown overnight on sucrose in either an induced (1 mM TMG) or uninduced (no TMG) state. They were then diluted into media with defined levels of TMG and glucose. After 20 hours of growth, the cells were examined under a microscope. Under many conditions, cell populations exhibited a bimodal distribution, with induced cells having over 100 times the fluorescence level of uninduced cells. The distribution was also history-dependent—at the same final level of TMG and glucose, cells with an induced history were predominantly induced, while cells with an uninduced history were predominantly uninduced. These observations have been attributed to the existence of two steady states, i.e., bistability, in the induction of *lac* in *E. coli*.

The aim of our study was to predict whether *lac* induction would also exhibit bistability in response to a natural inducer (lactose) that is degraded by enzyme. To address this question, we first developed a model of *lac* induction in response to TMG (Fig. 1b). The model is applicable in the absence of external glucose, which is a physiologically relevant condition for lactose utilization by *E. coli*. The model was constrained using a large body of biophysical data from the literature, and was validated using the published data of Ozbudak et al. [3]—it exhibited bistability for a range of TMG levels that is consistent with the data (Fig. 2).

We then modified the model to consider induction by lactose (Fig. 1a). The model exhibited no bistability within the constraints from available biophysical data (Fig. 3). Further analysis of the model yielded predictions of specific factors that can promote bistability, such as hindering enzyme

kinetics, suggesting potential targets for engineering mutants that are bistable in response to lactose.

Our results are consistent with preliminary experimental studies of lactose induction of the *lac* operon [3], which showed no bistability. They emphasize the importance of metabolic fluxes in determining microbial responses, and suggest that it might be possible to predict microbial behavior in response to new environmental signals. Using our methods, we were able to predict genetic targets for engineering mutants that are bistable in response to lactose. Similar methods might be useful for optimizing microbial behavior to produce biofuels and manage carbon flow.

**For further information contact Michael E. Wall at [mewall@lanl.gov](mailto:mewall@lanl.gov).**

- [1] D.W. Dreisigmeyer et al., *IET Syst. Biol.* **2**, 293 (2008).
- [2] A. Novick and M. Weiner, *Proc Natl Acad Sci USA* **43**, 553 (1957).
- [3] E.M. Ozbudak et al., *Nature* **427**, 737 (2004).

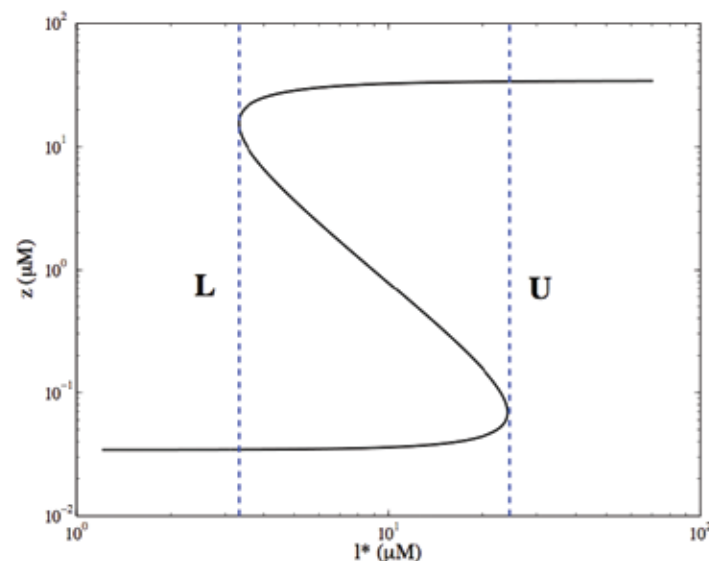


Figure 2. Simulated induction of *lac* by TMG. At external TMG levels ( $x$  axis) between the upper (U) and lower (L) turning points, there are three steady-state expression levels ( $y$  axis): a high level, which is stable, an intermediate level, which is unstable, and a low level, which is stable. The system is therefore predicted to be bistable for TMG levels between U and L—the range shown here is consistent with that in [3].

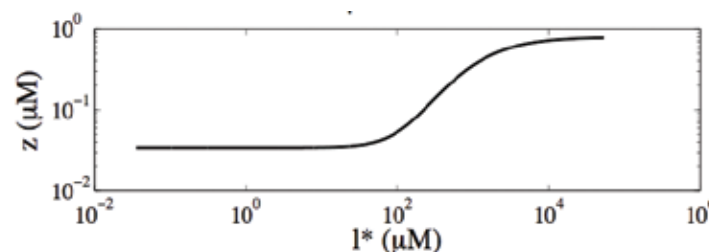


Figure 3. Simulated induction of *lac* by lactose. At all external TMG levels ( $x$  axis), there is a single steady-state expression level ( $y$  axis). The system is therefore not bistable.

#### Funding

#### Acknowledgments

LANL Directed Research and Development Program





# Climate Modeling

**Modeling and simulation play a key role in understanding the global climate and how it is evolving. LANL plays a central role in the global climate simulation community, as the Laboratory bears responsibility for all advanced numerical models for ocean and sea ice that are used in the climate community's global climate change predictions. The LANL research team focuses their attention on developing ocean and ice models for the climate community, as well as using the models to address scientific issues such as high-latitude climate changes and their impact on the world.**

**Papers in this section describe recent advances and results in ocean and sea ice modeling this year, with**

**emphasis on arctic ice sheet thickness, ocean/ice shelf interaction, ice sheet mass, biogeochemistry, evolving CFC concentrations as a function of time within eddy resolving ocean simulations, and the dynamic effects of wind on ocean circulation.**

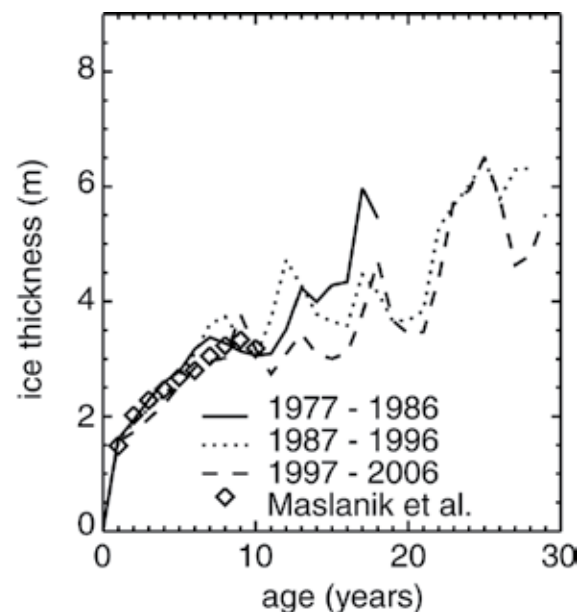
**This is world-class science that plays an important role in the global community and national policy that affects our nation and the world.**

## Age Characteristics in a Multidecadal Arctic Sea Ice Simulation

Elizabeth C. Hunke, T-3; Cecilia M. Bitz, Atmospheric Sciences, University of Washington

Beginning in the late 1970s, the satellite era opened a viewing window for the large-scale variability of the polar regions. Substantive changes to the Arctic sea ice pack over the past decade are becoming apparent, most notably as reductions in area coverage in summer. Although more difficult to observe, other fundamental characteristics of the pack ice are also changing, such as ice thickness. Ice thickness is closely related to the age of the ice, because thickening through growth and ridging accumulates over time. Older ice, and by association thicker ice, possesses different characteristics than younger, thinner ice by virtue of the aging process, particularly desalination through brine channels and associated changes in albedo. Changes in the

*Fig. 1. Average March thickness of ice plotted against ice age, for three decades, and the Maslanik et al. [1] proxy ice thickness estimates for 2003–2006. Model data are plotted only for age bins that are populated for all 10 years of each averaging period. Thus our results show that ice age is not a good proxy for sea ice thickness in a given year.*



physical characteristics of the ice pack due to its transition from older to younger ice will have ramifications for the strength of feedbacks and ecosystem structure.

In light of research suggesting recent thinning of Arctic sea ice, and in the absence of basin-wide, detailed thickness observations, there has been much interest in obtaining ice age estimates from satellite data with which to infer and understand changes in the volume of Arctic sea ice. Recently, Maslanik et al. [1] used correlations of laser altimeter ice thickness data for 2003–2006 with estimates of sea ice age, inferred from a simple advection scheme using satellite-observed ice concentration and velocity, to develop an ice thickness proxy that could be used to create maps of ice volume in prior years.

Their results are shown in Fig. 1 against the output from our simulation using the Los Alamos sea ice model, CICE 4.0, a numerical sea ice model used for global climate studies. The model allows consistent simulation of ice age, dynamics, and thermodynamics, which satellite-based estimates lack. Agreement is remarkably good for ice up to 10 years old. However, neither spatial patterns nor interannual variability of ice age and ice thickness are as closely related as might be deduced from the Maslanik et al. proxy. Figure 2 illustrates modeled ice thickness and age in March of 1976, 1986, 1996, and 2006. Near the Canadian Archipelago, where ice is very thick and old, and near the Siberian coast, where ice tends to be thin and young, the age and thickness contours line up well. In the central Arctic, however, dynamic processes contribute to the complexity of the pack's physical characteristics through large-scale ice motion and smaller scale processes such as rafting and ridging.

Our model simulation reinforces the observationalists' story: older ice types have declined in the Arctic ice cover. However, although our model exhibits the expected relationship between ice age and thickness on multiyear and Northern Hemisphere-wide averages, we find that the correlation between ice age and thickness breaks down at the local scale (100s of kilometers and smaller) in [2].

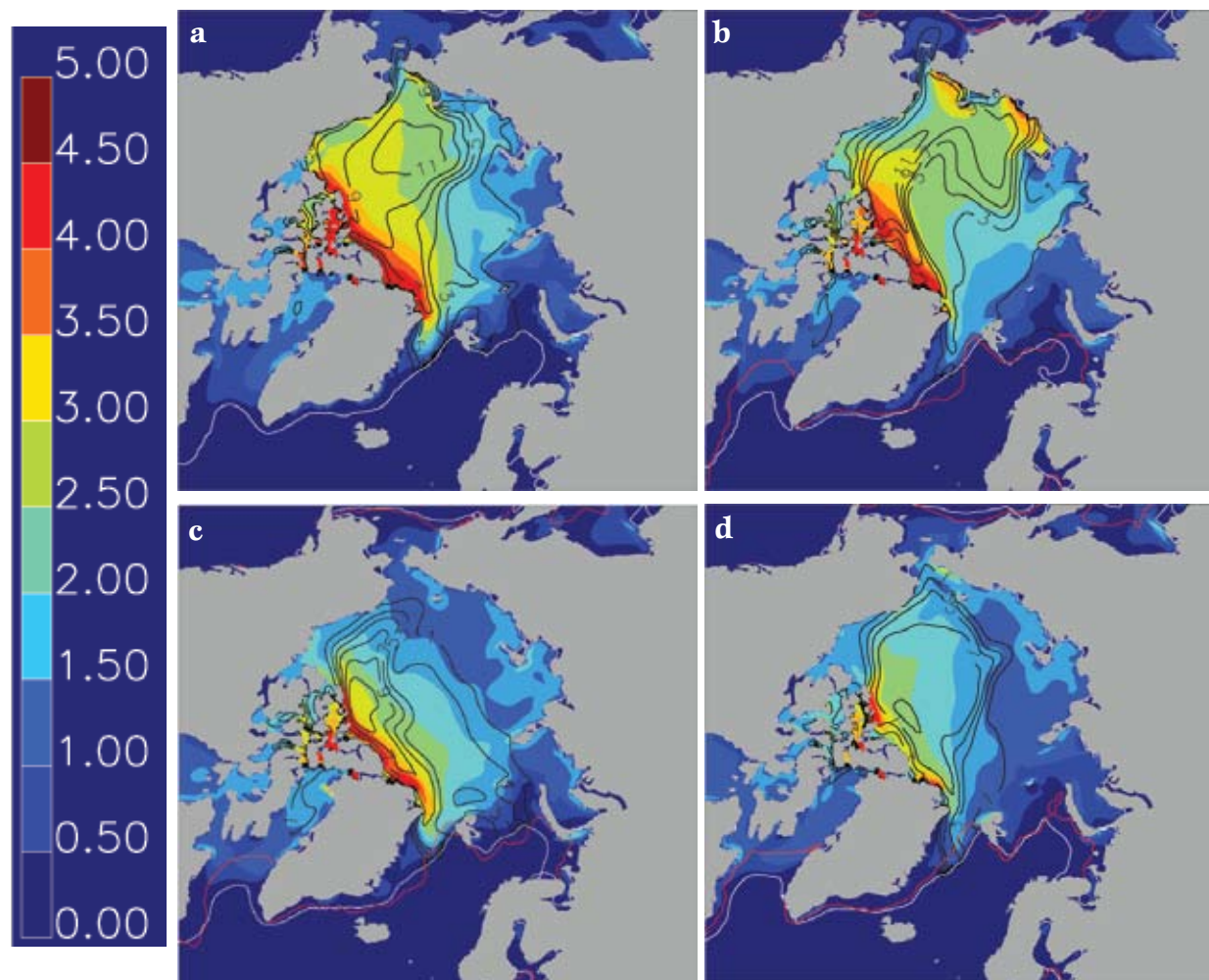


Fig. 2. March ice thickness, in m, for (a) 1976, (b) 1986, (c) 1996, and (d) 2006, overlain with ice age contours in black (2-year increments). The 15% simulated area concentration contour is white, and the satellite-observed 15% area contour is red.

For further information contact Elizabeth C. Hunke at [eclare@lanl.gov](mailto:eclare@lanl.gov).

- [1] J.A. Maslanik et al., *Geophys. Res. Lett.*, **34**, L24501, doi:10.1029/2007GL032043 (2007).
- [2] E.C. Hunke, C.M. Bitz. "Age characteristics in a multidecadal Arctic sea ice simulation." *J. Geophys. Res.*, in review (2009).

#### Funding Acknowledgments

- DOE, Office of Biological and Environmental Research Climate Change Prediction Program
- National Science Foundation

## Climate, Ocean, and Sea Ice Modeling

Philip Jones, Elizabeth Hunke, William Lipscomb, Mathew Maltrud, Stephen Price, Todd Ringler, Bin Zhao, T-3; Scott Elliott, Matthew Hecht, Balu Nadiga, Nicole Jefferey, Mark R. Petersen, Wilbert Weijer, Beth Wingate, CCS-2

The Climate, Ocean and Sea Ice Modeling (COSIM) project develops and maintains advanced numerical models of the ocean and sea ice for use in global climate change projections. Our Parallel Ocean Program (POP) and Community Ice Code (CICE) are the ocean and sea ice components of the Community Climate System Model and other coupled climate system models. These coupled models are the tools needed for future climate change projections in both national and international climate assessments. In addition to ocean and sea ice models, COSIM scientists are working on a new Community Ice Sheet Model (CISM) to more accurately simulate and predict the fate of large ice sheets covering Greenland and West Antarctica. Ocean ecosystems and their impact on the carbon and sulfur cycles have been another important addition to the physical models.

While the emphasis is on developing ocean and ice models for the climate community, COSIM researchers also use the models to address scientific issues. Our scientific focus is on high-latitude climate changes and their impact on the rest of the globe. This year, much of our focus has been on ice sheets and the interactions between the ocean and ice shelves. Understanding the physical processes behind ice sheet melt is critical for quantifying the rate of melting and the subsequent rise in sea level. We held a workshop at Los Alamos this year to evaluate the most important outstanding issues in ice sheet modeling and to initiate the community-wide development of the CISM model. This workshop was highly successful in unifying and motivating the ice sheet modeling community.

In addition to the ice sheet progress, COSIM scientists released a new version of the CICE model with several physical improvements. We also continued simulations using a very high-resolution configuration of the fully coupled CCSM model with 10-km resolution in the ocean and ice (see Fig. 1). Finally, new efforts have begun in Arctic biogeochemistry and understanding the potential large release of methane from sea-floor methane hydrates. These efforts should lead to exciting new results in the coming year.

**For further information contact Philip Jones at [pwjones@lanl.gov](mailto:pwjones@lanl.gov).**



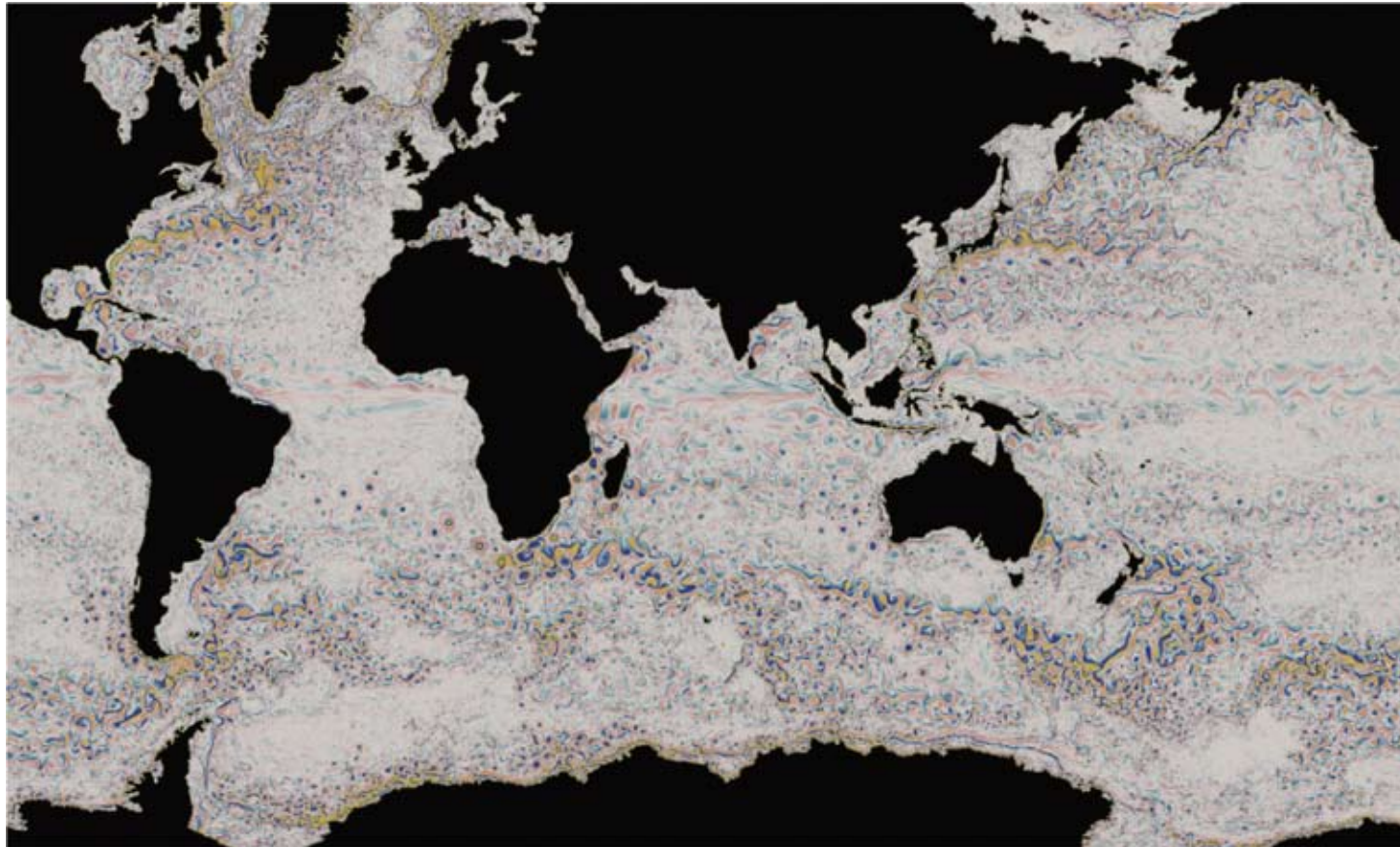


*Fig. 1. Relative vorticity (a measure of fluid rotation) at 15m depth from a global eddy-resolving ocean simulation.*

#### **Funding**

##### **Acknowledgments**

- DOE, Office of Biological and Environmental Research, Climate Change Prediction Program
- DOE, Office of Science, Scientific Discovery through Advanced Computing Program

## Tracking Chlorofluorocarbons in a Global Eddying Ocean Model

Mathew Maltrud, T-3; Synte Peacock, Frank Bryan, National Center for Atmospheric Research, Boulder, CO

The ocean plays a critical role in the earth's balance of heat, water, and chemicals such as carbon dioxide. After exchanging properties with the atmosphere at the surface, the ocean can store energy and dissolved gases for hundreds to thousands of years at depth. This "ventilation" process, which ultimately influences climate, is very difficult to measure directly, but can be inferred from observations of dissolved chemical compounds if enough is known about the ocean circulation.

One particularly useful class of chemical tracers for seeing how chemicals are moved through the ocean is chlorofluorocarbons (CFC), which human activity has introduced into the atmosphere. CFCs are ideal for inferring ventilation pathways and timescales in the ocean, because they have a well-known atmospheric time history and solubility, and they are inert once in the ocean (unlike, for example, oxygen and carbon dioxide). The task then becomes to relate the measured CFC concentration to its equilibrium surface value in order to determine the ventilation age of the water. However, to obtain a meaningful result, researchers also need accurate information about how the water was transported to the observed location. This is where Ocean General Circulation Models (OGCM) can play an important role by providing insight into transport processes.

Most previous studies of CFC distributions using ocean models have been done using fairly coarse resolutions (grid spacing greater than 100 km), for which some important transport processes are either poorly resolved or parameterized. We have vastly improved upon previous work by performing a simulation of the ocean circulation in the

eddy regime (grid spacing of 10 km or less) that explicitly resolves the mesoscale oceanic transport. In order to obtain information about ventilation processes and pathways, a host of model tracers, including CFCs, were carried along in the century-long run.

The distribution of CFCs in the model (Fig. 1) compares very well with what has been measured from research vessels in the ocean, which provides critical model validation. A number of interesting questions will be addressed with the output from this simulation, including quantifying the level of eddy "noise" that is likely to be present in the measurements, and understanding the biases that are present when using CFCs to estimate the ventilation age of the sampled water. Studies such as these, which use a combination of modeling and real-world measurements to gain insight into oceanic transport processes, will be crucial as we improve our understanding of the ocean's role in the earth's climate system.

**For further information contact Mathew Maltrud at [maltrud@lanl.gov](mailto:maltrud@lanl.gov).**

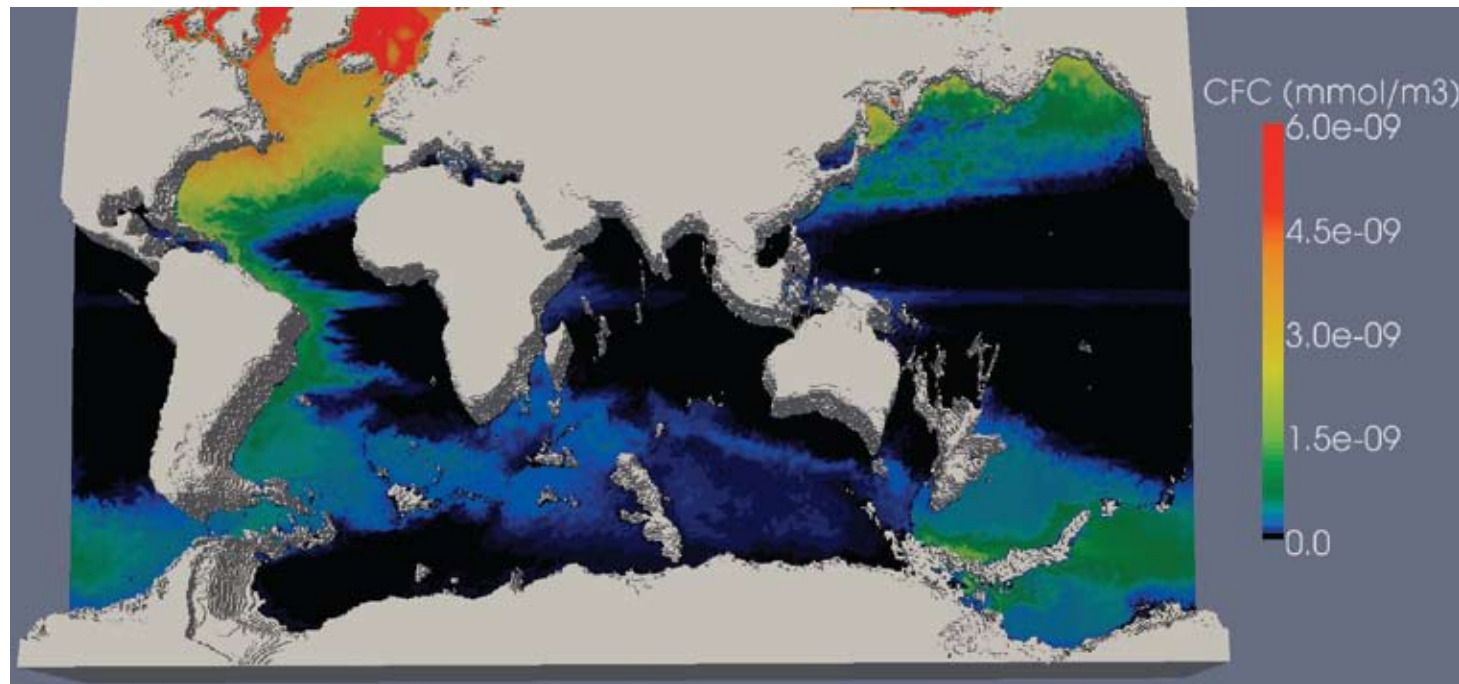


*Fig. 1. Concentration of the simulated CFC distribution (millimoles/m<sup>3</sup>) from year 55 of a POP global 1/10<sup>0</sup> model run. The image plane slopes from near the ocean surface in the north to the abyss in the southern part of the domain.*

#### **Funding**

#### **Acknowledgments**

- DOE, Office of Biological and Environmental Research Climate Change Prediction Program
- National Science Foundation



## A New Dynamical Feature of Wind-driven Ocean Circulation

Balu Nadiga, CCS-2

The Climate, Ocean, and Sea Ice Modeling (COSIM) project at LANL aims to develop, test, and apply ocean and ice models in support of DOE Climate Change Research and to deliver improved climate data and models needed to determine acceptable levels of greenhouse gas emissions (<http://climate.lanl.gov>).

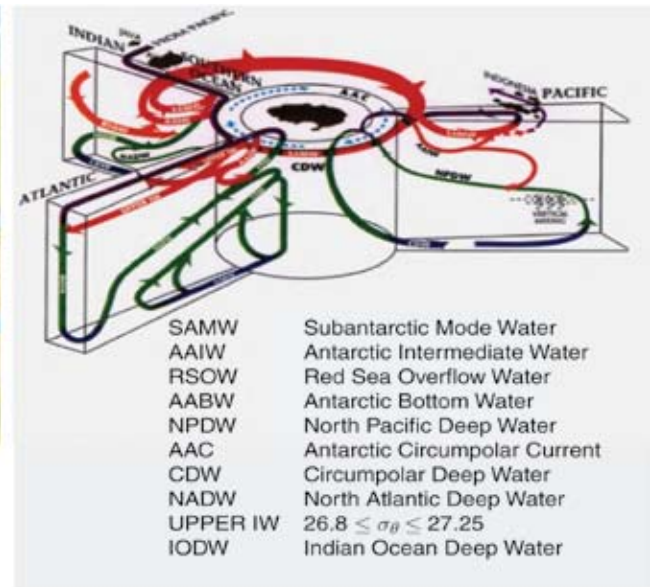
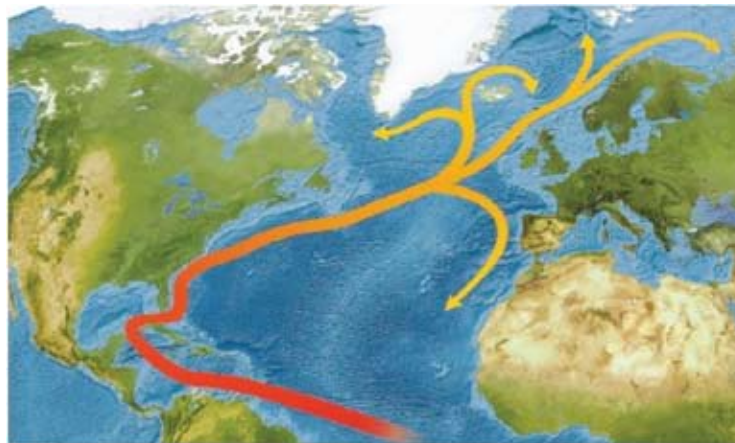
Roughly half of the heat from the tropical regions that receive an excess of insolation is transported poleward by the world's oceans to the higher latitudes as part of the global climate system. While this is achieved through a combination of complicated and interlinked circulation patterns, it is useful to separately consider the swifter and mainly horizontal wind-driven circulation of the upper ocean (e.g., Fig. 1) and the large-scale overturning, but more sluggish buoyancy-

driven “conveyor belt” circulation of the full ocean (Fig. 1), since the dynamics of these two circulation patterns are distinct.

The classical picture of wind-driven gyre circulation is one of broad, sweeping flows associated with the interiors of the large-scale wind-driven subtropical gyres of the upper ocean (see Fig. 2). The subsequent discovery of mesoscale eddies seemingly rounded off our understanding of such wind-driven gyre circulation. However, in a fundamental departure from this understanding, we find that multiple, alternating zonal-jet structures can develop in the ocean (in addition to the usual gyre circulation and mesoscale eddies) in response to purely large-scale and steady-wind forcing (see Fig. 2 [1,2]).

To place these results in context, we note that recent observational [3] and computational (e.g., [4,5]) evidence point to the occurrence of alternating zonal jets in the world oceans (see Fig. 3). These jets bear a similarity to the more exotic alternating zonal jets in Jovian atmospheres (e.g. [6])—a crucial difference, however, is their weaker amplitude with respect to other dynamical features in Earth's

*Fig. 1. Global ocean circulation that accounts for roughly half of the poleward heat transfer (that drives the climate system) is a combination of a) surface-intensified wind-driven circulation, as exemplified by the Gulf Stream and the subtropical gyre of the North Atlantic (shown on the left), and b) large-scale overturning circulation that is buoyancy-driven and popularly called the “conveyor-belt” circulation (schematic on right from [7]).*





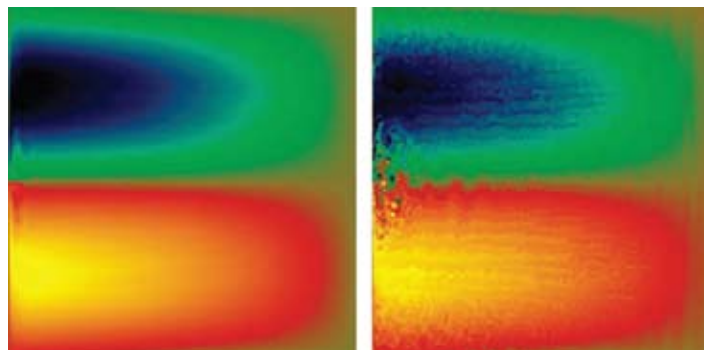
## Climate Modeling

oceans. Studies of zonal jets in the presence of the important oceanic effects of continental boundaries and nonuniform stratification are at present lacking, and this study aims to fill an important gap in the understanding of the dynamics of these jets.

As to the practical relevance of the study, consider: the way in which the rapidly rising levels of CO<sub>2</sub> in the atmosphere plays out in terms of climate change is crucially controlled by the dynamics of ocean circulation. However, ocean circulation itself is a strongly coupled multiscale phenomenon with important dynamics spanning vast ranges of spatial and temporal scales. Also note that a striking aspect of ocean circulation is that the dynamics over this vast range of scales is associated with a multitude of coherent features at different scales (somewhat in contrast to idealized studies of classical 3D turbulence, which is homogeneous and soup-like). Alternating zonal jets in the world oceans is one such new feature at scales intermediate between the gyre scale circulation and mesoscale eddies. Thus, from the point of view of modeling ocean circulation, a removal of the scale-gap that was assumed to exist between mesoscale eddies and gyre-scale circulation makes the parameterization problem more difficult for coarse-scale studies, but opens up the possibilities for more sophisticated and anisotropic parameterization schemes. Furthermore, the likely ubiquitous presence of multiple zonal jets and their effect on the transport of important scalars could lead to fundamental improvements in our understanding of global ocean circulation. For example, the enhancement of potential vorticity gradients at the boundaries of these jets acts as a barrier to mixing.

**For further information contact Balu Nadiga at [balu@lanl.gov](mailto:balu@lanl.gov).**

- [1] B.T. Nadiga, D. Straub, *Interaction of wind-driven gyres and zonal jets in oceans*. to be submitted to *Ocean Modeling* (2009).
- [2] B.T. Nadiga, *Geophys. Res. Lett.* **33**, L10601 (2006).
- [3] N. Maximenko, B. Bang, H. Sasaki, *Geophys. Res. Lett.* **32**, L12607 (2005).
- [4] A.M Treguier et al., *J. Phys. Ocean.* **33**, 580–599 (2003).



- [5] K. Richards et al., *Geophys. Res. Lett.* **33**, L03605 (2006).
- [6] M. Baldwin et al., *Science* **315**, 467-468 (2007).
- [7] R.W. Schmitt, *Oceanus* **39**:2, inside cover (1996).

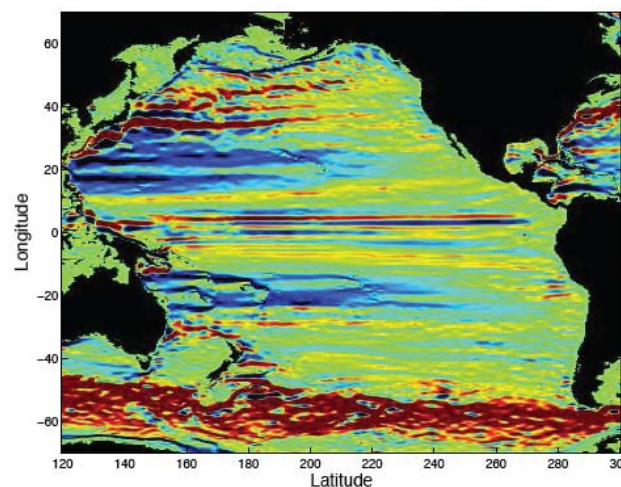


*Fig. 3. Computational and observational evidence for alternating zonal jets in the world oceans have emerged in the past few years. For example, in this figure from [5], showing zonal velocity at 400 m, alternating zonal jets are evident in the Pacific. This study used POP, developed at LANL (<http://climate.lanl.gov>), and is forced by unsteady winds and buoyancy. Simplified process studies as in Fig. 2 help us better understand the dynamics and importance of such jets.*

*Fig. 2. In an idealized setting of the wind-driven circulation, broad, sweeping flow in the interiors accompanied by swift return western boundary currents are expected (as on the left). Instability of such a circulation gives rise to mesoscale eddies (as seen in the western central region in the picture on the right). But we find for the first time that even with steady and large-scale winds alone, distinct multiple zonal jets—jets that are narrow in the latitudinal direction and elongated in the zonal direction—can appear (as in the picture on the right). In these pictures, the baroclinic stream function is colorcoded—the domain is a mid-latitude ocean basin forced by steady double-gyre wind forcing. The x-axis points eastward and the y-axis points northward.*

### Funding

#### Acknowledgments

DOE, Office of Biological and Environmental Research Climate Change Prediction Program

## Ice Sheet Modeling for the Prediction of Sea Level Rise

Stephen Price, William Lipscomb, Todd Ringler, John Dukowicz, T-3; Antony Payne, Bristol Glaciology Centre, University of Bristol, Bristol, UK

The Antarctic and Greenland ice sheets are losing mass at rates that contribute a total of  $\sim 0.35 \text{ mm a}^{-1}$  to global sea level rise [1]. This contribution is expected to increase in the future but, as noted in the recent IPCC report [2], current ice sheet models are too crude, in their representation of both ice sheet dynamics and fundamental physical processes, to provide a best estimate, or even an upper bound, for 21st century sea level rise due to changes occurring on ice sheets. At the same time, observations and modeling indicate that atmospheric and oceanic forcing are responsible for mass loss on both the Greenland and Antarctic ice sheets [3,4]. Coupling of ice sheet models and other climate model components will be necessary in order to make accurate predictions of future sea level rise.

The Climate Ocean and Sea Ice Modeling (COSIM) project has recently begun building an ice sheet model with improved dynamics and physics. The initial model is based on the model of Payne and Price [5,6], which includes an improved treatment of dynamics and physics. Advances to this model will follow from a new formulation [7] that will ultimately allow for efficient large-scale, high-resolution simulations on massively parallel architectures. The model will be coupled to COSIM's existing world-class sea ice and ocean circulation models to investigate a wide range of possible feedbacks among these climate components.

The model is currently being used to estimate how ocean-forced perturbations at the calving fronts of Greenland's outlet glaciers [3] translate to mass loss within the larger ice sheet (Fig. 1). We are also working on coupled ice sheet and ocean circulation experiments as part of the new

DOE Investigation of the Magnitudes and Probabilities of Abrupt Climate Transitions (IMPACTS) initiative. These experiments will assess the likelihood that intrusions of warm seawater beneath ice shelves could trigger rapid retreat of the West Antarctic ice sheet during the next several decades.

**For further information contact Stephen Price at [sprice@lanl.gov](mailto:sprice@lanl.gov).**

- [1] A. Shepherd, D. Wingham, *Science* **315**, 1529-1532 (2007).
- [2] S. Solomon et al., *Climate change 2007: the physical science basis*, Cambridge University Press (2007).
- [3] D.M. Holland et al., *Nature Geosc.* **1**, 659-664 (2008).
- [4] M. Thoma et al., *Geophys. Res. Lett.* **35**, doi:10.1029/2008GL034939 (2008).
- [5] A.J. Payne, S.F. Price, "A three-dimensional, first-order model of ice flow." In preparation.
- [6] S.F. Price, A.J. Payne, A.J. Shepherd, *EOS Trans. AGU* **88(52)**, Fall Meet. Suppl., Abstract C43A-06 (2007).
- [7] J.K. Dukowicz, S.F. Price, W.H. Lipscomb, "Consistent Approximations for Ice Sheet Dynamics from a Principle of Least Action." In preparation.

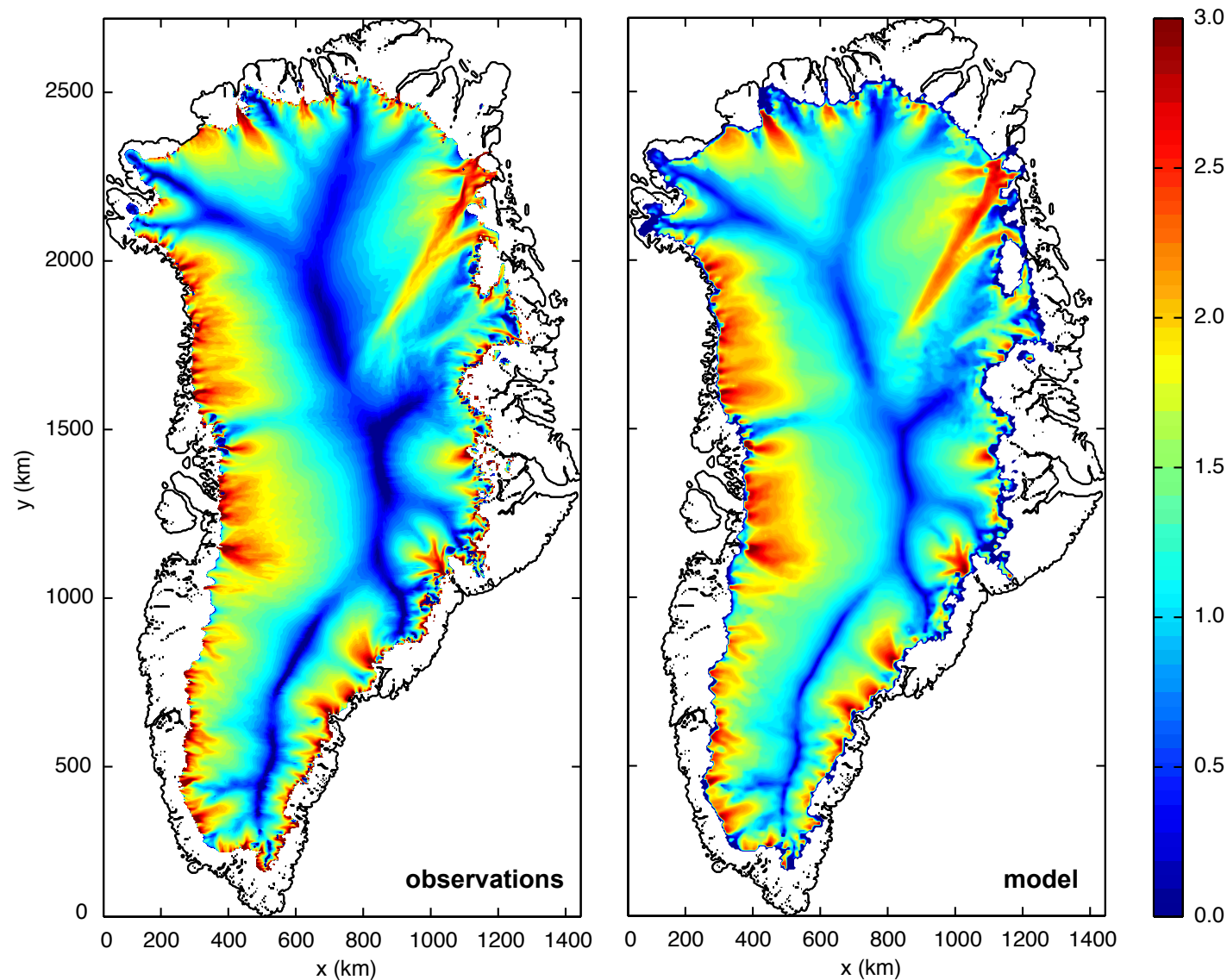


*Fig. 1. Steady-state velocity field (log 10 scale) for the Greenland ice sheet based on modern-day observations of geometry and surface mass balance (left panel), and modeled velocity field with basal sliding tuned to match the velocity field inferred from observations (right panel). The model results are being used as initial and boundary conditions for high-resolution experiments to examine the susceptibility of particular outlet glaciers to dynamic mass loss induced by perturbations at their marine calving fronts.*

#### **Funding**

#### **Acknowledgments**

- DOE, Office of Biological and Environmental Research Climate Change Prediction Program
- DOE, Office of Science, Scientific Discovery through Advanced Computing Program
- LANL Postdoctoral Fellowship Program



## Modal Variability of the Southern Ocean

Wilbert Weijer, CCS-2

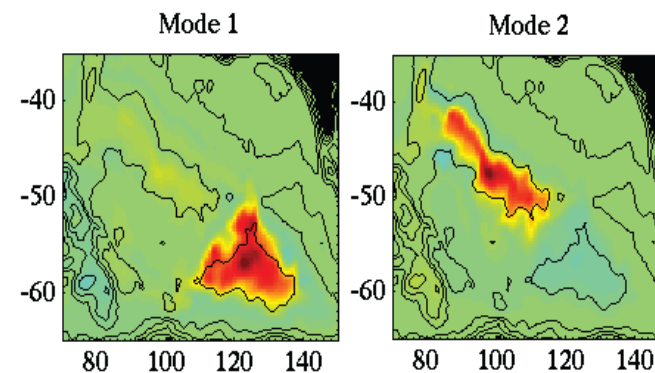
Wind stress is one of the main forces driving the ocean circulation. The ocean responds to synoptic variability of the atmosphere by generating so-called barotropic flows—these motions reach all the way to the ocean floor, and are not influenced by the density stratification of the ocean. The resulting currents are hence strongly steered by the topography of the ocean floor. In fact, currents do not like to flow across isobaths, since the resulting stretching or squeezing of the water column requires a change in a quantity called vorticity (the continuum-mechanical equivalent of angular momentum). This gives special significance to a few basins where isobaths (or more precisely, contours of potential vorticity  $H/f$ , where  $f$  is twice the local rotation rate of the Earth and  $H$  is ocean depth) are closed onto themselves. These areas can often be identified using altimeters (satellite-borne instruments that measure sea-surface height from space), since the circulation is particularly energetic. Examples are the Argentine Basin, the Mascarene Basin, and the Australia-Antarctic Basin, an abyssal plain in the Indian sector of the Southern Ocean.

An appropriate way to describe the circulation in these basins is in terms of modes. Modes are specific circulation patterns that retain their spatial coherence when evolving in time. A category of modal circulation patterns is flows along contours of  $H/f$ . These motions are, in a sense, balanced: once such a flow is generated (excited) by wind stress, it decays only slowly under the influence of frictional processes. Information about modal decay can help us to constrain the energy pathways in the ocean—work done by the winds is the most important energy source for the ocean, and an important part will be used to mix water masses and drive the global overturning circulation (see Fig. 1). A few studies have hypothesized that enhanced variability

in the Australia-Antarctic Basin can be explained by the excitation of modes. However, their estimates of the decay time scale suggested that these modes decay in only a few days, apparently at odds with a slow, frictional spin-down mechanism. In a recent paper [1] we addressed this discrepancy, using a combination of theory, numerical modeling, and observations. First, we calculated the normal modes in a numerical model of the Southern Ocean to show that the observed enhanced variability is indeed consistent with the excitation of barotropic modes (Fig. 1). Then, by projecting these modes on altimeter data, we confirmed their apparent rapid decay. Subsequent numerical analysis revealed the reason for this: arbitrary circulation patterns, like those generated continuously by the synoptic atmospheric variability, have only a small projection onto the actual mode—the remainder can be considered unbalanced flow. The apparent rapid decay reflects the disintegration of the unbalanced flow only—it can take a week for the unbalanced flow to die out and reveal the decay of the balanced, modal circulation. Since altimeter data seems to be unsuitable for estimating the mixing efficiency, we have to rely on field programs (involving current meter moorings) to provide us with the appropriate data.

Another category of modes is characterized by oscillatory motions, and is equivalent to so-called planetary basin modes. These modes can be described as a superposition of planetary waves and their reflections in a closed basin. However,

*Fig. 1. The two dominant topographically trapped modes of the Australia-Antarctic Basin. Shown are their expressions in sea-surface height. The associated circulation is in the anticlockwise sense around these high-pressure areas. Their natural decay time scale is of the order of 3 weeks.*





## Climate Modeling

unequivocal observations of such modes were absent until a very energetic, bimonthly oscillation was found in the Mascarene Basin. Weijer [2] showed that this oscillation is indeed consistent with the excitation of a planetary basin mode. However, the application of classical theory is indeed challenging when the bathymetry is more complicated. Case in point is the Argentine Basin, an abyssal plain with a pronounced seamount (Zapiola Rise) in its center. Previous observations indicated the presence of very energetic oscillations, but estimates of the dominant periodicity ranged from 19 to 28 days. Weijer et al. [3] predicted that the Argentine Basin could house no fewer than four distinct modes, with periods between 19 and 32 days. The spatial patterns of these modes are rather spectacular, as they consist of dipoles in sea-surface height that rotate (in 3 to 4 weeks time) around Zapiola Rise (Fig. 2). By projecting the modes (obtained as eigenmodes from the model) onto altimeter data, we were able to show that each of these modes becomes excited in the Argentine Basin. It took a complicated exercise to show that these rotating modes are indeed equivalent to the planetary basin modes of classical theory[4].

**For further information contact Wilbert Weijer at [wilbert@lanl.gov](mailto:wilbert@lanl.gov).**

- [1] W. Weijer, S.T. Gille, F. Vivier, "Modal decay in the Australia-Antarctic Basin." Submitted to *J. Phys. Ocean.* (2009).
- [2] W. Weijer, *Deep-Sea Res. I* **55**, 128-136 (2008).
- [3] W. Weijer et al., *J. Phys. Ocean* **37**, 2855-2868 (2007).
- [4] W. Weijer et al., *J. Phys. Ocean* **37**, 2869-2881 (2007).

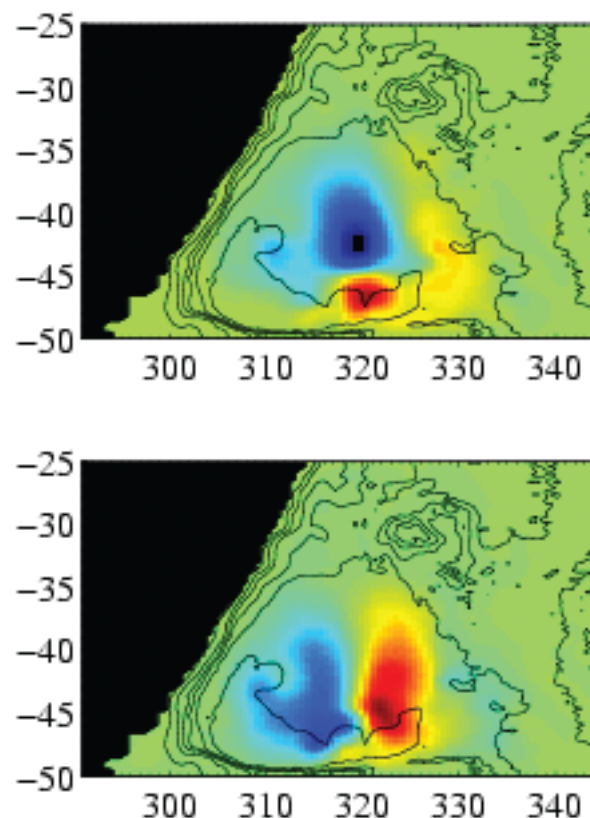


*Fig. 2. The dominant oscillatory mode of the Argentine Basin, as expressed in sea-surface height (SSH). The plots show two subsequent phases of an oscillatory cycle, and clearly suggest rotation of the lobes of high (red) and low (blue) sea level around Zapiola Rise. The Argentine Basin is bounded in the west by the South American continent, in the south by the Falkland Escarpment, in the east by the mid-Atlantic ridge, and in the north by the Rio Grande Rise. Depth is indicated by contours at 1000-m increments. The cycle completes in about a month.*

### Funding

#### Acknowledgments

DOE, Office of  
Biological and  
Environmental Research  
Climate Change  
Prediction Program





# Information Science and Technology

Information Science and Technology is a newly emerging discipline, forged from the juxtaposition of the ubiquitous nature of enormous amounts of heterogeneous data and the computer science, mathematical, and technological tools with which to extract insight from such data. LANL research and outreach activities are helping to shape this new discipline as a powerful tool for science, and point the way to the creation of new technologies for future applications.

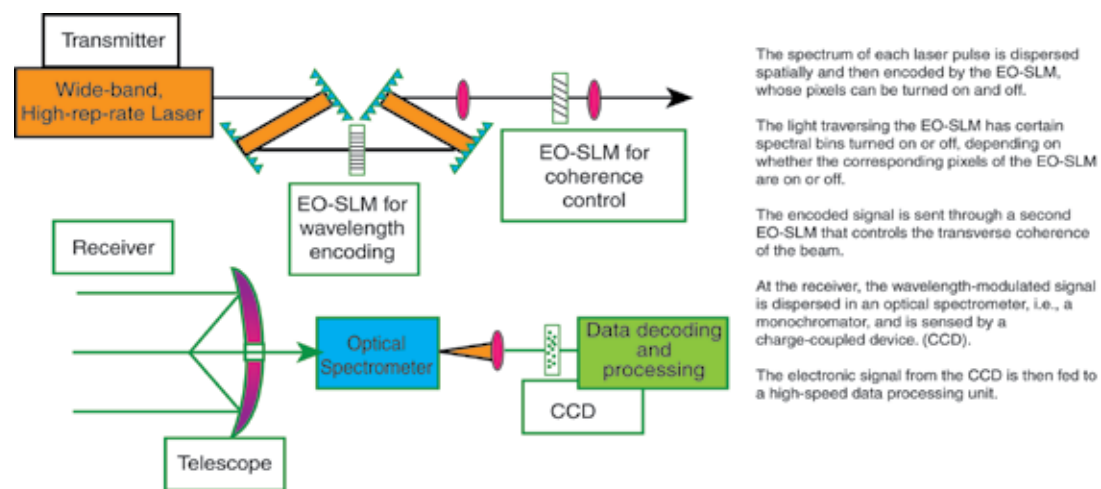
Papers in this section discuss recent advances in the creation of a new high-speed optical communication system, the study of cellulose stability for biofuels, new discoveries affecting the design of new neural networks, and new tools for the derivation of knowledge from heterogeneous digital sources.

# High Data-rate, Free-space Laser Communication Based on Frequency Encoding of a Partially Coherent Beam

Gennady Berman, Boris Chernobrod, T-4; Alan R. Bishop, ADTSC

In this paper we present a new concept of a free-space, high-speed optical communication (FSOC) system based on spectral encoding of radiation from a broadband, pulsed laser. It is known that the intensity fluctuations of a partially coherent beam in combination with a time-averaging photodetector lead to a significant scintillation reduction with the corresponding improvement of the bit error rate (BER) by several orders of magnitude. Unfortunately, the time-averaging method cannot be applied directly to gigabit data rate communication. The main limitation of this method is related to the requirement that the correlation time between different spatially coherent spots be shorter than the response time of the photodetector. We propose to extend the technique of scintillation suppression, based on time averaging of a partially coherent beam, to gigabit data rate FSOC. In our approach, information is encoded in the form of amplitude modulation of the spectral components of

*Fig. 1. The concept of spectral encoding of a partially coherent beam (PCB). Shown below is a schematic of the wide-band free space laser communication with wavelength encoding.*



the laser pulse, which has a broad spectrum. To examine the intensity fluctuations of a partially coherent beam under the conditions of strong turbulence, we developed an asymptotic method for solution of the kinetic equation for the photon distribution function. We show that, for long distances, scintillations and beam wandering can be significantly suppressed.

FSOC has data rate limitations due to atmospheric turbulence. Laser beams experience three major effects under the influence of turbulence. First, the beam phase front is distorted by fluctuations in the refractive index, causing intensity fluctuations or scintillations. Second, eddies whose size is greater than the beam diameter randomly deflect the laser beam as a whole—this phenomenon is called beam wandering. Third, propagation through turbulent atmosphere causes the laser beam to spread more than predicted by diffraction theory. Scintillations are the most severe problem and result in a significant increase of the BER and consequent degradation of the laser communication system performance. For example, a gigabit data rate communication channel cannot operate with BER of  $10^{-9}$  over distances more than 2.5 Km, even for clear weather. Several approaches have been developed to mitigate the effects of turbulence on laser communication, including aperture averaging, partially coherent beams, adaptive optics, and array receivers. Nevertheless, scintillations continue to limit the performance of FSOC, and new approaches are needed to overcome this limitation. It is well known that partially coherent beams (beams with multiple coherent spots in their transverse section) are less affected during propagation through atmospheric turbulence than a fully coherent beam. Specifically, the additional beam spreading due to the atmospheric turbulence, the beam quality degradation, and the scintillation index are less pronounced for a partially coherent beam compared with a fully coherent beam. Recently we demonstrated the techniques of scintillation reduction based on the utilization of partially coherent beams. To form partial coherence, scientists were using a static phase diffuser. In their approach, a combination of partially coherent beams with time-averaging leads to a significant scintillation reduction with the corresponding



improvement of the BER by several orders of magnitude. Another possibility is related to utilization of a spatial light modulator (SLM). The main advantage of SLM compared with a rotating phase diffuser is that the random phase distribution at the transmitter plane could change at higher rates. As we show, higher SLM frame rate corresponds to higher data rate of the communication channel. In previous research an alternative approach was proposed that uses multiple beams with different wavelengths. This approach was experimentally demonstrated using a multiemitter beam, constructed by spatially combining outputs of several single-mode fiber-coupled diode lasers. It was shown theoretically and experimentally that the scintillation index can be substantially reduced if individual beams overlap at the detector aperture and are properly separated at the transmitter plane. At the same time, the time-averaging method cannot be applied directly to gigabit rate communication. The main limitation of the time-averaging method is related to the requirement that the correlation time between different spatially coherent spots be shorter than the response time of the photodetector. This means that the SLM must have an operating frequency,  $\nu$ , that is higher than the bandwidth of the photodetector, corresponding to its inverse response time  $\nu \gg T^{-1}$ . Since the photodetector bandwidth must be higher than the data rate of the communication channel  $\nu_{\text{com}}$ ,  $T^{-1} \gg \nu_{\text{com}}$ , the highest data rate is limited by the highest frequency of SLM,  $\nu \gg \nu_{\text{com}}$ . To date, the highest frequency SLMs based on multiple quantum wells (MQW) can only operate at frequencies up to tens of MHz.

We propose to extend the technique of scintillation suppression, based on time averaging of a partially coherent beam (TAPCB), to gigabit rate FSOC. Our idea is to combine TAPCB with a spectral encoding technique. Originally, spectral encoding was applied to fiber optics communication for code-division-multiple-access. In this method, information is encoded in the form of amplitude modulation of the spectral components of the laser pulse, which has a broad spectrum. For long-distance communication, the broad-spectrum light source could be a Ti:sapphire laser. For short-distance communication it could be an LED as

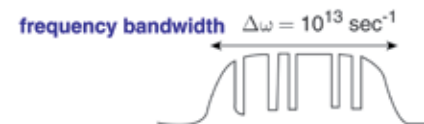
well. Each pulse or sequence of pulses (depending on the averaging response time of the photosensor) can contain kilobits of data. If the pulse repetition rate is about 1 MHz, then the transmitted data rate is gigabits per second. SLMs based on MQW technology with a frame rate of several MHz are now available.

**For further information contact Gennady Berman at [gpb@lanl.gov](mailto:gpb@lanl.gov).**

- G.P. Berman, A.A. Chumak, *Phys. Rev. A* **74**, 13805 (2006).  
 G.P. Berman et al., *Optics Commun.* **280**, 264-270 (2007).  
 G.P. Berman et al., A.R. Bishop, D.C. Nguyen, B.M. Chernobrod, V.N. Gorshkov, Inventors, "System and method that suppresses intensity fluctuations for free space high-speed optical communication." LANL provisional patent application S-109, 082.  
 G.P. Berman, A.A. Chumak, *Quantum Communications and Quantum Imaging V*, edited by Ronald E. Meyers, Yanhua Shih, Keith S. Deacon, *Proc. of SPIE* **6710**, 67100M (2007).  
 G.P. Berman, A.A. Chumak, V.N. Gorshkov, *Phys. Rev. E* **76**, 056606 (2007).  
 G.P. Berman et al., Invited talk: "Suppression of scintillations and beam wandering in free space gigabit rate optical communication based on spectral encoding of a partially coherent beam." SPIE Photonics West, January 24-29 (2009).

**1) PCB reduces the scintillations**  
 (but requires some time for averaging ~ 1 ms)  
 One cannot see a time domain for encoding the information!

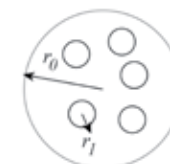
**2) Spectral encoding provides high bit rate**



Pulse duration ~  $10^{-10}$ s  
 Pulse repetition rate ~ 30 MHz  
 Encoding density ~  $10^3$  bit per pulse  
 Frame rate of the encoding spatial light modulator 10 MHz  
 Bit rate ~ 1 Gb/s  
 $r_0$  = beam radius  
 $r_l$  = coherence radius  
 $I$  = intensity of laser beam

**Scintillation index**

$$\sigma = \frac{\langle I^2 \rangle - \langle I \rangle^2}{\langle I \rangle^2}$$



**Parameters (example):**  
 $r_0 \sim 5 \text{ cm}$ ,  $r_l \sim 0.1 \text{ cm}$   
 $L \sim 10 \text{ km}$

*Fig. 2. Schematic of the wide-band free space laser communication with wavelength encoding.*

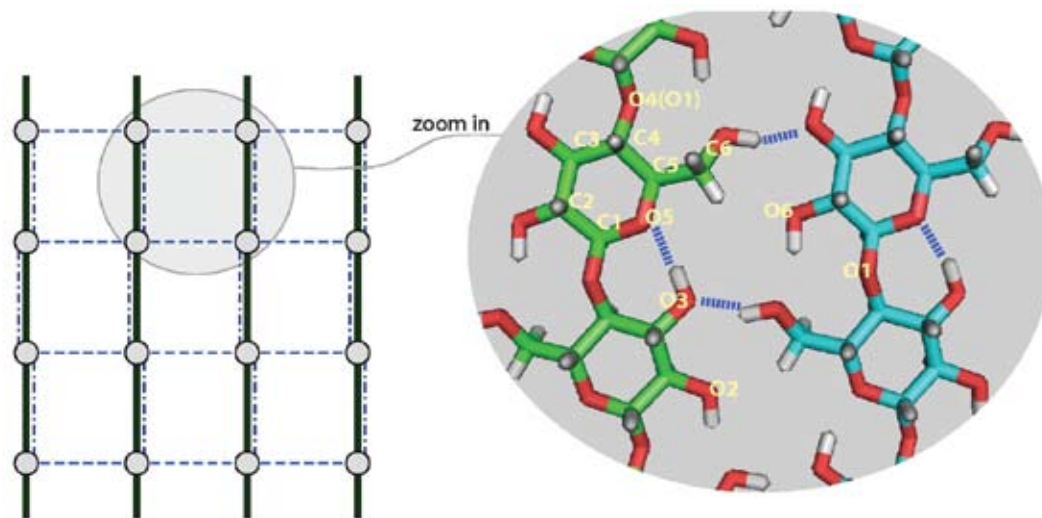
**Funding Acknowledgments**  
 Office of Naval Research

# The Stability of Cellulose: A Perspective from the Statistical Mechanics of Hydrogen Bond Networks

Tongye Shen, CNLS and T-6; S. Gnanakaran, T-6

*Fig. 1. An illustration of the sheet structure of cellulose I- $\beta$ . Cellulose chains (solid vertical rods) are linear collections of monomers (filled circles), which can be potentially linked using H-bonds residing in intrachain (vertical, dot-dashed lines) and interchain positions (horizontal, dashed lines).*

Biofuels derived from lignocellulosic biomass offer a cleaner and sustainable alternative to fossil fuels, with several advantages over ethanol derived from corn and sugarcane. Challenges encountered during the conversion of biomass to ethanol are critically linked to the uncertainties of the physical properties of the feedstock. In particular, a better understanding of cellulose and its biodegradation will allow one to address the factors preventing an efficient fuel economy based on cellulosic biomass conversion. A central problem is how cellulose, an assembly of polymers of glucose, can be effectively isolated and disassembled to its basic building block, glucose. The underlying stability of cellulose comes from the dense hydrogen bonding (H-bond) network constructed among the crystalline-ordered polysaccharide chains. We have performed computations both at the atomistic and coarse-grained level to investigate the thermal responses of various H-bonding networks of cellulose. Here



we describe the results from coarse-grained computations of H-bonding in cellulose I- $\beta$ , the main form of cellulose found in plants.

We constructed a statistical mechanical model at the resolution of explicit H-bonds that takes into account both intrachain and interchain H-bonds in naturally occurring cellulose crystals. As shown in Fig.1, the stability of a sheet of chains in I- $\beta$  is considered using a statistical description of H-bonding networks on a square lattice. The partition function and subsequent statistical properties of this lattice were calculated using the transfer matrix method. This theoretical model describes the state of the system as a collection of discrete representations of the state of each potential H-bonding position, i.e., each type of H-bond is either formed or not formed at a position. In such a binary description, when a bond is formed we associate it with a gain in bonding energy. Similarly, a gain in entropy is assigned when H-bonds are absent for a particular bonding position. The specific gain in entropy also depends on its neighboring states. Finally, we can associate each particular state of the hydrogen bond network with a statistical weight based on its free energy. A major simplification that makes the evaluation of the partition function of this lattice model solvable is that consideration is limited to “native” H-bonds.

Our calculations suggest that such plasticity of an H-bonding network (owing to frustration and seeming redundancy of the H-bonding elements) keeps the overall H-bonding stability persistent over a wide range of temperatures. An interesting and unique feature of this assembly is the multiple possibilities of H-bonding patterns within a single, stable structure of the cellulose. Instead of only one stable pattern, different H-bonding patterns dominate at different temperatures until the disassembly occurs at very high temperatures. As shown in Fig. 2., intrachain H-bonding is more stable than the interchain bonding throughout the temperature range that is considered. This model is able to capture important equilibrium properties at the resolution of individual bonds (see Fig. 3). Specifically, we found that intrachain H-bond O3 H3  $\cdots$  O5 is always stable until disassembly. Intrachain H-bond O2 H2  $\cdots$  O6, and

interchain H-bonds  $O6\ H6 \cdots O3$  and  $O6\ H6 \cdots O2$ , are stable at low temperature. However, with increasing temperature, the H-bonding network undergoes a switch in the connectivity of H-bonds. A role exchange between donor and receptor for the two hydroxyl groups  $O6\ H6$  and  $O2\ H2$  is observed. As a result, H-bond  $O2\ H2 \cdots O6$  switches off as an intrachain H-bond and shows up as an interchain H-bond. These computations may provide useful clues on rational design for the efficient degradation of cellulose.

**For further information contact S. Gnanakaran at [gnana@lanl.gov](mailto:gnana@lanl.gov).**

## References

T. Shen, S. Gnanakaran, *Biophys.J.*, April issue vol. 96, in press (2009).

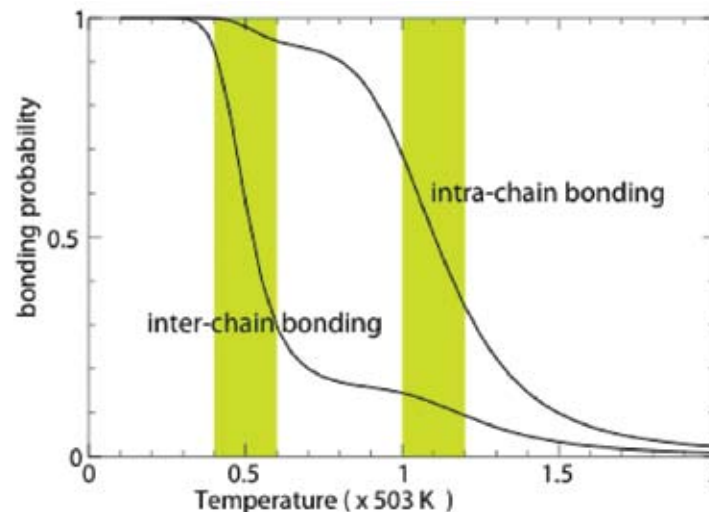


*Fig. 2. The intrachain and interchain H-bonding probabilities are shown as a function of temperature.*

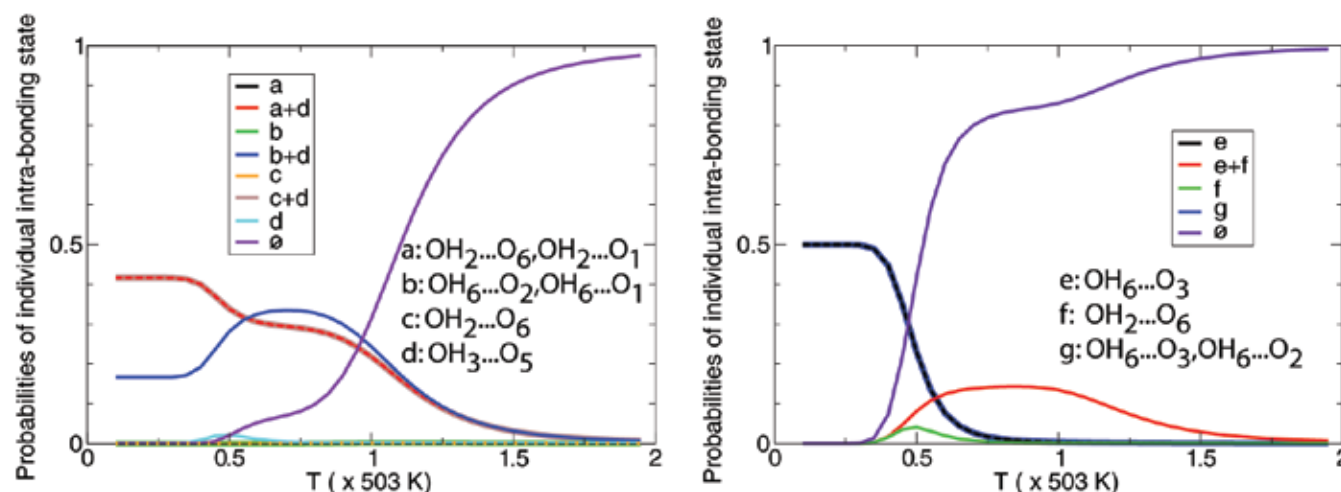


*Fig. 3. The probabilities of individual states (different colors) of intrachain H-bonding (left) and interchain H-bonding (right) are shown as a function of temperature.*

## Funding

## Acknowledgments

LANL Directed Research and Development Program



## Uncovering Computational Primitives that Endow Neural Networks with their Information Processing Abilities

Ilya Nemenman, CCS-3; Geoffrey Lewen, Hun High School, Princeton, NJ;  
Rob de Ruyter van Steveninck, Indiana University; William Bialek, Princeton University

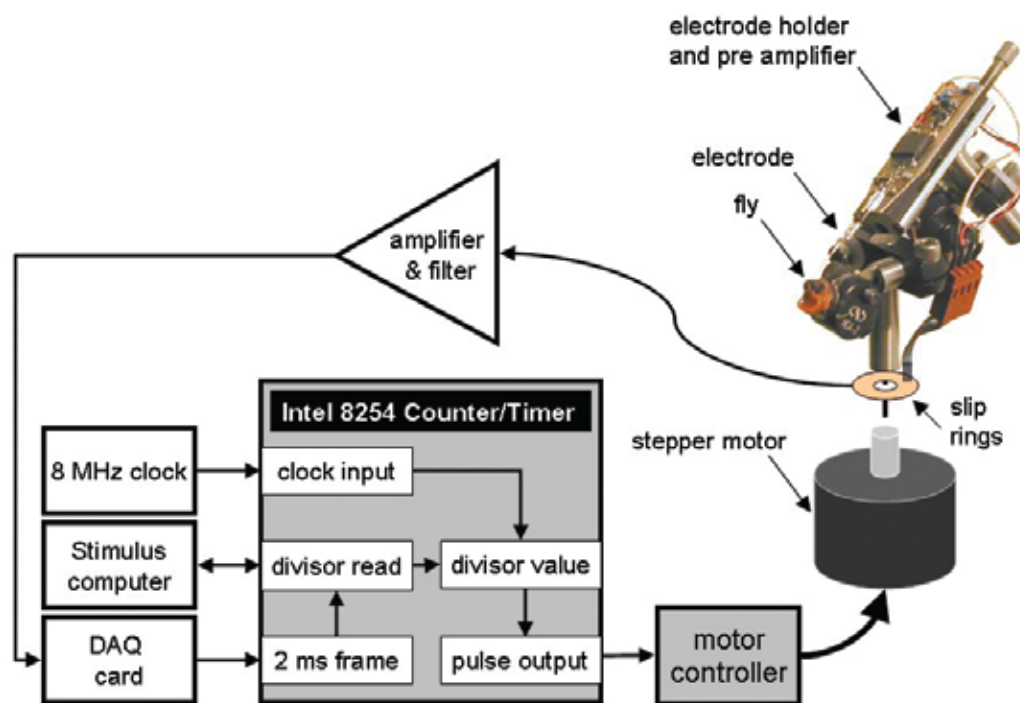
*Fig. 1. A schematic of the experimental setup: a fly was immobilized with wax, its body in a plastic tube, with its head protruding. Through a small hole in the back of the head an electrode was inserted to record extracellular potentials from a specific neuron (called H1), a wide-field neuron sensitive to horizontal motion. This signal was amplified, fed through a slip-ring system to a second-stage amplifier and filter, and recorded by a data acquisition card. The signals were recorded in response to rotation of the whole setup around the vertical axis on a stepper motor. The angular velocity signal supplied by the motor was, in its turn, extracted from movies of flight behavior of real free-flying flies.*

Which computational primitives endow animal brains with their information-processing abilities, abilities that far exceed those of even the best modern computers? Answering this question would drastically change every facet of the society we live in, allowing the design of computers that are able to analyze satellite images and other intelligence data, recognize human faces, drive cars in urban centers, and help solve other national and global security problems.

Since the work of Emil du Bois-Reymond in 1848 and a series of discoveries by Santiago Ramón y Cajal (Nobel Prize in Physiology, 1906), it has been known that animal brains derive their powers from networks of interacting neurons of different types, which communicate with each other using stereotyped impulses, called action potentials or spikes. However, most experiments, going back to E. D. Adrian and Yngve Zotterman (1926) [1], seemed to suggest that the precise times of occurrence of these spikes matter little, and only the number of spikes over long

time intervals (up to 100 ms or more) is used by neurons to encode their messages. This result has influenced the design of artificial neural networks, which, starting with the Perceptron [2], has neglected precise spike timing in favor of what has become known as the rate coding hypothesis [3].

However, such artificial neural networks have largely failed to deliver human-like cognitive performance. It has been suggested that one of the reasons behind this failure is the neglect of precise spike timing. A series of experiments by different scientists, summarized in [2], has shown that timing down to about 2 ms may be important for neuronal communication in visual information processing, supporting the argument. However, the duration of a single spike and the minimum distance between two successive spikes in real



neurons is smaller than that. Could it be that animals use the spike timing to even higher precision, but the experiments have failed to see this usage?

In a 2008 article [4] the LANL-led team has explored the possibility that, when put in a natural environment (compared with earlier experiments done in a laboratory) with rich, dynamic, interesting stimuli, animals use spike timing with a precision down to a fraction of a millisecond. We used microelectrodes to record from the motion-sensitive neurons in the visual system of a common blowfly. To ensure that the fly's experiences were close to those in free flight, we immobilized the animal in an elaborate turntable-like mechanism, which was rotated to mimic the fly's natural acrobatic flight and was placed outdoors in the fly's natural environment (see Fig. 1).

We viewed the recording from the visual neuron as one would view a digital communication stream. We have explored how much information, in bits, is available in this stream when the position of each spike is known to a different accuracy. Data analysis for this experiment was even more difficult than the experiment itself: it took six years and required development of conceptually new statistical tools. When all the dust settled, we found that precise spike timing is important down to a resolution of 0.2-0.3 ms, an order of magnitude more precise than previous estimates in the literature (see Fig. 2). That is, neurons communicating with each other use precise spike timing to encode their messages, and this precision can be seen by observing that the information content of a spike train is higher if spike positions are known to a higher precision.

Such temporal accuracy is very far from Adrian's rate-coding theory, and it re-examines fundamental assumptions that became the basis of computational neuroscience and neuromimetic approaches to artificial intelligence. It is now clear that next-generation neural networks must consider precise spike timing as the mode of communication between their neurons as a very important computational primitive. Correspondingly, a new LANL Directed Research project

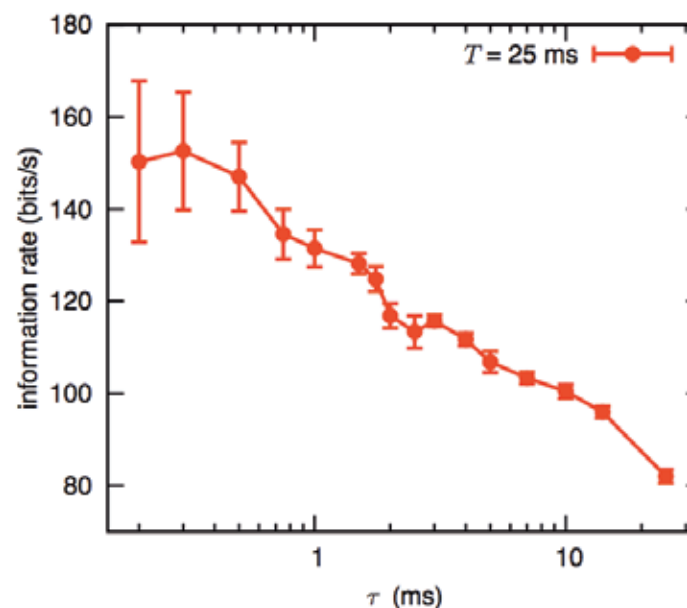


*Fig. 2. The information content of the spike train as a function of time resolution  $t$ . The information is measured in “words” of duration of 25 ms, which corresponds to the fly’s behavioral time scale. We plot this as a rate, in bits per second. Notice that the rate increases as the accuracy of spike-timing resolution increases.*

started in FY09 will do just that, aiming at building the world-leading neuromimetic visual data processing platform based, in part, on proper incorporation of spiking into neuronal communications.

**For further information contact Ilya Nemenman at [nemenman@lanl.gov](mailto:nemenman@lanl.gov).**

- [1] E.D. Adrian, Y. Zotterman, *J. Physiol.* (London) (1926).
- [2] F. Rosenblatt, *Cornell Aeronautical Laboratory, Psychological Review* **65**(6), 386-408 (1958).
- [3] F. Rieke et al., *Spikes: Exploring the neural code*. MIT Press (1997).
- [4] I. Nemenman et al., *PLoS Comput Biol* **4**(3), e1000025 (2008).

### Funding Acknowledgments

LANL Directed Research and Development Program

## Derivation of Knowledge from Digital Content

A. Shelly Spearing, Jorge H. Román, HPC-1; M. Linn Collins, STBPO-RL

As electronic content proliferates, it becomes nearly impossible to fully consume and assess all of the available information. Over the past 7 years, LANL's Digital Knowledge Factory (DKF) has created a suite of digital-content-analysis tools. This combination of commercial off the shelf (COTS), Open Source, and homegrown code is used to gather, reduce, annotate, organize, synthesize, and visualize digital content for human consumption.

The tools can be applied to collections of text-based documents from virtually any source. The algorithms go beyond traditional natural language processing and statistical analysis—word-location algorithms automatically extract the gist of the content, while others annotate targeted concepts, organize documents, and calculate goodness-of-fit with respect to a specified conceptual area. Additional modules extract features, such as dates and locations, and group documents for comparative analyses. In some cases we are also able to compute the trustworthiness and/or mood of the author. When looking at larger collections, we categorize subject-matter expertise, emerging and fading trends, and distill entire collections into a variety of single-page graphical representations.

Structured information (i.e., metadata) can augment the digital knowledge to facilitate analyses of time trends, geographical colocation, and authorship, among others. Through information reduction, annotation, fusion, and organization, the analyst is able to assimilate content and form hypotheses more quickly.

A goal of the DKF project is to expedite knowledge assimilation by synthesizing digital content into a

set of knowledge visualization schemes. In particular, it is hoped that an information consumer can look first at a few graphical representations of the concepts contained within thousands of pages of text, draw conclusions about the documents in aggregate, formulate hypotheses, and then focus attention on the particular documents that are relevant to the conclusions and hypotheses. Through a reduction process we focus the analyst on the important concepts and the relationships among them.

A first step in trend identification is depicted in Fig. 1, a timeline summary of 475 documents containing “Iraq” that were extracted from the White House Press Archive website. DKF tools were used to identify the top-level concepts

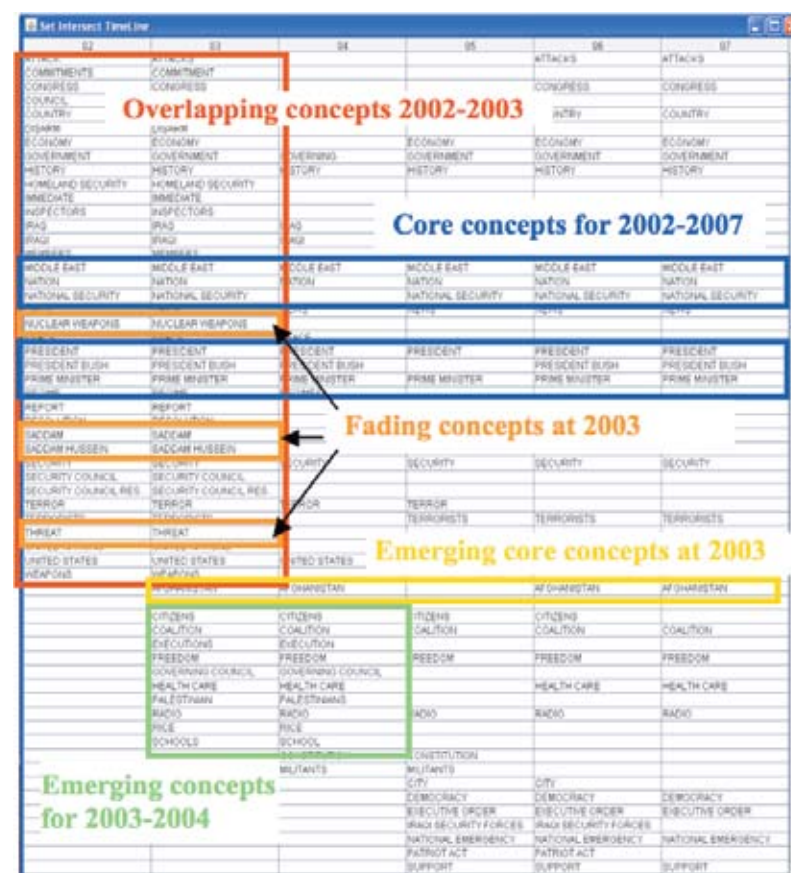
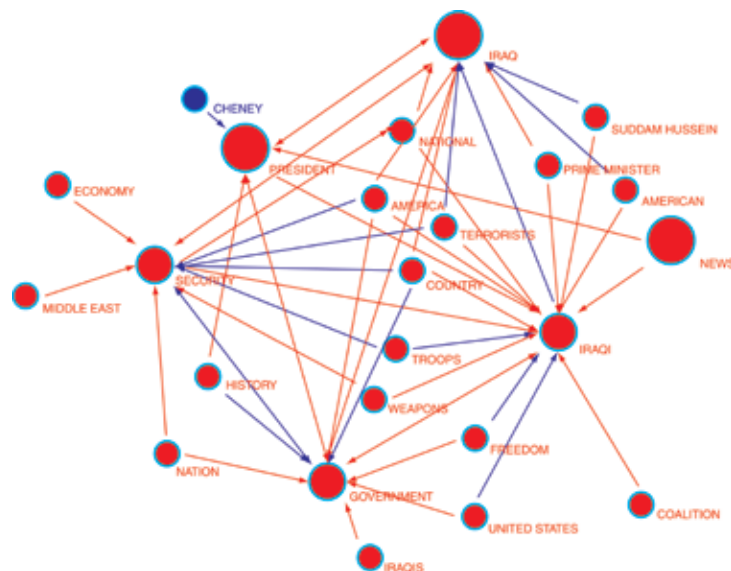


Fig. 1. Timeline summary (right) of 475 documents.





of each document, aggregate those concepts by year, and compare each year's important topics with those of other years. Overlapping concepts are those that appear in two or more consecutive years, although when they are found in all or most of the time intervals, they are considered "core" to the collection. Fading concepts are present for a few years at the beginning but not at the end of a time sequence, while emerging concepts do the opposite. In this particular example, the reader may observe that "Nuclear Weapons," "Saddam Hussein," and "Threat" were frequently found as key themes in the 2002-2003 timeframe, but not afterward. In their place, we see the emergence of "Afghanistan."

Figure 2 depicts a knowledge network representation of the same 475 speeches. In this case, secondary, or supporting, concepts are considered in relationship to the concepts they support. Top-level concepts and relationships are shown in red, second-level concepts and relationships are shown in blue. Node size and edge thickness represent frequency within this set, and direction of edge (arrows) signifies a concept relationship. Tertiary concepts and low-frequency concepts and relationships are omitted here, but can be explored using interactive tools. In the network depicted

above, "President," "News," and "Iraq" are revealed as the most important concepts. The concept "nation" is supported by the concepts "government" and "security," meaning that these concepts are often found in close proximity (i.e., within the same sentence or paragraph) in speeches. "Security" is a supporting concept for many others, as depicted by the numerous edges flowing into "Security."

Through the use of these two representations, someone totally unfamiliar with world politics might quickly conclude that the source of the data is newsfeed somehow involving the President, Iraq, and national security and that, over time, the news shifted away from weapons and to Afghanistan. In other, potentially less politically prominent, contexts, the DKF tools can be used to quickly highlight changes that might warrant further human interrogation. Beyond the collection-level analysis techniques illustrated here, some other capabilities of the DKF tool suite include the targeting of specific concepts of interest and the generation of "drill down" versions of individual documents in which key and/or targeted concepts are hyperlinked and colorcoded.

The process is automated and interactive, allowing analysts to quickly focus on topics of interest in a particular set or subset of documents. DKF tools provide Knowledge Discovery capabilities out of the box, and these capabilities can be enhanced through the use of ontologies and other context-aware knowledge. Currently, we have a set of working prototypes and expect to field some of these tools to other government agencies. Our current work has focused on developing working instances of digital knowledge management (DKM) operations of the first-, second-, and third-order. We envision many more DKM operations, as these are only the core operations.

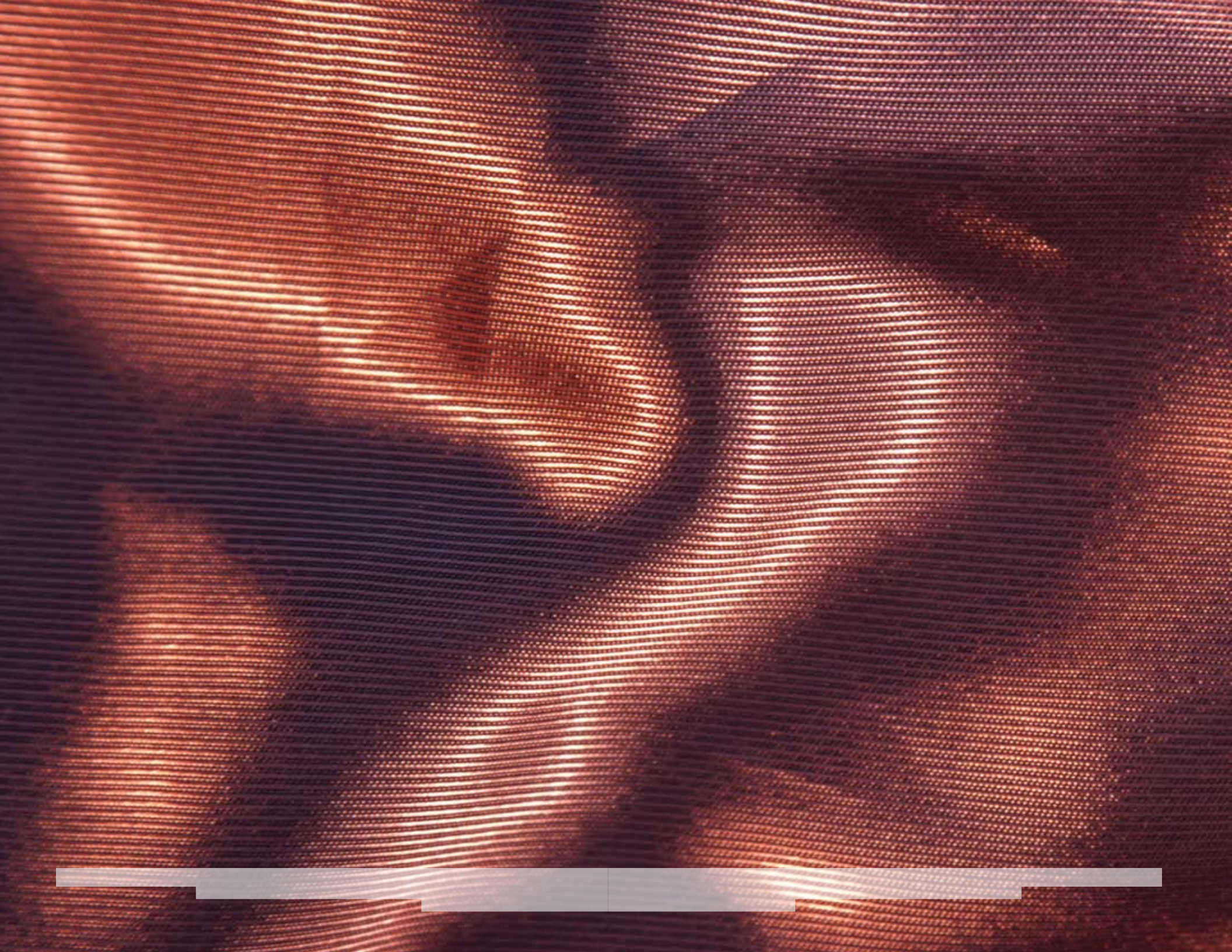
**For further information contact Shelly Spearing at [shellys@lanl.gov](mailto:shellys@lanl.gov).**

*Fig. 2. Knowledge network (left) of the 475 documents in Fig. 1.*

#### **Funding Acknowledgments**

- LANL Research Library, Emergency Situation Overview and Synthesis
- Various other programs







# Materials Science

The properties of materials and their phase transitions at macro and microscopic levels are explored in the articles in this section. At the fundamental level, materials lie at the heart of much of what we do for the Nation at LANL—from creating new and efficient forms of energy production to stockpile stewardship—and live at the heart of everything we touch in our daily lives—from telecommunications to transportation. The Laboratory has an obvious deep and rich scientific history in the science of materials, reaching back to the origins of the Laboratory itself. It is therefore not surprising that LANL is applying its scientific acumen to the furthest reaches of materials science at the fundamental theoretical and applied levels.

Material science exists at the confluence of many disciplines, and the articles in this section reflect this diversity in both scientific

discipline and application. Some topics represented in this section are:

- breakthroughs in theory and modeling for materials at multiple scales (nano to macro), to the applications of statistical methods for extracting new insights on corrosion and the endurance of the nuclear weapons stockpile;
- the determination of phase transformation pathways and energetics in plutonium;
- modeling and simulation using accelerated molecular dynamics to study properties with time scales far beyond those approachable with conventional molecular dynamics; and
- theoretical and modeling developments for large scale phase transitions, deformations and behavior under extreme conditions.



## Analysis of Dynamically Driven, Single-crystal Experiments

Irene J. Beyerlein, Francis L. Addessio, Zhiqiang Wang, T-3; George T. Gray, Ellen K. Cerreta, Fang Cao, MST-8

Experiments are being conducted in the Materials Science and Technology (MST) Division to investigate the response of single crystals of copper to impact-loading scenarios. For this purpose, plate impact experiments using a 2.184-mm flyer plate and a 2.261-mm target plate are being considered. Impact velocities of 271 m/s and 518 m/s have been used in the current studies. A target plate that was composed of a bicrystal was employed in the initial experiments. That is, half of the target contained a single crystal that had an orientation of [100], and the other half had an orientation of [011]. A representation of the bicrystal target is provided in Fig. 1. Future targets will contain only a single crystal. In addition to obtaining the particle velocity history on the back surface of the target, postmortem microscopy was performed to quantify the deformation mechanisms within the target material. Phenomena that include substructure evolution, deformation twinning, and damage can be identified in this manner.

Both theoretical and computational support for this experimental investigation are being pursued within the Theoretical Division. The intent is to develop a next-generation, high-rate constitutive model for materials that

are of interest to the DOE community. A multilength scale approach is being employed for this support. That is, dislocation dynamics (DD) simulations are being used to develop single-crystal hardening laws applicable to a wide range of strain rates. Of interest is the transition from thermal activation to the dislocation drag regime ( $\sim 10^4$ - $10^7$ /s). The single-crystal models that result from the DD investigation are being implemented into a plate impact analysis, which uses a continuum mechanics model for the flyer plate and the single-crystal model for the target. A simulation of the plate impact experiments for a target material that is a single crystal of copper oriented in the [100] direction is provided in Fig. 2. The propagation of the stress wave into both the flyer ( $0 < x < 0.2184$  cm) and the target ( $0.2184$  cm  $< x < 0.4445$  cm) is shown in Fig. 2 at four different times. The evolution of both the elastic precursor and the plastic waves may be seen from the simulation. The single-crystal model that was used in the analysis has its basis in the thermal activation regime and introduces a threshold stress characterized for Cu in this regime, which is relatively rate insensitive. The large spike close to the wave front in the single-crystal material (i.e., the target) is a result of large values of resolved shear stresses several times greater than the critical resolved shear stress provided in the model—their ratio is raised to a large power in the model. It is anticipated that a more realistic wave profile will result if the dislocation drag regime with a higher rate sensitivity is included in the model.

**For further information contact Francis L. Addessio at [addessio@lanl.gov](mailto:addessio@lanl.gov).**

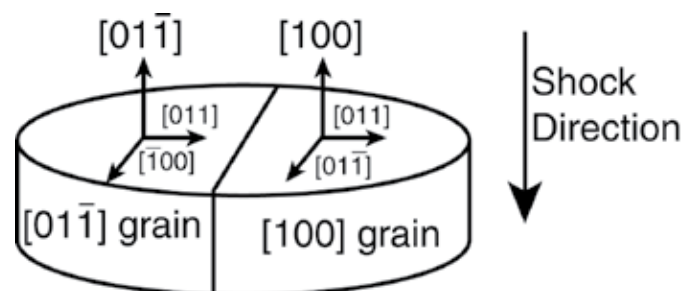


*Fig. 1. Diagram of the bicrystal target plate.*

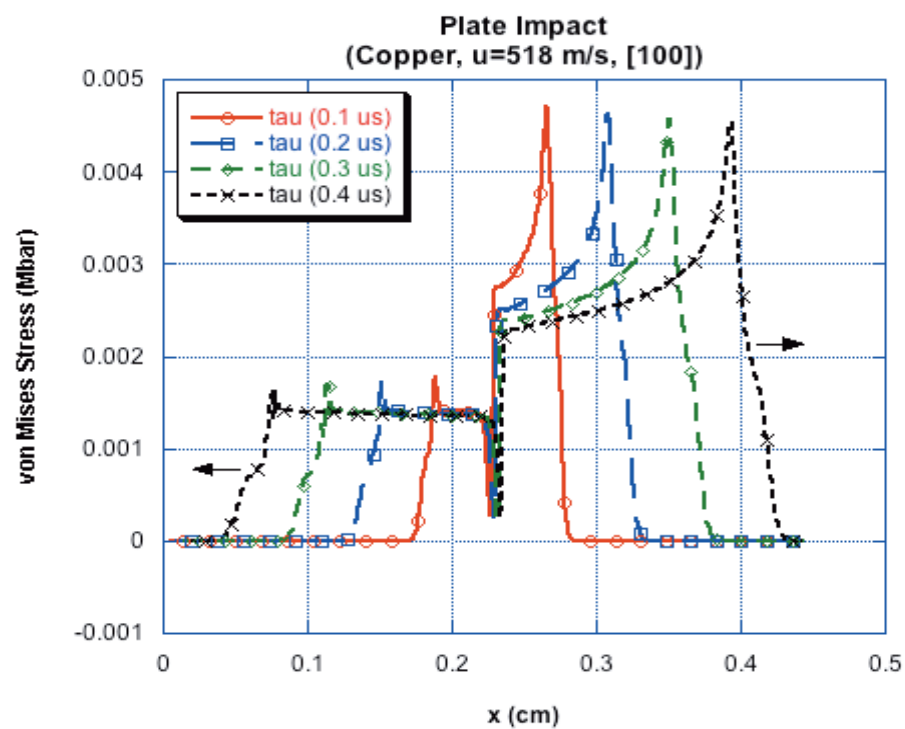


*Fig. 2. Single-crystal analysis of a [100] oriented copper crystal at an impact velocity of 518 m/s.*

**Funding****Acknowledgments**

DOE, NNSA, Advanced Simulation and Computing Program

## Modeling the Microstructural Evolution of Metallic Polycrystalline Materials under Localization Conditions

Curt A. Bronkhorst, T-3; Benjamin L. Hansen T-3 and California Institute of Technology;  
Ellen K. Cerreta, John F. Bingert, MST-8

In general, the shear localization process involves initiation and growth. Initiation is expected to be a stochastic process in material space where anisotropy in the elastic-plastic behavior of single crystals and intercrystalline interactions serve to form natural perturbations to the material's local stability. A hat-shaped sample geometry was used to study shear localization growth. It is an axisymmetric sample with an upper "hat" portion and a lower "brim" portion with the shear zone located between the hat and brim. The shear zone length was 870,890  $\mu\text{m}$  with deformation imposed through a Split-Hopkinson Pressure Bar system at maximum top-to-bottom velocity in the range of 8–25 m/s. The deformation behavior of tantalum tophat samples is modeled through direct polycrystal simulations. An embedded Voronoï-tessellated 2D microstructure is used to represent the material within the shear zone of the sample. A thermomechanically coupled elastoviscoplastic single-crystal model is presented and used to represent the response of the grains within the aggregate shear zone. In the shoulder regions away from the shear zone where strain levels remain on the order of 0.05, the material is represented by an isotropic J2 flow theory based upon the elastoviscoplastic mechanical threshold stress (MTS) model for flow strength. The top surface stress-versus-displacement results were compared with those of the experiments, and overall the simulated stress magnitude is overpredicted. It is believed that the reason for this is that the simulations are 2D. A region within the numerical shear zone was isolated for statistical examination. The vonMises stress state within this isolated shear zone region suggests an approximate normal distribution with a factor of two difference between

the minimum and maximum points in the distribution. The equivalent plastic strain distribution within this same region has values ranging between 0.4–1.5 and is not symmetric. Other material state distributions are also given. The crystallographic texture within this isolated shear zone is also compared with the experimental texture and found to match reasonably well considering the simulations are 2D.

**For further information contact Curt A. Bronkhorst at [cabronk@lanl.gov](mailto:cabronk@lanl.gov)**

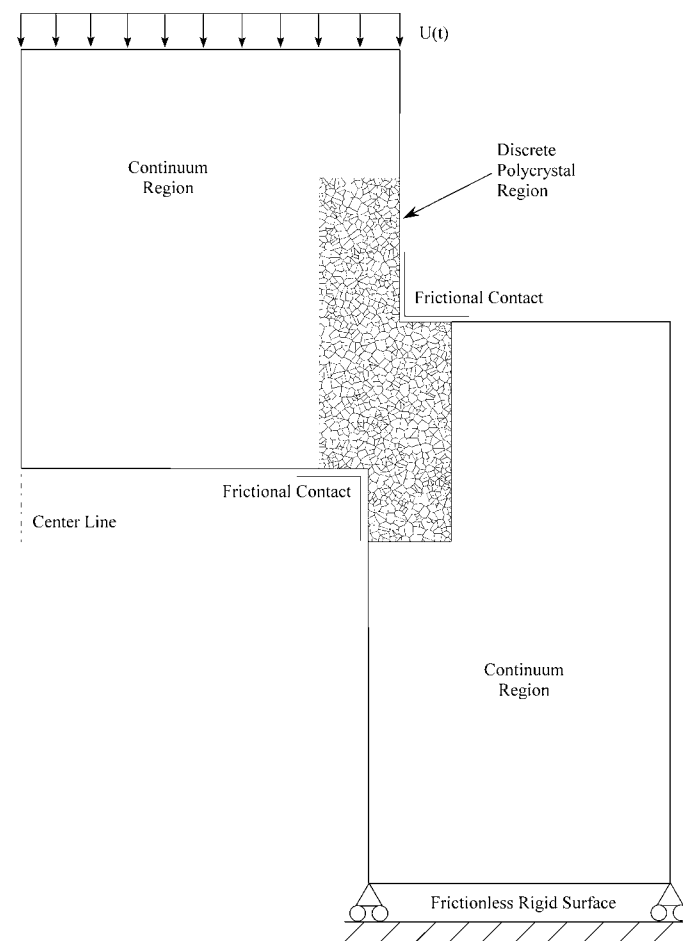


*Fig. 1. Two-length scale numerical model used to simulate the tophat sample. This figure is drawn to scale.*



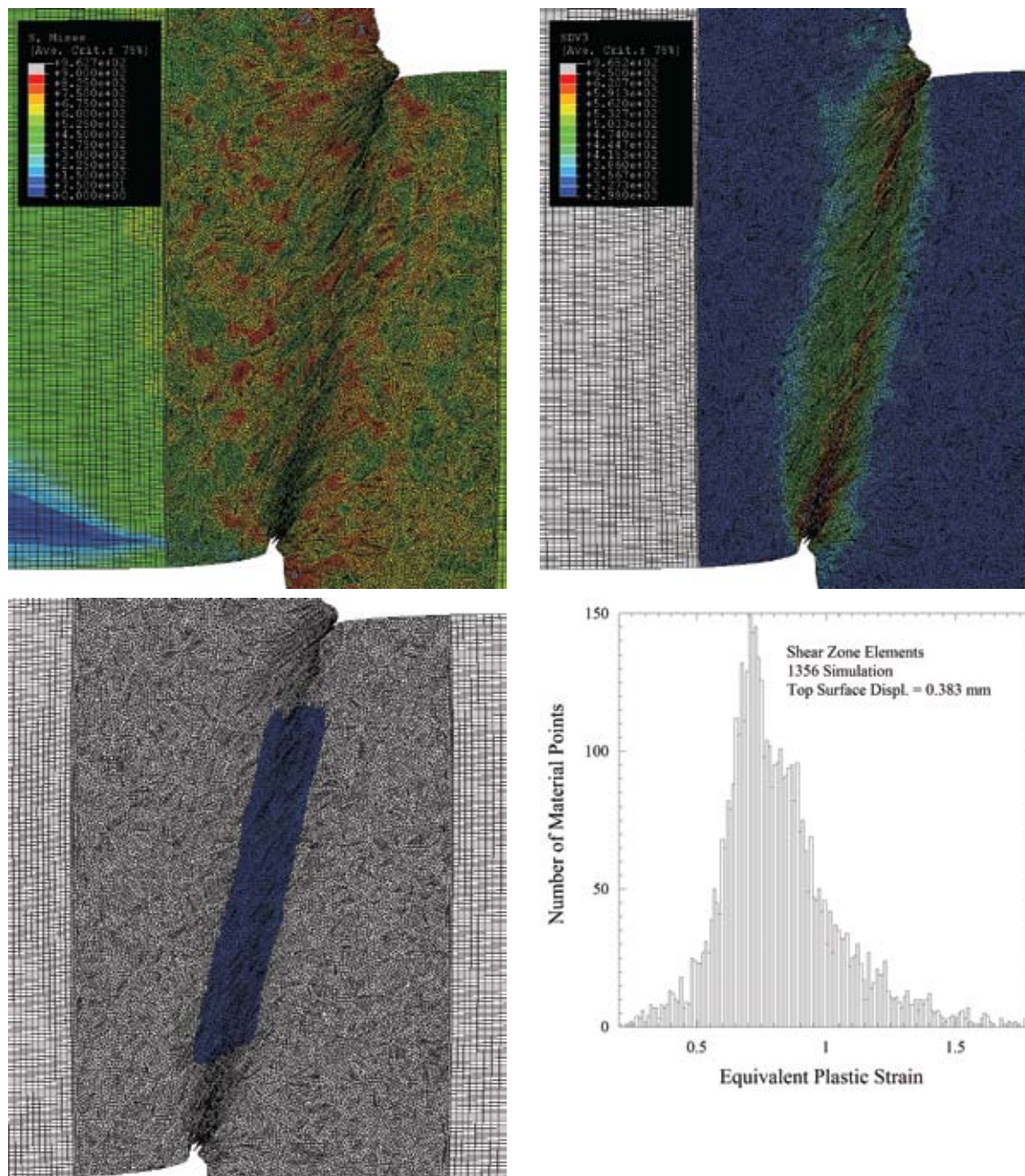


*Fig. 2. vonMises stress (left, MPa) and temperature (right, K) results from the Tantalum top hat experiment numerical simulation.*

*Fig. 3. Distribution of equivalent plastic strain in the highlighted region of the shear zone.*

#### **Funding**

#### **Acknowledgments**

- DoD and DOE Joint Munitions Technology Development Program
- DOE, NNSA, Advanced Simulation and Computing Program

## Finding Relevant Atomic Processes Using Accelerated Molecular Dynamics

Abhijit Chatterjee, Arthur F. Voter, T-1

**S**tudy of thermally activated phenomena in solid-state materials at experimental laboratory length and time scales is essential for designing materials with desirable characteristics. In these materials, atomic processes that govern macroscopic phenomena often occur at time scales that are simply beyond the reach of atomistic simulation methods such as molecular dynamics (MD). As a result, current materials modeling techniques frequently make severe assumptions regarding the atomic processes in solid-state materials, assumptions that are likely to corrupt the dynamical evolution.

Over the last 10 years, a suite of accelerated molecular dynamics methods has been developed at LANL to overcome this challenge [1]. In particular, the temperature accelerated dynamics (TAD) method [2] is a powerful computational tool for studying thermally activated phenomena in solid-state materials over large time scales, such as seconds. In the TAD method, transitions from state to state are made to occur more rapidly by raising the temperature of the system. Although the wrong event sometimes occurs first at higher temperature, the TAD algorithm corrects for this, only allowing the correct events (with a desired confidence) to be accepted.

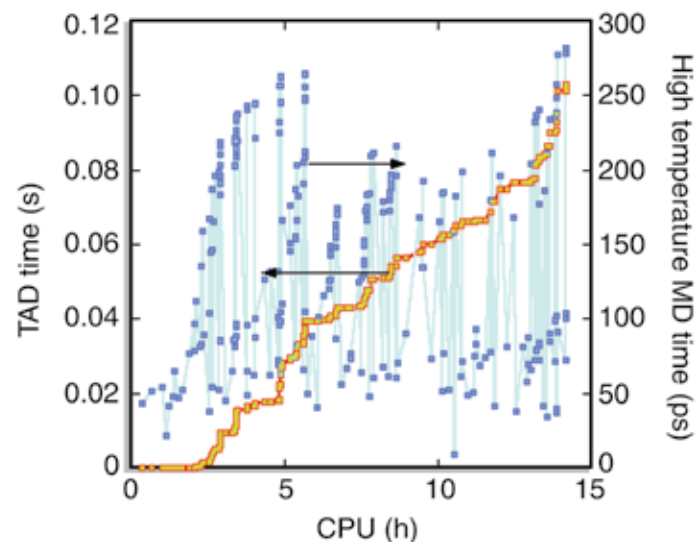
The TAD method gives statistically correct dynamics and it can reach large time scales. However, it is limited to small system sizes, e.g., 1000 atoms. We are pursuing different directions to develop multiscale methods for solid-state systems that overcome the materials length and time scale problem with the accuracy of the TAD method. One approach is to modify the TAD method so that it generates a proper list of reaction mechanisms as it proceeds. This list

of processes and associated rate constants is then used in the well-known kinetic Monte Carlo (KMC) framework to advance the dynamics.

Based on this philosophy, we have developed a new formulation of the TAD method called the process list-TAD method (p-TAD). The method guarantees that all relevant processes at a particular temperature have been detected with a user-specified confidence over large time scales. This solves the long-standing problem of how to find a complete (or complete enough with desired confidence) list of KMC rate processes for a given system in a given state. Generation of such accurate KMC process lists, with error control, is not possible with any other currently available technique. Though the p-TAD algorithm resembles the original TAD algorithm in many ways, the p-TAD method introduces significant improvements to the existing TAD method. For example, it offers a more direct way to parallelize the dynamics for small (or large) systems, and it can be made more accurate event by event if desired, because the accurate rate constant is directly computed at low temperature. It also offers the possibility of including quantum dynamical (e.g., tunneling and zero-point) effects.

To test the capabilities of the p-TAD method we have studied the dynamics in silver deposited on a copper [Cu(110)] surface at several different silver coverages at a temperature of 150K. The simulations were performed using embedded atom potentials for silver and copper. A confidence measure of 95% was used for generating the list of processes. Figure 1 shows that long time scales (up to 0.1 s) were simulated with reasonably low CPU requirements by performing several high-temperature MD simulations that were each shorter than 1 ns. Several many-atom processes were repeatedly observed in the p-TAD calculations. Two examples of such processes are shown in Figs. 2 and 3. Typically, most many-atom processes are completely ignored in a conventional KMC method, which is a major drawback of the KMC method that can lead to incorrect model predictions in certain materials, such as irradiated and multicomponent materials. Unlike conventional KMC models, which often assume that atoms reside on a lattice (i.e., a fixed set of





spatial positions), the TAD method does not have this restriction and it automatically allows for the strain relaxation resulting from the lattice mismatch between silver and copper atoms. This effect is visible in Figs. 2 and 3. Recently, the adaptive KMC method [3] has been developed by Henkelman and coworkers in an attempt to perform off-lattice KMC calculations by building a reasonably complete process list [4] via random transition state searches for a given state of the system. We believe that the TAD method, which follows the actual dynamics, offers a more correct way of establishing that *all* relevant KMC processes for a particular duration of time have been found with a certain confidence in a consistent manner.

In conclusion, we have demonstrated the strengths of a new variation of the TAD method called the p-TAD method. The p-TAD method is currently being further developed into the TAD-based KMC method. The latter builds on the former by generating process lists for small subsets of atoms. It combines the best of molecular dynamics, accelerated molecular dynamics, and kinetic Monte Carlo methods, to reach greater time scales, length scales, and accuracy

than has been possible previously. The resulting computer program will be used to study materials under irradiation and other problems.

**For further information contact Arthur F. Voter at [afv@lanl.gov](mailto:afv@lanl.gov).**

- [1] A.F. Voter et al., *Ann. Rev. Mater. Res.* **32**, 321 (2002).
- [2] M.R. Sørensen, A.F. Voter, *J. Chem. Phys.* **112**, 9599 (2000).
- [3] G. Henkelman, H. Jónsson, *J. Chem. Phys.* **115**, 9657 (2001).
- [4] L. Xu, G. Henkelman, *J. Chem. Phys.* **129**, 114104 (2008).

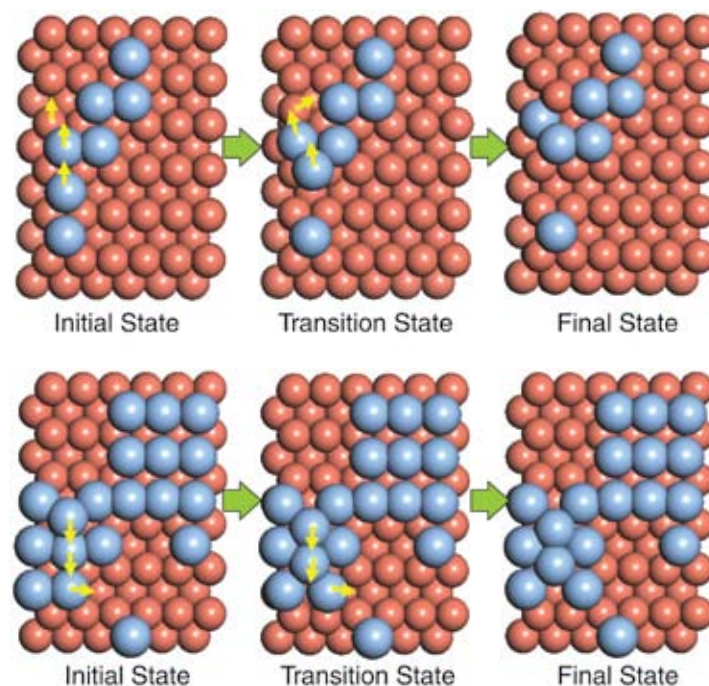


*Fig. 1. Accelerated time accessed during a 14-hour p-TAD simulation of silver deposited on copper. The high temperature molecular dynamics time is also plotted.*

*Fig. 2. Initial, transition, and final states for a three-atom process involving silver (blue) and copper (brown) atoms at 0.19 ML silver coverage. The activation barrier for this process is 0.74 eV.*

*Fig. 3. Initial, transition, and final states for a three-atom process involving only silver (blue) atoms at 0.53 ML silver coverage. The activation barrier for this process is 0.35 eV.*

#### **Funding Acknowledgments**

- DOE, Office of Science, Office of Basic Energy Sciences, Materials Science and Engineering
- LANL Directed Research and Development Program



## The Effect of Inclusions on Phase Transformations in Dynamically Driven Plates

Bradford E. Clements, T-1; Francis L. Addessio, T-3; Jeeyeon N. Plohr, T-1

**P**rocessing techniques, such as hot rolling, may result in the formation of high-aspect ratio inclusions or impurities within the material microstructure. These elongated and aligned inclusions are one source of material anisotropy. Although low in concentration, they may have a significant effect on the material behavior, resulting in an anisotropic plastic or fracture response. A study of the effect of inclusions on the phase transformation characteristics of a dynamically driven matrix material was considered.

The development of predictive material models can expedite the analysis of engineering systems and assist in the interpretation of experimental data. Many heterogeneous materials contain constituents that undergo phase transformations. A few examples are metal matrix composites, high-explosive materials, and alloys that are used in armor designs. In heterogeneous materials, details of the microstructure have a direct effect on the macromechanical response of the material. Consequently, it is important to include the effects of the microstructure when modeling composite materials. However, the length scales that are necessary to model the details of the composite microstructure are much smaller than those of the engineering structure. Therefore, it is impractical to resolve the microstructure for large-scale simulations. Homogenization techniques that use idealized representations for the microstructure and are computationally robust and efficient provide a viable compromise. The generalized method of cells (GMC) is one such technique, which has demonstrated versatility and has been applied to numerous applications.

In dynamically driven structures, there are a number of characteristic time as well as length scales that must be considered. For example, the deformation rate characteristics of the material must be included to accurately model the material response to high-rate loading scenarios. Also, in materials that exhibit solid-solid phase transformations, the kinetics of the transformation process must be addressed. These processes are evident in plate impact experiments. Distinct signatures of rate-dependent plasticity and of the phase transformation are obtained from the measured velocity history on the back surface of the plate.

We developed a macromechanical model for the thermomechanical deformation of heterogeneous materials, which includes the effects of plasticity and phase transformations of its constituents. The model does not resolve the details of the transformation process. Instead, the evolution of the transformation process is addressed by tracking the mass fractions of each phase within the constituents. Each phase is allowed to have distinct material properties. Free energies for each phase, which are derived from ab initio calculations coupled with experimental data, are used. These free energies provide the constitutive response of the constituents. The kinetics of the phase transformation are also expressed in terms of differences of the free energies of the transforming phases.

One example, which illustrates the utility of the homogenization-phase transition (GMC-PT) analysis, considers situations where the phase transformation occurs nonuniformly at the microlevel. This example is different from heterogeneous nucleation and growth phenomena where regions of transforming material begin at a nucleation site and spread outward until the entire material is transformed. Indeed in Fe, using diamond anvil cell (DAC) hydrostatic experiments, it was observed that in addition to the standard nucleation and growth behavior, microscopically small independent areas in the Fe transformed simultaneously. This resulted in a mottled transformation surface as measured by X-ray diffraction and high-pressure light metallographic techniques. To simulate this behavior, a

small concentration of Fe was forced to remain in the  $\alpha$ -phase, while the remaining subcells were allowed to transform. The effects on the velocity profile then were calculated. For impact velocities of 0.9916 and 1.567 km/s, the calculated velocity profiles are shown in the Fig. 1. Regions of transformation-prohibited Fe (i.e., the impurities) up to 30 volume percent are shown. For the low velocity simulation, while the transformation plateau is reduced, it remains clearly visible even up to a 30 percent impurity level. However, at the higher velocity, an impurity concentration of 30 percent is sufficient to nearly remove the appearance of the phase transformation in the calculated velocity profile.

A second example considered the case where regions of the Fe system were oxidized resulting in iron-oxide ( $\text{Fe}_2\text{O}_3$ ) inclusions. The addition of oxygen is known to suppress any phase transformations to higher values of pressure than those probed in the simulations. This is evident from a phase diagram for  $\text{Fe}_2\text{O}_3$ . The second example provides velocity profiles for Fe containing 10 percent  $\text{Fe}_2\text{O}_3$ . To illustrate the flexibility of the GMC-PT analysis,  $\text{Fe}_2\text{O}_3$  inclusions with aspect ratios of approximately 3 were used in the simulations. The effects of adding 10 percent  $\text{Fe}_2\text{O}_3$  inclusions to the Fe are shown in Fig. 2. Recall that only the Fe subcells are allowed to transform from  $\alpha$  to  $\epsilon$ . The  $\text{Fe}_2\text{O}_3$  elastic bulk and shear moduli are taken from the literature. Values of 98 and 93 GPa were used for the bulk and shear moduli, respectively. It is noted that the bulk modulus of the  $\text{Fe}_2\text{O}_3$  inclusions is substantially less than for pure Fe. In this example,  $\text{Fe}_2\text{O}_3$  is modeled as a linear elastic material. Clearly, a full equation of state would provide more representative simulations. For this example, studying the single impact velocity of 0.9916 km/s suffices. The velocity profiles for pure Fe and for 10% nontransforming inclusions are provided in Fig. 2. Two orientations of  $\text{Fe}_2\text{O}_3$  inclusions, each having an aspect ratio of 3, are simulated. One orientation has the long-axis of the inclusion aligned with the strain axis of the plate impact simulation. The other simulation has the inclusion aligned perpendicular to the strain axis.

For further information contact Francis L. Addessio at [addessio@lanl.gov](mailto:addessio@lanl.gov).

#### Citations

- F.L. Addessio, B.E. Clements, T.O. Williams, *J. Appl. Phys.* **97**, 083509 (2005).  
 B.E. Clements, J.N. Plohr, F.L. Addessio, *J. Appl. Phys.* **100**, 123520 (2006).  
 J.N. Plohr, B.E. Clements, F.L. Addessio, *J. Appl. Phys.* **100**, 123521 (2006).

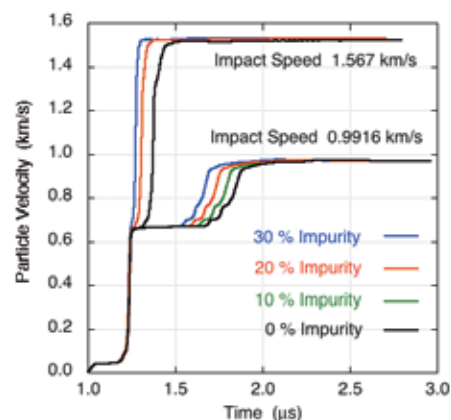


*Fig. 1. Theoretical particle velocity profiles for a heterogeneous system where small regions of the Fe phase transformation are suppressed.*

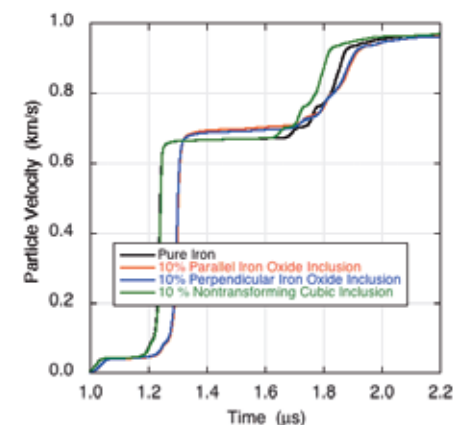


*Fig. 2. Theoretical particle velocity profiles for a heterogeneous system containing pure Fe and  $\text{Fe}_2\text{O}_3$  inclusions.*

#### Funding

##### Acknowledgments

- DoD and DOE Joint Munitions Technology Development Program
- DOE, NNSA, Advanced Simulation and Computing Program

## Statistical Models for Understanding the Enduring Conventional and Nuclear Weapons Stockpile

Aparna V. Huzurbazar, Christine Anderson-Cook, Todd Graves, Michael Hamada, Geralyn Hemphill, David Higdon, Richard Klamann, Scott Vander Wiel, CCS-6

The LANL Statistical Sciences Group (CCS-6) executes a broad range of applied work to facilitate understanding of the enduring conventional and nuclear weapons stockpiles. The effort involves developing methods and software tools, appropriate data collection, and implementing solutions to help with stockpile stewardship for stockpiles. The technical issues associated with understanding the stockpile are complex and involve diverse data types and sources. Our goal is to provide improved confidence in future weapons reliability, safety, and performance. CCS-6 works within LANL to apply the best methods to improve the understanding of weapon assessment, complex system reliability, and to support decision making about the enduring U.S. stockpile.

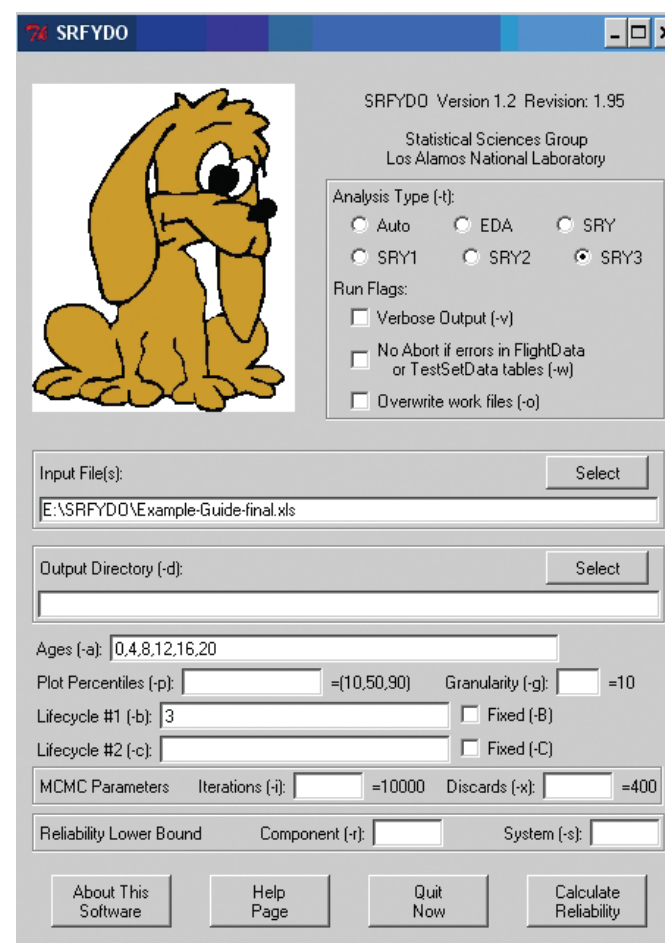
Much of this work has been a continuing effort in research methods for the health assessment for complex systems. Each weapon in the stockpile is an aging system of dynamic parts. Many of these parts are tested individually, but new methodology and tools are required to integrate the various data streams derived from these parts to enable decision-makers to better understand the nature of the stockpile. We validated much of this methodology in our collaborative partnerships with the DoD through the Munitions Stockpile Reliability Assessment project of the Joint Munitions Program. Partnering with DoD collaborators provides a way to test and validate our methods [1]. DoD systems provide a data-rich environment, in contrast to our Stockpile Stewardship work.

Our recent successes in supporting the weapons program have included work in three major elements: statistics-based quantification of margins and uncertainties (QMU),

resource allocation, and age-aware analyses and reliability assessments.

We have developed statistics-based QMU methodologies for combining separate tests, and physics and engineering codes to map the effect of input variation and aging effects on performance [2,3]. We have also created new methods for combining data from surveillance and experiments with physics simulations to provide performance-based lifetime assessments. We have formulated new resource allocation methodology to guide the choice of future types and quantities of tests to be collected for predictive, age-

*Fig. 1. Graphical user interface for the SRFYDO software tool developed for system reliability and prediction using Bayesian methods.*





aware reliability assessment [4] and methodology to integrate heterogeneous sources of data into age-aware system-level reliability assessments with quantified uncertainty. For example, we developed methods for aggregating reliability uncertainty for a specific subsystem of the B-61 with Sandia National Laboratories. We have also performed age-aware assessments of components and stockpile parameters critical to performance or engineering assessments [5-7].

Such tracking and trending of data of stockpile parameter data streams provides a context for understanding the stockpile data. We have developed software tools to facilitate, implement, and operationalize these statistical methods and models. For example, the newly developed SRFYDO [8] is an application designed to simplify the process of system reliability modeling and prediction using Bayesian methods and Markov chain Monte Carlo. In addition, we have created foundational work on Bayesian reliability [9], models for multilevel data using methods from Bayesian networks, graphical models, and imprecise probability [10].

**For more information contact Aparna V. Huzurbazar at [aparna@lanl.gov](mailto:aparna@lanl.gov).**

- [1] C. Anderson-Cook et al., *J. Mil. Op. Mil. Res. Soc.* **13**(3), 5-18 (2008).
- [2] D. Higdon et al., *J. Am. Stat. Assoc.* **14**, 570-583 (2008).
- [3] D. Higdon et al., LA-CP-08-0520 (2008).
- [4] C. Anderson-Cook, T. Graves, M. Hamada, "Resource allocation for reliability of a complex system with aging components," *Qual. Reliab. Eng. Int.*, In press (2009).
- [5] T. Graves, S. Vander Wiel, LA-CP-08-1217 (2008).
- [6] M. Hamada et al., LA-CP-08-0896 (2008).
- [7] M. Hamada et al., LA-CP-08-1103 (2008).
- [8] C. Anderson-Cook, A. Huzurbazar, R. Klamann, LA-UR-08-6161 (2008).
- [9] M. Hamada et al., *Bayesian Reliability*, New York: Springer (2008).
- [10] A. Wilson, A. Huzurbazar, *Reliab. Eng. Syst. Saf.* **92**, 1413-1420 (2007).

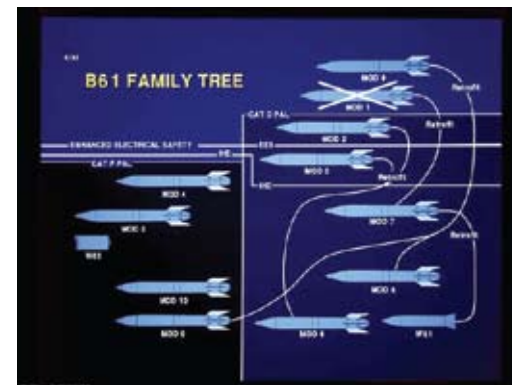


*Fig. 2. Our reliability methods are developed in collaboration with DoD and LANL Core and Enhanced Surveillance for systems such as RAM and the B-61.*

### **Funding Acknowledgments**

- DOE, NNSA, Enhanced Surveillance Campaign
- DOE, NNSA, Defense Programs and Core Surveillance
- DoD and DOE Joint Munitions Technology Development Program

# Multifield Fragmentation

Bucky Kashiwa, Mark Schraad, T-3; Larry Hull, DE-6

A solid object subjected to external forces will deform. If the forces are large the deformation can be rapid and the object can break up into fragments. Hand grenades and pipe bombs are simple examples in which the forces are created by a high explosive whose pressures cause fragmentation of the confining case. Prediction of the fragmenting process, and in particular its prevention, is ubiquitous. The subject is central to applications including the safety of buildings, bridges, vehicles, and manufacturing equipment, as well as in weaponry.

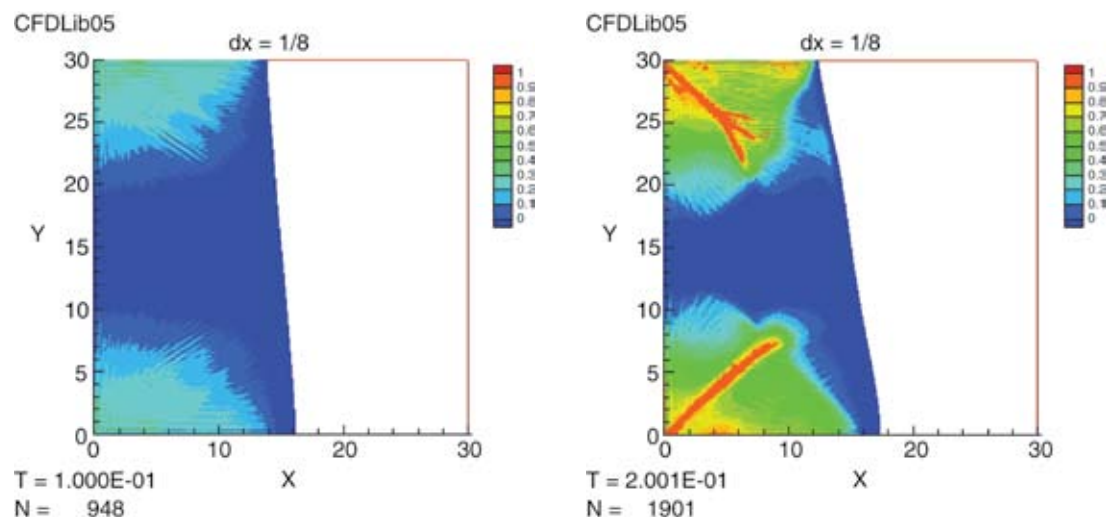
An understanding of the physics of fragmentation is facilitated by a so-called multifield formulation, which permits the study of the force-generating media concurrently with the force-affected media, so that their interactions are fully coupled. Each medium is represented by a set of averaged variables, called field variables, representing the thermodynamic state of the medium at all points. When the

field variables are associated with an element of mass, the description is said to be in the Lagrangian frame of reference; when the field variables are associated with a fixed location in space, the description is in the Eulerian frame.

We have developed a scheme that permits the choice of frame according to the medium. For a solid material, initially intact, and for which eventual fragmentation is of interest, the Lagrangian frame is appropriate because it affords the highest possible accuracy of the material stress. For a fluid material (like a high pressure gas or liquid) the Eulerian frame is most accurate because it permits arbitrary deformation.

The strip of images in Fig. 1 illustrates use of this mixed-frame approach to the simulation of a fragmenting slab of metal. Here in the simulation time increases from left to right. An initially rectangular metal slab occupies the left side of the space, and a nonviscous fluid is in the right side. At time zero, a uniform acceleration is applied to the domain (as if it were a very fast elevator) causing the slab to press against the bottom boundary, and pull at the top boundary. Colors show values of a damage progress variable: blue is completely undamaged; light-blue and green indicate intermediate damage; red is fully damaged (failed) material.

*Fig. 1. A mixed-frame approach to the simulation of a fragmenting slab of metal. The simulation time increases from left to right.*



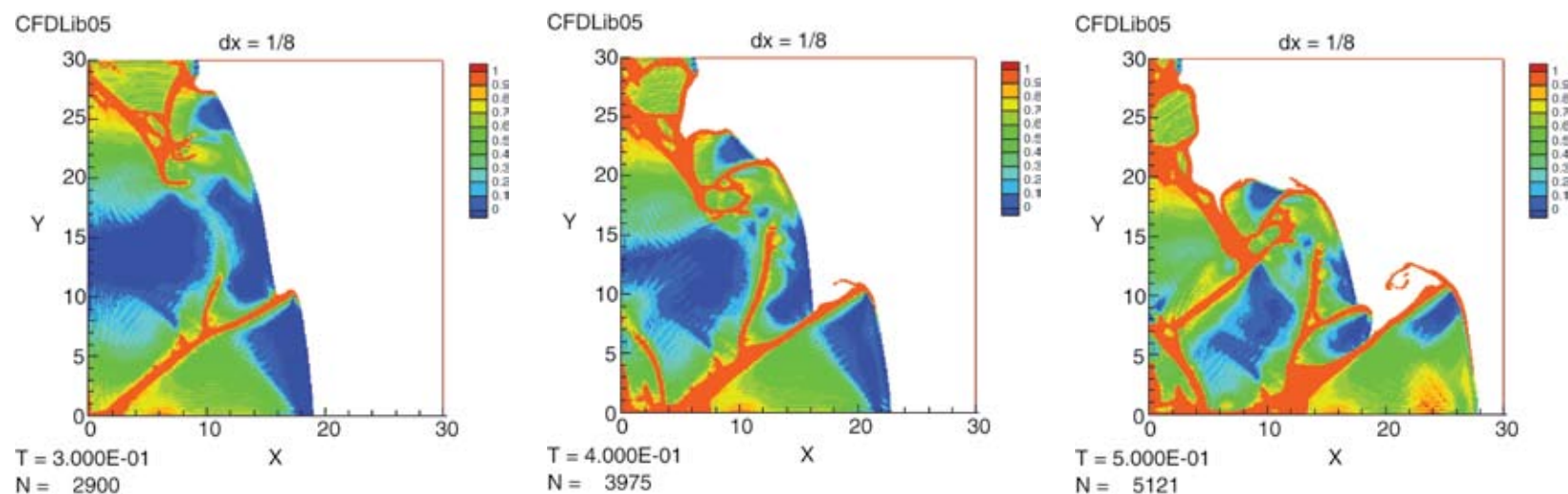
Initial damage occurs in the upper and lower left corners where the forces are the greatest, and where a crack first appears in each corner. As the damage progresses, the cracks are seen to branch out and intersect, leaving a pile of rubble consisting of a variety of large and small fragments. Calculations of this type are used to verify theoretical expressions for the material stress history of the solid medium. Once verified, these theories are used for a wide variety of technological applications in defense, industry, and in academia.

For more information contact B. A. Kashiwa at [bak@lanl.gov](mailto:bak@lanl.gov).

### Funding

### Acknowledgments

DoD and DOE Joint  
Munitions Technology  
Development Program





# Molecular Dynamics Investigation of the Rapid Diffusion of Very Large Heteroepitaxial Islands

Obioma U. Uche, SNL; Danny Perez, Arthur F. Voter, T-1; John C. Hamilton, SNL

Even when created in carefully controlled conditions, surfaces of crystalline solids do not consist of perfectly ordered rows of atoms. They are rather akin to a flatland populated by a whole ecosystem of defects like adatoms (isolated atoms standing on the surface), vacancies, islands (small groups of bound adatoms), pits, steps (partially filled layers), or dislocations. The way these defects move and interact with each other controls the static and dynamic properties of the surfaces, which are in turn crucial to technological applications like epitaxial film growth or heterogeneous catalysis. Traditionally, it has been assumed these surfaces evolved mainly through the repeated motion of single defects (i.e., adatoms or vacancies). More recently, practitioners in the field realized that more complex defects like islands can also move coherently through mechanisms such as glide [1], dislocation [2], or reptation [3]. However, these mechanisms are thought to apply mainly to relatively small defects. In this work, we simulated the evolution of a heteroepitaxial metallic system and discovered a new mechanism by which islands of unexpectedly large size can rapidly diffuse. We show that such a large island can actually diffuse orders of magnitude faster than a single adatom, thus demonstrating that the evolution of surfaces can, in some cases, be significantly affected by the movements of large defects.

We consider the case of an island of 169 silver atoms resting on an otherwise perfect copper (001) surface (Fig. 1). The island is taken to adopt a compact hexagonal shape reconstructing into a (10x2) unit cell as observed experimentally [4]. This reconstruction is driven by the large size mismatch between Ag and Cu. The evolution of this system was simulated at temperatures between 300K and

225K using molecular dynamics (MD), while we resorted to an accelerated dynamics method developed at LANL by one of us (namely the Parallel Replica Dynamics method [5]) to access the very long time scales required to observe movement of the island at temperatures down to 175K.

The most surprising feature of our simulations is that, despite its very large size, the island is able to hop (jump to a neighboring stable site) on the surface very rapidly, even at low temperatures. These results are presented in Fig. 2, where the hopping rate of the island is reported as a function of temperature. To put these results in perspective, the hopping rate of a single silver adatom on the same

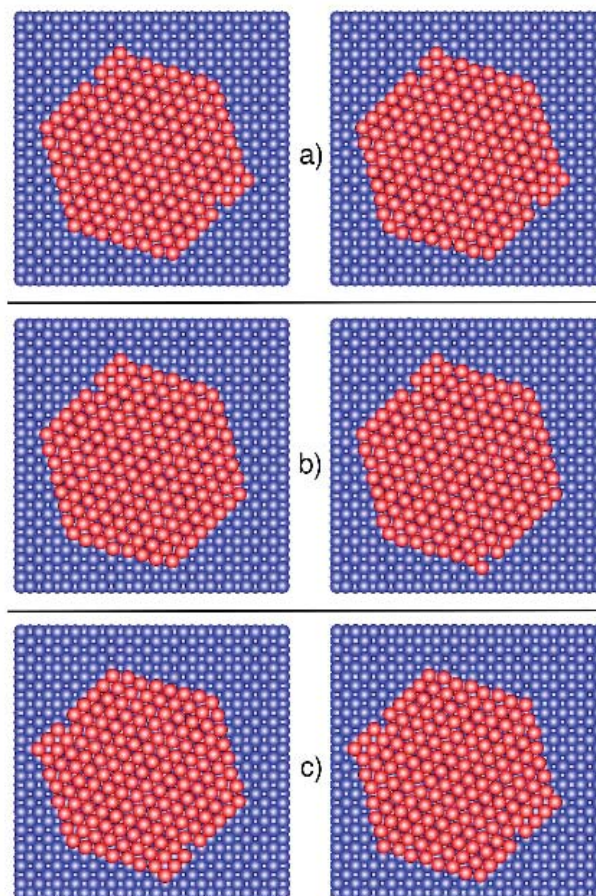


*Fig. 1. Various conformation changes observed during a hop of the island: a) simple vacancy hop, b) lower edge advancing through a vacancy hop, and c) glide of the lower section of the core and vacancy diffusion.*

surface is also shown. The data indicates that, around room temperature, the island hops about fifty times more rapidly than a single adatom, and that this difference increases even more as the temperature is lowered. This result demonstrates that large defects can actually be much more mobile than small ones, even at low temperatures. We were also able to explain, quantitatively, the curved temperature dependence of the hopping rate using a generalization of transition state theory with many intermediate states.

The fact that such a fast diffusion was unforeseen can easily be understood in light of the extremely complex mechanism by which it proceeds. Indeed, while the hopping process is cooperative, the island does not monolithically hop from one site to the other, but rather continually changes its conformation until a favorable sequence of such changes leads the island to the next site. Here, transitions are of two kinds: gliding (all or part of the core of the island coherently slides), and vacancy hopping along the edges of the island. Once again contrary to intuition, the hopping of these vacancies are the rate-limiting steps, while the rest of the island effortlessly follows the edges by gliding. The extreme complexity of the dynamics is shown in Fig. 3, where the network of states visited during a single Parallel Replica simulation of 6.5  $\mu$ s at 175K is presented. In Fig. 3, each circle corresponds to a conformation, and two of them are joined by an arrow when a transition between them has been observed. Boxes contain conformations corresponding to perturbations around the same site, while the others correspond to intermediate conformations. The most efficient pathway for hopping is marked by colored arrows. A glimpse of some of the conformation changes occurring along this path is shown in Fig. 1.

In conclusion, we have shown that some metallic heteroepitaxial surfaces can evolve through the diffusion of very large islands containing many tens of atoms. We have also identified a novel mechanism involving vacancy diffusion and gliding that can confer mobility to such large defects. This work demonstrates that complex collective motions are often crucial in determining how crystalline surfaces behave and evolve.

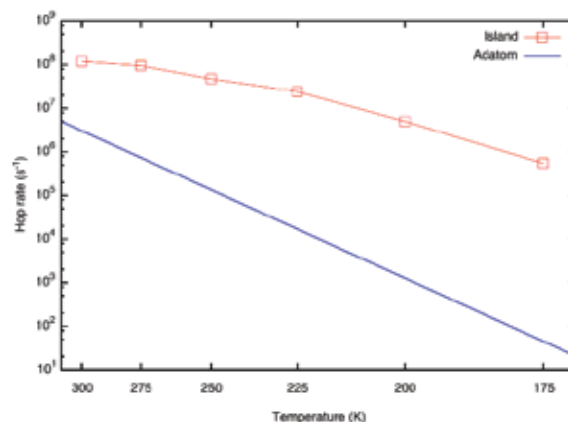


Fig. 2. Temperature dependence of the hopping rate of the island (red squares) and of a single adatom (thick blue line).

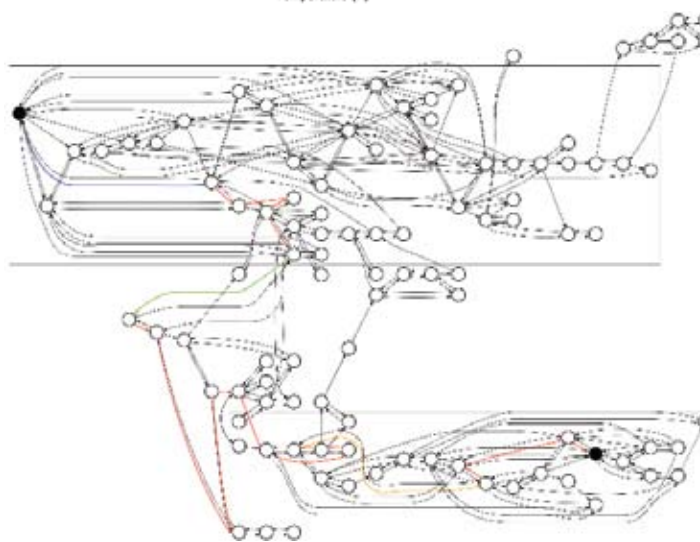


Fig. 3. Network of transitions observed during a Parallel Replica Simulation at 175K. Filled circles correspond to the conformations before and after the hop. Colored arrows correspond to transitions along the optimal pathway. The blue, green, and orange arrows correspond to transitions a), b), and c) in Fig. 1, respectively. See text for details.

For further information contact Danny Perez at [danny\\_perez@lanl.gov](mailto:danny_perez@lanl.gov).

- [1] C.-L. Liu, J.B. Adams, *Surf. Sci.* **268**, 73 (1992).
- [2] J.C. Hamilton et al., *Phys. Rev. Lett.* **74**, 2760 (1995).
- [3] V. Chirita et al., *Thin Solid Films* **370**, 179 (2000).
- [4] P.T. Sprunger et al., *Phys. Rev. B* **54**, 8163 (1996).
- [5] A. F. Voter, *Phys. Rev. B* **57**, R13985 (1998).

### Funding

#### Acknowledgments

- DOE, Office of Science, Office of Basic Energy Sciences
- LANL Postdoctoral Fellowship Program

# Transformation Pathways and Energetics in Plutonium

Turab Lookman, Avadh B. Saxena, Robert C. Albers, Roman Groger, T-4

*Fig. 1. Transformation pathway from fcc to monoclinic via a simple hexagonal intermediate. Atoms move continuously from fcc to the hexagonal via a common trigonal subgroup. Sixteen primitive hexagonal cells then combine to form the 16-atom monoclinic cell, a process mediated by phonons that break translational symmetry.*

An outstanding problem in Pu science is understanding the mechanism of the structural transformation from the high temperature face-centered cubic (fcc)  $\delta$  phase to the low temperature monoclinic  $\alpha$  phase. The transformation is accompanied by changes in the shape of the unit cell and numbers of atoms within the unit cell. Thus, a combination of strains and displacement modes (the order parameters) are involved in describing these transformations, and the challenging problem is to obtain the atomic pathways from one crystal structure to another. This information is necessary if we are to obtain a faithful free-energy potential (and hence phase diagram) in terms of the order parameters for the transformation.

The problem is highly nontrivial as the nature of the transformation mechanism depends crucially on orientation relationships between the structures, and therefore a solution requires exploring myriad symmetry relationships among the structures. However, with the aid of large symmetry databases, and by integrating ideas from metallurgy to phonon physics, we have recently demonstrated that the transformation can be accomplished via an intermediate hexagonal structure with specific strains and displacements [1]. Figure 1 shows one of two possible paths from fcc to the monoclinic via the simple hexagonal intermediate. The trigonal three-atom unit cell is the common subgroup between the fcc and the simple hexagonal, and the arrows indicate the displacement of atoms from the fcc. At their end positions, the atoms are located at a simple hexagonal lattice and 16 primitive simple hexagonal unit cells combine to form a 16-atom unit cell that subsequently distorts to the  $\alpha$  unit cell.

*Fig. 2. The predicted mechanism is consistent with anomalies in the experimental phonon dispersion (arrows in the inset) for  $\delta$  Pu. The fcc and hexagonal Brillouin zones are embedded with the appropriate orientation and the ovals are predicted locations of anomalies.*

Transformation path via simple hexagonal intermediate

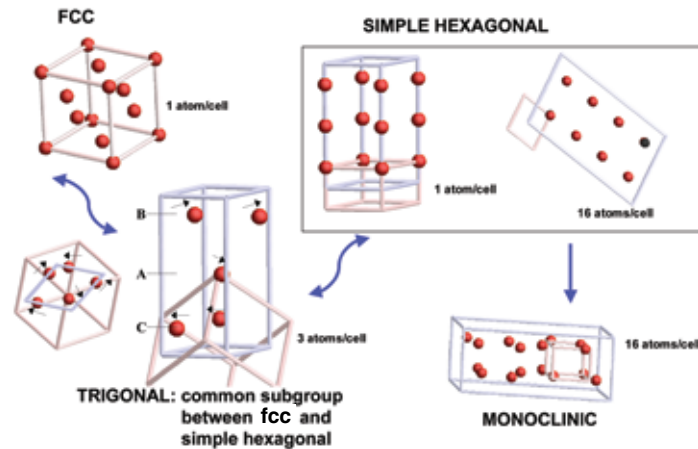
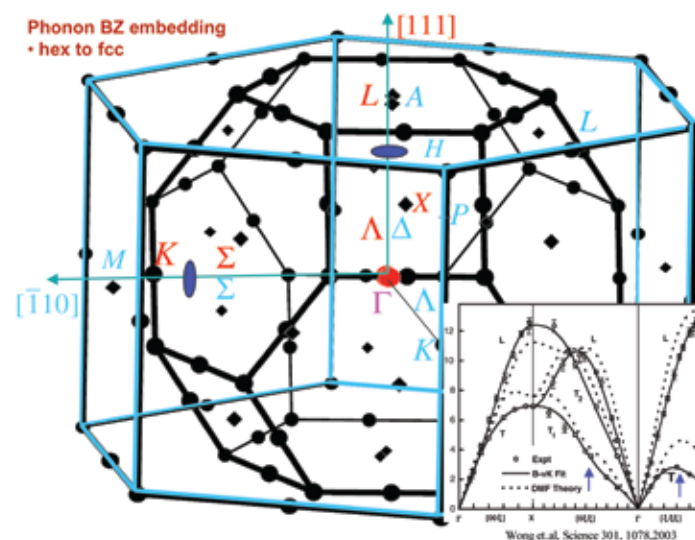


Figure 2 (inset) shows the phonon dispersion data for the  $\delta$  phase (black lines) as compared to the predictions of dynamical mean field calculations (dashed lines). The anomalies in the experimental data suggesting instabilities or softening in specific directions (away from the  $\delta$  and towards  $\alpha$ ) are indicated by arrows. The locations of these anomalies are consistent with the





predictions from our mechanism, and are shown by the blue ovals in the combined embedding of the fcc and hexagonal Brillouin zones that takes into account the orientations of the two crystal structures. Of the two pathways we have predicted, only energy calculations can determine which of these would be favored. Figure 3 shows the result for the volume and energy for the two candidate pathways (via simple hexagonal and hexagonally closed packed [hcp]) from a molecular statics calculation [2] using the modified embedded atom potential (MEAM). The path via the hcp is clearly energetically preferred, and the calculation shows that the volume change occurs in the second step, from the intermediate to the monoclinic. The work points to difficulties with the MEAM potential from the intermediate to the monoclinic structure and illustrates the need for reliable electronic structure calculations for Pu.

Our work implies that orientation relations in actinides severely restrict transformation pathways, so that the problem of obtaining a free energy to describe the process becomes tractable. Moreover, Pu sits at a threshold of a change in character of the orientation relationship from lighter to heavier actinides, correlating with changes in the character of electron itinerancy, magnetism, and volume.

**For further information contact Turab Lookman at [txl@lanl.gov](mailto:txl@lanl.gov).**

[1] T. Lookman, A. Saxena, R.C. Albers, *Phys. Rev. Lett.* **100**, 145504 (2008).

[2] R. Groger, T. Lookman, A. Saxena, *Phil. Mag. B* March (2008). arXiv:0812.0985 on [lanl.arXiv.org](http://lanl.arXiv.org)

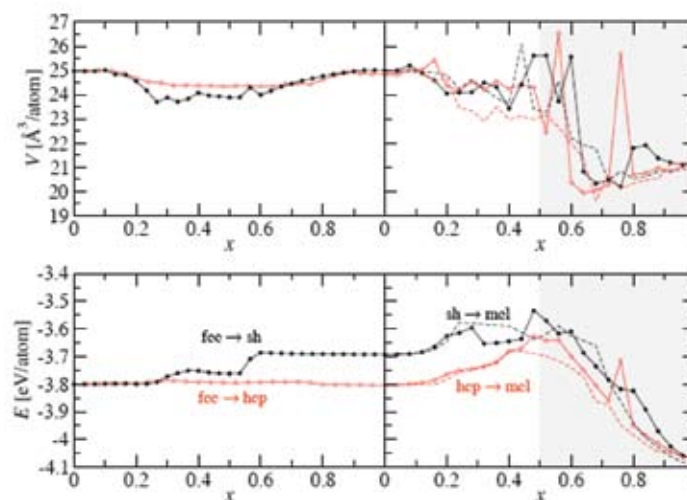


*Fig. 3. Energy and volume calculated as a function of atomic displacements from fcc ( $x = 0$ ) to the intermediate hexagonal and then to the monoclinic, using the MEAM potential for Pu. The favored intermediate structure is the hcp and the volume change occurs in the second step from the hexagonal to monoclinic symmetry.*

#### Funding

#### Acknowledgments

- DOE, NNSA, Advanced Simulation and Computing Program
- Glenn T. Seaborg Institute
- LANL Directed Research and Development Program
- Center for Nonlinear Studies

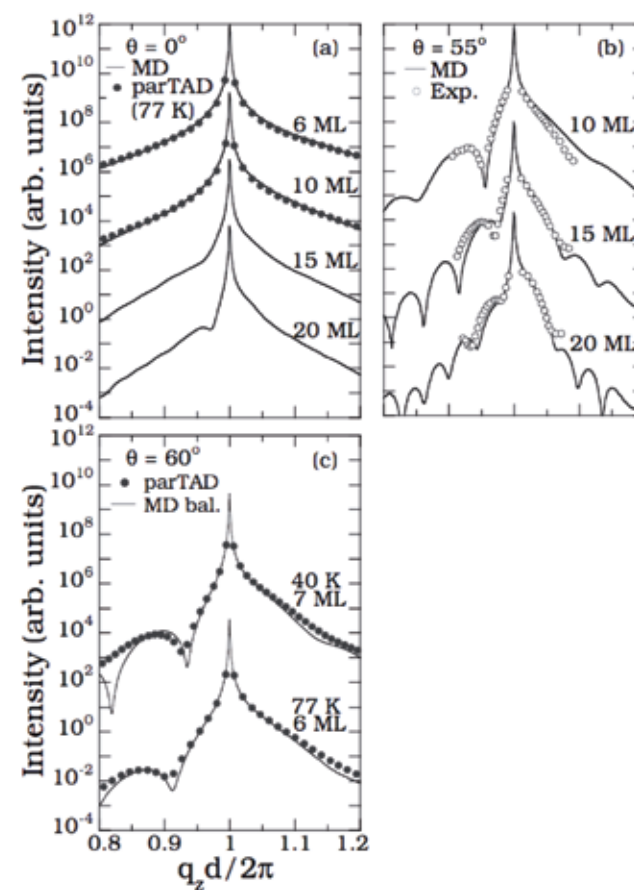
# Nanoscale Roughness and Cliffs in Low-temperature Growth of a Copper Surface

Yunsic Shim, Valery Borovikov, Jacques G. Amar, University of Toledo;  
Blas P. Uberuaga, MST-8; Arthur F. Voter, T-1

*Fig. 1. X-Ray diffraction (XRD) patterns for copper films grown on Cu(100). a) synthesized XRD spectrum from molecular dynamics (MD) and ParTAD simulations at normal deposition angle. b) Comparison of experimental XRD pattern [4] with XRD pattern predicted from MD at deposition angle (from normal) of 55 deg. c) Comparison of XRD spectra predicted by MD and ParTAD at 60 deg. The ParTAD films, grown 100,000 times slower, show a softening of the XRD peaks due to the smoothing of the surface caused by the thermal diffusion events during deposition.*

The process of vapor-deposited film growth, in which a crystal or film is grown one atom at a time as atoms arrive at the surface, can give rise to a surprisingly rich variety of surface morphologies [1]. Even for a simple metal like copper or silver, raising the temperature at which the growth is performed can give a surface that is smooth, then rough, then smooth, and then rough again. This effect results from the interplay of the deposition events with the various atomic diffusion and relaxation mechanisms that are active at a given temperature. The deposition angle and deposition rate also come into play, and having more than one atom type complicates matters further, so the overall complexity is daunting if one is trying to choose experimental conditions that will give a desired film morphology. It is thus valuable to have atomistic simulation tools with which we can probe and build an understanding at the microscopic level.

While the standard atomistic simulation approach, molecular dynamics (MD), is limited to time scales of less than a microsecond, the temperature accelerated dynamics (TAD) method developed here at LANL [2] offers a way to reach the time scales of milliseconds and seconds on which film growth takes place (a typical growth rate is of the order of a monolayer per second). TAD achieves this by raising the temperature of the system to cause more frequent attempted activated events, and then correcting the dynamics by allowing only those events that would have occurred at the desired lower temperature. We have used TAD to study film-growth problems in the past, but we have been limited to systems of roughly 1000 atoms or fewer due to the poor scaling of the TAD method with system size. This has precluded studying film growth problems where the feature



size in the morphology is larger than a few times the lattice constant.

Recently, building on a development of Shim and Amar [3], we have developed an effective way to spatially parallelize a TAD simulation, so that we can reach a larger length scale at the same time as we extend the time scale. Although this ParTAD method [4] has additional overhead, it allows us to study systems many times larger than before, opening the way for studying more complex film growth systems, as well as many other processes in materials science that involve substantial time and length scales simultaneously.

A good example of a film-growth system that can benefit from atomistic interpretation is the low-temperature, off-axis growth of copper on Cu(100), recently studied experimentally by Miceli and coworkers [5-7]. Using X-ray diffraction analysis, they observed large compressive strains normal to the surface for films grown below  $T = 100\text{K}$ , from which they concluded that large concentrations of vacancies were incorporated into the films as they grew.

Using MD and ParTAD, combined with an accurate embedded atom method [8] interatomic potential for copper [9], we have simulated the growth of these films [10]. The X-ray diffraction curves synthesized from the atomistic simulations are in impressively good agreement with the experimental ones (see Fig. 1), but we find a striking difference in the interpretation of what gives rise to the compressive strain and the features in the spectrum. There are almost no bulk vacancies in the film, but we do find an anisotropic nanoscale roughness when the films are grown off-axis, as shown in Fig. 2. Moreover, we find a surprising tendency for the film to form perfectly vertical [100] walls, or “cliffs,” as shown in Fig. 2d. The roughness arises from a combination of suppression of key activated events (due to the low temperature) that would otherwise smooth the film, and a shadowing effect due to the off-axis nature of the arriving atoms. Even at these low temperatures, thermally activated events do occur, but they do not strongly affect the film morphology—direct MD simulations of the growth on artificially fast time scales, allowing only a few picoseconds between successive depositions so that most activated events do not have time to occur, give films that are qualitatively similar (see the X-ray spectrum comparison in Fig. 1c). However, when the growth is simulated using kinetic Monte Carlo, a widely used model built on standard assumptions about the activated-event mechanisms, the result is a very different film morphology with nanoscale pyramids, so realistic atomistic detail is important in understanding this type of film growth process.

**For further information contact Arthur F. Voter at [afv@lanl.gov](mailto:afv@lanl.gov).**

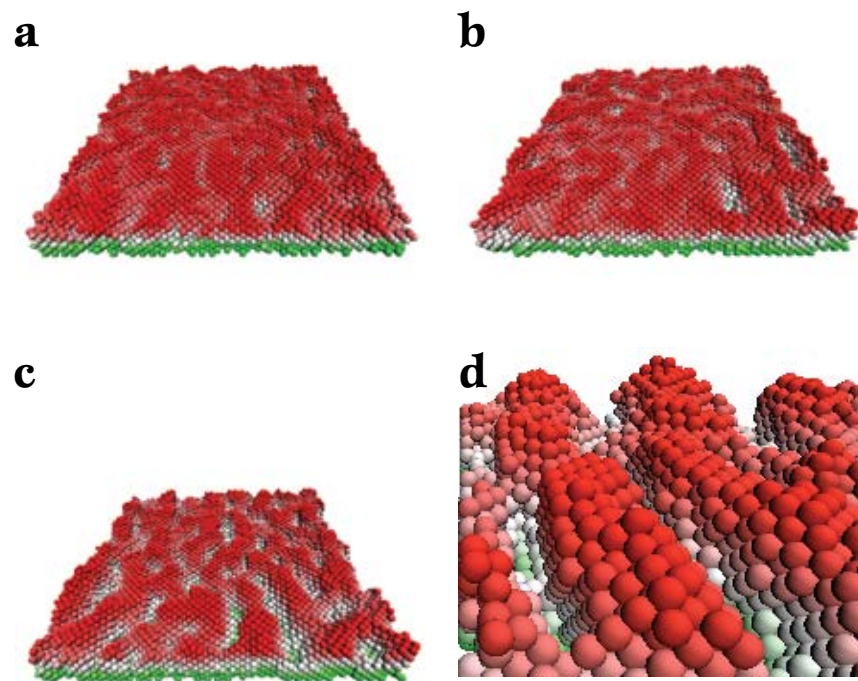


*Fig. 2. Surface morphology for copper films grown to seven monolayer thickness on Cu(100) at  $T = 40\text{K}$  using ParTAD. The deposition rate is 5000 monolayers per second. a) Normal deposition incidence – note the smoothness. b) Deposition angle (from normal) 30 deg, and c) 60 deg. Note the increasing nanoscale roughness with increasing deposition angle (arrows show the direction of deposition) and the steep canyon walls at 60 deg. d) Close-up of c), showing completely vertical cliff walls.*

- [1] J.W. Evans et al., *Surf. Sci. Rep.* **61**, 1 (2006).
- [2] M.R. Sørensen, A.F. Voter, *J. Chem. Phys.* **112**, 9599 (2000).
- [3] Y. Shim, J.G. Amar, *Phys. Rev. B* **71**, 125432 (2005).
- [4] Y. Shim et al., *Phys. Rev. B* **76**, 205439 (2007).
- [5] C.E. Botez et al., *Phys. Rev. B* **66**, 075418 (2002).
- [6] C.E. Botez et al., *Phys. Rev. B* **66**, 195413 (2002).
- [7] C.E. Botez et al., *Appl. Phys. Lett.* **81**, 4718 (2002).
- [8] M.S. Daw, M.I. Baskes, *Phys. Rev. B* **29**, 6443 (1984).
- [9] A.F. Voter, *Phys. Rev. B* **57**, 13985 (1998).
- [10] Y. Shim et al., *Phys. Rev. Lett.* **101**, 116101 (2008).

### Funding

### Acknowledgments

- National Science Foundation
- LANL Directed Research and Development Program



## Statistical Design for Uranium Corrosion Experiments

Joanne R. Wendelberger, Leslie M. Moore, CCS-6

---

*Fig. 1. Blisters on the surface of a uranium coupon sample may be visible early in the uranium corrosion process. Statistical analysis of data from the uranium corrosion study will investigate uranium hydride initiation and growth.*

---

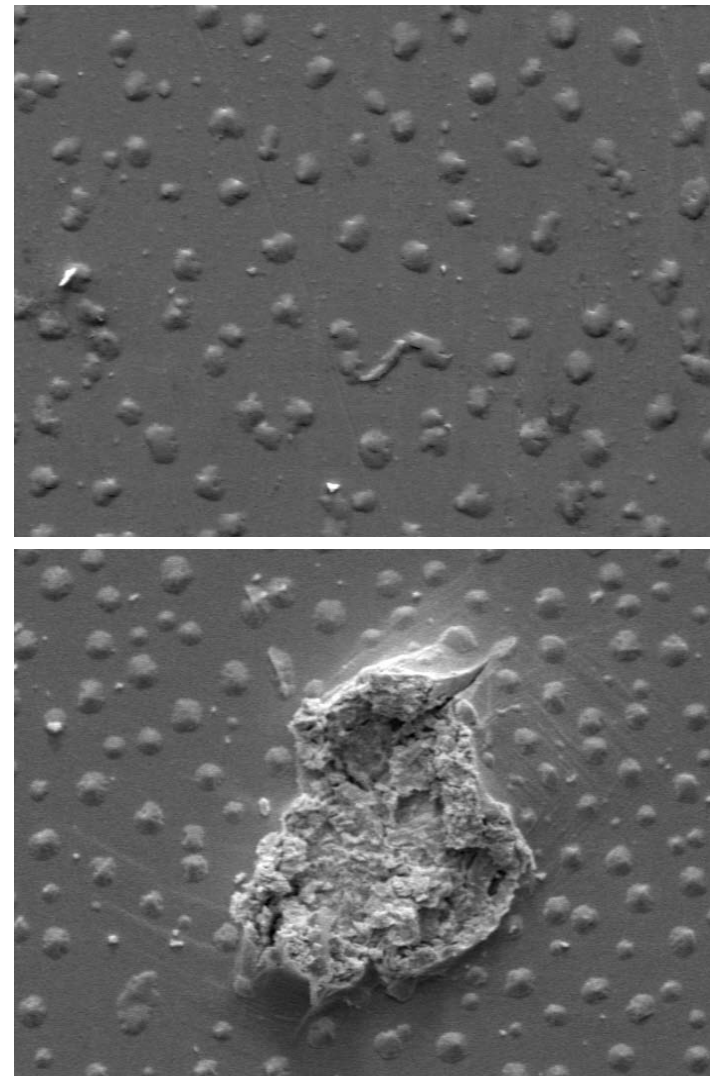
---

*Fig. 2. As the uranium corrosion process continues, the metal surface of the uranium coupon may rupture. A designed experiment provides information about the effects of the different experiment variables.*

---

Statistical experiment design techniques were developed for generating multilevel experiment designs in the presence of a linear trend variable. This work was motivated by the need for an efficient experiment plan for a uranium experiment being conducted by Roland Schulze and Mary Ann Hill, MST-6, to study hydride formation, one of the most important forms of corrosion observed in uranium and uranium alloys. The results of this experiment will contribute to the understanding of uranium corrosion processes. The study goals and objectives of the experiment are described in [1], and the work described here focuses on development of an approach for generating a statistical experiment plan. The experiment planning methods used allow for robust data collection accommodating other sources of variation such as the density of inclusions, which, in this case, varies linearly along the cast rods from which samples are obtained.

The uranium hydride study, now underway, will examine the effects of headspace gas pressure, gap size, and abrasion on uranium hydride initiation and growth. The statistical experiment plan for the uranium hydride study was designed to efficiently collect data to aid in understanding the impact of the experiment factors on initiation and growth of corrosion. Uranium hydride behavior will be measured by quantifying corrosion density, spatial distribution, and volume as a function of aging time on surfaces of uranium coupons. The actual measurements include hydrogen pressure measured over time and digital images, similar to those shown in Figs. 1 and 2, of the metal surfaces from which corrosion can be observed and quantified.



A common statistical approach for experiment planning involves the use of factorial or fractional factorial designs where all or a specially selected subset of all combinations of several variables are included in experimentation [2]. In addition, to collect information on variability, some of the experiment conditions may be repeated. Specifically, for this study, three replicates were planned for each experiment

condition. In order to keep the number of possible combinations manageable, generally only two or three values are considered in initial experiment studies. For headspace gas pressure, three values were planned based on results from a preliminary study to investigate reaction rates. Three values for uranium interface gap were selected that included no gap and two different size gaps. The abrasion variable has two values corresponding to either presence or absence of abrasion. Hence, for these three variables, the full factorial experiment set includes  $3 \times 3 \times 2 = 18$  combinations, so with three replicates each, a total of 54 experiments are planned. Some additional control samples are also included in the experiment.

During sample preparation, the casting procedure for the rods from which the uranium coupons were cut was observed to have variable properties, particularly with respect to inclusions along the length of the rod. Measurements of the density of inclusions in a rod exhibited a clear linear trend. As a result, inclusion density needs to be considered in experiment planning. Since inclusions provide possible hydride corrosion entry points, the number of inclusions is expected to have an effect on the variability in hydride corrosion behavior. Inclusion density effectively adds an additional nuisance variable, along with the three main variables of initial interest for the current experiment plan.

An experiment plan was required that could assign three samples to each of the 18 conditions defined by the three main variables (headspace gas pressure, uranium interface gap, and coupon surface abrasion) such that the anticipated trend with inclusion density does not bias estimation of effects of the three variables of primary interest. This type of experiment planning is referred to in the statistics literature as trend-free experiment design [3-5]. Although the desire for a trend-free design generally arises with an anticipated time trend, and the literature generally considers factorial structure with two or three levels, the new experiment planning issues here include accommodating factorial structure with mixed numbers of levels. The mixed levels structure means that the balance needed to achieve trend-free estimates is not perfectly attainable but only nearly so.

An experiment plan was developed to investigate headspace gas pressure, uranium interface gap, and coupon surface abrasion effects on uranium hydride initiation and growth on coupon samples. The experiment plan was constructed to accommodate the presence of the trend variable associated with density of inclusions varying with location in the cast rods, by carefully assigning samples cut from the different locations on the rod to the combinations of experiment conditions to achieve a nearly trend-free design.

**For further information contact Joanne Wendelberger at [joanne@lanl.gov](mailto:joanne@lanl.gov).**

- [1] R.K. Schulze, M.A Hill, LA-UR-08-1879 (2008).
- [2] C. Wu, M. Hamada, *Experiments: Planning, Analysis, and Parameter Design Optimization*, John Wiley & Sons, New York (2000).
- [3] M.L. Lin, A.M. Dean, *Annals of Statistics* **19**(3), 1582-1596 (1991).
- [4] P.W.M. John, *Technometrics* **32**(3), 275-282 (1990).
- [5] A.C. Atkinson, A.N. Donev, *Technometrics* **38**(4), 333-341 (1996).

**Funding  
Acknowledgments**  
DOE, NNSA, Enhanced  
Surveillance Campaign

## Blast Effects Analysis with the CartaBlanca Computer Code

Paul T. Giguere, Xia Ma, Duan Z. Zhang, T-3

**C**artaBlanca [1] employs modern discretization schemes and solution methods for nonlinear physics problems on unstructured grids in 1D, 2D, and 3D. CartaBlanca has been used to simulate multiphase flows, fluid-structure interactions, heat transfer and solidification, and free-surface flows. The Arbitrary Lagrangian-Eulerian (ALE) method is used to provide flexibility with regard to physical models, and the Material Point Method (MPM) is used to effectively trace large deformations of materials with mechanical strength. In MPM, state information such as density and stress of the material is carried by discrete computational particles that are free to move within the problem domain. The basic equations solved in CartaBlanca are based on multiphase flow theory. Each phase is allowed to have its own stress (or pressure) field evolving according to its constitutive relation (or equation of state). Heat, mass, and momentum transfer can be calculated. One of CartaBlanca's greatest strengths is in the tight coupling between fluids represented by ALE meshes and solid structures represented by MPM particles.

Shown here are results from a CartaBlanca simulation of an explosion in a parking garage, at 55 ms and 146 ms after the explosion of a truck bomb. The calculation used MPM to represent the garage structure (light gray particles) and an underlying substrate (dark gray particles). The response of the ambient air is calculated with the ALE method. An

isosurface of air pressure at 5 bars is shown with the solid (red) surface. In these figures the front of the garage is removed to allow a clear view of the interior of the explosion and the garage response.

**For further information contact Duan Z. Zhang at [dzhang@lanl.gov](mailto:dzhang@lanl.gov).**

[1] <http://www.lanl.gov/projects/CartaBlanca/>



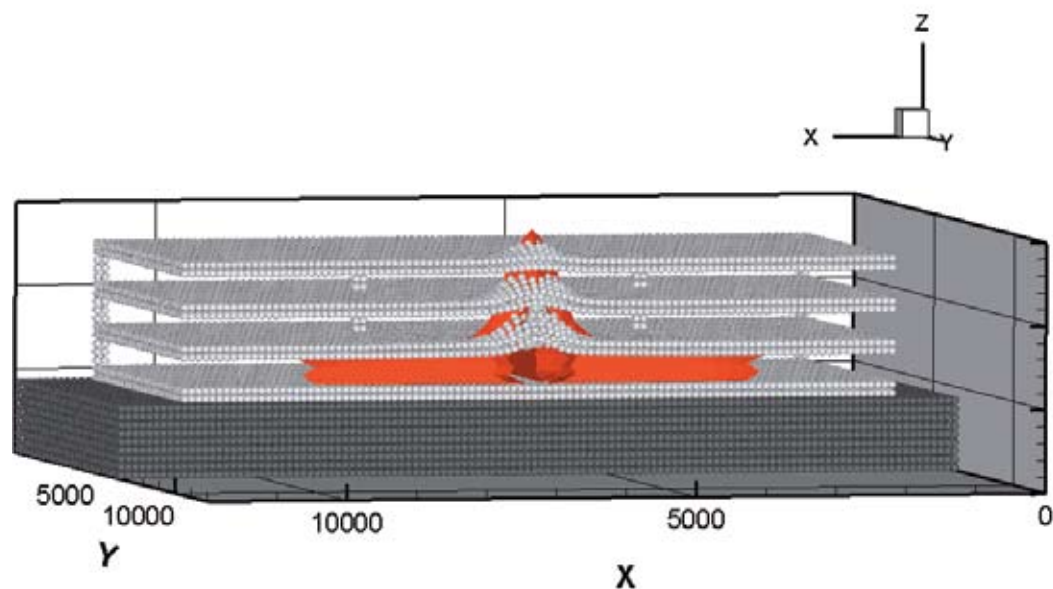


*Fig. 1. Simulation of an explosion in a parking garage 55 ms after the explosion of a truck bomb.*

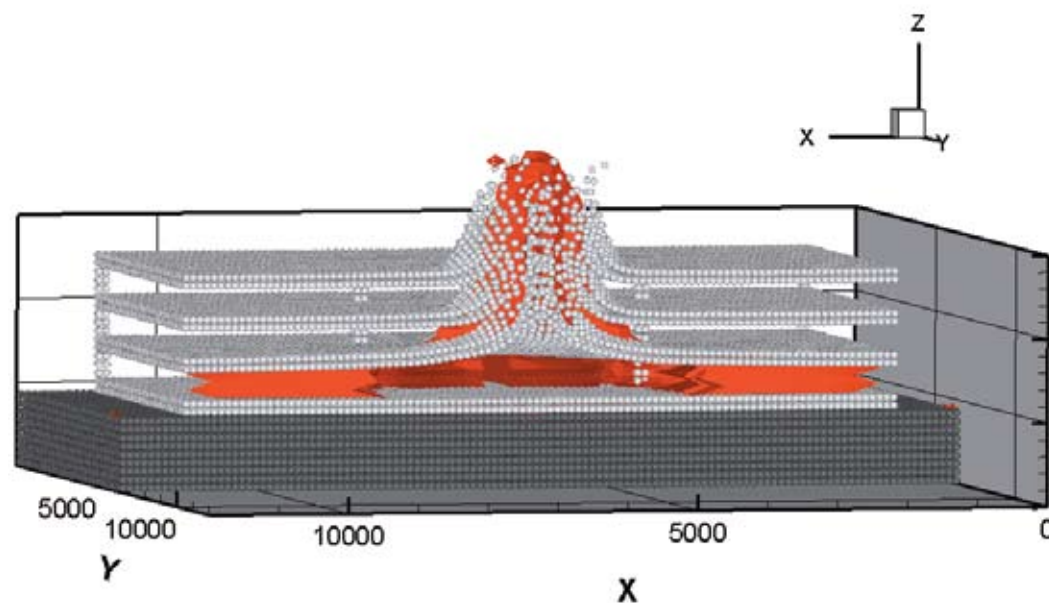


*Fig. 2. Simulation of an explosion in a parking garage 146 ms after the explosion of a truck bomb.*

#### **Funding**

#### **Acknowledgments**

DOE, Office of Science,  
Office of Advanced  
Scientific Computing  
Research Urban Nuclear  
Consequences Project





# Modeling Complex Networks

As abstract as the term “complex network” sounds, we create and use such networks in our daily activities. A complex network refers to social, biological, or technological fabrics and interconnections with nontrivial topological structures. Each of us is part of, interacts with, and creates new complex networks every day. Each time we interact with someone in our social network, search for information on a network, use any network-connected device (like a cellular telephone), drive to work, purchase an item, or consume electricity, we are part of, and interact with, a plethora of active complex networks. Central to extracting useful information from such networks is to discover within them islands of related

entities and the connections between them.

Papers in this section describe recent advances in the modeling of complex networks, from basic theory on equilibrium states in the presence of noise, to new mathematical methods to identify protein similarities, to a variety of ground-breaking simulations of human activities for infrastructure simulation and the analysis of the critical National Internet Infrastructure.

This exciting and emergent field, along with the unique scientific capabilities at LANL, has the power to transform infrastructures we utilize each day, our National response to disaster, and our fundamental quality of life.



## How Far is Far from Equilibrium? A Deeper Understanding in the Presence of Noise

Antonio M. Cadilhe, T-1 and GCEP-Centro de Fisica da Universidade do Minho, Braga, Portugal; Arthur F. Voter, T-1

**N**onequilibrium systems have both fundamental and technological interest as they usually provide a richer behavior than their equilibrium counterparts. For example, driven systems are those acted on by a time-dependent generalized force. In spite of the present research interest in nonequilibrium systems across different scientific disciplines, little research effort has been devoted to the diagnosis of how far a system has been pulled away from its equilibrium state. Addressing such an issue is both scientifically and technologically relevant, as well as challenging. Understanding how far a system has moved away from its equilibrium state benefits not only the overall understanding of driven systems, but also equilibrium ones.

Consider a particle of mass  $m$  in contact with a heat reservoir, at temperature  $T$ , evolving in a basin of attraction provided by a potential  $V(x)$ . The coupling to the heat reservoir is achieved using the well-known Langevin dynamics [1]. Langevin dynamics adds a noise term to Newton's equation of motion so that the dynamics accounts for the presence of the heat reservoir. Two initial conditions, namely,  $x(0) \equiv x_0$  and  $\dot{x}(0) \equiv \dot{x}_0$ , are required to describe the motion of the particle. Let us consider a parabolic potential depicted in Fig. 1 by the solid line with a natural frequency  $\nu_0$ . Now, consider two trajectories  $x_1(t)$  and  $x_2(t)$  evolving according to Langevin dynamics. It has been shown [1] that if the provided random noise sequence is common to both trajectories, they merge into a single trajectory, the so-called master trajectory. This *synchronization* effect is illustrated in Fig. 2a for a pair of undriven trajectories.

Now consider the case of a particle being kept away from its equilibrium state under the influence of a time-dependent parabolic potential basin with an initial frequency  $\nu_i$ . The

rate at which the initial frequency changes in time sets a natural time scale that we denote as the driving rate,  $\alpha$ . Similar to the static trajectories, Fig. 2b shows a schematic of a pair of driven trajectories also merging into a (driven) master trajectory. We were able to obtain an exact, closed-form, analytical solution for the case of a pair of trajectories in a time-dependent parabolic potential. At the instant the frequency of the driven system takes the value  $\nu_0$  at time  $t^*$ , one can also measure the mismatches between the driven and undriven (master) trajectories. Of course, one does not expect the driven and undriven master trajectories to exactly coincide at  $t^*$ , so this mismatch represents a measure of how far the driven system has been pulled away from its equilibrium state as it crosses  $\nu_0$ . One expects the synchronization level to be dependence on the driving rate,  $\alpha$ . The idea can easily be grasped by noticing that at vanishingly small driving rates, the synchronization level must match that of a static system. The dependency on the driving rate  $\alpha$  can actually be observed in the log-log plot shown in Fig. 3, where the mismatch in the synchronization increases with increasing values of the driving rate. At high driving rates, comparable to the natural frequency  $\nu_0$  of the basin, nonlinear terms become relevant.

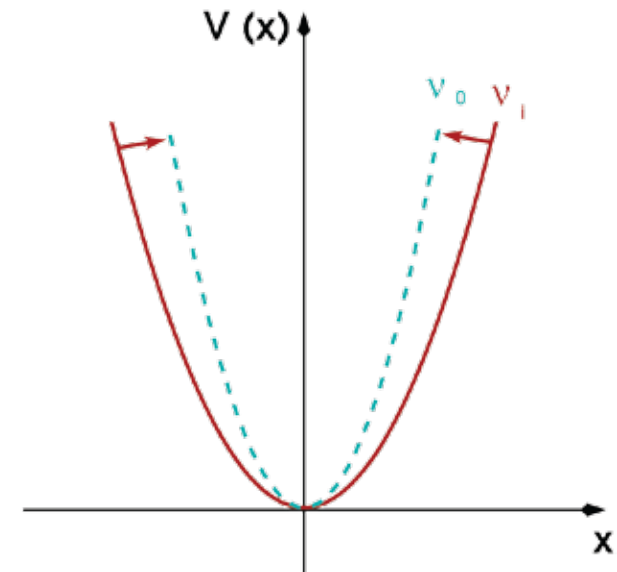


*Fig. 1. Plot of the parabolic potential. The dashed line represents the potential felt by a static system of frequency  $\nu_0$ . The time-dependent potential has an initial frequency  $\nu_i$  (solid line) and crosses the  $\nu_0$  value (dashed line) at time  $t^*$ .*

In summary, studying the synchronization of pairs of trajectories evolving according to Langevin dynamics and sharing the same noise sequence allows an understanding of the timescale required for their thermalization in a particular basin, as well as the degree of departure from equilibrium for a driven system. As Fig. 3 shows, for driving rates comparable to the natural frequency of the basin, nonlinear terms become relevant, which can help define more elaborate ways to classify departure from equilibrium. Even at extremely low driving rates, there is deviation from perfect equilibrium, which we can quantify with this approach. We are also exploring the connection between this disruption of synchronization and the deviations in the instantaneous rate constants in the system. This in turn will give us a simple way to quantify and control errors in the application of parallel replica dynamics [2] to driven systems [3]. In driven parallel replica dynamics, it is assumed that there are well-defined instantaneous rate constants that are independent of the driving rate. Finally, we point out that the present methodology can be straightforwardly extended to more realistic systems with complex potentials and larger numbers of particles.

**For further information contact Antonio M. Cadilhe at [cadilhe@lanl.gov](mailto:cadilhe@lanl.gov).**

[1] D. Frenkel, B. Smit, *Understanding Molecular Simulation*, Academic Press (2002).

[2] A.F. Voter, *Phys. Rev. B* **57**, R13985 (1998).

[3] B.P. Uberuaga et al., *J. Chem. Phys.* **120**, 6363 (2004).

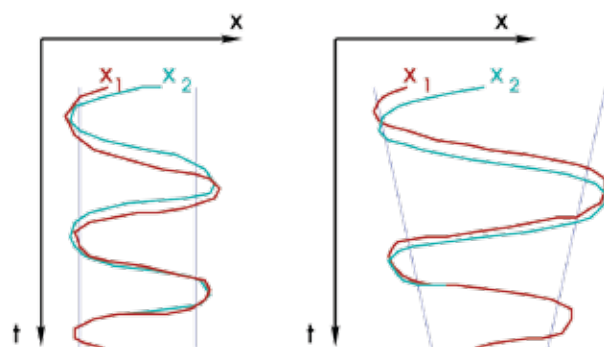


*Fig. 2. Schematic examples of pairs of trajectories merging into a master trajectory for the (a) time-independent and (b) time-dependent potentials. Jagged lines represent a way of cartooning the effect of Langevin dynamics. Both the static and driven pairs of trajectories synchronize into a master trajectory at a time  $t_s < t^*$ . Notice that  $t_s$  does not have to be the same for the driven and static systems. The synchronization level is computed as the driven system crosses  $v_0$  at time  $t^*$ .*

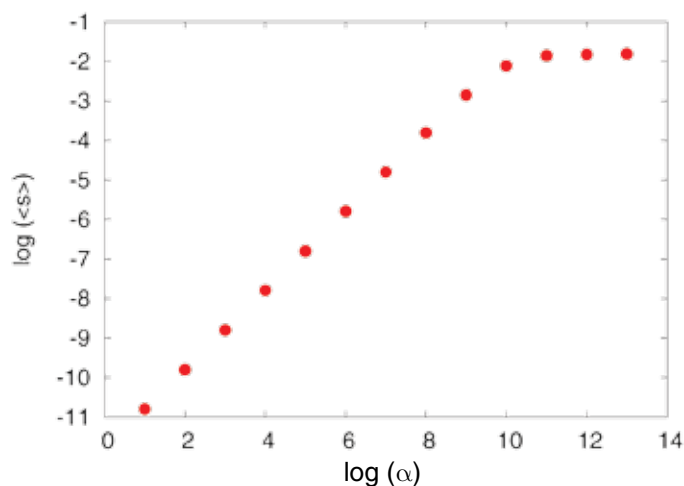


*Fig. 3. Mismatch (deviation from perfect synchronization) between the positions of the driven and undriven trajectories  $v(t) = v_0$ , averaged over  $10^4$  pairs of trajectories. The coupling strength to the heat reservoir is  $\gamma = 10^{12} \text{ s}^{-1}$ .*

### Funding

### Acknowledgments

DOE, Office of Science,  
Office of Basic Energy  
Sciences

## BIOGRAM: Algorithms for Identifying Similar Proteins by Functional Annotation

Judith D. Cohn, Susan M. Mniszewski, CCS-3; Hong Cai, Jennifer F. Harris, B-7;  
Ruy M. Ribeiro, T-6; Cliff A. Joslyn, PNNL; Karin M. Verspoor, University of Colorado  
Health Sciences Center

In the study of complex biological systems, it is often useful to identify proteins that exhibit a similar functional signature within a cell or organism but do not necessarily have homologous sequences or any single biological feature in common. BIOlogical GRaphical Measurement (BIOGRAM) is a software system under development that uses the mathematical structure underlying the controlled vocabulary of the Gene Ontology (GO) [1] to measure protein similarity based on annotations assigned to nodes in the three branches of the GO: Biological Process (BP), Molecular Function (MF), and Cellular Component (CC). This system builds upon the Partially Ordered Set Ontology Categorizer (POSOC), a software tool for automating protein functional annotation [2,3].

BIOGRAM uses a hierarchical adaptation of information retrieval (IR) performance statistics (recall, precision, and f-score) to measure protein similarity based on annotations assigned to the nodes of the GO. The network structure of the GO along with the use of hierarchical statistics allows us to make fuzzy comparisons of functional profiles, giving partial credit for matches to nearby nodes. Figure 1 illustrates the calculation of hierarchical recall (HR), hierarchical precision (HP), and hierarchical f-score (HF, the geometric mean of HR and HP) within a partially ordered set comparing the functional annotations of a target protein with those of a second protein (other). BIOGRAM is being developed to guide selection of experimental targets in the context of modeling host-pathogen interactions (pathomics) in avian influenza.

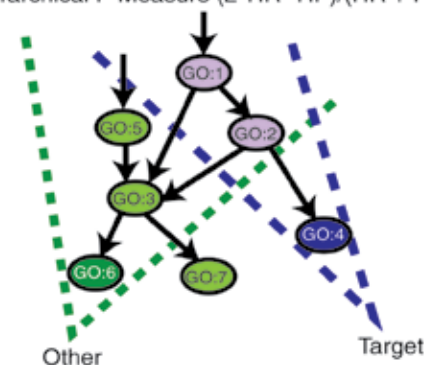
GO annotations for all human proteins in the Swiss-Prot database were obtained from the European Bioinformatics Institute (EBI). Our analysis was performed using

annotations drawn from all evidence codes (13,841 proteins) or a subset obtained only from curated evidence codes (9,090 proteins). In most cases, there were multiple annotations for each protein in each GO branch. Thus far, we have analyzed a number of proteins known to be involved in the response to influenza infection in humans by comparing annotations in the BP branch of the GO for each target protein (for example, tumor necrosis factor alpha or [TNFA]) against those of all other human proteins. A partial list of TNFA annotations includes response to virus, leukocyte adhesion, and anti-apoptosis. Only a small set of proteins show a high level of similarity to TNFA, whether using all or the curated subset of annotations (see Fig. 2). Protein similarity can be determined by rankings based on HR, HP, or HF. The top ten human proteins similar to TNFA based on HR using curated annotations are shown in Fig. 3. A detailed exposition of the specific annotations that underlie the hierarchical statistics can be obtained for any pair of proteins (e.g., TNFA and BCL3).

Future plans include the addition of reaction pathway and protein-protein interaction data.

*Fig. 1. Hierarchical recall (HR), hierarchical precision (HP), and hierarchical f-score (HF) calculations are shown in context of a partially ordered set structure, such as the Gene Ontology (GO). The use of overlapping filters allows for a fuzzy measure of similarity.*

HR = Hierarchical Recall  
HP = Hierarchical Precision  
HF = Hierarchical F-Measure  $(2 \cdot \text{HR} \cdot \text{HP}) / (\text{HR} + \text{HP})$



$G(\text{Target}) = \{\text{GO:4}\}$ , filter(GO:4) = {GO:1, GO:2, GO:4}  
 $G(\text{Other}) = \{\text{GO:6}\}$ , filter(GO:6) = {GO:1, GO:2, GO:3, GO:5, GO:6}  
 HR = 2/3, HP = 2/5, HF = 1/2



For more information contact Susan Mniszewski at [mmm@lanl.gov](mailto:mmm@lanl.gov).

- [1] The Gene Ontology website, <http://www.geneontology.org>.
- [2] C.A Joslyn et al., *Bioinformatics* **20** Suppl 1, i169-77 (2004).
- [3] K.M. Verspoor et al., *Prot. Sci.* **15**(6), 1544-9 (2006).

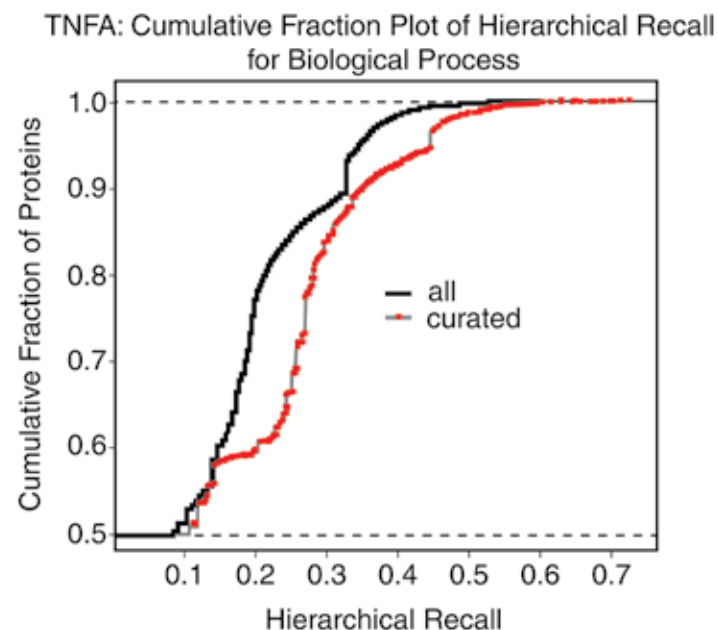


*Fig. 2. Cumulative fraction plot of hierarchical recall (HR) for TNFA against all human proteins: comparison between results obtained from annotations of all evidence types (black) vs curated only (red).*

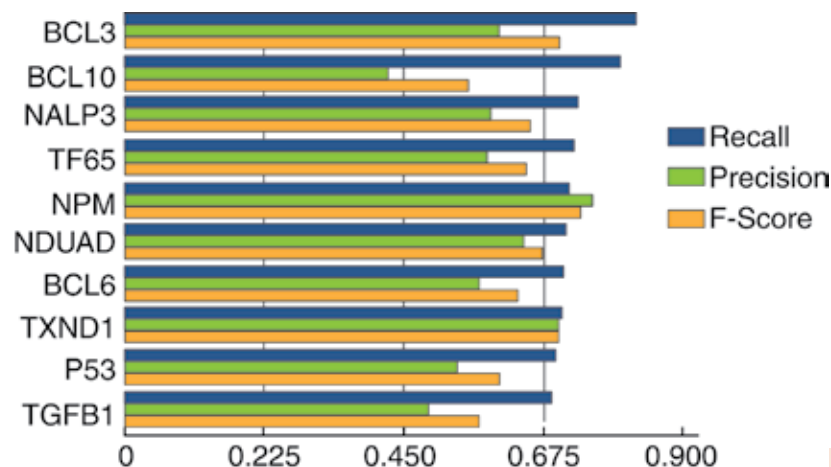


*Fig. 3. The top ten human proteins that were determined to be similar to TNFA based on the BIOGRAM hierarchical recall (HR) are shown, along with their corresponding hierarchical precision (HP) and hierarchical f-score (HF) values.*

## Funding

## Acknowledgments

LANL Directed Research and Development Program

## ActivitySim: Large-scale Agent-based Activity Generation for Infrastructure Simulation

Emanuele Galli, Stephan Eidenbenz, Susan M. Mniszewski, CCS-3; Leticia Cuellar, D-6; Mary Ewers, D-4; Christof Teuscher, Portland State University

The U.S. Department of Homeland Security aims to model, simulate, and analyze critical infrastructures and their interdependencies across multiple sectors such as electric power, telecommunications, water distribution, and transportation. Most infrastructure sectors rely on an underlying network that gets used by individual people and business entities, or alternatively speaking, there is a demand for the service that the network supplies. Demand on networks is largely generated by people as part of their daily activities, such as driving to work, using energy to cook or to heat the house, using water and sewage systems, or making phone calls. Thus, an accurate *model for the daily activities* of individuals is a prerequisite for a simulation of demand. An agent-based approach is the only modeling paradigm that allows us to generate demand shocks as an emergent property of the simulation. Demand can vary from a normal day to emergency scenarios. As an example, communication demand in emergency situations is different from a baseline demand due to individuals evacuating in large numbers leading to a geographic demand shift, and emotional turmoil leading to increased call volume. A model of dynamic demand that generates realistic data is an open research area.

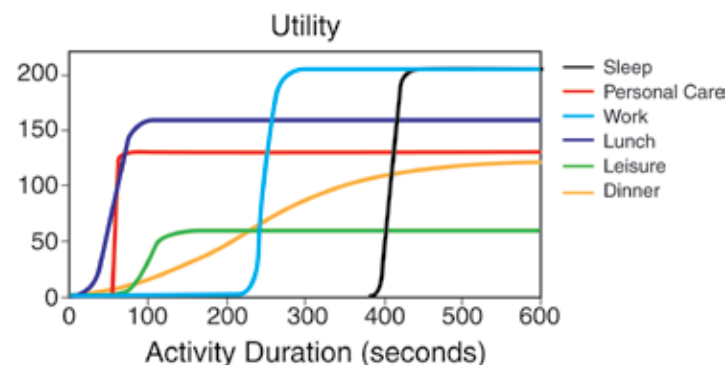
Fig. 1. Example Utility Functions.

ActivitySim is a scalable simulation tool that relies on a synthetic but statistically accurate population of the U.S. that was obtained using disaggregation methods applied to U.S. census data. ActivitySim is a part of a family of simulation applications that follow the SimCore modeling paradigm. SimCore is a library for building large-scale distributed-memory, discrete event simulations (DES) [1] using the open-source discrete event engine from the Parallel Real-time Immersive Modeling Environment (PRIME) [2] for passing

events, event queue maintenance, and synchronization. It is composed of Entities, Services, and Infos. An Entity is an object or component in the system that we want to model. A Service represents the functionality or behavior of an Entity. An Info is an event exchanged between entities or services. ActivitySim's architecture includes the "reactive agent" extension to SimCore called AgentCore with additional Entity capabilities to perceive, think and act, and process patterns of behavior or production rules.

SimCore applications can be integrated with each other by exchanging events. Therefore ActivitySim, communication network simulators such as SessionSim and MIITS-NetSim, and/or a transportation simulator FastTrans can be run as a coupled model. For example, an agent can select his/her activity schedule in ActivitySim and travel between locations via FastTrans. Events are used for the initiation and completion of trips.

ActivitySim agents are *utility-driven* [3,4]—that is, each activity gives a certain amount of utility to an agent depending on how long the activity is being executed (see Fig. 1). Agents also have *priority functions* for activity types, where the priority of an activity intuitively increases usually with the time that has passed since the activity was last executed. Activity types have *constraints* that allow us to guide the timing of certain activities (such as that work should happen during the business hours). As optional modules, we (a) allow agents to have *personality types* (guided by standard models from social sciences), and



## Modeling Complex Networks

(b) let agents guide their activity type selection by the *needs* that they want to satisfy.

The main loop of an agent consists of planning and replanning scheduled activities (see Fig. 2) and evaluation of the resulting updated schedule with respect to the agent's objective function. The objective function takes into account predicted utility as well as priority and constraints violations. The schedule optimization step can be performed through your favorite optimization method, such as the gradient method, local search, simulated annealing, or taboo search.

ActivitySim has been used to simulate the daily activities of a Twin Cities, MN synthetic population composed of 2.6 million individuals, with about 1M households and more than 480,000 different locations. The simulation was executed on the LANL Institutional Computing Coyote cluster and was run for 10 simulated days. Performance is shown in Fig. 3.

**For more information contact Stephan Eidenbenz at [eidenben@lanl.gov](mailto:eidenben@lanl.gov).**

- [1] L. Kroc et al., LA-UR-07-0590 (2007).
- [2] Parallel Real-time Immersive Modeling Environment (PRIME): <http://lynx.cis.fiu.edu:8000/twiki/bin/view/Publuc/PRIMEProject>
- [3] J. Vhang-Hyeon et al., *GeoJournal* **53**(4), 359-371 (2001).
- [4] E. Galli et al., "ActivitySim: Large-scale Agent-based Activity Generation for Infrastructure Simulation," Agent-Directed Simulation Symposium, Spring Simulation Multiconference (2009).

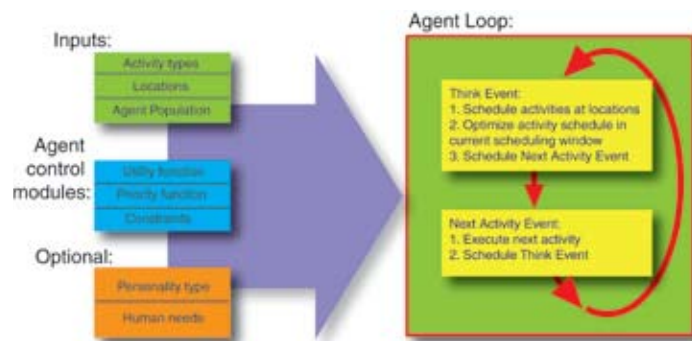


*Fig. 2. ActivitySim Inputs, Modules, and Think Loop.*

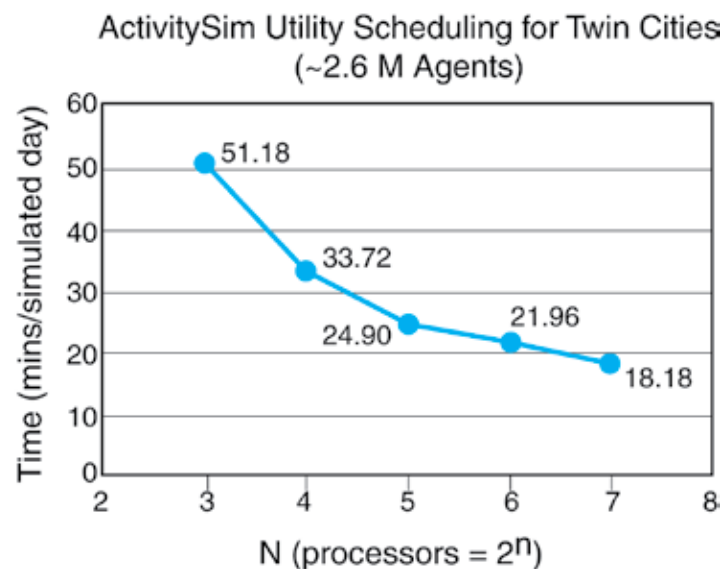


*Fig. 3. The run time per simulated day.*

**Funding  
Acknowledgments**  
Department of Homeland  
Security



## Using the MIITS-Internet Tool to Perform Criticality Analysis of National Internet Infrastructure

Guanhua Yan, CCS-3; Pallab Datta, Neurosciences Institute; Stephan Eidenbenz, Sunil Thulasidasan, CCS-3; Venkatesh Ramaswamy, Airvana, Inc.

As the Internet has permeated into almost every aspect of our daily lives, it is of crucial importance to ensure that its critical infrastructure functions properly. The Internet infrastructure can suffer severe physical damages due to disastrous natural catastrophes, such as hurricanes and earthquakes, or some physical attacks. Meanwhile, a malicious cyber attack (e.g., a distributed denial-of-service attack) can cause undesirable effects if it completely disables a critical Internet infrastructure facility, or even only makes it behave abnormally. As many other infrastructures such as power grids and transportation systems become increasingly dependent on the Internet for their normal operations, it is vital to protect the critical Internet infrastructure from severe physical damages and malicious cyber attacks.

Given the vast scale of the Internet, it is a challenging task to decide where we should dedicate our resources to protect its infrastructure, especially when the provided resources are limited. To tackle this challenge, we extended the capabilities of the LANL-developed modeling and simulation suite MultiScale Integrated Information and Telecommunications System (MIITS), and with this MIITS-Internet tool, we performed criticality analyses of the Internet infrastructure at a national level from three different methodological perspectives. A *graph-theoretical analysis* studies the structural properties of a geographical network condensed from the Internet backbone topology, including its degree of distribution, clustering structure, and its centrality measures. Although theoretically appealing, graph-theoretical analysis ignores the hierarchical routing scheme of the real Internet and uses the shortest-path routing scheme due to its simplicity. *Route-based analysis*, instead,

models realistic inter- and intradomain routing schemes used in the Internet and then identifies those facilities that appear most frequently on paths in the Internet backbone topology. Realizing that route-based analysis still produces biased results because all paths are evenly weighted, we propose another approach, traffic-based analysis, which weighs each path only by its traffic demands. To do this, we generate synthetic end devices and also session-level traffic among them. Different from previous efforts on Internet modeling, our work endeavors to achieve high fidelity by using realistic datasets such as U.S. census data, computer usage statistics, and market shares of Internet service providers.

Using the high-fidelity network model we have built, we find that the average number of locations each byte of domestic network traffic travels in the Internet backbone topology is about five—more specifically, the frequency histogram of the number of locations that a byte of domestic traffic visits in the Internet backbone is illustrated in Fig. 1. Furthermore, we rank different locations in the backbone based on the amount of traffic that travels through them and show the result in Fig. 2. We note that the top location is traversed by about 70 percent of the total traffic. Although surprising, this result is actually in concert with earlier observations that some locations witness more than 50 percent of the Internet traffic in the U.S. [1,2].

## Modeling Complex Networks

In a nutshell, the key findings with the MIITS-Internet tool include the following.

- (1) The geographical topology, which is condensed from a national-level IP backbone network and has a power-law degree distribution—it is a small-world network with a high clustering coefficient and a small characteristic path length. Moreover, the number of IP addresses at each location in the IP backbone network is well characterized by a power-law distribution.
- (2) A few locations appear much more frequently than others among all paths in the IP backbone topology, and these locations also witness a high percentage of the Internet traffic in the whole US.
- (3) Relative ranks of Internet facility locations from traffic-based analysis differ significantly from those derived from graph-theoretical analysis and route-based analysis, suggesting that a comprehensive, high-fidelity Internet model is necessary to assess critical Internet infrastructure facilities.

**For further information contact Guanhua Yan at [gghyan@lanl.gov](mailto:gghyan@lanl.gov).**

[1] <http://www.usip6.com/6sense/2005/sep/03.htm>

[2] <http://www.foxnews.com/story/0,2933,347035,00.html>

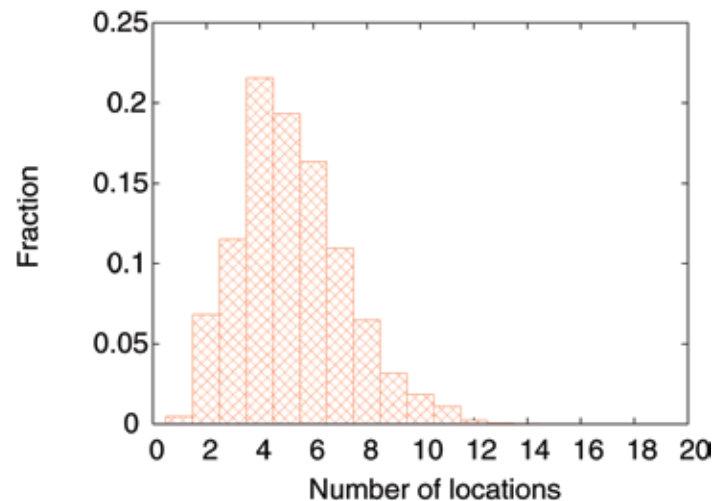


*Fig. 1. Number of locations that a byte of domestic network traffic traverses in the national Internet infrastructure.*

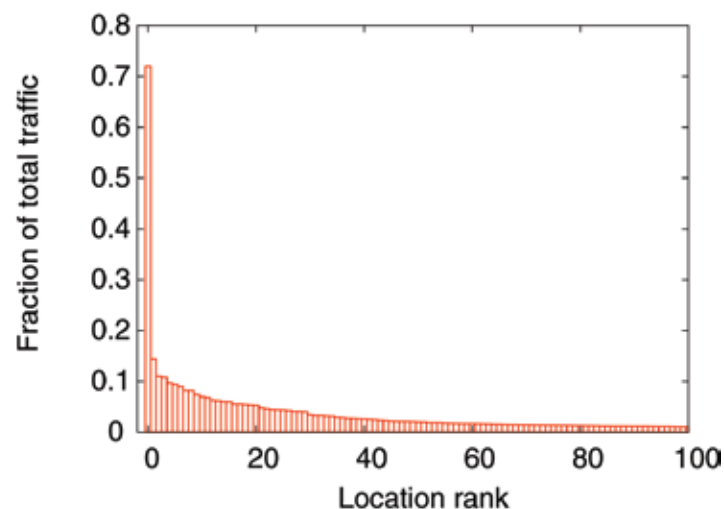


*Fig. 2. Rank of Internet backbone locations based on the frequencies of their appearances on the path of each byte of domestic network traffic.*

### Funding

### Acknowledgments

Department of  
Homeland Security,  
National Infrastructure  
Simulation and Analysis  
Center